In-Situ Monitoring and Control during Laser Powder Bed Fusion of Nickel Superalloys

University of Sheffield

George Maddison

University of Sheffield

Department of Materials Science and Engineering

A thesis presented for the degree of Doctor of Philosophy

December 2018 – November 2022

Abstract

Additive Manufacturing technologies present a pathway to the production of components with uniform properties independent of their geometry. Currently, one of the main barriers to the wider adoption of this family of technologies by industry is the reliability with which components can be printed, particularly with complex alloys that do not lend themselves to processing in this fashion. CM247-LC is an alloy of great interest for its outstanding strength and resistance to deformation at elevated temperatures. This alloy is classed as difficult-to-weld because of its high content of the nickel gamma-prime phase, a key component of its high-strength properties. A series of different experimental methods has been explored in this study to address the predisposition of the alloy to crack on production during the Laser Powder Bed Fusion (LPBF) process. Response-surface methodology has been applied to determine a suitable processing window for the alloy through the altering of laser parameters, using the temperature reading of in-situ sensors to examine the behavior of the material during the process. In addition, the use of a pre-heated build substrate for LPBF has shown a significant improvement in the consistency of the material, demonstrating the effectiveness of controlling the temperature of the powder bed.

Automatic control techniques for LPBF have also been explored, utilizing an advanced neural network to make changes to the laser processing parameters in real-time. This automatic control is demonstrated in this work, showing the power of live process control for the consistent property and microstructural control of nickel superalloys. Further development of in-situ monitoring methods and techniques is also presented, with both co-axial and off-axis techniques providing valuable insights into how CM247-LC behaves during the LPBF process and how these monitoring methods may be integrated into an automatic control system.

"You were made to soar, to crash to earth, then to rise and soar again".

- *Alfred Wainwright*

Acknowledgements

I would like acknowledge both the EPSRC and Siemens Industrial Turbomachinery for their financial contribution to this project.

I would like to thank several members of staff at the University of Sheffield for their continued support. I am grateful to Professor Iain Todd, for his guidance, sense of humour and occasional reality checks. Many thanks also to Drs Kathy Christofidou, Robert Deffley and Gavin Baxter, whose chats and advice have kept me sane during the last 6 months. To Professors Panoutsos and Wilmott of ACSE and EEE and their students and technicians for their outstanding technical knowledge and understanding. Big thanks to all of the staff in the RDC for all of the help you give and those in the Quarrell lab for keeping us all running for the years before the move.

I could not have made it this far without the support and camaraderie of friends both in Sheffield and beyond. Without your experience and support, I would not have enjoyed my time anywhere near as much, particularly the COVID years! I thank you all, for you have all made my time here wonderful in your own ways, but special thanks must go to Dr Alistair Lyle, who taught me so much about the Aconity printers (mostly how to fix them!) and to Dr Felicity Freeman, for your wisdom and common sense throughout the whole of my time at Sheffield.

Deanna, you are a wonderful companion, I cannot wait to continue our adventures together. Thank you for all your support during this time, I love you so much.

Of course, there are those who have supported me beyond the time of this PhD, who have been there for much longer. Words cannot express the thanks and gratitude I have for the wisdom of my Mum, Dad and my Uncle for supporting me through both this journey and beyond. I have eternal gratitude for my Nana and Grandmother and especially my Grandfather too, whose sense of humour, wisdom and determination have guided me (and will continue to guide me) throughout my entire life… and of course where would I be without my unexpected little friend Ponx, who has nuzzled, purred and scratched her way into all of our hearts. Mostly the latter.

I love you all to bits.

Finally, to Yevgeni Brif, without whose sudden departure to Canada I would not be here today. I wish you all the best mate, thank you.

Table of Contents

1. Introduction

Additive Manufacturing Technologies are a vital tool for the production of intelligently designed, high complexity components in a variety of different families of materials. This truly disruptive technology, capable of creating near net-shape parts with minimal post-processing [1], has revolutionised manufacturing despite arguably not yet reaching its full potential. However, despite enjoying rapid advances, there are still challenges to be faced in order to make Additive Manufacturing technologies into a staple part of materials processing [2]. Many materials can suffer from fatal levels of defects when produced through additive processes [3], [4], assuming they can even be printed at all. Nickel superalloys are regarded as a particularly difficult class of materials to work with [5]and provide a major obstacle to the further adoption of additive processes by metallurgical manufacturing industries.

Initially, this project began as a collaboration between Siemens Industrial Turbomachinery and the University of Sheffield. Siemens Industrial Turbomachinery produces blades for land-based turbo-engines, which are often employed in the energy and pipeline industries[6], but also see use in aerospace as well [7]. Turbine blades are commonly made from nickel superalloys due to their high creep resistance and strength at the high temperatures seen in turbo-engines [8]. Hence, the ability to produce highly complex geometries in a single processing step would be extremely beneficial for the company.

The intention of this work was to find a solution to the common problem of cracking encountered in the high-γ' nickel alloy CM247-LC during the LPBF process. However, given the large amount of already existing literature on this subject [9]–[13], it was determined that more novel approaches were needed to find solutions, including those not considered by the industrial partners of the project.

The use of sensors and in-situ monitoring can reveal the conditions under which defects are formed in additive processes [14]. Post-processing and heat treatment of the alloy was not considered as this adds a further degree of complexity and further strains the time allocated to the project, however in-situ heat treatment was considered by using a pre-heated build substrate. This heating technology is highly innovative, with few examples of studies in the literature devoted to the impact that it can have on the LPBF process [15]. Finally, small modifications to the alloy composition can be considered, particularly when examining expensive elements, like hafnium [13], [16] in the case of CM247-LC.

This study consists of two main streams of work. The first body of work details the suitability of novel alloys in AM processes and how those of poor process compatibility may be treated to make them viable for applications where consistency is paramount. The second body of work explores methods of in-situ monitoring and control that may be applied to AM processes, as well as how these techniques may improve both the final part quality and the material properties of the component in question.

Chapter 4 discusses the challenge of 3D printing CM247-LC, a material that has proven extremely difficult-to-weld and process in metallurgy for many years. Response-surface methodology is used to explore parameters, with tensile, material hardness and porosity measurements used to quantify and qualify the effectiveness of parameter changes. This chapter also highlights the ways in which basic monitoring can be used to inform on parameter space for dense components.

Chapter 5 examines the impact and effectiveness of in-situ heat treatment methods on the quality of LPBF-Produced CM247-LC, with an emphasis on processes that are performed without the need to extend the production time of a component. A model is also used to examine melt pool geometries at varying temperatures, to determine if this can be used to predict the quality of a component manufactured at an elevated ambient temperature. Finally, the absorptivity of the material is examined through in-situ measurements of the powder bed, informing on the effectiveness of simulations used earlier in the chapter.

In chapter 6, an explanation is proffered as to the extremely high levels of cracking observed in CM247-LC. This chapter examines the impact of cooling rate and alloy composition on the material's susceptibility to cracking. A set of modified alloy compositions is examined, with a combination of physical tests, monitoring data and micrographs used to qualify the impact of these changes.

The final chapter examines the impact of the use of advanced in-situ monitoring and control techniques to improve the LPBF process. Beginning with the employment of an advanced neural network model capable of altering the process in real time, the possibility of shortening the development time for novel alloys is demonstrated, with tangible results. However, the importance of controlling further parameters in-situ is also illustrated, using component surface roughness and porosity as an indicator of the impact of small changes in parameter choice.

2. Summary of Relevant Literature

2.1 Additive Manufacturing Processes

Additive Manufacture refers not to a single method of production, but to a family of similar processes that share common features. These processes are characterised by the fabrication of parts through the addition of material. According to the American Society for Testing and Materials (ASTM) AM is defined as:

"[The] process of joining materials to make parts from 3D model data, usually layer upon layer, as opposed to subtractive manufacturing and formative manufacturing methodologies"[17].

Whereas other methods of manufacturing involves the removal of material, additive technologies construct through the addition of material in short intervals, often on the order of tens to hundreds of microns in thickness [10], [18]. There are numerous ways to implement this style of manufacture and the technology varies for different families of materials. Very often, the material feedstock for these technologies takes the form of a powdered or particulate material, but can also take the shape of an extruded material, like wire [19]. Parts that are to be built using these technologies are designed using CAD software, then uploaded into the printing system to provide instructions for building on a layer-by-layer basis. DED processes often use layer thicknesses around 200 microns in thickness, but in LPBF these layers are normally between 20-100 micrometres in height, meaning that parts may be composed of hundreds, if not thousands of individual layers. Because of this, 3D printers can take a long time to produce their components.

Many of the materials used in these processes can be extremely dangerous if handled improperly and have been shown to have carcinogenic properties, meaning there may be a long-term human cost to progress in this field, if careful (and often expensive) steps are not taken [20]. There are also scientific and engineering challenges to the wider adoption of AM. Materials such as polymers are amenable to AM processing methods [21], likely due to the lower temperatures required to fabricate parts and the lower property requirements faced by this material family [22], [23]. Metals on the other hand often (though not always [24], [25]) require much higher temperatures to process, often on the order of hundreds if not thousands

of degrees Celsius. This, in addition with specific microstructural and alloying issues can be a source of frustration when trying to process more “difficult to weld” or novel alloys [26], [27].

Whilst metal AM has been shown to be capable of producing high-quality components and even superior ones to industry staple methods, its biggest barrier currently is in consistency. Due to the discrete nature of metal powders - the primary feedstock for most metal AM processes - there is a very large degree of uncertainty in produced parts caused by the often highly stochastic powder [28], [29]. Powder must be used carefully and be properly maintained to prevent issues such as oxidation or contamination from having a deleterious effect on either a microstructure or the component itself. Even if the powder is of high quality, defects present in the powder bed from poor spreading or component swelling may cause significant damage to both the fabricated part and the printer [30], [31]. In addition, poor processing parameter choices for parts can cause failure from swelling or can seed defects throughout the material [32]–[34].

To further advance the sector, artificial intelligence and automatic control systems are now being considered within industry as a method of controlling and even repairing parts during their fabrication [35], [36]. These techniques have their basis in the principle of machine learning, a set of computational techniques that can provide insight into numerous fields of scientific research [37], with data being captured from the input feedstock manufacture [38], during the process itself [39], [40] and the final product output [41], [42], rather than just the latter. Parts are designed not just with shape freedom in mind, but also with the desire for “Topology Optimisation” [43], [44], where an additive component can be made stronger through computer simulations and automatic design.

2.1.1 Laser Powder Bed Fusion

Laser Powder Bed Fusion (LPBF) – or Selective Laser Melting (SLM) as it is also known – is a process characterised by its use of a reservoir of powder feedstock to manufacture parts (figure 1).

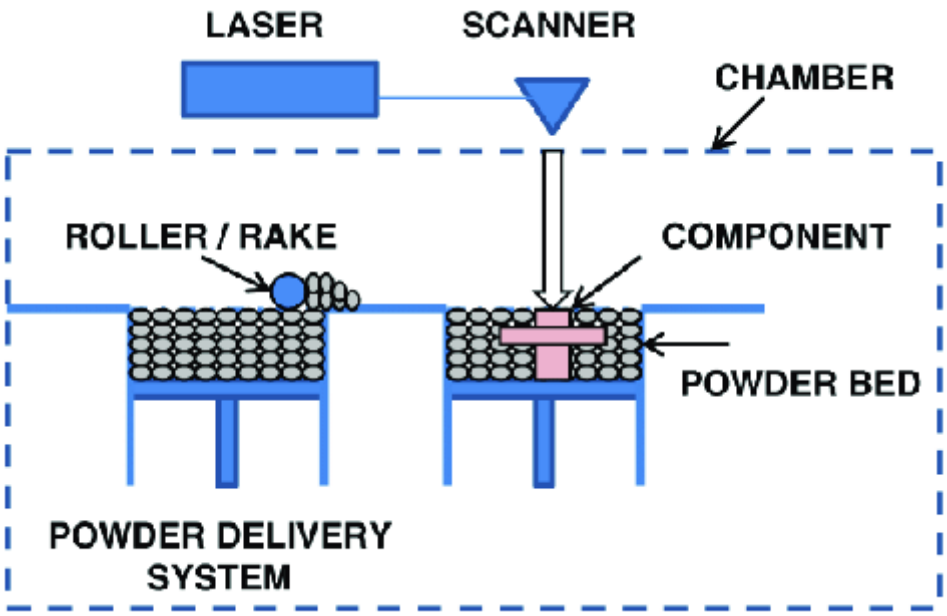

Figure 2.1: A basic schematic diagram of an LPBF system [45]. *The powder delivery system in this case is an identically sized piston hopper, which moves upwards with each layer to dose more powder into the build volume.*

Powder is manually loaded into a hopper or other receptacle and is then dosed in set small amounts into the building chamber. A wiper or rake then sweeps the dosed powder across an area that sits beneath a high-power laser. This laser is then used to melt the powder into the shape desired. During the process, the build chamber is either flooded with inert gas, or has the atmosphere removed via vacuum pump. This cycle is then repeated, with the laser-exposed shape potentially changing with each new layer. This continues until the component part is fully constructed, at which point it is removed from the chamber. Whilst normal is limited to one material *per build*, there is no limit to the type of material that can be processed. However, recent advances in powder deposition techniques has allowed LPBF printers to expand their scope into multi-material operations (figure 2.2). The downside of this is the level of powder scrappage, which is greatly increased and negates the benefit of the reduction in material usage.

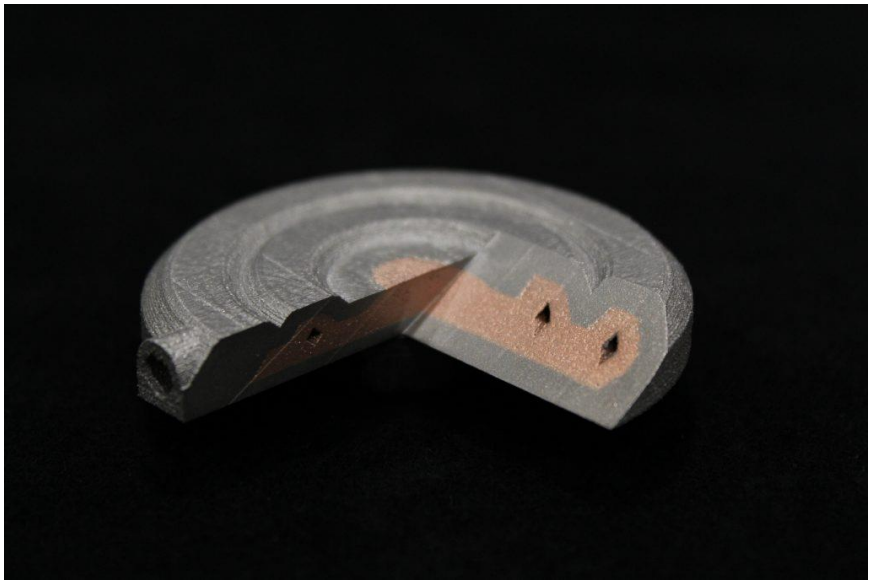

Figure 2.2: A multi-material LPBF component produced by Aerosint technologies [46]. *This advance in deposition technology greatly improves the versatility of the LPBF process, but does affect the scale to which material can be saved from traditional manufacture, due to remnant powder contamination.*

LPBF printers may also have (or can be retrofitted to have) a pre-heated substrate. In standard operation, the build substrate is a block or plate upon which the material is deposited. This promotes bonding between the substrate and the deposited material, providing an anchor for the printed material. It remains at an ambient temperature throughout the build, heating up very slightly from the energy that passes through from the laser. Because it is often a large section of material, thermal energy is conducted away very rapidly, meaning that it acts as a heat sink. The melted material in contact with the plate therefore solidifies very rapidly [47]. If manufacturing steels, or precipitation-hardening alloys, this may be undesirable for property tailoring, so heating the substrate becomes a desirable option to provide control over cooling rates. Furthermore, the heating of the substrate may be maintained for longer or shorter periods, meaning that the cooling rate can be controlled to promote particular microstructures. Many systems noted in literature have utilised resistive and induction heated substrates. Whilst these are easy to produce and use, they are often limited in terms of the amount of heat they can produce [48].

One final problem for LPBF is industrial scaling. Because a reservoir of powder is required to build the component, successively larger chambers require an ever-increasing amount of powder to manufacture larger components. At larger scales, powder dosing becomes difficult due to the quantity required and the size of the powder rake needed. Larger chambers also take longer to degas, making them increasingly more expensive to run on a larger scale due to the quantity of inert gas required to regularly cycle the atmosphere inside the chamber [49].

2.1.2 Directed Energy Deposition

Directed Energy Deposition (DED) is a form of AM that does not rely on a powder bed to manufacture parts, instead using a feedstock passed through a nozzle to place the material where it is desired (figure 2.3). A laser or other suitable energy source is used as the material is applied to melt it, fusing the newly applied material to the substrate or the previously built layer. This process is capable of producing multi-material parts, as new feedstock can be supplied at will to alter the material being sent to the nozzle. With this versatility and precise application of powder or wire, this technology is capable of producing complex parts similarly to powder bed processes, but its real strength lies in the field of component repair. Material can be applied accurately to complex parts such as turbine blades or blisks, allowing for repair and requalification for service, which can drastically reduce material wastage and cost. This technique can also clad newer materials to older base components, providing a platform for novel material testing in applications for functional grading of materials [35], [50].

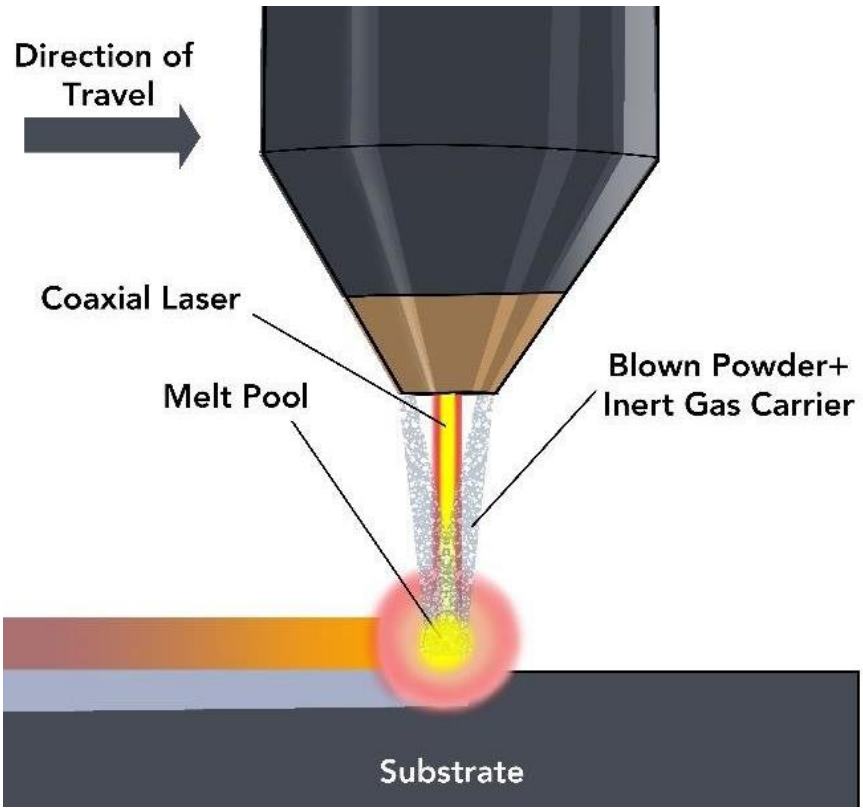

Figure 2.3: A schematic diagram of the DED process [51]. *Whilst LPBF requires a full degassing process, the larger chambers often used in this technology mean that the volume of inert gas required for this is unfeasible with industrial timescales so, local shielding is more regularly used to prevent powder flash fires.*

2.1.3 Melt Pools and Weld Tracks

As the laser passes across a layer of powder, powder that melts forms a pool at the site of laser incidence. As the laser moves through the powder, the pool effectively "moves" with the laser, causing the molten liquid metal to stretch into a teardrop shape (figure 2.4) [52]. The trailing material begins to solidify once the energy source has left the immediate vicinity, forming a solidified track similar to that of a weld bead (figure 2.5) [27].

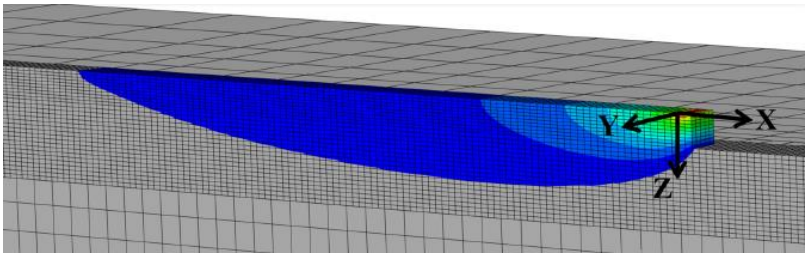

Figure 2.4: FE model of a moving melt pool that has stretched into a teardrop shape [52].

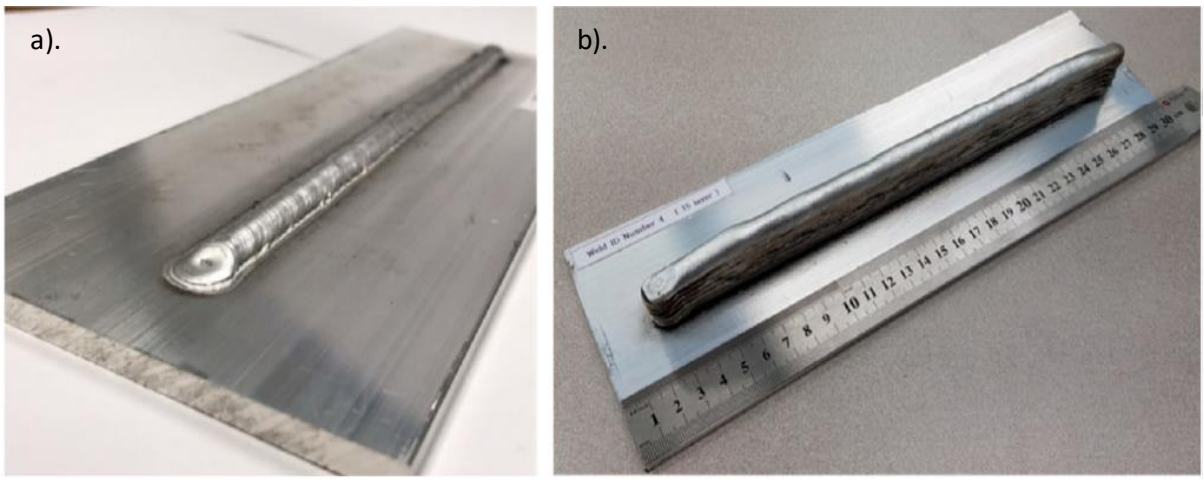

Figure 2.5: a). A single aluminium weld bead, b). a series of stacked weld beads atop one another [53]. *This technique of material deposition is the basis for much of additive manufacturing, where deposited material is "welded" together with a laser*.

Once the laser reaches the end of the geometry it has been told to melt, it may turn and pass back towards its original starting point if performing a meandering hatch. As the material passes near to a previously melted region within the same layer, this previously melted region may begin to either melt or be affected by the heat similar to the HAZ in welding. Melt pool tracks are often intended to overlap with one another to ensure total consolidation of the powder feedstock (see figure 2.6). The degree to which melt pools overlap requires knowledge of the width of the melt pool (for given parameters). Because of this, melt pools of scan tracks

produced from single layers can be used to determine both the necessary spacing of the hatch lines and the layer thickness to promote full consolidation.

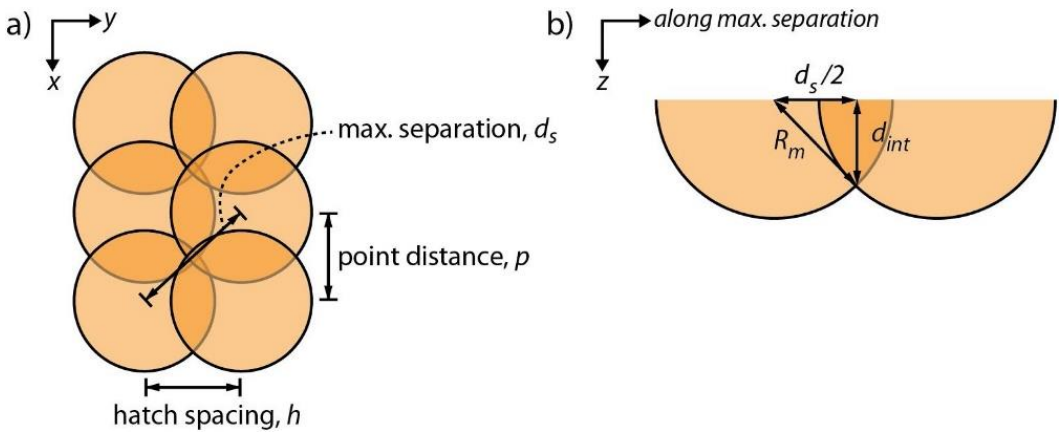

Figure 2.6: An example of how melt pools should overlap viewed as a). top-down and b). in plane [54]. *The overlap of melt pool tracks ensures that the powder bed is fully consolidated.*

If the laser in the LPBF process is too energetic, or if the laser does not scan quickly enough, too much energy can be imparted into the material. This can result in a phenomenon known as keyholing. In keyholing, the laser energy is too high for the material to conduct away, resulting in a very high local material temperature in the melt pool. If the temperature in the melt pool exceeds the evaporation temperature, then a void will begin to form underneath the powder layer that fills with plasma and vapour. This traps radiation and further exacerbates the rise in temperature, meaning that the melt pool can then go from a stable conduction mode (figure 2.7a) to a keyholing mode (2.7b). Transferring into keyholing mode means that pores are seeded into the material at regular intervals, as the laser effectively bores through the material and evaporates the lower regions. In this instance, vapour is trapped under the powder layer, forming a region of high pressure. This is a phenomenon often seen in the welding of solid metal sections, however in powder-based processing, this is often fatal for the manufacture of fully dense components. The shape of the weld bead also changes from a shallower, more hemispherical shape, to a much more elongated and stretched pool. This elongation of the melt pool can also cause cracking on solidification, due to the stresses involved between it and the surrounding material.

In LPBF, the top surface of a component is often highly reflective, as during melting, the surface tension produces a smoother surface to solidify. However, the top surface can still be very bumpy or rough. A process known as "balling" (figure 2.7d) can occur throughout builds produced in LPBF. This is caused primarily by unstable melt pools, causing partially or fully melted powder particulates to be ejected out from the melt pool. These particulates rapidly become spherical due to their surface tension in their liquid form as they travel through the

build chamber, before solidifying and dropping back to the build volume. These small spherical balls of material can be seen both on top surfaces and within solidified material. When the wiper blade sweeps the next layer of powder, these can damage the wiper blade, component or both through friction.

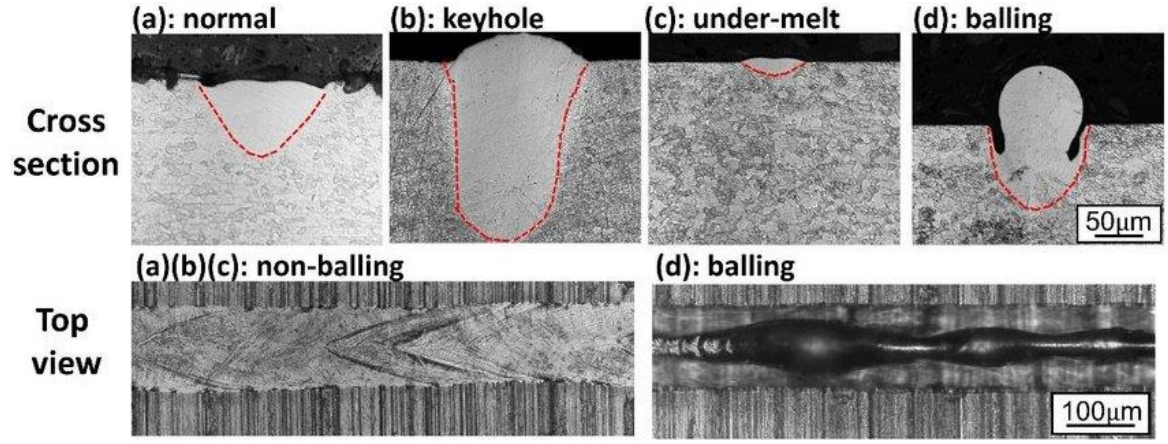

Figure 2.7: Examples of commonly encountered melt pool shapes in LPBF [55]. *a). A normal melt pool, b). a melt pool produced with higher energy, causing a deeper and more unstable pool, c). the opposite; insufficient energy has been supplied to the material to melt the powder, d). enough energy has been supplied to melt the powder, but the scan speed of the laser is too fast.*

2.1.4 Electron Beam Melting

Electron Beam Melting (EBM) is a similar process to LPBF [56]. Rather than using a laser to melt components however, this system uses an electron gun to fire a stream of electrons into the powder in a similar fashion to LPBF [57]. Because electrons cannot travel through gas of atmospheric pressure, a vacuum must be used to allow the beam to travel freely, rather than an inert atmosphere.

Due to the nature of the process (i.e. the use of electrons), only metal powders can be processed using this technology. However, this does mean that alloys with extremely high affinity for oxygen, or high reactivity in atmosphere can be more easily processed. The most common example of this is for titanium alloys, which are highly reactive with oxygen even at room temperature. However, the vacuum chamber limits the size of the build volume, as the larger a vacuum chamber is, the more difficult to manufacture and fully evacuate it becomes.

Electrons also interact with metal powder differently to a laser beam, often penetrating deeper into the material. These electromagnetic interactions can be catastrophic however, as an electrical charge build-up within the machine can cause powder (sometimes at temperatures of several hundred degrees) to be ejected from the powder bed in a phenomenon known as "smoking", which can cause the scattering of the powder [58], [59]. The powder bed itself is also different to LPBF, with powder sizes ranging from 45-90 microns rather than 15-45 microns. This powder size range, coupled with the larger beam size, means that the most fine of details for components are easier to manufacture using a laser-based system [60].

One advantage this method of production has over LPBF is the speed at which components can be fabricated. Because the electron beam is controlled by a magnetic field, the beam can be manipulated and controlled near-instantaneously, making toolpathing of complex geometries extremely fast. This differs from laser-based systems that rely on a type of galvanometer. Galvanometers (or galvo-mirrors) use electrical currents but require the physical movement of a component to direct the laser to its target, meaning that response time is longer, resulting in longer build times for components.

2.1.5 Metal Powder Manufacture

Many commercial additive processes require the production of a powder feedstock. Metal powders for AM are most commonly produced via gas atomisation, but are not limited to this alone. Both attrition milling and plasma atomisation are also options for powder manufacture, with each of these processes producing different powder morphologies.

Atomisation (figure 2.8) is the most common method of powder production. This process uses induction heating and can melt material in several different forms of feedstock. As the material melts, droplets of molten material detach and fall from the bulk material. These droplets fall through a high-pressure gas flow, which scatters the droplet, causing the metal to solidify into powder particles. These particles solidify into a range of sizes, providing feedstock for numerous near-net shape and additive processes. However, many processes require a specific range of powder sizes – for example, some powder bed based systems often use a powder size range of 15µm-45µm, whereas directed deposition systems often use larger size ranges such as 45µm-106µm. Larger powder sizes can be used in other near-net-shape manufacturing processes, such as FAST, a process that can even use coarser swarf from machining to produce re-consolidated material [61].

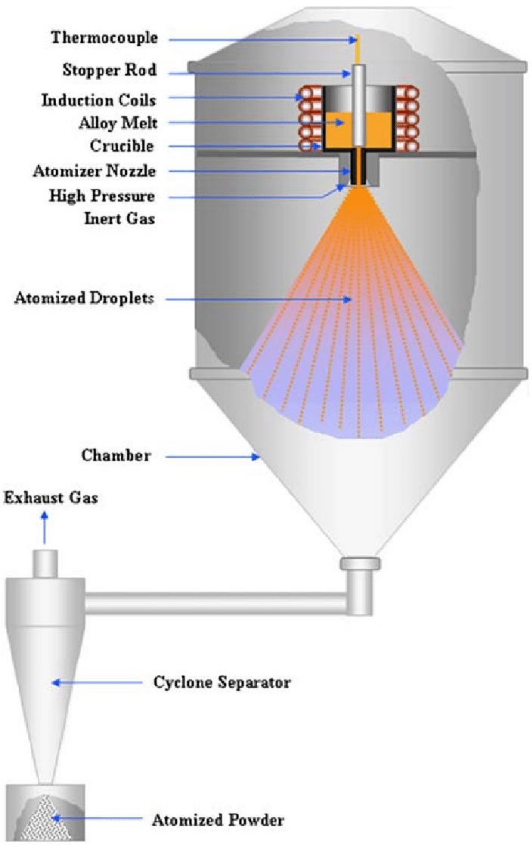

Figure 2.8: Diagram of a gas atomiser for the manufacture of metal powders [29].

In order to manufacture significant amounts of a particular size fraction, powder can be milled (depending on the hardness of the material) to reduce the average size fraction of a powder batch. Whilst this can be effective at reducing the size of the powder, it can also change the morphology of the particles. When gas or plasma atomised, metal powder is often highly spherical due to the high surface tensions involved due to the size of the particles. However, when water atomised or physically milled, these particles can become irregularly shaped from impacts. This irregularity can cause changes in particle surface area and thus surface chemistry. More importantly for AM, irregular powder particles may result in the particles becoming interlocked, which can adversely affect powder flowability and may result in the process being unviable in turn [30].

To rectify powder irregularity, powder can be processed through a spheroidiser. This process is similar to the original atomisation process, where powder can slowly drop through a funnel. Rather than using a rapid jet of gas however, this process uses plasma and an induction coil to rapidly melt falling powder. This rapid melting and re-solidification causes irregular particles to gain or regain a spherical shape, again due to the level of surface tension of the liquid droplet [31]. Spheroidised powder often requires further treatment however, as satellites are a common by-product of the process, requiring removal from the final powder batch. To achieve this, powders are "washed" in water then dried in a vacuum oven to remove the water. This detaches or flushes away many of the small satellites meaning that powders are then useable in AM processes.

2.2 Additively Manufactured Microstructures

2.2.1 Grain Growth and Orientation

Because components in LPBF, EBM and DED are manufactured in one particular direction - referred to as the "build direction" - they form columnar grains that are similar to those observed in directionally solidified [62] parts made using casting in a Bridgman furnace (figure 2.9). When new layers are deposited, the laser melts this new material, but also re-melts (or partially re-melts) the previous layers. This means that as a components is constructed, there is a general temperature gradient along the build direction. Because of this, the solidification process causes the grains to grow upwards in the build direction. Very often, these structures are made up of small "cells", caused by the extremely rapid cooling present in the LPBF process. These cells grow along the direction of the travelling melt pool. However, when the previous layers beneath the powder are remelted and recrystallised, they form grains that grow upwards towards the top layer – and the source of heat. This natural orientation of grains in the <100> direction provides a form of anisotropy in material properties.

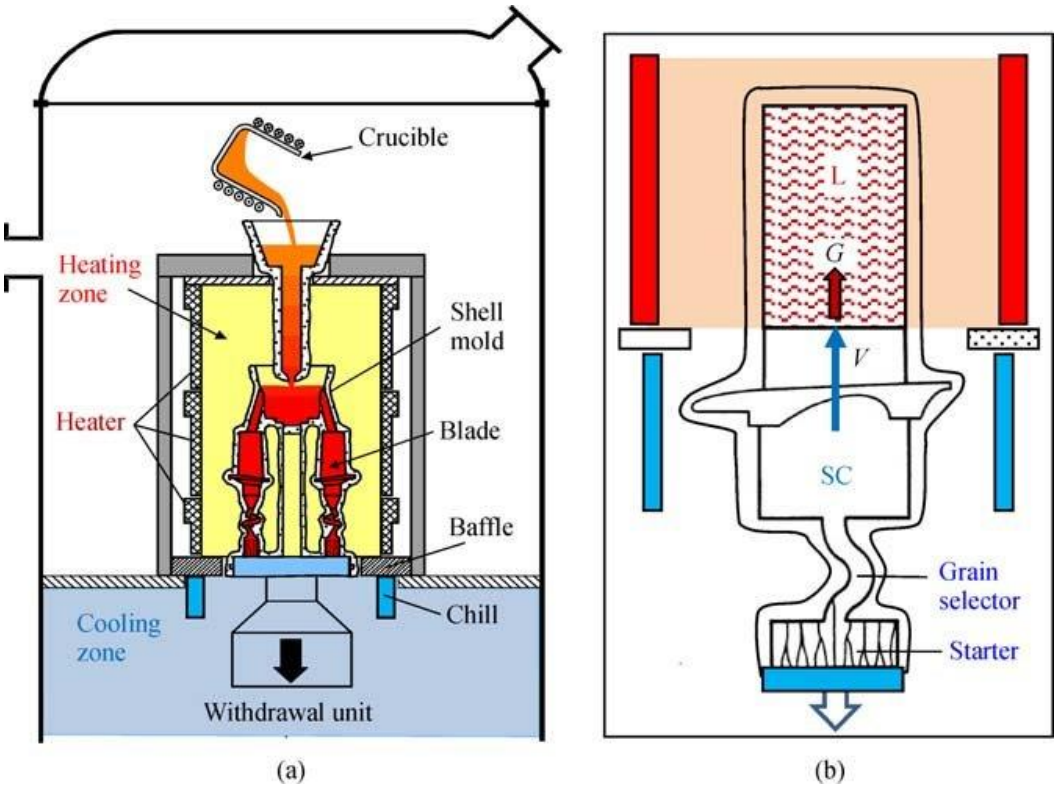

Figure 2.9: a). A directional solidification Bridgman furnace and b). the interior of a single-crystal selection furnace [63].

This anisotropy in grain structure further bolsters nickel alloys' suitability for use in turbine blades. Given that the majority of grain boundaries run perpendicular to the direction of the loading force, it is much more difficult for dislocation movement and slip to occur, particularly with the extremely high level of grain boundary strengthening that is present in high-temperature nickel superalloys.

In nickel superalloys, grain boundary effects provide a significant source of strength. Because the nickel family of alloys harden through precipitation, many alloy additions also find their way to grain boundaries. Commonly, various carbides and borides are found at grain boundaries in nickel superalloys. These carbides are often highly refractory, owing to their content of carbon and often ceramic nature, meaning that they can be extremely hard and rigid. Some, such as hafnium carbide, behave more like ceramics than metals. Because of this, these compounds provide a great deal of strengthening, but also serve to embrittle the material in some circumstances when internal stress becomes too high.

As in many other materials, grain boundaries serve to slow down dislocation movement through material, causing the dislocations to "pile-up". This results in material strengthening. Given that the more ceramic-like and refractory elements tend to segregate grain boundaries, they also serve to maintain the coherency of these alloys at elevated temperatures.

2.2.2 Slow and Rapid Solidification

In idealised solidification, alloys are considered to cool gradually from a given elevated temperature above the liquidus, to a temperature below the solidus. Consider the Fe-C phase diagram (figure 2.10).

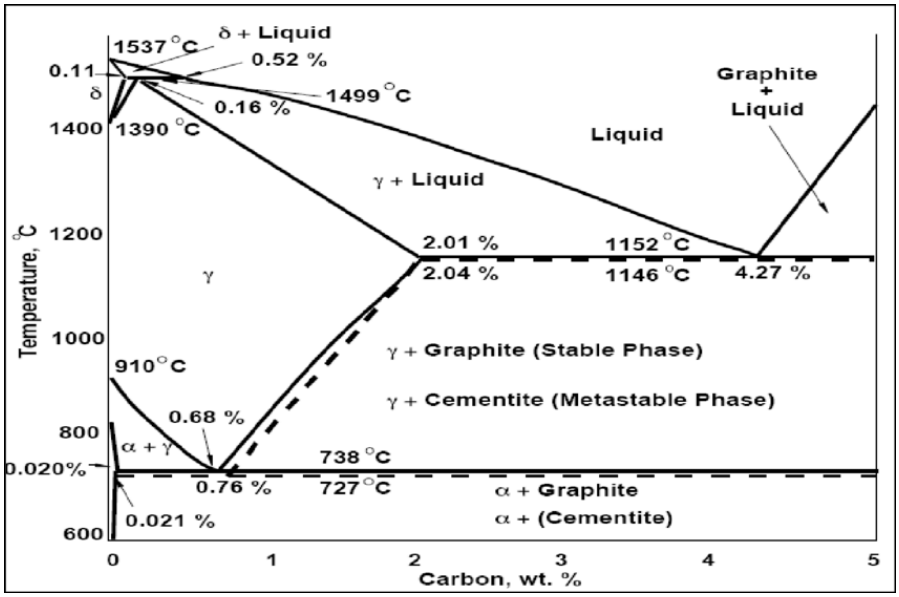

Figure 2.10: The Iron-Carbon binary phase diagram [64]. *This diagram is a relatively simple phase diagram commonly used to illustrate fundamental principles.*

Depending on the specific combination of the two elements, solidification will produce different phases as cooling takes place. If the solidification occurs slowly, at rates less than the order of centimetres per second, each phase has time to form an equilibrium as it solidifies, meaning that processes such as segregation can occur as the specific composition of different regions changes over time. This is the case for a material such as bainitic or pearlitic steels, which require time at elevated temperatures to form alternating laths of high and low carbon content (cementite and ferrite). If solidification happens very quickly however, the material does not have time to form an equilibrium phase as it cools. Instead, solidification occurs faster than most elements can diffuse, resulting in little change as the metal freezes. This can result in metastable microstructures being formed, such as retained martensite in low carbon steels because of quenching.

Due to a combination of factors, solidification in AM processes is faster than most other thermomechanical processes [47]. The size of the heat source, coupled with the substrate material's effect as a heat sink results in a very fast extraction of heat from the melted powder

layers. Because of the very high speed that the laser scans at – and thus the solidification front –, the melt pool typically does not remain liquid for very long in any one place. This causes the material to undergo rapid solidification, similar to undercooling in traditional manufacturing processes.

In slower solidification processes, a solidification front may move slowly enough for diffusion of atoms and molecules to outpace it. In this instance, certain elements that diffuse more quickly than others may stay ahead of the solidification front. As more material is solidified, the total concentration of the fast diffusers in the molten material increases, until the solidification front finally catches up. This results in regions of material that are enriched with certain elements, which is characterised by the lever rule [47].

In the case of a rapid solidification scenario, the freezing front may move too quickly for even the faster diffusing elements. In this instance, the elements are trapped where they were in the liquid phase, resulting in a much more even microstructure. These two methods of cooling are seen in different thermomechanical processes such as quenching or age hardening, which both provide very different properties from the same material. Because rapid solidification can produce results that vary drastically from slow cooling, it is characterised by Scheil solidification [47].

An exception to this general regime of undercooling in LPBF can be seen where pre-heating substrates are employed. The intention of these systems is to act as a way of slowing the cooling of the material being processed. At higher temperatures (depending on the material being processed), this can also act as a way of performing heat treatment within the manufacturing process itself (in-situ). An example of this can be seen in Renishaw systems, where a resistive module can be used to heat the substrate up to around 250°C. However, this is still relatively cool for metal processing and serves only to slow the cooling rate, rather than to act as a form of in-situ heat treatment. Most materials require much higher temperatures to promote recrystallization or recovery [65].

When metals are rapidly solidified, the microstructure that is formed contains precipitates that are more evenly spread out and far smaller than in processes that involve heat treatment or directional solidification. This can provide benefits to certain alloys that are "difficult-to-weld", such as nickel-based alloys. The reduction in large precipitates from rapid solidification means that dislocations and defects can slip and move through the material more easily. Whilst this effectively reduces the strength of the alloy, it also makes the material far more workable where machining is concerned. However, rapid solidification is not without its problems. In steels, rapid solidification produces martensitic phases [63]. Whilst these phases are very hard, they also serve to embrittle the material. This embrittlement is caused by the transformation of the phase from an FCC to a BCT cell structure. This change in volume causes interfacial stresses

between the phases present within the material, effectively reducing the energy required to cause brittle fracture. Similarly in CM247-LC, though at a higher temperature between 600°C and 850°C, a phase change occurs, resulting in a significant change in volume and the creation of very large interfacial energies at the boundaries between phases [66]. This is further exacerbated if precipitation occurs, as the matrix struggles to contain the far more numerous and large particles of γ' without cracking.

In instances of material processing where cooling is faster, the formation of dendrites is a common feature of solidification [47] and one that can be detrimental if not carefully controlled. When complex metals such as nickel superalloys solidify, local instabilities along the solidification front can cause the formation of primary and even secondary dendrites [67]. These branching arms grow as solidification continues and as the dendrites themselves grow wider, the space between becomes smaller and smaller. At this point, the specific alloy composition plays a major role. Those elements with low solubility will be left in the small liquid region that remains between the dendrites. This form of elemental segregation results in a region that cannot accommodate the strain of metal shrinkage. These are known as liquid films and are a common site of initial micro-crack formation that occurs when the internal stress exceeds the local strength of the material.

This problem is exacerbated in complex chemistry alloys, as these materials often have wide solidification ranges, providing more time for the liquid films to form. The Scheil model of solidification can be used to calculate phases present during the solidification process. What is also apparent from this graph is the sheer complexity of the solidification path and the number of potentially deleterious phases present in this material, including laves, tau and numerous carbides, which can further aggravate the cracking situation.

In LPBF, most microstructures seen consist of cells – dendrites are generally not common in a final product except in regions where powder particles have not been fully melted. Cells act as the initial nucleation site upon which dendrite arms can grow along crystallographic orientations. Because of this, cells can be considered as "primary dendrite arms" when considering spacing for calculations involving determination of liquid film stresses. Davies et.al [67],[68],[69] developed a model to determine the primary dendrite spacing by examining the microstructure of IN718 under different solidification conditions (equation 2.2).

$$\lambda_1 = (97 \pm 5)\dot{T}^{-0.36\pm0.01} \qquad \text{(Equation 2.2)}$$

Where $\dot{T}$ is the cooling rate in the material. A rearranged version of this equation will be used in chapter 6 to estimate cooling rates of a nickel alloy.

If the solidification front velocity is assumed to be equal to the velocity of the melt pool, then the following can be stated:

$$\dot{T} = GV \qquad \text{(Equation 2.3)}$$

Where G is the thermal gradient of the material and V is the laser scan velocity. This is assumed to be true at the tip and tail of the melt pool. However, this is only the case for a solid that is growing parallel and in the opposite direction to the moving heat source. When the laser changes direction at the end or beginning of a meander hatch, the heat and melt pool changes direction. If hatches are overlapping during this change in direction, then this relationship completely breaks down.

2.2.3 Material Defects

In terms of material defects, there are two major classes that are commonly seen in LPBF: cracks and voids. Both of these different types of defect have numerous subgroups and can form in a multitude of different ways. They often require parametric studies to eliminate them from fabricated parts. They are also not necessarily mutually exclusive – several of these can appear in any one sample under the correct circumstances.

2.2.3.1 Voids

There are three main types of voids that can form, with each being formed from different effects. They also range greatly in size, the smallest being sub-micron; their only upper limit is the size of the part itself.

Lack-of-Fusion occurs when the powder layer does not fully or properly adhere to the previous material (figure 2.11). If insufficient energy is supplied via the laser, powder has the potential to not fully melt and thus not fully adhere to the previous layer. LoF can also be caused by irregularities in the level of the powder bed in the build volume [70]. If a component swells above the powder bed, this can cause damage to the wiper blade or rake, which in turn adversely affects the spread of powder. If powder fails to spread to the site of the component manufacture, the component will not build correctly and large LoF voids will be seen in the subsequently manufactured material. Common features of LoF are long elongated regions of porosity that run along or in line with the powder layer, often with clearly visible powder particles that have not fully melted (figure 2.11).

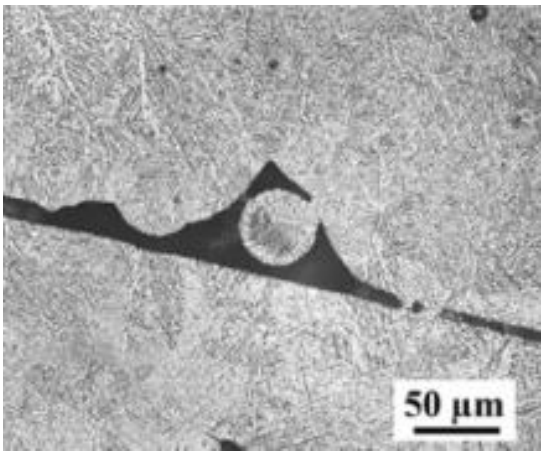

Figure 2.11: Lack of fusion defect in Ti-6Al-4V produced by LPBF [57]. *The circular object in the centre is a powder particle that has failed to melt during the process.*

Gas porosity is a less severe though still undesirable type of defect. This defect often takes the form of smaller, more spherical pores than LoF. It arises mainly from defects in the powder feedstock from the powder atomisation process (figure 2.12) and from evaporation of volatile elements during the process [71]. Particularly with gas-atomised powders, small pores of gas can be trapped within the powder particles during formation or particle collision. When these particles are melted in LPBF, the gas trapped within the reformed material does not always have time to escape and thus remains after solidification.

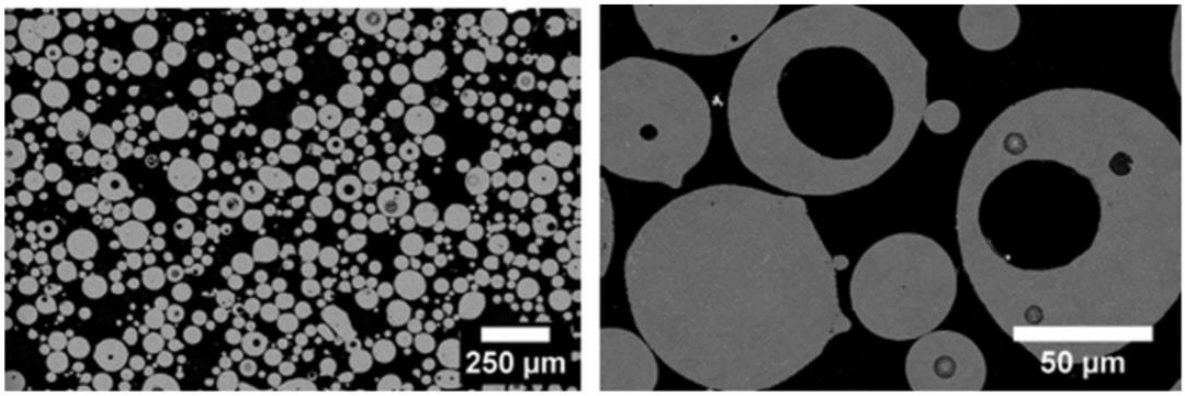

Figure 2.12: Porosity present in MAR-M-247 powder. This type of porosity is formed during atomisation and is then re-introduced during the LPBF process [72].

Keyholing occurs when too much energy is imparted via the laser [73]. A phenomenon often seen in laser welding, this defect has a detrimental effect on part quality. If too much energy is provided by the beam, the melt pool can become unstable. This instability gives rise to gas and plasma becoming trapped underneath the surface of the material, producing large, irregular but still highly spherical pores underneath the supplied powder layer (figure 2.13).

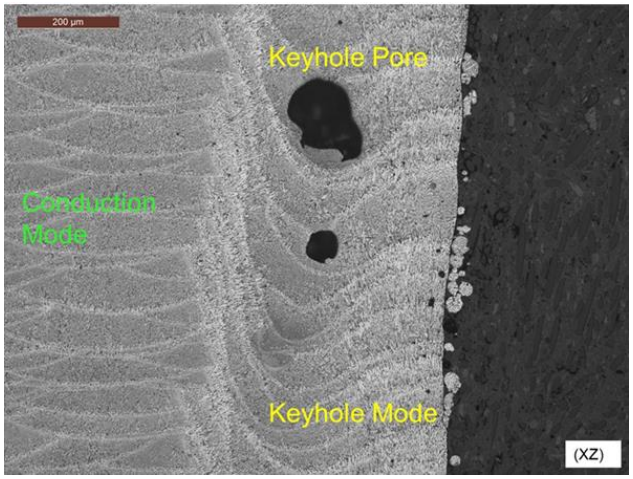

Figure 2.13: Micrograph of AlSi10Mg produced by LPBF [74]. *In this instance, the laser weld bead has gone from conduction to keyholing mode, producing defects and a very different microstructure.*

2.2.3.2 Cracks in AM

Cracks and micro-cracks are one of the most common form of defect found in Additively Manufactured components. The predisposition of a component to suffer cracking in LPBF is far more dependent on specific material or alloy composition, but does still rely on parameter choice from the user to determine the correct processing window to remove these defects. As with voids, there are several different types of crack mechanisms [75].

Liquation cracking is a type of weld defect that can also be formed during AM processes. This defect commonly forms in the region between the melt and the HAZ, where high stresses are produced during solidification. It is often characterised by a crack that runs along the perimeter of the weld bead (figure 2.14). In AM processes, liquation cracking can occur if thermal stresses become too high. This often happens as a result of the laser re-heating the previous layers, resulting in very thin liquid films being produced in interdendritic regions [hassan x]. These liquid films have very high stresses and can result in crack formation.

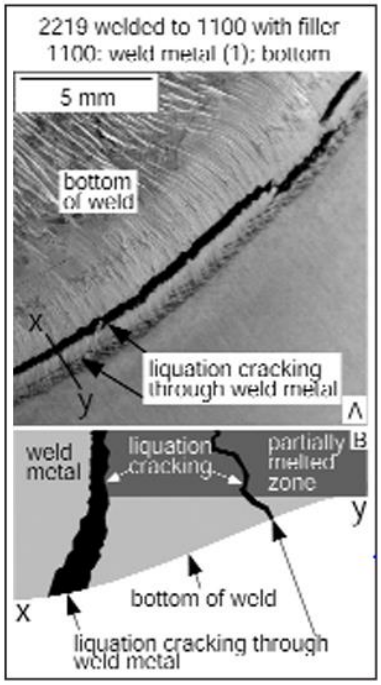

Figure 2.14: Liquation cracking as illustrated by Huang and Kou [76]. *As described, these cracks often run close to the melt pool boundaries.*

Solidification cracking occurs in welding and is regularly seen in laser-based AM processes. This type of crack is produced during the solidification of the molten material and is produced as the last liquid films solidify. As the last solidification occurs, stress builds up in the material because of metal shrinkage. During earlier solidification, this is offset by the presence of liquid metal still undergoing the solidification process, which feeds into the solidification front. However, at the end of solidification, there is no more liquid, meaning that the stress increases rapidly.

This stress causes rupture and the resultant crack is often seen where grains have grown into one another, such as at the centre of the weld track or melt pool. This phenomenon is also known as hot tearing in AM and is seen most commonly at grain boundaries [77], [78]. Because of this, they often run along the direction of grain growth, which in AM is the build direction (figure 2.15). Because this type of crack is formed by alloys during solidification, the length of time solidifying plays a critical role. Because of this, many models designed to describe solidification cracking involve examining the length of time the alloy requires to solidify – such as the Clyne Davies model [67].

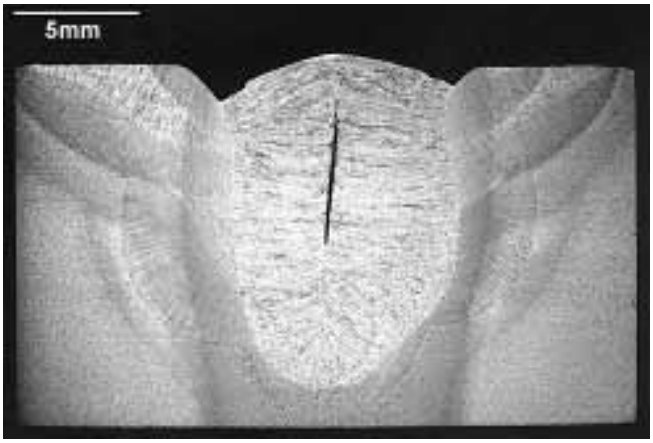

Figure 2.15: Optical micrograph of solidification cracking occurring within a weld bead [79]. *This cracking can occur along the entire length of the weld bead if the conditions are right, making it potentially an extremely destructive mechanism.*

Strain Age Cracking has been observed in numerous precipitation hardening nickel alloys and is a common cause of cracking for CM247-LC. This type of cracking occurs most often during heat treatment as γ' precipitates are formed. As these precipitates begin to form, the ductility of the material naturally drops as a result of dislocation pinning. As the material heats up during the heat treatment, the material forms residual stresses as the grain boundary segregating carbides begin to form. If the material is then cooled too slowly, too much γ' will form and will cause fracture, before the stress relief temperature is reached [Hashmi x].

Material defects is one of the largest areas of research in all of materials science. The susceptibility of a material to suffer from defects can be the most important factor for selecting a material in specific applications. Many - though not all - nickel superalloys are known for their severe predisposition to cracking, which has long been tied to the content of gamma prime within the alloy [80].

Most methods of processing metals have associated defects that can occur if the process is not correctly controlled or otherwise improperly carried out. In metal casting for example, a part may crack if cooled too quickly due to the creation of internal stresses. Casting defects are common, particularly in complex shapes. AM processes are no different. Depending on how aspects of the process such as the laser parameters are controlled, defects may be sporadic, may dominate the material completely or somewhere in between [81]. It is vital for an understanding to be established as to how each type of defect arises and how they can be prevented in order to reduce their impact on final component properties [82].

In AM research, this has been performed previously using normalised processing maps and by cataloguing the parameters that produce particular defects. An example of this can be shown with density measurements. By plotting the density of a component against the laser parameters used to produce it, it is possible to determine not only the effect of individual parameters on density, but of combinations as well [83]. These plots often take the form of contour plots, where different colour shades denote differing levels of part density. Further processing windows can be determined using energy density as a tool, however energy density alone is not sufficient to make an informed judgement on parameters. More recent research has utilised in-situ monitoring systems as a method of collecting data that can be used to create response-surface plots and determine processing windows.

Loss or leak of the protective atmosphere or vacuum can cause unwanted elements (such as oxygen) to enter the system. In extreme cases, this can cause the process to be automatically halted – in order to prevent a powder fire – but normally causes embrittlement or oxidation of the component if the process continues during a smaller ingress. Component warping may occur if the manufactured component is not properly designed. This form of defect is often dependent on the choice of substrate to build on. As long as a similar material to the feedstock powder is built upon, the material will form a bond to the baseplate similar to that of a welding joint. Any distortion of parts, regardless of its cause, will in turn cause damage to the wiper blade, which then has the effect of creating a feedback effect as tracks are left in the powder bed, further exacerbating the problem. A part that is not sufficiently anchored in place can also be swept away by the wiper blade as it doses the next powder layer, which is a fatal event in any build.

2.2.4 The Impact of Part Geometry

AM processes are distinguished from traditional manufacturing methods by their ability to produce highly complex components in a single step. The geometries produced by these processes are near limitless, with software packages developed solely for topology optimisation. Whilst this is a unique selling point of this family of processes, there are some limitations to current 3D printers.

Consider the geometry of a tensile test piece (figure 2.16). At first glance, this geometry appears to be trivial. However for LPBF, there are multiple considerations to be taken into account before a part can be built. The first is the orientation that the component will be built in. For the tensile bar, the two most common orientations would be or vertically, or horizontally. Either of these presents a different set of problems that may arise. Building vertically will significantly increase the number of layers that will need to be deposited, but more of these tensile specimens may be built in a single process. Building horizontally is the inverse of this, but with far fewer layers there is much less chance of swelling or detachment from the baseplate. This would leave a very large overhang on the underside of the central part of the tensile coupon. Overhangs (where the component is built into unsupported powder) have a tendency to overheat and warp due to having no adherence to the baseplate. The grain growth direction must also be considered with the build orientation, as a tensile test piece will have different levels of strength depending on the direction it is built in.

Figure 2.16: A typical cylindrical test coupon used in mechanical testing [84]. *The long aspect ratio of this component can be a problem in LPBF, depending on scan direction or length.*

The second consideration is the specific geometry of the component being built. Consider again the same tensile coupon in the upright position. Initially, the section being printed will be a simple elongated section. However, as the shape changes to a thinner necking section, the laser will take shorter and shorter times to complete the section. Whilst this speeds up the printing

process, the shorter laser tracks will change how the material cools. The example of a tensile test coupon is very simple, but geometries with far higher complexity are common in LPBF.

Another phenomenon seen in LPBF is the "baseplate effect". When building parts, a substrate materials is present to provide an anchor for building on. Given that this baseplate is a large section of solid metal, its large thermal conductivity means it acts as a heat sink during the process. For the first few layers (layer thickness affects how many) of a build, the cooling rate of a material will be far higher, as the baseplate acts as a form of undercooling. As the build becomes taller, the heat has to travel further through the deposited material to reach the cooler region. Because of this, there is a general buildup of heat in the higher layers of a part. This effectively reduces the energy required for printing, as the ambient temperature plays a role in determining energy densities (M.Thomas et.al. [85]).

A significant area of research in LPBF involves the use of support or anchors and how they affect the produced components. Most printed components in AM are manufactured using a substrate material to deposit material onto. This acts to hold the material in place during printing, preventing the component from warping during the process. However, this often means that a significant area of contact between the part and the substrate is required, meaning that parts are effectively welded to the plate and must be machined off before use.

This machining step limits the potential of AM processes, as it adds further post-processing to the component. To avoid this, support structures or alternative anchoring techniques are used to limit the component's surface contact to the baseplate, whilst keeping the constructed component free of warping. This allows for the part to be snapped off of the substrate after the build is complete, drastically reducing the lead time for a component.

2.3 Microstructural Control in AM

2.3.1 Microstructural Control Methods and Techniques

Creating a component that has a shape or form for a specific purpose is only one aspect of the fabrication process. Whilst shape is often a vital aspect for a part, its microstructure will also have a crucial bearing on how the part performs.

One of the most useful examples of microstructural control is in turbine blade casting. In order to have a turbine blade that is capable of withstanding the pressures and temperatures encountered within a jet engine or turbomachinery, not only must the shape of the component be correct, but the microstructure must be carefully controlled as well. This level of control allows for the part to withstand these conditions for longer and allows for components to be manufactured to a far greater level of consistency – a quality that is particularly important in the aviation industry, where safety is paramount.

A crucial aim in aerospace applications for microstructural control is to create a part with a single crystal orientation. This is difficult to achieve, due to the heterogeneous nature of solidifying metal, which solidifies along the direction of the thermal gradient. Whilst a columnar grain can be achieved through use of a thermal sink (figure 2.9), reduction of these grains into a single orientation part requires extremely careful control. A "pig-tail" grain selector (figure 2.17) is often employed in conjunction with a Bridgman furnace to force a single grain to grow during the solidification by preventing the rest of the grains from growing, with careful temperature control over the rest of the casting. Through this method, it is quite possible to produce parts that are a single crystal. This is very useful for turbojet applications, as it drastically reduces the effect of high-temperature creep on the material.

Another method for microstructural control using AM is through the use of two-step processing. The first step is to produce a component using an AM process. This can be nearly any shape desired, but is often demonstrated using lattices. The second step involves the use of the near-net shape process known as Spark Plasma Sintering (SPS).

SPS is reminiscent of HIP, involving high pressures and temperatures. However, the temperatures in SPS are achieved through the use of an extremely large electrical pulse. This electrical pulse is passed across the dies and feedstock of the material, generating an enormous amount of heat, enough to sinter and bond similar metals together. Figure 2.18 shows a simple diagram of an SPS system.

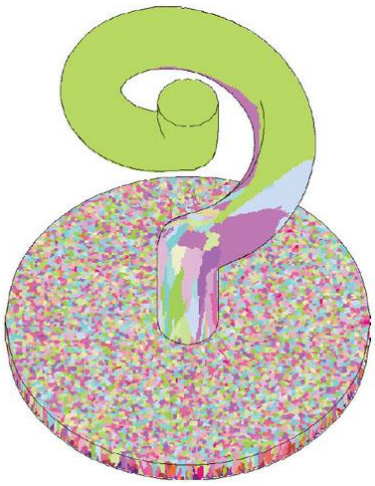

Figure 2.17: An example of a pig-tail grain selector commonly used in turbine casting. This system is used to grow a single crystal turbine blade from a larger number of crystal orientations [86].

To make use of SPS in conjunction with AM for the purposes of microstructural control, the AM-produced part is placed within the SPS chamber and has the feedstock packed around it. The sintering process is then performed, consolidating the packed material and bonding it to the already solid AM structure. The end result of this is a form of metal composite, with a dual microstructure. Because the temperature is not sufficient to melt the material, very little changes in the AM-produced part. This results in a fine, columnar AM lattice within a matrix of larger grains. This dual microstructure material retains the toughness and flexibility of the exterior, whilst maintaining a rigid frame from the interior lattice. The main limitation of this method of microstructural control is the loss of shape freedom, as SPS uses dies and moulds, meaning that the final product is often a very simple shape that must then be machined again.

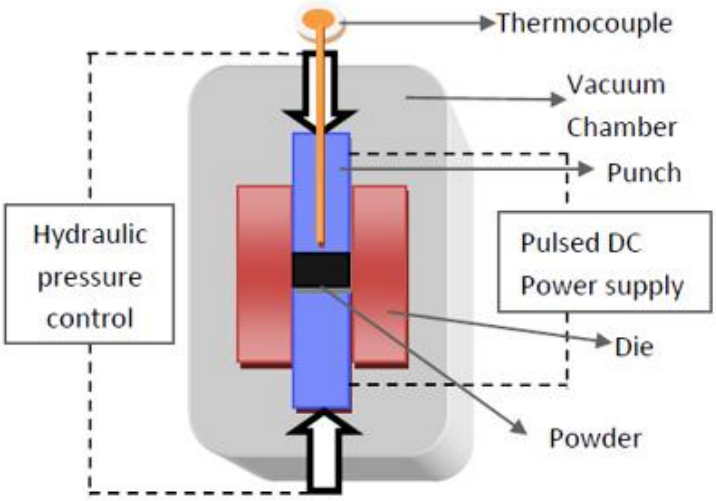

Figure 2.18: A basic diagram of an SPS system [87]. *SPS can be used to consolidate both metal and ceramic material, making it invaluable for the recycling of both swarf and powder.*

A final method of microstructural control in AM is through the use of beam parameter changes within a component. By putting more or less energy into the powder bed by manipulating the laser or electron beam parameters, differing microstructures can be produced with a high degree of accuracy. Work by Hernandez-Nava et.al [88] demonstrates that complex microstructural patterns are possible in solid sections through the use of electron beam parameter changes and external post-processing (figure 2.19).

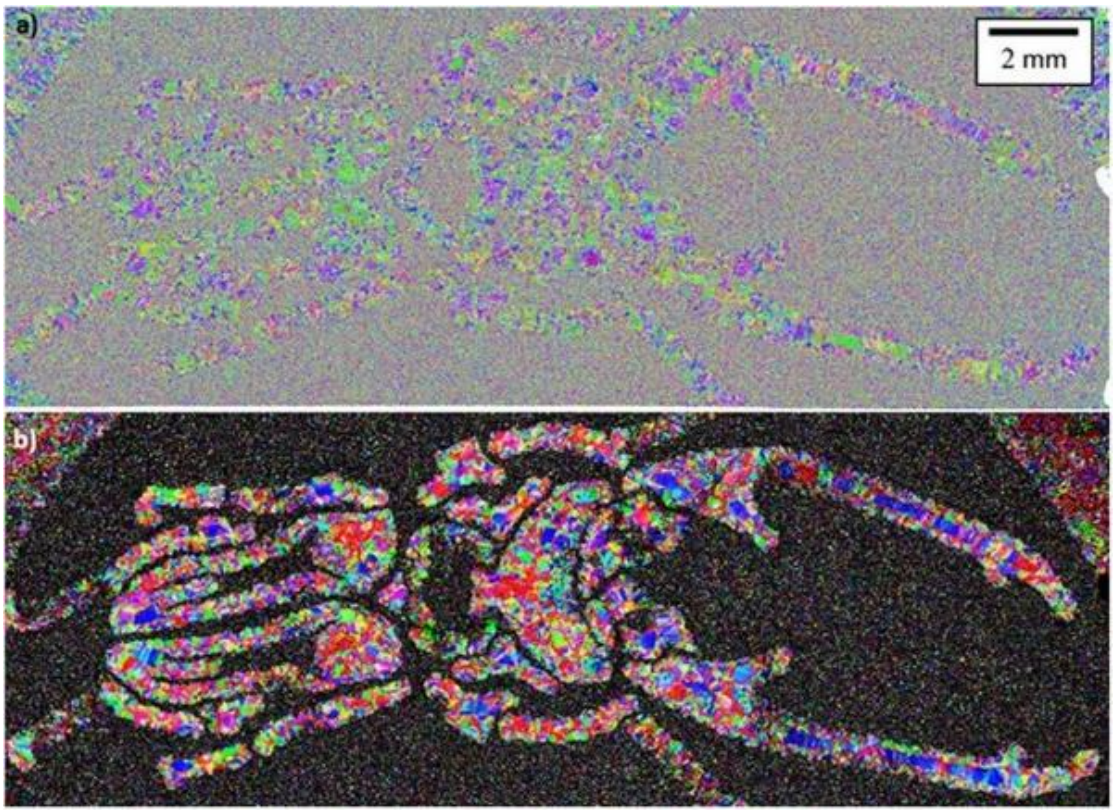

Figure 2.19: An example of microstructural control in an EBM-produced capsule that was post-processed via HIP [88]. *The colour in the image is generated from EBSD mapping.*

In terms of application and macroscopic properties, control of microstructure can be seen very clearly in 17-4Ph stainless steel. Work done by Freeman et.al. shows how material phase can be "selected" at will via change of laser processing parameters in certain materials [89], [90]. On a microstructural level, the phase of 17-4Ph steel can be controlled by suppressing martensite growth via the size of the material cells. This results in a drastic improvement in the magnetic properties of the material, as the metastable martensitic phase of 17-4Ph is a ferromagnetic material. This allows for the material to be magnetically graded through variation of process parameters across a single solid section, with no post processing. However, the material is susceptible to transformation-induced plasticity, meaning that great care must be taken when handling these components to prevent their transformation back into martensitic material – and thus losing their magnetic properties.

2.3.2 Heat Treatment

Heat treatment refers to a family of processing techniques that involve heating (or re-heating) material to promote a microstructural change within that material [47]. Different results can be achieved with these techniques and they are often vital to successful tailoring of materials for specific properties. Metals are often held for hours at a time, in order to promote full transformation of microstructures [47].

Stress relief via heat treatment is referred to as annealing [91]. This process involves heating the metal to a point where grain growth can occur before allowing the material to cool slowly - often in air or in a furnace- to prevent re-introducing internal stresses. The growth of the grains in the material reduces the number of sites for dislocation pile-up, effectively increasing its ability to accommodate deformation. This process is performed on harder metals in order to impart some toughness or ductility, at the loss of some of its strength and hardness.

Precipitation hardening (or age hardening) is a method of heat treatment used to strengthen a material [12], [13], [92], [93]. This process involves developing a secondary material phase within the material that is capable of reducing and preventing dislocations from moving throughout it. This is a very common occurrence in nickel based superalloys, as the infamous γ' phase acts as the strengthening phase for this family of materials [80]. In addition to the γ' phase, there exists also a γ'' phase that further strengthens the material but it is believed that this form of solid solution strengthening (in addition to TCP phases) that may cause many nickel-based alloys to be very brittle and susceptible to cracking, particularly during processing or machining[94].

Commonly, components that are manufactured for aerospace or other safety-critical applications undergo some form of heat treatment. Because manufacturing techniques are not guaranteed to provide perfect results, the components manufactured through them must be further consolidated or treated to ensure their integrity. This is often done through some form of heat treatment such as Hot Isostatic Pressing (HIP).

HIP helps to consolidate material on the microscopic scale, reducing large cracks and pores and sometimes entirely removing smaller defects. This has a proven effect of increasing the time a component can be kept in service, however in higher temperature applications, pores that have been closed can re-open and fail in the same fashion as if they had not been processed via HIP. Work performed by Tammas-Williams et.al. has shown the limits to what can be achieved by using HIP as a "silver bullet" to fix cracking or defects in AM-produced components [91]. Ideally, components should instead be manufactured without (or with minimal) defects to begin with, which largely negates the need for a HIP step in the manufacturing chain.

2.3.3 Heated Build Substrates

Work by Mercelis and Kruth [95] demonstrates the importance of the temperature of the build substrate during LPBF. Residual stresses in LPBF produced material change dramatically when the material is removed from the substrate. When anchored to the substrate, the residual stress within the material is extremely large, due to the mechanism of rapid solidification onto the room-temperature substrate. Effectively, the substrate constrains the material as it solidifies and locks in stress. Subsequent removal from the substrate often results in warping or a change in shape of the component. Further work by Kempen et.al. [15], [96] shows that properties of a material may be improved through heating the build substrate during processing. Even a relatively small amount of heating – as in this instance – has been shown to dramatically alter the material's behaviour by reducing the amount of residual stress within the material. This reduction in stress drastically improves the performance of the material (figure 2.20).

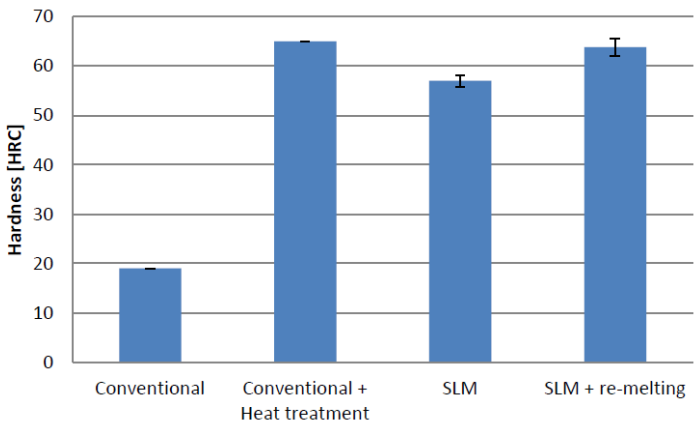

Figure 2.20: Rockwell hardness of M2 tool steel produced by LPBF, with and without the use of a pre-heated build substrate – as produced by Kempen et.al [96].

This study also appears to show that rescanning or remelting the built parts with the laser after the initial solidification is nearly equivalent to conventional methods of post-process heat treatment. Primarily, heated substrates are powered by resistive units. This type of heater is normally capable of raising the temperature of the substrate to around 400°C. Whilst this is capable of relaxing material stresses, its impact may not be effective once a component begins to increase in height during the build process.

2.3.4 Scan Strategy

In LPBF, one of the most successful ways to control the microstructure of a part is in the method of laser scanning. When a laser moves across a build volume, numerous parameters can be changed in order to control how the material behaves. Laser parameters such as power, velocity and hatch spacing are often chosen depending on how each specific material behaves during the process, leaving little room for manoeuvre. However, the style of the laser scan and how it changes with each layer can also have a large impact on the way a component is built.

Consider the tensile test piece in figure 2.16. If the laser scans normally along the length of the manufactured tensile bar, the laser will have to travel all the way from one end to the other and back again – a travel distance often around 200mm. Compare this to scanning normally across the width of the part, which would be 10 times shorter at 20mm. For the laser to return to a particular location, it will take 10 times longer, which will drastically change how the surrounding material solidifies. The more rapid undercooling experienced by a component scanning along the length of a bar may result in cracking or lack of fusion defects due to a lower local energy density.

One way to control the orientation of grain growth is through control of the laser scan [97]. Normally in LPBF, parts are constructed using a rotating hatch pattern, in order to prevent both internal stresses from arising and to ensure a more consistent microstructure. This usually changes by between 45°-90° per layer. However, if the scan rotation changes by small amounts, it is possible to see a gradual change in the direction of solidification once the material is sectioned and polished [98].

Furthermore, the scanning strategy of the LPBF process may be changed depending on the style of scan motion. Commonly, three different methods are employed in LPBF. These are Meander, Stripe and Checkerboard. Meander and Stripe share many similarities, involving the laser travelling along the length or width of a part during manufacture. However, whereas a meander will turn at the end of each hatch to return in the opposite direction, stripe will stop the laser entirely and return to its original position. The laser will then move by its designated hatch spacing and repeat the scan. Whilst this method can prevent some problems with edge overheating, it also produces components that have inferior surface finishes to meander scan parts.

Checkerboard strategies involve segmenting each component layer into a series of evenly sized regions that are scanned in turn (figure 2.21). These regions are often 10x10mm squares, hence the name “checkerboard”. This allows parameters that generate fully dense 10x10mm cubes to be used in the manufacture of larger components. However, these squares must be connected in order to form a solid component. Because of this, these squares often slightly overlap. Whilst

this does help to bond the regions of the component together, the main problem that then occurs is that these regions overheat and can suffer from keyhole defects due to a greater energy density input.

Carter et.al demonstrate this method for LPBF scanning (figure 2.21) [99]. This splits components into small regions of identical hatch lengths. Whilst this would appear to solve the problems that arise from hatch lengths, a careful design approach must be taken to ensure these sections are properly fused together and do not contain defects between melted regions.

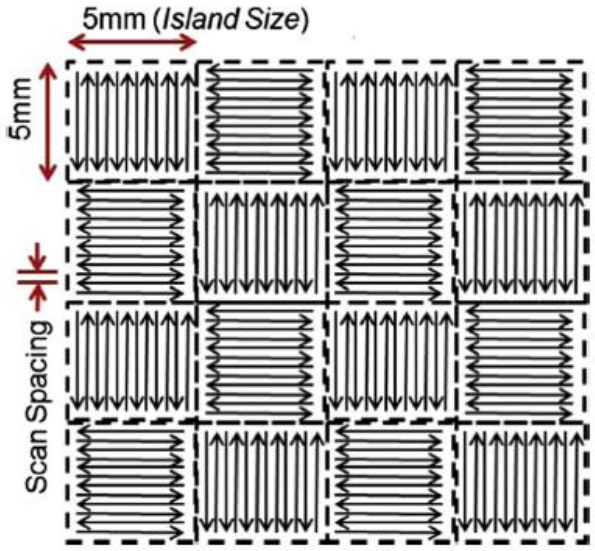

Figure 2.21: Island/checkerboard scanning pattern [99]. *While this keeps the length of scans consistent, it can be susceptible to defects between islands.*

This method of scan strategy also does not take into account component geometry. If sections are thinner than the islands themselves, this technique begins to lose effectiveness and can cause more problems than it solves.

2.3.5 Laser Rescanning

An alternative method for heat treatment and consolidation [100] of components in laser-based AM involves the use of lasers to induce an effect similar to that of a heat treatment procedure. In many studies, this is performed by having the laser repeat its path over an already melted part at the end of the initial scanning procedure, thus effectively re-heating the material. This can be done at the end of every layer or intermittently throughout the build process [101].

There are two important considerations to take into account when designing a rescanning scan strategy. Firstly, the laser rescan must not melt the material. If this occurs, then the material will re-solidify in a very similar fashion to its initial deposition layer and little will be improved. Secondly, as more layers of material are deposited, the previous layers will be affected less and less by the heat from the laser, but will still be affected slightly. Contrast that with the final layer, which may only have been rescanned once (or not at all). This means that the top surface will always be different to the lower bulk material. Kempen [96] details this (figure 2.22) alongside pre-heating the substrate, as a method of in-situ control of the material. In this instance, the roughness of the top surface of M2 tool steel deposited via LPBF is reduced through the use of re-melting the component with the laser scan on every layer of the build. This has the effect of improving the density of the material, but because two scans are required for the component, the length of the build increases.

Laser shock peening (LSP) is a technique used in industry to reduce surface stress of complex components[102], [103]. Unlike the theory of component rescanning however, laser shock peening is a completely mechanical process, utilising the physical shock of the laser's impact to promote consolidation, similar in mechanism to normal peening methods. This process functions through the imparting of compressive stresses into the surface of the components, which act to counterbalance the tensile stresses elsewhere in the component. This technique, used in-situ in LPBF systems, has been shown to improve the quality of the top surface of AM components once sectioned, polished and examined using optical microscopy, with a significant reduction in defect density in the affected regions [104], [105].

In-situ LSP in LPBF would also reduce the need for further post-processing steps after the completion of component fabrication. It is also an ideal method for treating components with extremely complex internal structures precisely. It likely would not be utilised in the manufacture of TRIP susceptible materials such as 17-4Ph, as this could trigger a transformation of the martensite [90], causing loss of magnetic properties.

2.4 Experimental Design

Because each material requires different sets of laser parameters to properly manufacture components, a great deal of effort has previously gone into determining effective combinations of laser powers, scan velocities and hatch spacings (as well as other parameters), that are ideal for producing dense components. When a new material is received by a developer or industrial platform, the first task is to determine which combination(s) of laser parameters are effective for that material. A method initially detailed by Ion et.al [106] and further developed by Thomas et.al. [85] demonstrates one technique for designing experimental plans. This method is known as a response-surface methodology.

To begin with, two or more parameters for study must be chosen. In the case of LPBF, this is often performed with parameters such as laser power, laser scan speed, scan hatch spacing and the thickness of each subsequent new layer of powder. These parameters are easy to control, with most 3D printers currently able to produce multiple parts, all with different parameters.

An experimental space is then determined through the use of a statistical design-of-experiment (DOE) approach, to determine the explored range of each parameter. Statistical software packages (such as Minitab) are often employed to provide the specific parameter values used in the design process. The specific pattern of points in the explored space may vary with both the number of factors, model type (i.e. Box-Behnken or Central Composite Design), whether Axial or Nodal points are chosen and the actual range chosen for each specific parameter.

Once the experiment has been performed – i.e. the production of parts with different parameter combinations via LPBF – the effect of the changes in independent variables must be quantified through the examination of affected dependent variables. In AM research, this is often chosen as porosity or defect density. The resultant porosity can be plotted for each point in the experimental space, resulting in a contour plot (figure 2.22) that acts as a "processing map".

With this methodology, a "processing space" or "processing window" can be determined for each different alloy that is processed. Alternatively, energy input density can be used to generate a correlation between defect density and parameters, by taking into account all of the input parameters.

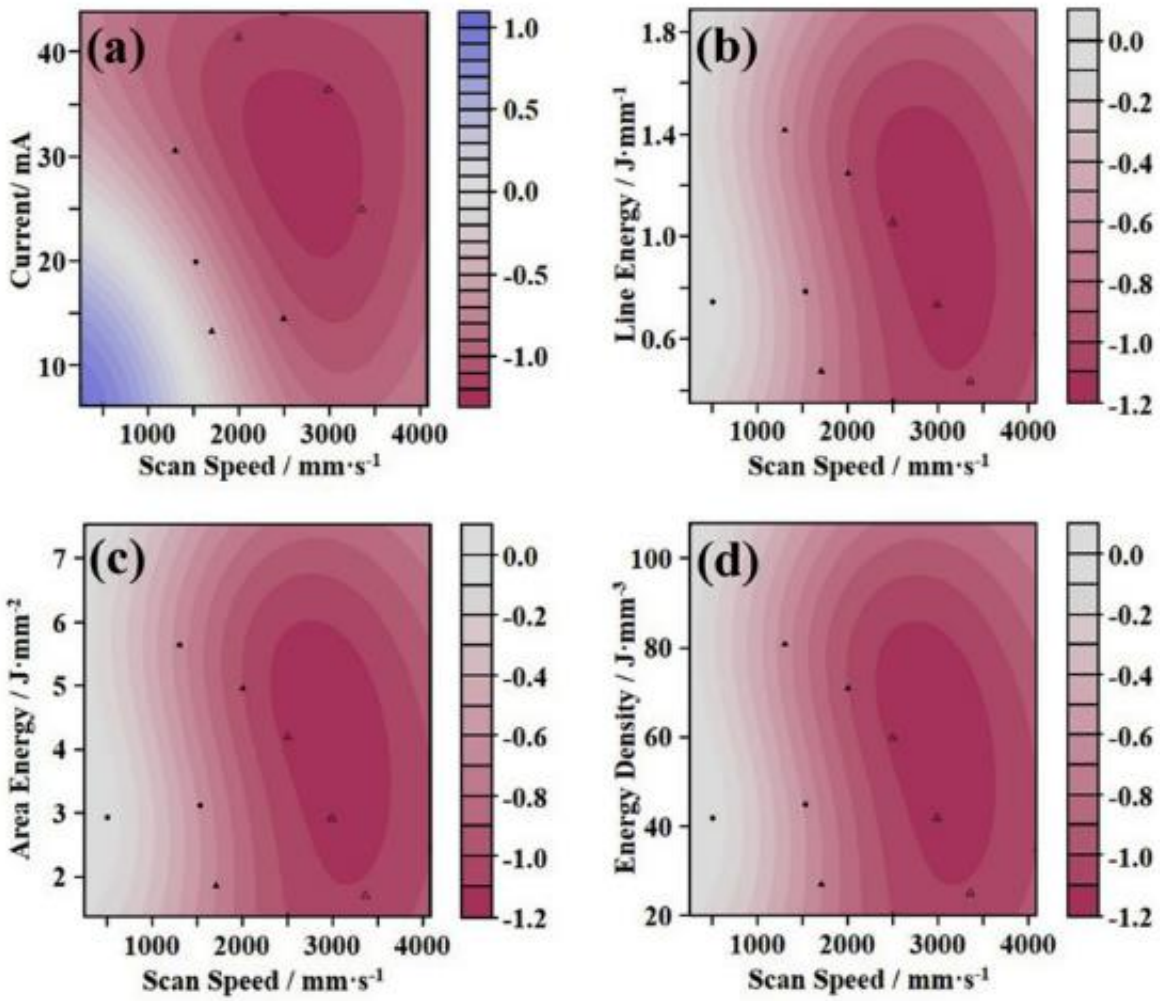

Figure 2.22: An example of processing contour maps [83]. *In this instance, each map demonstrates the impact of parameters on surface flatness and deviation. The colour scales in this figure illustrate the variation in millimetres of surface roughness in AM parts.*

Energy input density in LPBF can be determined by using the following equation:

$$E = \frac{P}{vlh} \qquad \text{(Equation 2.4)}$$

Where P is the laser power, v is the laser scan velocity, l is the thickness of the powder layer and h is the hatch spacing. It has been shown that certain defects such as cracking or keyholing tend to be created at lower or higher levels of energy input, respectively.

M.Thomas et.al. describe the use of a normalised energy density equation to determine the amount of energy applied during the LPBF process [85]. The equation is shown below as equation 2.5:

$$E_0^* = \frac{q^*}{v^* l^* h^*} \qquad \text{(Equation 2.5)}$$

Where E^*_0 is the normalised energy density, and q^*, v^*, l^* and h^* are the normalised power, scan velocities, layer thicknesses and hatch spacings respectively. This can be expanded to be written as:

$$\frac{q^*}{v^* l^* h^*} = \left[\frac{Aq}{(2lvr_b)}\right]\left[\frac{1}{(\rho C_p(T_m - T_0)}\right] \qquad \text{(Equation 2.6)}$$

Where A is the absorptivity of the material, q is the laser power, l is the layer thickness, v is the scan velocity, r_b is the beam radius, ρ is the density of the material, C_p is the specific heat of the material, T_m and T_0 are the melting temperature of the material and the ambient temperature of the powder, respectively. This expanded equation takes into account all of the parameters that can affect the processing of a material in LPBF. This also takes into account the material characteristics and the ambient temperature. This means that different materials can be plotted on the same scaled graph, allowing for direct comparisons (figure 2.23).

The main disadvantage of this parameter window method is that it is often slow and laborious. Often, multiple iterations of this experiment must be performed to discern specific windows or conditions that produce high-quality product material. In some cases, this may take several months of research and may not yield viable results at all.

This method also does not consider the specific machine used in the processing of the materials. Given that different machines have alternating methods for powder dosing, different time gaps between layers, different types of lasers and different inerting methods, this is not an exhaustive list of parameters.

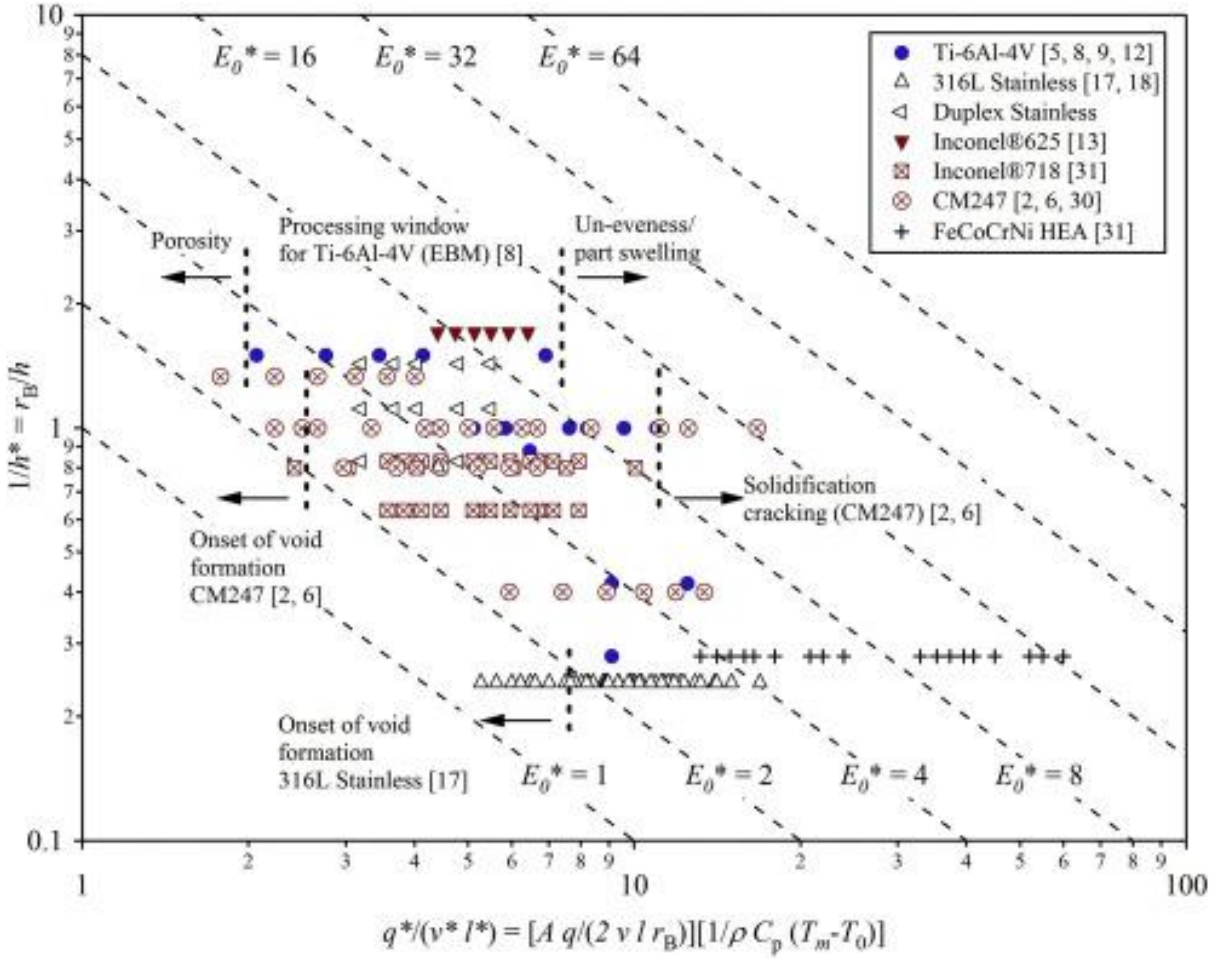

Figure 2.23: A normalised processing map [85] *used to determine the processing windows for several different materials. The dotted lines indicate increasing levels of energy input, similar to a contour. References in this figure are from the original source paper* [85].

2.5 In-Situ Monitoring and Control

2.5.1 In-Situ Monitoring

In LPBF, numerous factors can affect the outcome of a build. Whilst some of these are monitored in printers (such as oxygen levels), many are not monitored due to the level of technology required to monitor such things. An example of this in LPBF is the melt pool. Because of the tiny size – often tens to hundreds of microns - of this feature coupled with the very high speed that it moves and changes, it can be difficult to monitor or track melt pools across an entire build, which may be on the order of tens to hundreds of millimetres. This can be on the order of 10^3-10^4 times smaller than the size of a fabricated part. As well as this, it can often be challenging to apply in-situ monitoring tools to existing 3D printing systems [107]. Because most metal 3D printers require an inert atmosphere, care must be taken not to rupture the chamber walls through the additions of access ports for cables or sensors. Some companies are hesitant to allow external groups to modify their machines for reasons relating to intellectual property, often leading to delayed publication or release of results. Finally, the amount of data produced by these sensors often produce very large quantities of data. This means that the challenge of applying in-situ monitoring and control techniques is often also a challenge of data management. These factors have meant that adoption of in-situ monitoring and control techniques by industry has not been a quick process.

In LPBF, a lot of interest is turning towards the digitisation of this process, especially concerning the creation of techniques such as digital twins and automatic control systems. Many of the heterogeneities that cause faults or defects in AM-produced parts may be rectified or prevented entirely with a greater focus on automation and digitisation within this family of processes, including now the use of neural networks and AI-driven models [108], [109].

2.5.2 Sensors and Emission Sources

2.5.2.1 Thermal Emissions

Thermal emissions occur in all materials. Because all bodies are composed of charged particles, they constantly emit some amount of "ambient" thermal emission. This ambient radiation is composed of a very wide range of electromagnetic emissions at longer wavelengths. When the temperature of a material increases due to the addition of heat, the charged particles that make up a body vibrate more, resulting in a greater amount of emission. This radiation emitted from thermal vibrations is emitted at shorter and shorter wavelengths as the temperature of the material increases, eventually moving into the range of visible spectra (around 400nm-700nm). This is why objects glow when heated. The relationship of heat transfer from radiation can be described through the Stefan-Boltzmann law:

$$H = Ae\sigma T^4 \qquad \text{(Equation 2.7)}$$

Where H is the heat emitted, A is the surface area of an emitting body, e is the emissivity of the body, σ is the Stefan-Boltzmann constant (5.67×10^{-8} W/m^2K^4) and T is its temperature. This can be used to approximate the temperature of an object via the intensity of the light that is emitted. This rate of emission is different for every material and so an emissivity value is factored in to describe this change. For a blackbody, the emissivity is equal to 1.

The radiance B of an emitting blackbody body is given by Planck's law [110]:

$$B = \frac{2hc^2}{\lambda^5}\left(exp\left(\frac{hc}{k_B\lambda T}\right) - 1\right)^{-1} \qquad \text{(Equation 2.8)}$$

Where h is Planck's constant, c is the speed of light, λ is the wavelength of the radiation, k_B is the Boltzmann constant and T is the temperature of the emitting body. Infrared emissions are classed as those with a wavelength ranging from 1mm to 1μm. As the temperature increases, the range of emissions increases as electrons gain and emit more energy in the form of higher energy photons. Figure 2.24 shows the emission curve at different temperatures for a blackbody emitter.

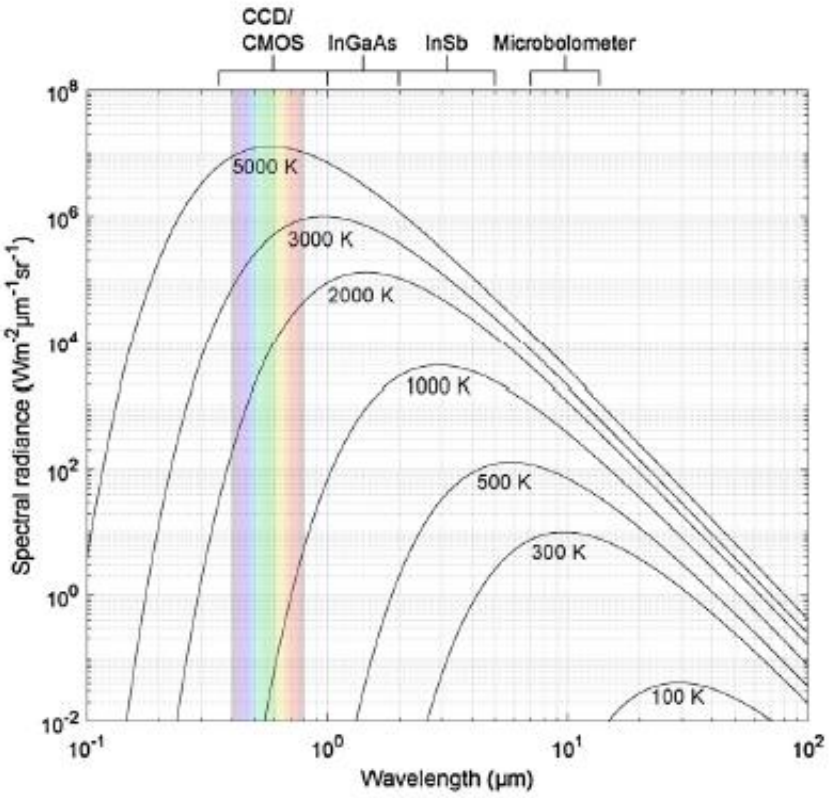

Figure 2.24: Example of a blackbody radiance curve [110]. *Each curve corresponds to a different temperature. The notation at the top of the graph denotes the type of sensor required for each of the wavelength ranges, with the rainbow denoting the range of visible light.*

Being a generalised blackbody emitter, this does not take into account the specific material properties that cause the material to emit more radiation at different temperatures. The emissivity of a material must be accounted for to provide an accurate reading of temperature for any given material.

Work by Chechik et.al demonstrated the ability of a simple camera setup to monitor a DED build and generate data that showed correlation between thermal profile and the grain orientation determined by EBSD mapping. This methodology still struggles with determination of exact temperature, as the emissivity is required to provide an exact value and instead utilises a radiance temperature [111].

2.5.2.2 Thermocouples

Thermocouples are one of the most widely used sensors in the modern world, due to their relative simplicity, reliability and ease of use. These sensors often come in the form of a probe-like metal rod, which contains two different metal wires with dissimilar thermal conductivities. The two wires are joined at both the tip and base of the probe. When the probe is heated, electrons begin to flow from the heated end towards the cooler end, in order to escape to a lower energy state. This flow of electrons generates a minute electrical current (figure 2.25). This is sufficient to generate a detectable signal, which can be used to determine a local temperature. The greater the temperature, the greater the provided electrical signal.

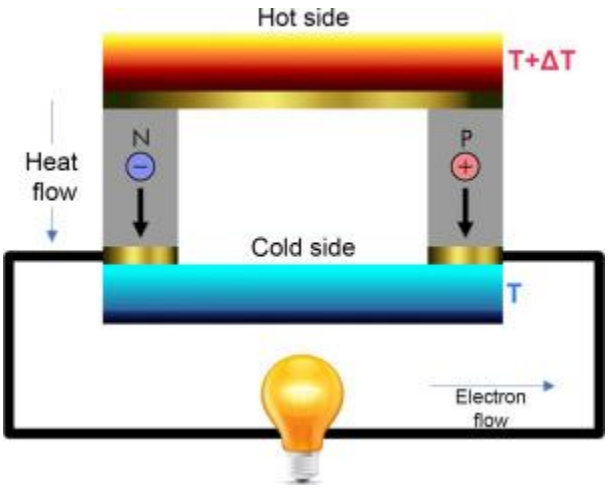

Figure 2.25: A basic diagram of a Seebeck circuit used in thermocouples [112]. *The temperature change across the hot and cold areas results in an electrical signal being produced.*

Thermocouples are most commonly used in furnaces and heating elements to provide a method of feedback for electrical control. In additive manufacturing, they may be used to control or monitor the temperature of the build substrate. It is more difficult to use thermocouples to measure temperature in-situ in powder bed processes, as they interfere with powder spreading. However in a recent paper by Trapp et.al [113], thermocouples were used to analyse the amount of energy absorbed by materials in a scaled down LPBF process using only a single layer of powder. By analysing the temperature change detected by thermocouples, it is possible to estimate how different forms of material behave under the thermal loading seen in additive processes.

2.5.2.3 High Speed Optical Imaging and Photography

Data can also be acquired from AM processes from high-speed imaging cameras that are mounted either coaxially or within a chamber. Optical imaging typically collects electromagnetic radiation between 400-800nm. This means that most thermal emissions are not detected by these systems. Instead, they rely on the reflectance or re-emission of light from another source, or on visible emissions from the melt pool.

An example of this is in photogrammetry (also known as structured light) where an optical camera is coupled with a projector to collect the reflected light, in order to determine topographical information of a component [114]. Other systems may require an illumination beam to provide accurate data. These illumination beams consist of a coaxially mounted visible beam that is designed to reflect off features on the target surface, in order to produce an image in the first place. In many in-situ monitoring systems for LPBF, the incredibly intense light from the laser and any reflections must be filtered out to avoid damage to the CCD, as these devices are very sensitive and can easily be over-saturated if care is not taken. This often also results in a loss of resolution close to the melt pool, as the emissions from this feature often drown out and saturate the surrounding region.

Recent work by Freeman et.al [115] has shown how simple optical monitoring devices in DED systems can be used to provide data from the process and to perform direct control of an AM system in real-time. By examining the intensity of melt pool emissions in the optical range, it is possible to discount those with low or near-zero signals (i.e. when the laser is off or when only spatter is detected) and focus solely on the actual melt pool track.

In contrast to live, immediate control of the process, other researchers have focused on the use of in-situ cameras to control other aspects of the LPBF process. Craeghs et.al demonstrated the ability to track powder bed and spreading defects during the LPBF process through simple photographic analysis. Using a simple intensity analysis, raised and lowered areas in the powder bed can be detected, providing an insight into how effectively the powder spreads [116].

During the LPBF process, the high-energy input from the laser can also cause the denudation of material from the powder bed. In many LPBF systems, a rapid current of gas is passed over the build volume to "blow away" this denudated material. However, some heavier pieces may settle back down on the powder bed. These pieces, which are often relatively large compared to the rest of the powder distribution, are sometimes quite detrimental to the process and can often cause fatal problems in the process. With high-speed optical imaging, these denudated particles of matter can be observed and characterised.

2.5.3 Data and Data Handling

Live-feed cameras (thermal or optical) provide a near-continuous stream of data for processing. However, the size of data produced by these sensors can quickly become too much for normal computers to process on a timescale relevant to AM. This is exacerbated with high-speed cameras, as images can be obtained at rates of approximately several hundred KHz. Two options currently present themselves to deal with this problem.

The first option is to improve the local computing power of the detection system being used. Whilst this is a very attractive option, the amount of computing power required for a single high-speed imaging sensor would be equivalent to a small server cluster. This is an extremely costly endeavour, in both setup and operating costs and would drastically increase the area footprint of a machine.

The second option is to reduce the amount of data being collected to only that that is necessary for the monitoring and control process to function correctly. In a recent piece of work by Freeman et.al [115], a DED system was controlled through analysis of optical emissions. The images were obtained at around 30Hz and were parsed to reduce the image data into a single value. This drastically cuts the amount of data that the control algorithm needs to work with, whilst still ensuring that it can function correctly.

Despite the clear benefits that the aforementioned monitoring and control techniques can bring to LPBF, one continuous problem is that of data management. Many sensors produced in the present day are capable of reaching very high sampling rates, or can produce images that are of exceptional resolution. In addition, most sensors now accept automatic trigger functions, making rapid and automatic sampling very easy to achieve. Whilst the fidelity and efficiency of these sensors is to be lauded, the side effect of this is that a vast quantity of data is produced, even from very small operations.

Whilst this huge amount of data can reveal much about the underlying physics of processes, the sheer quantity of information means that it rapidly becomes impossible to handle on a short timeframe. In order to compensate for this, it may be necessary to use novel computing techniques in the future. An alternative to this is to crop or simply filter the data collected by the sensor. Reductions in field of interest and caps on the maximum frame rate can help in sensors such as high-speed thermal or optical cameras. In sensors that produce outputs as text files or a series of raw values however, it may be more challenging to reduce the amount of data without compromising on its accuracy. One option in this regard is to examine data or information that passes through a filter set to particular values. In a paper recently published by Chechik et.al [40], relatively low capture rates coupled with data filters were shown to be effective at controlling the size of a melt zone in a DED process.

2.6 Nickel Superalloys

2.6.1 Nickel Alloys and their Applications

The primary reasons that nickel is chosen as a base material is for its resistance to corrosion and oxidation and also for its ability to retain its shape and strength at elevated temperatures. A primary application for nickel superalloys is in the extreme environments found inside turbine engines, particularly land-based ones where the density of the alloy family is not a concern. These extreme environment, coupled with the intense loading on components means that most other families of alloy cannot compete with nickel-based superalloys in these settings. While titanium alloys are a popular choice for similar components, they do not retain their strength or resistance to creep deformation at as high temperatures as nickel alloys do. Because of this, turbine blades and disks are currently almost exclusively made from nickel-based superalloys. The Inconel family of alloys has long been an industry staple for these types of applications. CMSX-4, Hastelloy and IN718 have been regarded as industry staples for many years, showing very high performance in these settings. However, with an increasing emphasis on engine performance and component lifespan, more exotic nickel alloys with even greater properties are being considered for use. As well as this, alloys like CMSX-4 contain elemental additions like rhenium [117]. Whilst this addition is a key reason for the alloy's success, it is exceedingly rare, making finding suitable alternatives a high priority.

One nickel alloy of great interest for high temperature applications is CM247-LC. This material has received a great deal of attention in the scientific community, due to its outstanding ability to withstand high-temperature creep and corrosion and maintain a high level of strength at elevated temperatures. However, its high-temperature properties are offset by its extremely low ductility, poor weldability and tendency to crack on fabrication or after a short time in service [118], [119]. Due to the extreme complexity often required in turbine components, internal stress and short cracks both become a major issue, resulting in a chronic tendency for failure, often before the part has even left the production line. Furthermore, CM247-LC has a predisposition to crack when heat treated [10]. Given that nearly all additively manufactured components used in safety-critical applications are heat treated before use, this is a major problem.

Turbine blades do not rely on the temperature resistance of the nickel alloy alone however. Blades often have their surfaces coated with another more thermally or chemically resistant material so that the base nickel alloy remains unaffected for as long as possible. These coatings may be applied through a variety of methods, but are often sprayed or otherwise deposited as evenly as possible to avoid porosity within the coating itself. Only a thin layer needs to be

applied to improve temperature resistance, and corrosion can be prevented as long as the coating totally masks the base material. Coatings are often composed of some form of ceramic, whose thermal conductivity and chemical reactivity is far lower than that of most metals, providing an effective shield [120], [121]. Various different types are available, each having specific advantages.

As well as coatings, blades often are manufactured with complex features (figure 2.26). Internal cooling channels allows cooler air to be circulated through the blades, helping the engine's temperature to be regulated to prevent components from getting too close to their melting point. With the ever-widening adoption of additive techniques in industry, these internal structures are becoming more complex, with fully internalised structures becoming a reality. In addition, topological optimisations can now be applied to internal structures, meaning that more efficient and intelligently designed internal structures within hollow turbine blades are possible, providing longer-lasting components.

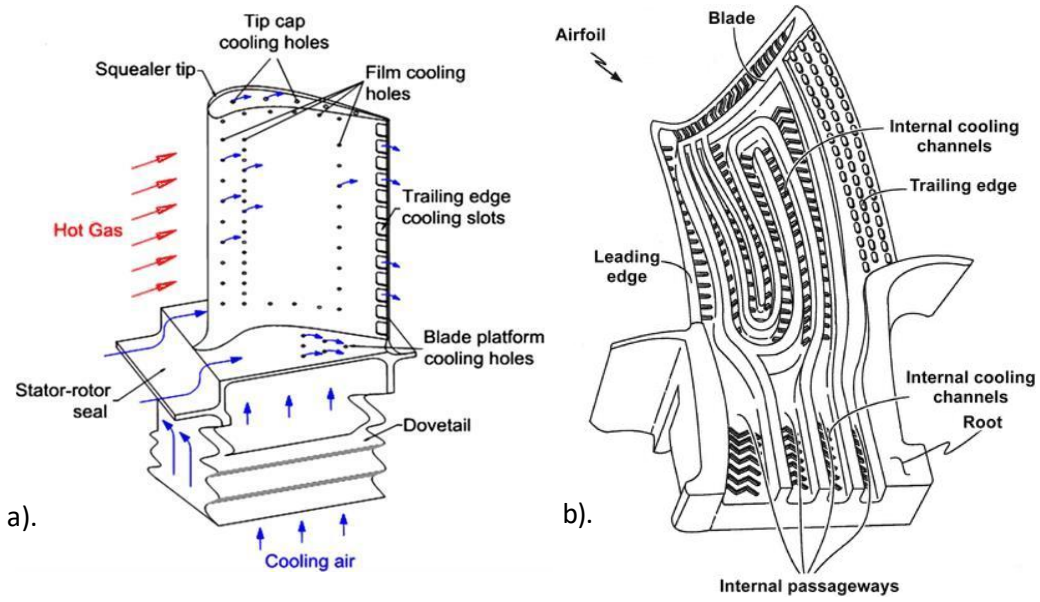

Figure 2.26: a). An example of a turbine blade exterior with simple cooling holes and vents in the trailing edge. b). A patent design for an additively manufactured turbine blade with an internal structure to maximise surface area [122], [123].

In order for coatings to be effective, their thermal expansion rate must be well matched with the alloy base being used for the blade. If the two parts expand at different rates, the barrier coating can suffer from catastrophic failure. Furthermore, the force exerted on a turbine blade during service is akin to the weight from a double decker bus applied to its tip [124]. This extreme cyclical loading, coupled with high temperatures means that most materials undergo creep deformation to some extent. This deformation also causes coating failure, so the material chosen for the turbine blade must be as resistant to high-temperature deformation as possible.

2.6.2 Common Phases of Nickel Superalloys

As with many families of alloys, nickel alloys contain a wide variety of material phases. These phases change both with temperature and material composition, meaning that for applications at elevated temperatures, alloy additions must be carefully chosen to provide the best properties at the desired temperature. Taking further the example of CM247-LC, a list of its alloy additions and their segregation phases is shown below (table 2.1).

Element	Weight Percent Range (wt%)	Partition Phase
Al	5.4-5.8	γ'
B	0.01-0.02	Grain Boundaries
C	0.04-0.08	Grain Boundaries
Co	9-9.5	γ
Cr	8-8.5	γ
Hf	1.2-1.6	Grain Boundaries, γ'
Mo	0.4-0.6	γ
Nb	<0.1	γ',γ''
Ni	Balance	All
Ta	3.1-3.4	γ
Ti	0.6-0.9	γ'
W	9.3-9.7	Grain Boundaries
Zr	0.005-0.015	Grain Boundaries

Table 2.1 The nominal chemical composition of CM247-LC[125]. *This alloy is an extremely difficult to weld material, in part due to the number of elements that partition to the grain boundaries and γ `phases.*

Nickels are composed of several common phases [126]. Primarily, there is a matrix phase, often referred to as the gamma (γ) phase. This FCC phase makes up the bulk of the material in nickel superalloys, with most of an alloy's additions present within it.

For high-temperature applications, the most important material phase in nickel superalloys is the strengthening gamma prime (γ') phase. As the alloy melt begins to cool, γ' segregates from the γ, forming particles that impinge on dislocation movement. This phase integrates well into the bulk γ matrix at room temperature, as both γ and γ' are formed as a cubic crystal structure. When cooling from elevated temperatures however, the

can undergo a phase transformation from FCC to HCP if cooled too slowly. This causes a major change in volume, resulting in significant internal stresses being induced into the alloy system. This increase in stress can be catastrophic for some alloys, as the material tears itself apart and effectively reduces the strength of the alloy. Furthermore, some nickel alloys such as

CM247-LC undergo further phase transformations as the alloy is heated or cooled, causing even more stress to be induced into the system when in service. Most industrial high-temperature alloys contain some fraction of γ', as it provides the desirable high-temperature strength, creep resistance and corrosion resistance that is not often seen in other families of materials. The fraction of γ' varies considerably across the range of nickel alloys, but a few alloys of interest are shown in figure 2.27 to provide a comparison. As a general rule however, the more γ' there is in an alloy, the more difficult that alloy is to process.

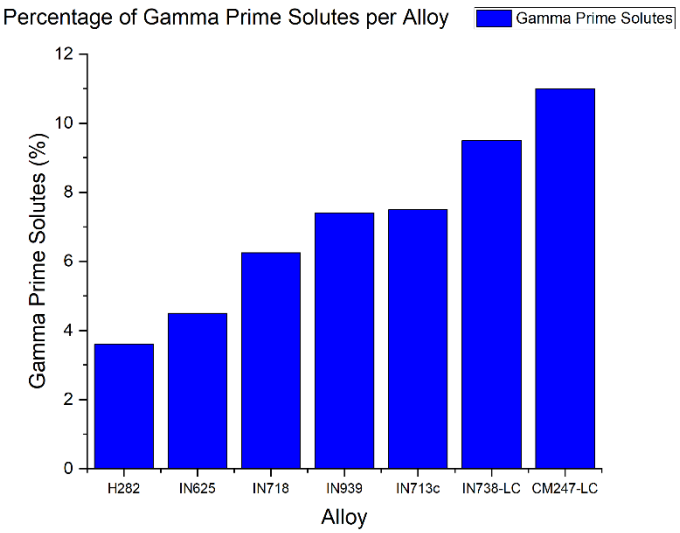

Figure 2.27: The content of the gamma prime segregating elements in several notable nickel-based alloys. The gamma prime content of an alloy has long been tied to its weldability and the ease of which it can be processed [18], [127]–[131], [132]–[134].

Carbides are also present in nickel superalloys, acting as a further strengthening mechanism at high temperatures by impeding the movement of grain boundaries and dislocations. Tungsten and hafnium often segregate to grain boundaries, acting as very effective high-temperature strengtheners due to their refractory properties [135].

Another phase is the gamma-double-prime (γ'') phase. This is a further strengthening phase that arises in alloys with high niobium contents. Whilst this can provide even greater strength, it is similar to the γ' phase in that whilst its properties are highly desirable this increase in strength also pre-disposes it to very large internal stresses due to lattice mismatch forces, making it difficult to work with [80]. This phase is induced by Niobium and Vanadium additions, which is why they tend to be added in very small amounts.

TCP (Topologically Close-Packed) phases can also exist within nickel alloys. This is the name given to the myriad phases that can also arise in extremely complex nickel alloy systems after

long periods in service. These phases are usually considered to be deleterious due to their tendency to embrittle the material through oversegregation [136]. These phases typically do not exist in newly manufactured components due to the very careful temperature control used to solidify and cool the parts, however they may be present if care is not taken in their production. The numerous phases that make up this family are of varying interest due to their wide ranges of properties. Of particular note is the Laves phase. This phase is extremely hard, but is very brittle. Alloys with high quantities of this phase are often used in tribological applications [137], where hardness and frictional wear resistance are paramount. Because of this, they are often used in coatings that provide a shield to a more ductile and workable bulk material.

When initially investigated for use in directionally solidified components, the alloy MAR-M-247 was identified as a prime candidate for its resistance to deformation creep at high temperatures [125],[138]. However, its predisposition to cracking meant that casting the original alloy was impossible. A new alloy variant - CM247-LC - with a lower carbon content (hence the "LC" suffix), was produced by the Cannon-Muskegon corporation with the intention of producing fewer carbides [9], [12]. This alloy variant also included changes to other alloy additions such as a reduction in titanium content, which reduces the amount of γ' formation and makes the alloy slightly easier to process.

Another nickel alloy of great industrial interest is IN939 [93], [139]. This alloy belongs to the Inconel series of alloys and is known for its extreme corrosion resistance at high temperatures. Like many nickel alloys, it is used for the manufacture of high-performance aerospace components and is normally heat treated to cause hardening via precipitation. IN939 has been shown to have extremely high UTS values in its aged form, with some values being over 1400MPa [92], [140]. This extreme tensile strength relies on post-process aging however, as the alloy appears to be particularly prone to γ' suppression when printed via LPBF [92], making the as-built form much more ductile, but less capable of handling extreme force.

2.6.3 Segregation and Strengthening

Segregation [141] is the name given to the process by which different material atoms separate naturally from one another in a material system, forming regions of particularly high contents of one or more particular element. This partitioning of elements on a microscopic scale can provide drastic changes to macroscopic qualities. The process of segregation is driven largely by the cooling rate of the material during solidification. A slow cooling rate allows solute atoms time to diffuse throughout the material, resulting in large particles of segregated alloy additions being dispersed throughout the matrix phase. In nickel alloys, this is seen when γ' segregates from the γ phase.

The driving force for segregation is commonly the reduction of the material's free energy. This is seen in nickel superalloys in the form of grain boundary segregation, where heavier solute atoms that fit poorly into the matrix material will gradually move to the edge of the surface of the grain. This diffusion reduces the strain energy in the lattice, but makes the grain boundaries highly non-stoichiometric and disordered.

Segregation is augmented by longer cooling times, which can be demonstrated by the process of precipitation hardening (also known as age hardening). The longer that a material is held at or around its precipitation temperature, the more the solute atoms will precipitate to form larger particles. These larger particles, often harder than the matrix material, act as obstacles to dislocation movement by pinning the dislocations. Prevention of movement means that more energy is required to force the dislocations to move past the obstacle, effectively increasing the yield strength of the material. Nickel superalloys are precipitation-hardening materials, which accounts (to an extent) for their high strength. In industry, this process is performed by bringing the metal back to an elevated temperature and holding it for a given amount of time, before air cooling it back to room temperature.

A rapid cooling rate may create a solidification front that moves faster than the diffusion of most materials. This rapidly moving solidification front traps the solute atoms, preventing them from being able to diffuse any further and undergo segregation. However, whilst rapid cooling can prevent segregation strengthening, it does introduce another form of strengthening, known as grain-boundary strengthening.

This can be explained through what is known as the Hall-Petch relationship; the smaller the size of the grains in a material, the stronger that material becomes (to an upper limit) because of grain boundary strengthening effects (equation 2.1) [142].

$$\sigma_y = \sigma_0 + k_y d^{-\frac{1}{2}}$$ (Equation 2.1)

This reduction in grain size prevents movements like slip and glide and prevents the material from deforming. However, it does serve to make the material less ductile. This is relevant to rapid solidification, because when a metal solidifies very quickly, its grains do not have time to grow. These smaller grains provide a different form of strengthening, but it is far more uniform than segregation strengthening.

2.6.4 Alloy Design

The immediate aspect of alloy design is choosing a base material to act as a matrix phase. Base material choice has a major impact on what kinds of alloying elements can be added. An example of this can be seen with iron and nickel, with a wide range of alloys containing both of these materials (such as Invar or IN718) existing in regular use in the modern world. As well as determining the alloy additions, the base material also governs the general properties of the final alloy. For nickel, this provides a strong, chemically resistant material base that is capable of resisting deformation at higher temperatures, but retains some workability once alloyed. Nickel-iron alloys tend to find many uses in magnetic applications because of the two materials' soft magnetic properties.

For nickel alloys in high-temperature or highly corrosive applications, the ability of the material to resist deformation when subjected to these extreme environments is paramount. Nickel superalloys are often designed with these applications in mind. For example, IN939 contains ~22wt% chromium, which drastically improves the corrosion resistance of the alloy, particularly for its use as a high-temperature material [143]. This resistance to corrosion means that in applications such as industrial turbomachinery, these devices can be operated for longer between services and components require replacement less frequently.

As mentioned in section 2.2.3, the γ' phase is regarded as the most important phase for high-temperature applications. To produce this material phase, smaller amounts of aluminium and titanium are added, normally between 1-10wt% in total. In some alloys, the level of γ' can be as high as 70%. This phase can be very well-integrated into the γ matrix with relatively low interfacial energy if properly utilised, providing a method of strengthening for the alloy. The cubic structure of γ', with alloy additions at the corners of the unit cell, provides a good fit with the matrix γ phase, thus reducing lattice misorientations between phases (figure 2.28).

Other metallic elements are added to provide specific qualities on a smaller level, without affecting the positive behaviours of the base material. An example of this is found in tungsten, which is often added to higher-temperature alloys. Whilst its high-density prevents larger amounts from being added, a small percentage is usually enough to impart its nature as a more refractory element, increasing melting points and preventing loss of cohesion at higher temperatures.

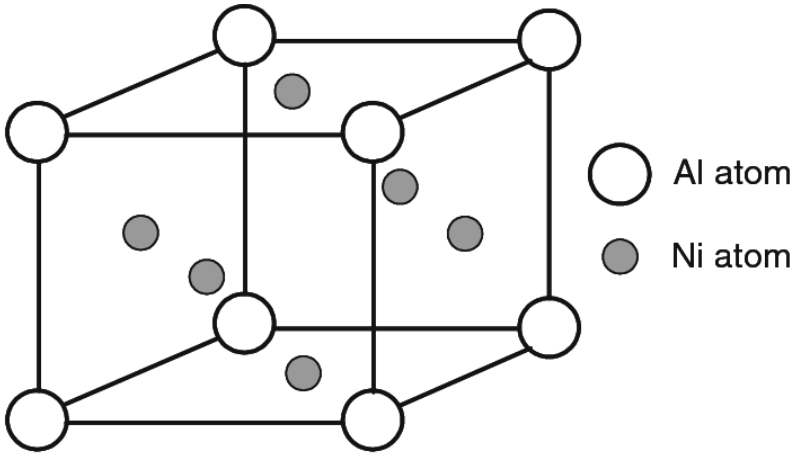

Figure 2.28: The FCC crystal structure of Ni_3Al [144]. *This is representative of the structure of the γ' phase in nickel superalloys, which often have their Al atoms replaced with Ti ones.*

As mentioned previously, CMSX-4 contains around 3% rhenium. This addition acts as a grain boundary-strengthening agent, pinning dislocations as they travel through the material. At higher temperatures, this reduces the amount of deformation that the material suffers due to creep. This addition acts in a similar fashion to that of hafnium in CM247-LC, however hafnium is more common, as it is produced as a by-product of the refinement of zirconium due to the natural occurrence of the pair [145]. Hafnium acts to improve the corrosion resistance of nickel alloys. Small additions around 1% have been shown to increase drastically the chemical resistance of nickel alloys. In CM247-LC, hafnium has also been proven to act as a grain boundary strengthener in directionally solidified alloys, suppressing cracking in certain amounts [146].

When hafnium segregates in nickel superalloys during solidification, it generally either segregates to the grain boundaries or to the γ' phase. In the γ' phase, this element tends to replace aluminium in Ni_3Al [147]. More commonly however, hafnium tends to segregate to the grain boundaries, where it acts to form carbides, along with boron and zirconium. It is grain boundary segregation that acts to form the level of strengthening that prevents high-temperature creep.

2.6.5 In-Situ Alloying

In powder metallurgy, most powders used are pre-alloyed. This means that when the powder is first atomised, it is done so from a feedstock of the same material. In order to change the composition of a pre-alloyed powder, one would need to re-melt the powder and add whatever compositional changes were required, then re-atomise the solidified material. This is both costly and wasteful. An alternative to this is to use a process known as in-situ alloying [148].

In-situ alloying is a method of changing the composition of a material that does not involve altering the composition of the powder before the process. Instead, powder of one alloy composition can be mixed with another powder batch in precise amounts, in order to provide a specific composition. Care must be taken in this instance to mix powders thoroughly, in order to ensure as homogenous a mixture as possible. An automatic mixing, stirring or tumbling process is usually used to ensure an even composition in the resultant batch, however alternative methods include using alternating powder size fractions to induce a "satelliting" effect [149]–[151]. This acts to produce a more homogeneous mixture of material, however for LPBF, this may have a negative impact on the spreadability of the powder feedstock.

This method of on-demand control of alloy composition has been shown to produce good levels of mixing of constituents. Indeed, the more similar the alloys, the more effective this method becomes. More recently, this method has been utilised as a method of manufacturing more exotic alloy compositions, such as HEAs [152], [153]. This novel family of alloys can be expensive to produce, making in-situ alloying from easily mixable elemental batches a very attractive route for processing. Challenges are still faced by this method however, with larger powder particles resulting in highly concentrated regions of particular compositions, which can sometimes result in highly uneven properties, even with a good mix.

2.7 Summary

While LPBF presents a novel and effective method of part fabrication for numerous applications and industries, there are clear and present challenges to progress in this field. Novel methods of process control such as pre-heated substrates present an ideal method of process control through manipulation of cooling rates during the build process and different types of scan strategy can be used to affect the orientation and direction of microstructural growth during the process.

Arguably, the biggest challenge is in understanding how materials behave during the LPBF process. Whilst the main family of materials involved in industrial-facing applications is metals, other fields of research such as in polymers [154], ceramics and regolith [155] are also of interest for their own sets of properties. To explore the emerging field of process monitoring, new sensors and monitoring techniques are being developed to be used in-situ inside machines. Melt pool emissions can inform as to how the material behaves under the high temperatures and how materials behave during rapid solidification [110], [156], whereas techniques such as powder bed scanning can characterise the behaviour of the powder bed [116], [157].

These monitoring techniques may lead to more sophisticated process control methods. This could potentially pave the way for automated control through use of advanced neural networks and other data-driven methods. To that end, more studies are focusing on the use of lower-resolution data streams to inform on process control, in order to increase the response rate of systems.

3. Equipment, Methods and Materials

This chapter covers the equipment, materials and techniques utilised for work in this thesis. Each of the results chapters includes an explanation as to specific operation required for the work performed (such as the exact temperature(s) of the heated substrate). This section focuses on the general operation and use of the equipment, specific materials and processes and seeks to provide an overview of the capability of each in turn.

3.1 Experimental Equipment

3.1.1 Aconity Mini

The Aconity Mini is a LPBF 3D printer produced by Aconity3D GMBH (figure 3.1) [158].

Figure 3.1: The Aconity Mini. The modular and largely open construction of this equipment allows for the rapid changing of many different components.

The system uses a continuous 1064nm Nd:YAG laser with a powder of up to 190W. The focal length of the laser can be controlled, providing a method of significantly altering the laser spot size. The chamber is backfilled with argon, producing an inert atmosphere for the process to take place in. Whilst the primary function of this system is research-based work, the cylindrical powder bed has a diameter of 140mm and a maximum height of 200mm, meaning that larger parts can still be produced if desired. Powder feedstock is supplied to the powder bed (figure 3.2A) through a manually filled, equally sized supplier volume (3.2B) in front of the build volume (figure 3.2). As the build volume drops, the supplier rises to provide the required powder (which can be increased or decreased through the software), which is then swept into the build volume by a wiper rake (3.2C). Excess powder is captured in the overflow trap (3.2D), where it can be collected and re-used once it has been sieved.

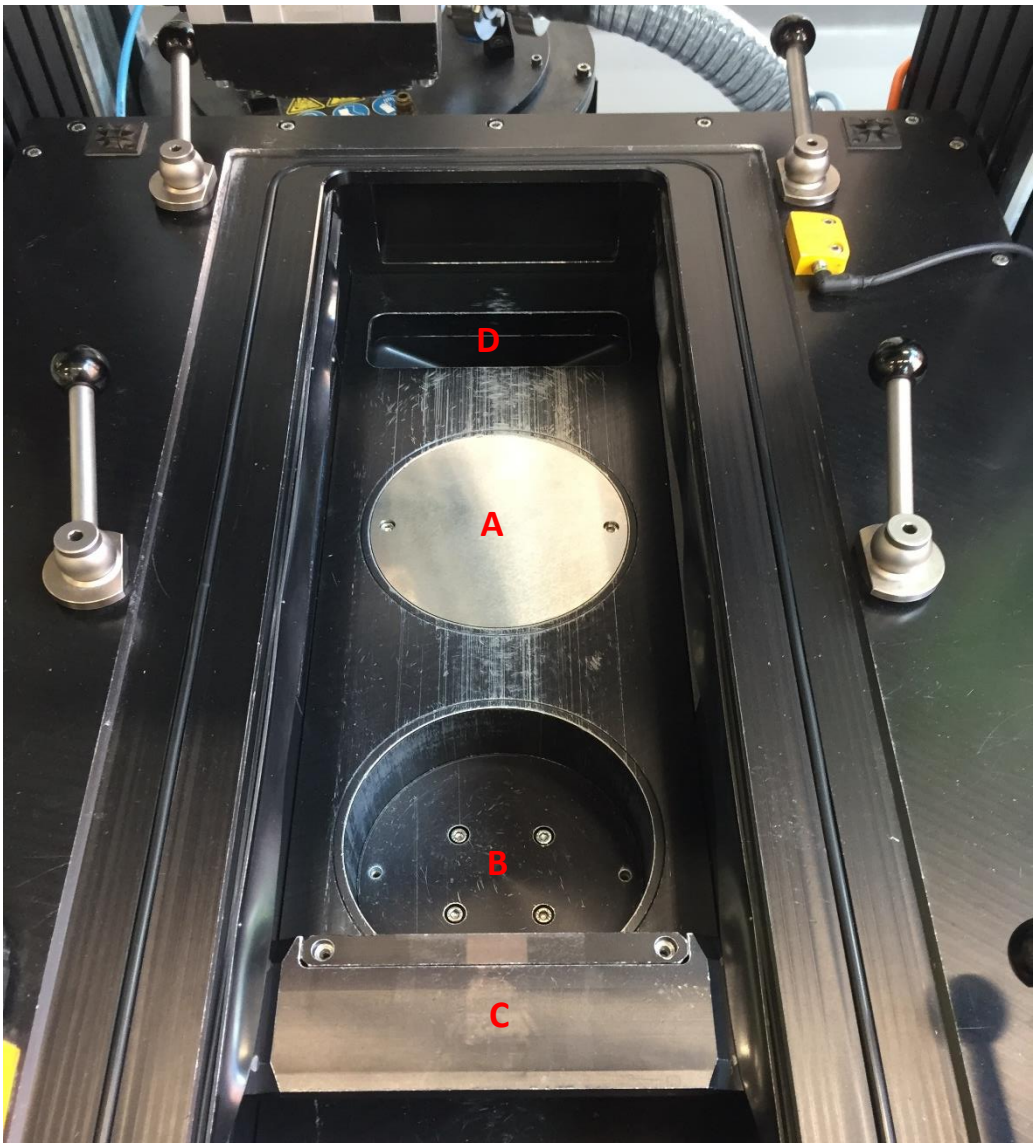

Figure 3.2: The chamber interior of the Aconity Mini, photographed from above. Key components are denoted as follows: A: The build volume. B: The supplier volume. C: The wiper rake. D: The overflow trap, leading to a sealable container.

Upon commissioning, Aconity3D provided technical data for the spot size of the Aconity Lasers. The provided data is appended at the end of this thesis in Appendix A. The X and Y dimensions of the spot were tabulated and graphed to provide a simple reference chart for estimated spot size of the laser beam, which is provided here in figure 3.3.

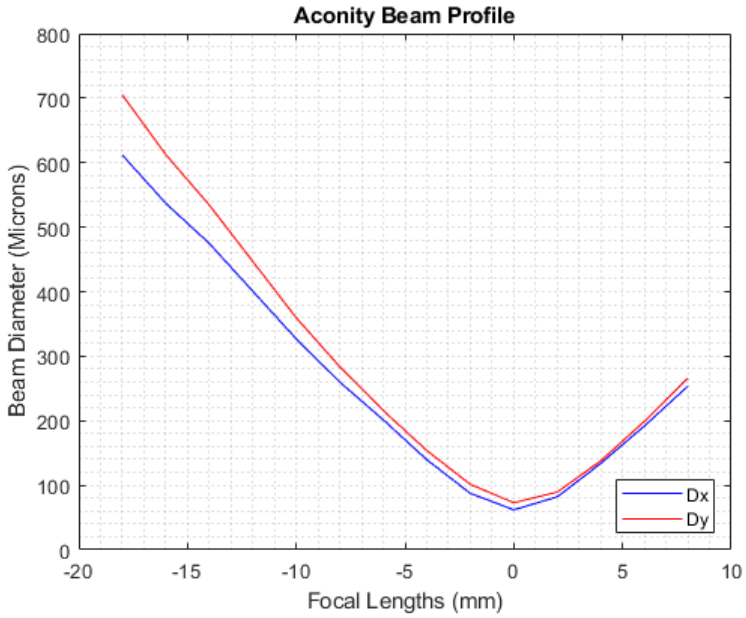

Figure 3.3: Aconity laser beam profile. The laser's focal length can be adjusted, providing control over the effective spot size. Data for this was provided by Aconity, and was interpolated to provide a graph for easier visualisation (see appendix A).

The advantages of using the Aconity Mini over other systems (such as Rensihaw or EOSINT systems) are numerous. Firstly, the printer is designed for small-scale, rapid turnover parts and jobs. This reflects its design as a research platform, differing from the Renishaw or EOS which are systems that were originally intended as workhorse systems to make batch-produced parts from a single material. Whilst all machines are capable of producing very high-quality parts, the Aconity is far superior in the research role. It is much simpler to use, much more reliable, with far fewer moving parts and operational issues. It is also much easier to clean when a material change is required, only taking around an hour to clean compared to around five (or more) hours for Renishaw systems.

The second major advantage to the Aconity Mini is the (albeit basic) in-situ monitoring systems that are incorporated into the design. The laser head has an optical breadboard attached (figure 3.4), which is capable of providing a coaxial signal from the laser target site. This allows for the associated pyrometers to provide data on the relative temperatures in the produced parts on a layer-by-layer basis. In addition, this optical system (figure 3.5) is modular in its design,

meaning that parts can be exchanged freely on the whim of the operator. A high-speed optical camera is also mounted to the same optical rail as the pyrometers.

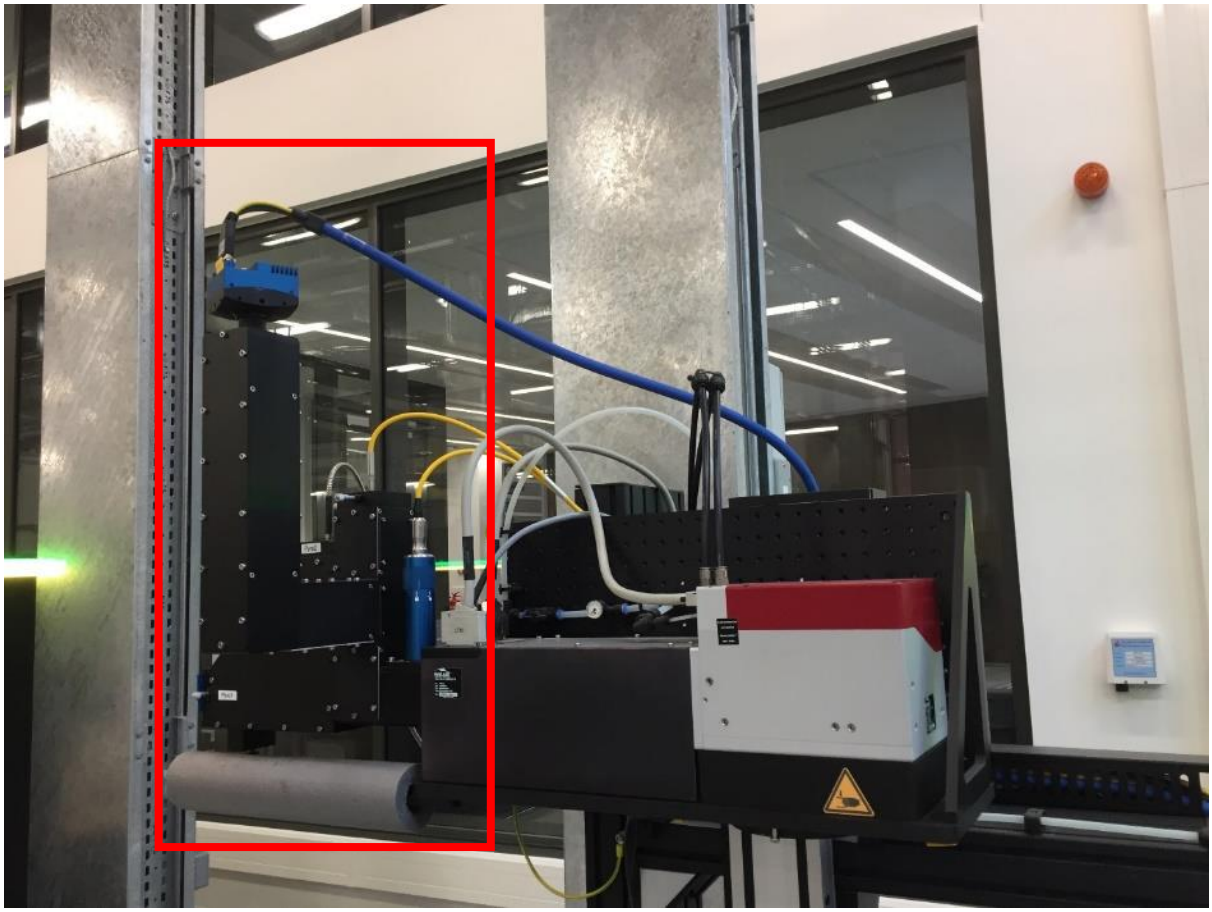

Figure 3.4: The Aconity Mini's optical system. This system consists of a coaxially mounted suite of sensors (highlighted in red box), including two pyrometers and a high-speed optical camera. The concurrent measurements are made possible using a beam splitter.

The final major advantage is the "open source-like" nature of the system. The software of the Aconity Mini is controlled by a python interface, meaning that coding extra functionality is possible. This freedom of control over the process can also be extended to the collection of data in the in-situ monitoring systems. By analysing the data provided by the monitoring systems, it has been possible to produce a script that automatically changes the laser parameters within the framework of the Aconity Mini, and provide "real-time" adjustments during a build.

The pyrometers' collection of data is activated at the start of each layer and only stops when the end of the layer occurs. This means that data is collected when the laser is on and when it is off, often resulting in slightly anomalous readings making the parts appear cooler.

This includes when the laser is switched off and moves between components, which appear as a series of dark lines between components.

Two pyrometers are present on the Aconity system. The modular nature of the system allows these devices to be exchanged for other sensors, if so desired. These devices collect data coaxially to the laser spot's position, meaning that emissions are always centred on the melt zone. Data is collected by the pyrometers from the zone being observed and is then averaged to provide a single value approximately every 6µs. This builds a picture of the surface being produced, providing an insight into where hot or cold regions are forming in parts.

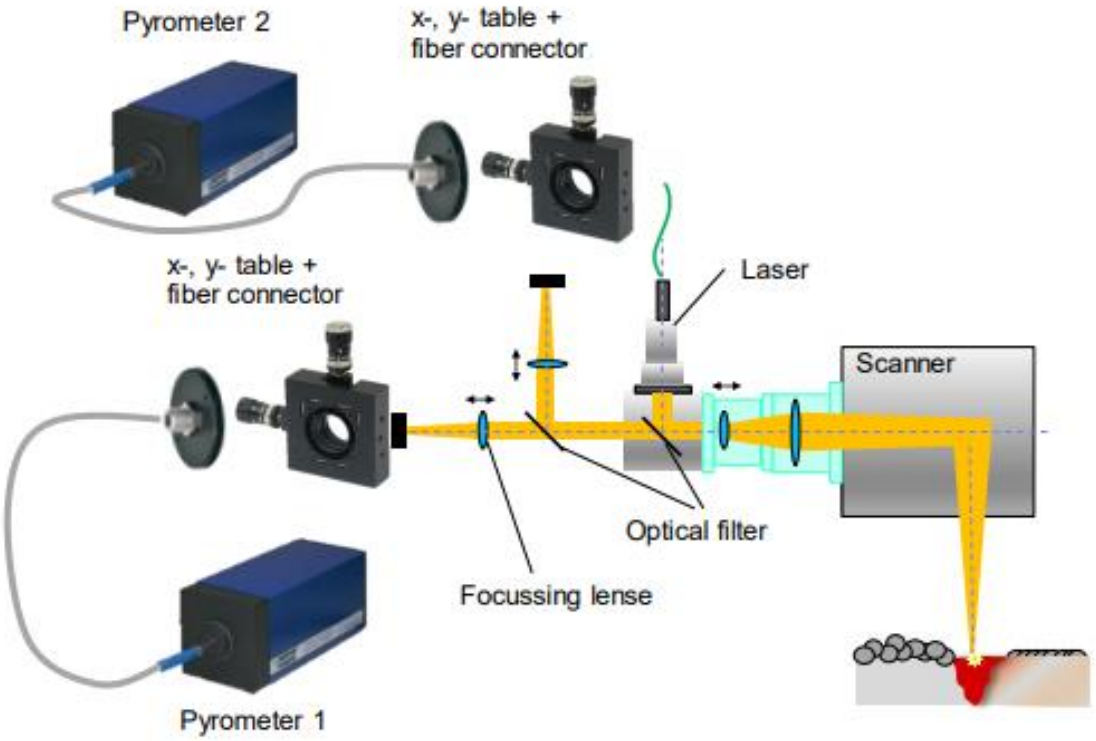

Figure 3.5: The Aconity Mini's pyrometer optics [159]. *The thermal emissions travel back through the system to the filters and lenses from the melting material and are collected by the two pyrometers. Specific lenses or filters can also be modified interchangeably, owing to their manufacture.*

As well as these more specific advantages, the Aconity Mini is not specifically restricted to any one family of material. Whilst the focus in this project was on Nickel-base superalloys, other metals such as steels [160], aluminium [43] and various HEAs [152] have been successfully printed on this system by members of the Materials Science department in Sheffield.

3.1.2 Aconity Lab

The Aconity Lab (figures 3.6-3.8) is largely similar in terms of its base design to the Aconity Mini, but has several key features that distinguish it. Firstly, it uses a 390W Nd:YAG laser with a similar beam size to the Aconity Mini, at a wavelength of 1064nm. This higher power allows for more efficient processing of materials such as copper and aluminium, which often require high powers due to their high rates of thermal conduction. Secondly, the system features a wider build volume of 170mm (figure 3.7A), making it more suited to manufacturing larger components. The powder supply mechanism is also different. Whilst the Aconity Mini uses a reservoir that is shear-fed, the Aconity Lab uses a gravity-fed hopper mounted above the build chamber (3.7D). The powder travels downwards into a set of small holes within a piston. The system then uses the piston to dose a set amount of powder into the chamber, which is then swept over the build volume, again by a wiper rake (3.7B).

The Aconity Lab can also be set up to use a unique and experimental module; the induction-heated build substrate (figure 3.8). This module uses a copper coil to produce a magnetic field, which joule heats a molybdenum holding plate. This plate then heats the build substrate via conduction. The system can reach temperatures of up to 1200°C, providing a completely different environment in which to perform the LPBF process and allowing for microstructural control. This technique does reduce the build plate's diameter to 70mm however, meaning that it is unsuitable for producing larger parts. In addition, whilst the molybdenum heating element can reach 1200°C, there will be a thermal gradient across the fabricated components and build substrate, meaning that the taller the build, the less effect the heating unit will have on the higher layers. What this does mean however, is that the substrate should be capable of reaching temperatures where recrystallization and recovery will occur in most materials, making it a useful tool for microstructural control. Use of this module is explored in chapter 5 and a more detailed schematic of its design is shown in figure 3.9.

Similarly to the Aconity Mini, there are no limits to the materials that can be used. However, due to their low melting points, some materials cannot be used in conjunction with the induction heating unit as this presents a safety hazard. Conversely, the higher laser power of the Aconity Lab allows for more effective processing of materials with extremely high thermal conductivity, such as aluminium and copper.

Figure 3.6: The Aconity Lab. While this system lacks the monitoring systems provided with the Aconity Mini, it retains the modular design, meaning that monitoring systems can still be installed easily if desired.

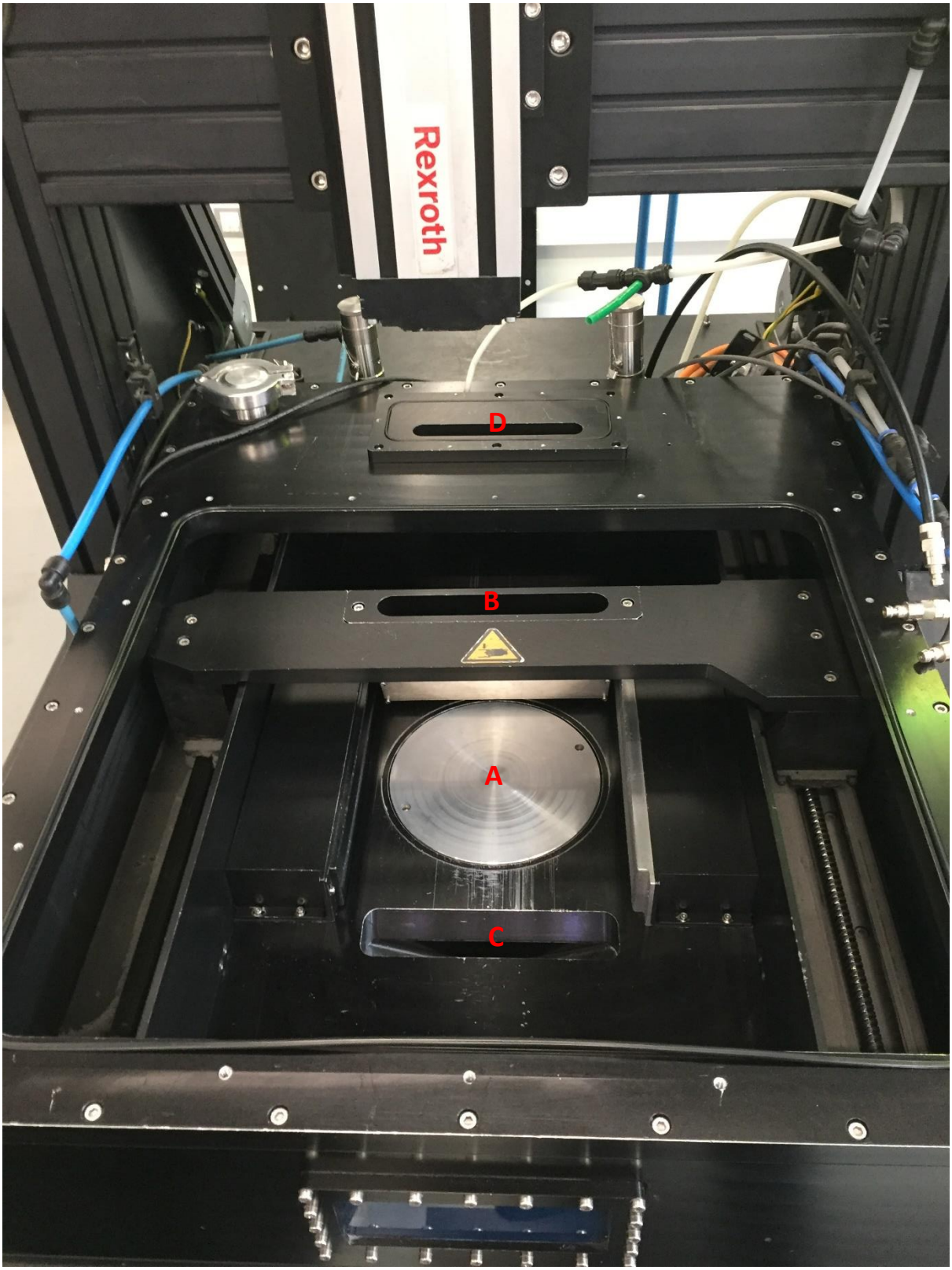

Figure 3.7: The Aconity Lab's interior, photographed from above. Key components are denoted as follows: A: The build volume. B: The wiper rake. C: The overflow trap. Note that the supplier differs from the Aconity Mini. It is a gravity-fed dosing mechanism that feeds from a hopper at the rear of the machine, mounted over the slot labelled "D".

Both the Aconity Mini and Aconity Lab utilise a rake system which allows for numerous different types of rake. Carbon fibre brushes, metal scrapers and silicone rubber are all options for the wiper rake material that can be used sweep the feedstock through the system. For this study, silicone rubber rakes were used exclusively to ensure consistency.

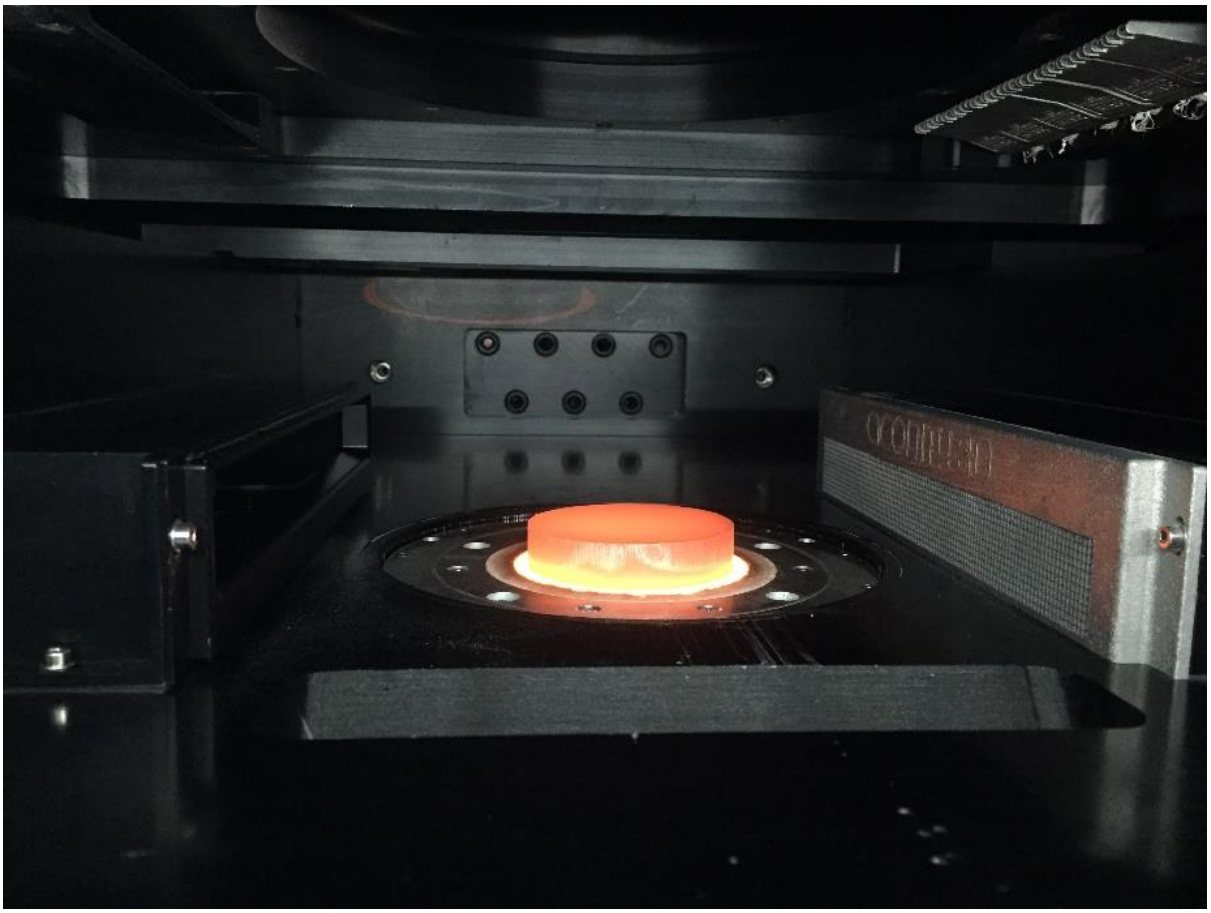

Figure 3.8: The Aconity Lab Heated Bed: This allows for the preheating of the build substrate. The heating is provided using an induction loop, heating a molybdenum element, which in turn heats the substrate via conduction. This unit replaces the build volume of figure 3.7, reducing the area that can be initially built on.

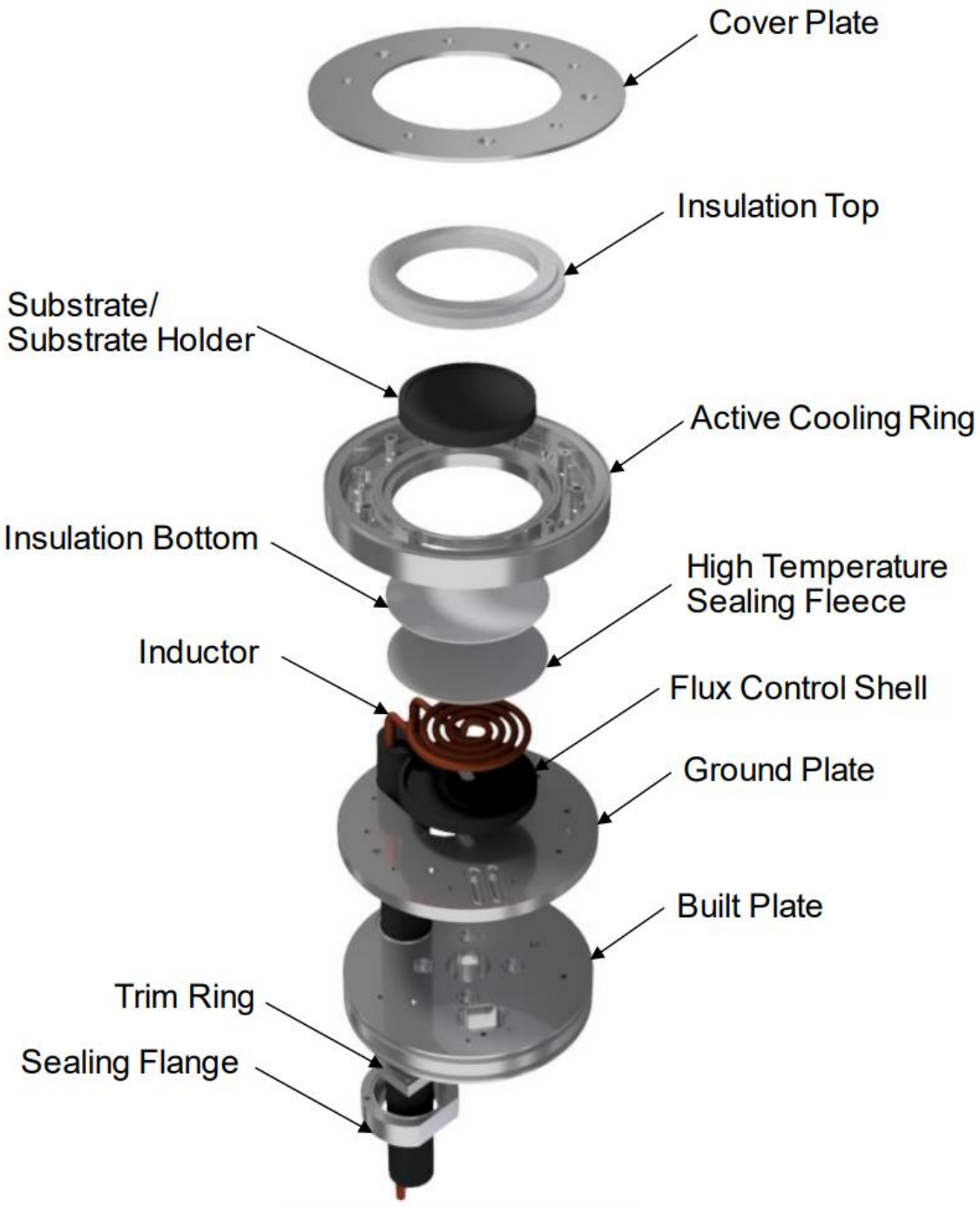

Figure 3.9: Schematic deconstruction of the Aconity Lab's heated bed. The substrate holder acts as the heating element, with the control thermocouple resting between it and the insulation bottom, feeding through the sections of the construction similarly to the inductor coil's housing.

3.1.3 Taraz Metrology 3D Scanner

A final method of sample characterisation involves the use of a 3D scanner. A point of great interest in AM-produced parts is the surface finish of the component. Whilst in traditional manufacturing this could often be overlooked or fixed through post-process machining, in AM, it is often necessary to achieve an ideal surface finish on fabrication. The bottom surface of an overhang for example is likely to be covered in partially-to-little melted particles of powder, resulting in a rough surface. This roughness can serve as a crack initiation site, or may provide an increased surface area for chemical attack and erosion. Because of these factors, it is vital that the impact of process parameters on surface roughness be investigated. The 3D Scanner obtained from Taraz Metrology (figure 3.10) is an example of a system that is capable of providing a quantitative analysis of a surface.

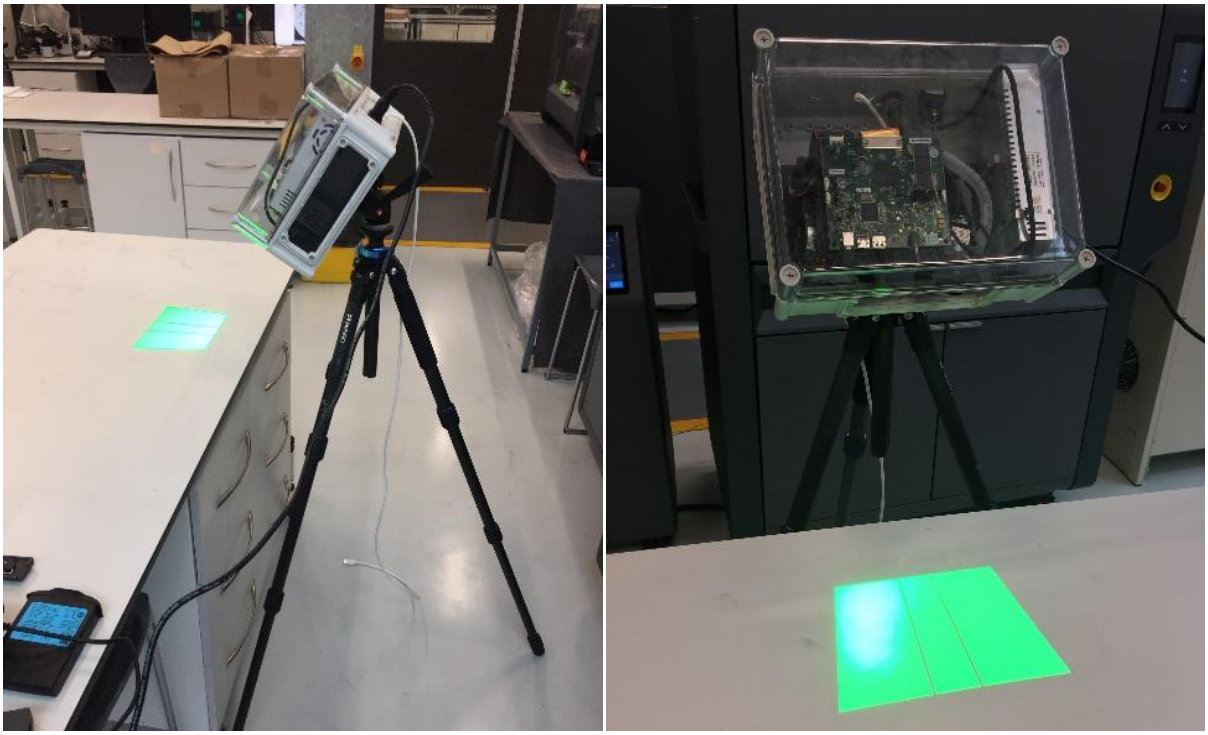

Figure 3.10: The Taraz Metrology 3D Scanner. This system also presents a method for producing a 3D scan to perform digital twinning of components.

This system uses the principle of photogrammetry. A surface is scanned with a known pattern of light and dark shapes and the distortions in that moving pattern are detected by a camera.

The images are then analysed in order to generate a 3D map of the surface in the form of a point cloud. This point cloud can then be manipulated using a piece of suitable software such as CloudCompare to produce a 2D colour map, which can then be exported to Matlab (or another language) in order to provide analysis of the variation in the height of the component. This data can be used to provide feedback for parametric studies and has the potential to be included in the development of an automated control system within the Aconity Mini.

This scanner uses a structured light-based approach to create a 3D point cloud of its target. The scanner consists of two main parts: the projector and the camera. The projector produces a series of dark and light lines and scans them across the surface in question, with the camera capturing images to allow for a comparison between expected and actual line shapes. This allows for the detection of powder bed defects, which are the primary source of build failures in LPBF. By creating a map of the powder bed every 5-10 layers, the system will be able to detect whether or not there are problems with the powder bed and can pass the data to the automatic control system. For example, if the powder bed has dips in it, this could be caused by insufficient spreading, so the control system would increase the powder dosage. On the other hand, if parts begin to swell from overheating and protrude from the powder bed, the system would detect this and reduce the power of that component part. This could even extend to suppressing it altogether until the next scan if the swelling is severe. This in-situ control system would allow the system to prevent damage to the powder bed, thus allowing for builds that are more consistent. In addition, the data from the model that is then passed to the learning algorithm will then be used for determining which sets of parameters are good and bad in terms of component swelling, further reducing the chance of build failure.

3.2 Software Used

3.2.1 Netfabb

Both the Aconity Mini and Aconity Lab require a CAD file in order to produce components. This CAD file is produced in Autodesk NetFabb. The file begins as a .stl file which is a combination of the geometric shapes and the associated laser parameters that are desired by the user. This includes laser power, scan speed, hatch spacing, defocus, scan strategy and rotation strategy. The .stl file is then converted into a .ilt file, which contains the raw code required by the Aconity Mini and Lab in order to perform the building process. In order to keep the design process simple, users often produce 5 or 10mm cubes on the Aconity if performing a parameter study or investigating microstructure. However, parts must be removed from the build substrate before being analysed. In this study, this was performed using wire EDM, a technique that machines without physical contact between materials. Whilst this is useful for materials that undergo stress-induced phenomena such as TRIP, it is a more expensive and time-consuming process than other forms of machining.

To circumvent this, supports can be built to attach loosely a sample to the build substrate. However, because the powder acts as an insulator (being around 1/4 - 1/3 argon gas due to powder packing fractions) the material often cools more slowly. The slower cooling leads to overheating, meaning keyholing can occur which in turn leads to swelling. This swelling can cause a catastrophic build failure in the initial layers after the support is built, meaning that swelling may catch on the powder rake, resulting in either the rake being stopped from sweeping, or destroying the component currently being fabricated.

To prevent failure by warp detatchment, a more sophisticated support system must be employed. The solution used in this study can be seen in the diagram below (figure 3.11). By creating a supported upturned cone beneath a sample, it is possible to create a support that allows for rapid removal without the need for wire EDM. Critically however, this method of component support solves the problem of first-layer failure that often occurs when building with supports in LPBF.

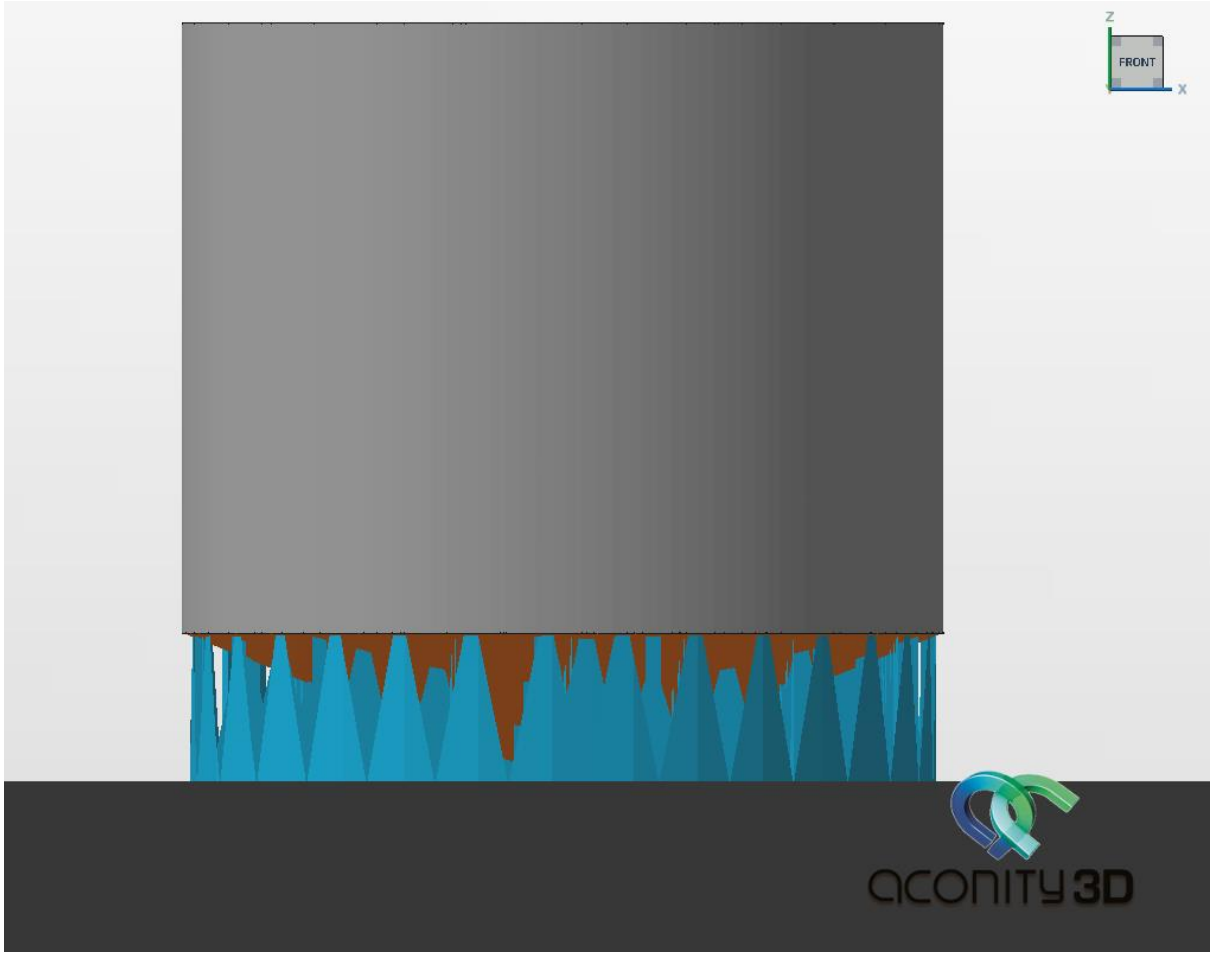

Figure 3.11: A basic diagram of the support structure used in this study to remove the need for EDM. This structure allows the desired sample to be built on a small sacrificial platform (orange/blue), which can be removed quickly once the process is completed.

The support creates a sacrificial zone at the bottom of the component, allowing the heat from the actual desired sample to escape quickly, preventing catastrophic warping. The bulk material of the upturned support can still fabricate successfully, as it is connected to the build substrate via the centre of the cone, providing a heat sink.

3.2.1 Thermo-Calc

Chapter 6 of this thesis examines the use of the software package Thermo-Calc to predict the Scheil solidification and crack susceptibility of different alloy compositions. The specific alloys and compositions are detailed later in this chapter (chapter 3). In order to utilise Thermo-Calc correctly, it is important to know the exact composition of each alloy, as this can cause major changes to how the alloy solidifies during Scheil solidification.

Thermo-Calc has been used regularly in published work to produce phase diagrams of alloy systems. However these diagrams can be highly complex and difficult to follow, particularly for nickel-based superalloys which tend to be extremely complex alloys, with dozens (or more) of phases. For this thesis, Thermo-Calc's Scheil solidification package also allows for the determination of the constituent phases that form at different temperatures during the solidification process. The concentrations of phases in an alloy at different temperatures and liquid concentrations are non-trivial to calculate, meaning that a software package such as this can be extremely useful for examining and predicting how minor changes to alloy systems will affect the behaviour of the material before actually producing large amounts of the alloy in question.

To ensure consistency across different simulations, each alloy system was simulated in Thermo-Calc 2021b using the same nickel alloy database (TCNI8: Ni-Alloys v8.2). A Scheil simulation was performed for each alloy system, with the fraction of liquid ranging from 1 to 0.01 (i.e. 100% to 1% liquid concentration). The simulations were repeated to produce both graphical and tabulated outputs, allowing for an analysis of the data as well as a convenient visualisation of which phases begin to form at different temperatures.

3.3 Materials Used

3.3.1 CM247-LC

This alloy's lack of processing routes is largely attributed to its content of the gamma-prime phase. This is the material phase observed in nickel superalloys that imparts their characteristic high strengths, particularly at high temperatures. CM247-LC contains significantly more gamma-prime phase than other, easier to manufacture with alloys such as IN718. The composition of the specific batch used is shown below in table 4.1:

Table 3.1: The chemical composition of the CM247-LC powder batch used in this study.

Element	Weight Percent Range (wt%)	Batch Weight Percentage (wt%)
Al	5.4-5.8	5.6
B	0.01-0.02	0.013
C	0.04-0.08	0.06
Co	9-9.5	9.44
Cr	8-8.5	8.38
Hf	1.2-1.6	1.35
Mo	0.4-0.6	0.51
Nb	<0.1	<0.01
Ni	Balance	Balance
Ta	3.1-3.4	3.26
Ti	0.6-0.9	0.78
W	9.3-9.7	9.61
Zr	0.005-0.015	0.009

CM247-LC powder was obtained from LPW (prior to its assimilation into the Carpenter Group). Before being processed in the Aconity Mini or Aconity Lab, it is vital to examine and characterise the powder feedstock to ensure that it will flow effectively in the system. A small sample of powder was taken using a conductive sticky pad, in order to check the morphology of the powder. SEM imaging is required, as optical microscopes cannot properly image the particles. Figure 3.11 shows a representative sample of the batch. The SEM image was obtained using the Inspect F50 (section 3.3.5). In addition to SEM images, a proper analysis of the powder's PSD is also necessary to check the suitability of the powder. Figure 3.12 shows the cumulative PSD of this batch of powder.

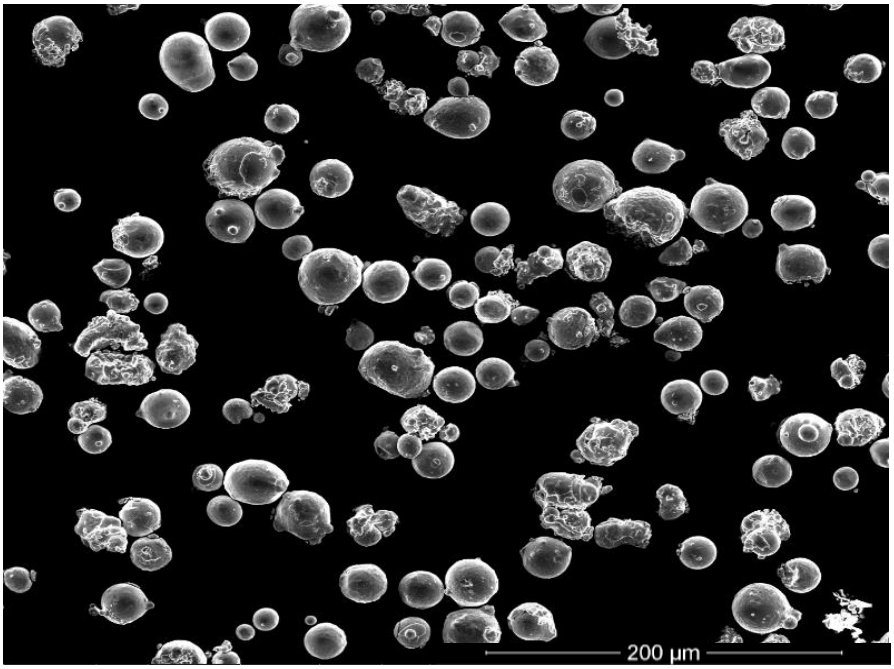

Figure 3.12: SEM micrograph of CM247-LC powder. Whilst some of the powder is malformed or non-spherical, the relative sphericity of the batch is consistent, and the powder size range does not pose any problems for packing or flowability.

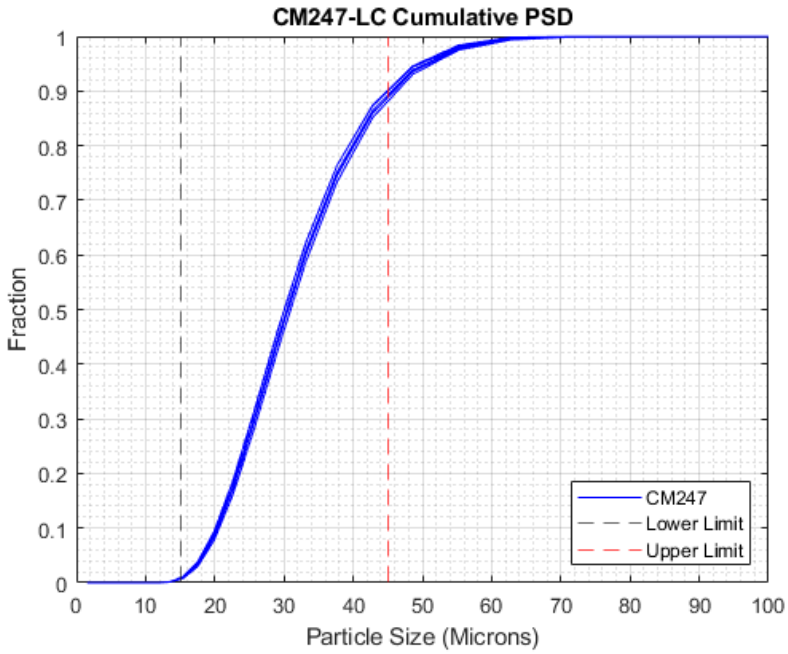

Figure 3.13: Cumulative PSD of the CM247-LC batch used for this study. Note the upper and lower limits at 15 and 45 microns. Around 10% of the sampled batch is above the upper limit. Whilst this is beyond the accepted limits for the Aconity systems, it is not a problem for the LPBF process as it does not impede flowability.

Examining the powder, most particles exhibit a high degree of sphericity. This is highly desirable in AM, as the more spherical a particle is, the better it tends to flow. Spherical powders do not agglomerate or lock together as much as non-spherical powders do.

3.3.2 Powder Feedstock Comparison

Each powder that was used in this study was subject to a PSD test before use. This is to ensure that the powder is within the specified range (15-45µm in this instance) and to ensure no artefacts are present. Performing this test also provides an insight into how the powder will behave during the spreading phase of the LPBF process. The distributions of each material used in this study are shown below in figure 3.13, with a cumulative chart in figure 3.14. None of the size distributions are completely within 15-45µm. This is not a concern for CM247-LC as the majority of powder still lies within the 15-45µm range. However, for CM247-NHf around 20% of the powder is in the sub-15µm category (figure 3.13b). This presents a significant problem for powder dosing within the Aconity systems.

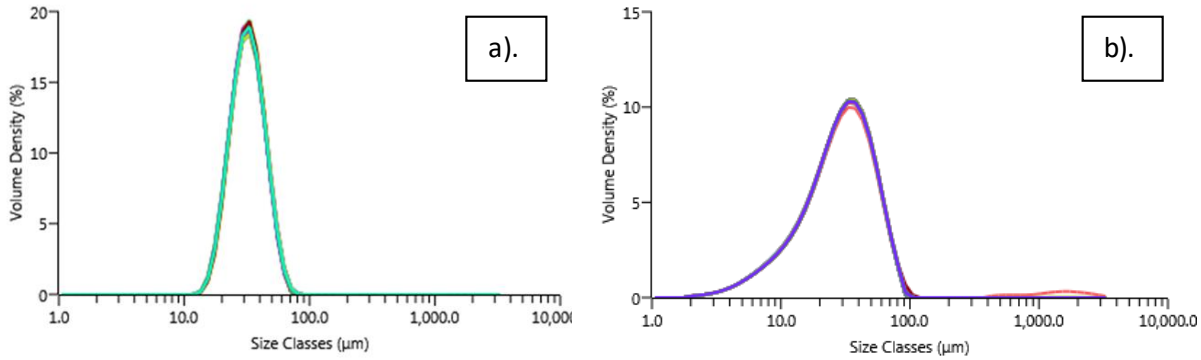

Figure 3.14: Particle Size Distributions (PSDs) of: a). CM247-LC, b). CM247-NHf. Whilst a). is within an acceptable range, b). presents a significant obstacle for powder spreading.

The issue lies with the powder packing fraction. In normal, spherical powder that is within the optimal size range, the packing fraction is around 65-70%. This means that around 30-35% of the space in a powder sample is indeed that – empty space. Because of this, powder particles can move freely when a force is exerted upon them, similarly to a set of ball bearings being poured from a container.

By contrast, the powder distribution seen in figure 3.13b has a packing fraction that tends to 99.9%, due to all the small particles taking up the space between the larger particles. Because of this, the powder particles are more difficult to pull apart, making the powder flow of a population of this size range more difficult. These small particles can prove to be a particular nuisance when passed through a narrow channel, such as that found in a Hall Flow funnel test. The narrow passage – 2.5mm in diameter – reduces the rate at which powder can flow due to gravity. This means that even a small powder agglomeration can clog the channel and halt the flow entirely. The Van-der-Waals forces between the particles, coupled with frictional forces at the channel wall, become stronger than the gravity pulling them through the channel.

A similar effect can be seen with the supplier system in the Aconity Lab. The narrow channels that provide the set amount of powder to the dosing mechanism can very easily become clogged by small powder distributions, as happened with the Hafnium-free variant of CM247 when it was first used. This clogging of the supplier mechanism is fatal for the Aconity Lab, and prevents the use of this powder in its as-received state. The Aconity Mini, which uses a shear-fed reservoir system also encounters problems with fine powders, as the powder does not spread evenly, instead agglomerating in lines parallel to the deposition rake as it travels. However, the effect is not quite as destructive to a build as in the Aconity Lab.

In order to ensure that the powder's problem was with its size rather than its morphology, the Inspect F50 electron microscope was used to image a powder sample. Figure 3.15 shows a micrograph of the CM247-NHf powder feedstock. Whilst the particles are mostly spherical, a significant number of very small bodies are present within the sample. Two methods can be employed to rectify the problems faced from having too much sub-15μm powder. Firstly, the powder can be sieved to remove this size fraction. However, this is a very time-consuming process, as smaller particles take longer to remove from a distribution than larger ones. The second method and the one that was eventually used, was to use a flow additive to alter the packing behaviour of the material.

When small (<10μm) particles are in contact, a capillary bridge may form between the two bodies if one or more of the particles has even a small layer of moisture. Because of the high surface area to volume ratio of the powder, many of these "liquid film bridges" are formed on each particle. The flow additive works by adding very small amounts of nanoparticles of fumed silica into the powder sample. These nanoparticles settle sporadically throughout the powder, and act to reduce the amount of area that is available for bridges to form between the particles, thus impeding their formation. This results in a final powder that is much more amenable to the powder spreading process in LPBF. Care must be taken however, as adding too much fumed silica can have a deleterious effect on the bulk material properties. Small amounts however (around 0.01wt% and below), are nigh undetectable in the final product. Once treated with a fumed silica additive, the CM247-NHf powder began to flow more easily than before.

A test spread in the Aconity Mini showed that the treated powder spreads in an even fashion, meaning that it can be used. Table 3.2 shows the D10, D50 and D90 values for the two powder batches. It is clear from these values that the very low D10 value of the hafnium-free variant is likely to blame for the low flowability of the powder.

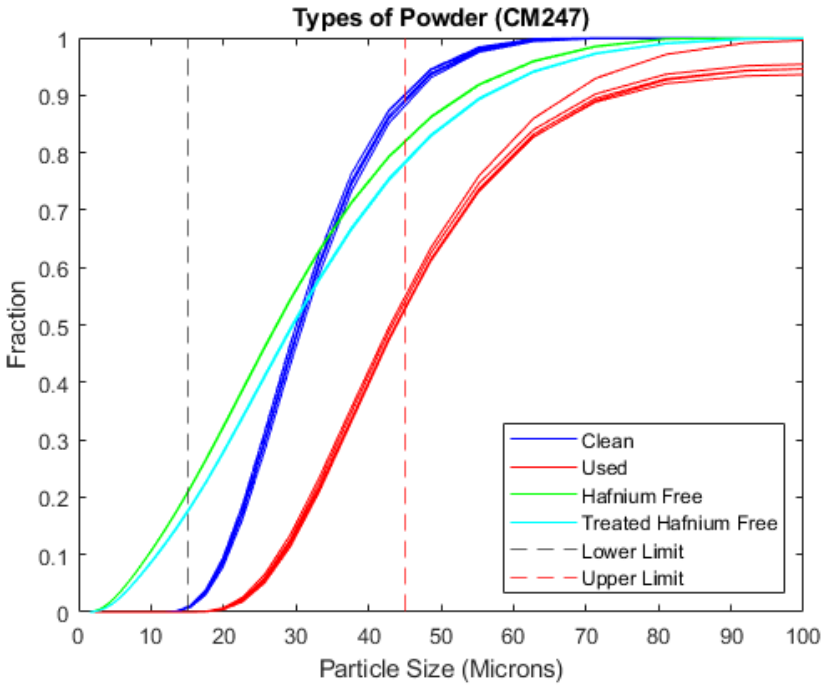

Figure 3.15: A cumulative powder size distribution chart to compare the different types of CM247 powder that were present in the project. The solid red lines denote powder that was removed via sieving with a 53µm aperture sieve after a single pass through the Aconity Mini.

Chapter 6 details the usage and analysis of samples produced using CM247-LC and CM247-NHf. In addition, an experiment involving a blend of the powders in various fractions is also considered. To achieve the two alternate blends, CM247-LC and CM247-NHf were mixed in a 1:2 and 2:1 ratio by passing the powders through a sieve shaker concurrently, in order to grade the hafnium content of the resultant product after melting. This acts effectively as a form of in-situ alloying, and should provide a thorough and even mix of the two grades. The two resultant blends are referred to as CM247-1Hf and CM247-0.5Hf, given their approximate resultant hafnium contents from mixing.

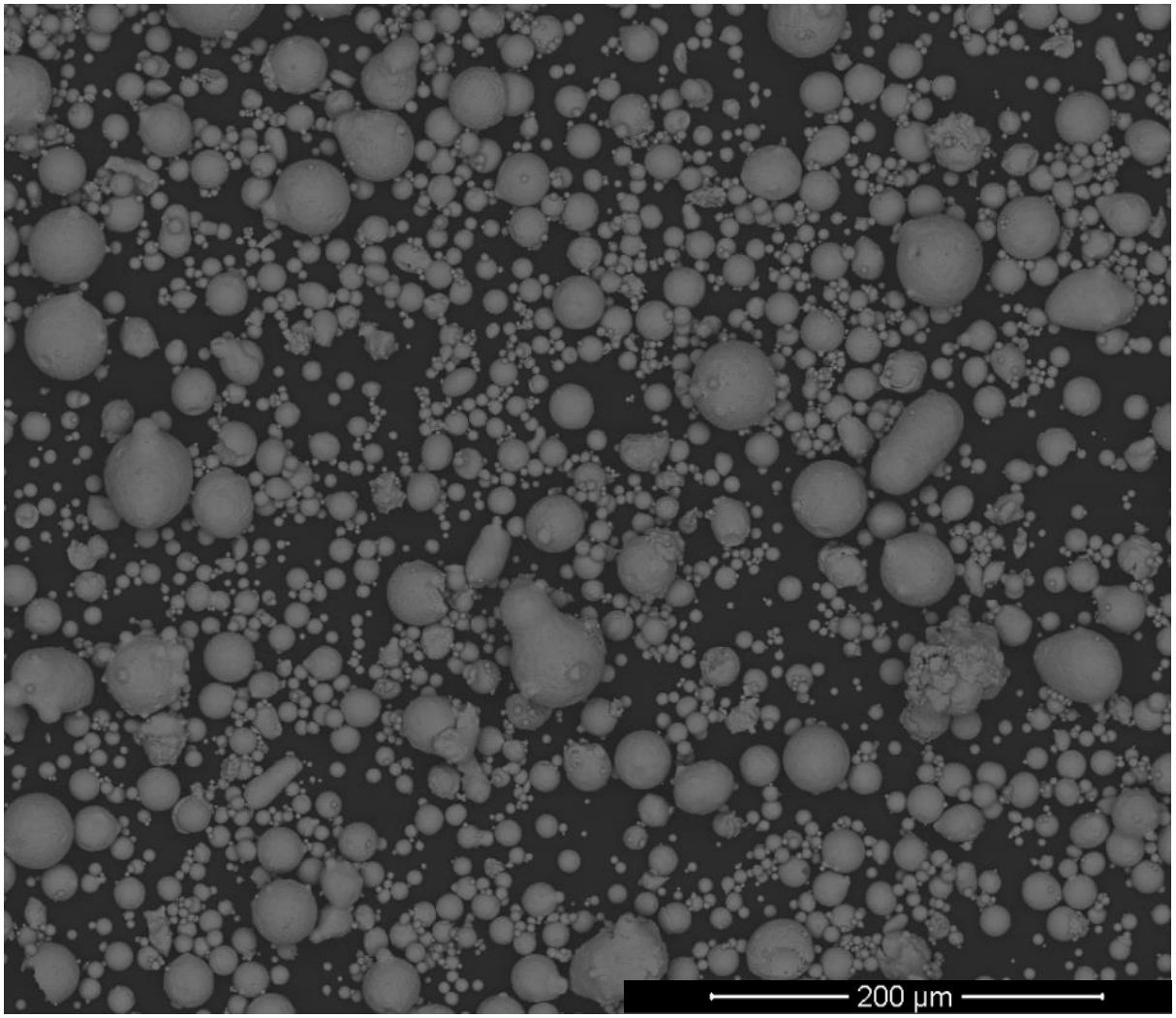

Figure 3.16: Hafnium-free CM247 powder as imaged by the Inspect F50. This image shows the extent to which the powder size range varies throughout the batch, despite the sample's PSD being 15-45µm according to the manufacturer.

Table 3.2: Percentile values for the average particle size distribution of the two CM247-LC batches. The drastic drop in D10 value suggests that a significant portion of the powder is small enough to cause packing-based flow problems.

Alloy	D 10	D 50	D90
CM247-LC	21.5	31.9	47.4
CM247-NHf	10.2	27.5	53

3.3.3 IN939 Powder Feedstock

Despite the significant amount of interest from both researchers and industry CM247-LC has received, it remains a difficult alloy to process consistently. An emerging alloy that is beginning to gain significant attention is IN939 [92], [93], [139], [140], [161], [162]. This nickel-based superalloy has recently become well known for its outstanding corrosion resistance, particularly at elevated temperatures. Whilst traditional investment casting of this alloy has been shown to produce high-quality parts, little has been published regarding the additive manufacture of this alloy. Similarly to CM247-LC, this alloy contains a significant volume fraction of gamma-prime phase, which is essential for high-temperature applications. Whilst it does not contain quite as much gamma-prime phase, it does contain a significant (22.5%) amount of chromium. Because of this, it boasts outstanding resistant to corrosion, whilst still being capable of withstanding extremely high temperatures. The composition is shown below in table 3.3.

Table 3.3: Chemical composition and partition phases of IN939 [143]. *The large chromium content of the alloy imparts massive corrosion resistance without adversely affecting the matrix material.*

Element	Weight Percent (wt%)	Partition Phase
Al	1.9	γ'
B	0.01	Grain Boundaries
C	0.15	Grain Boundaries
Co	19	γ
Cr	22.5	γ
Nb	1	γ', γ''
Ni	Balance	γ, γ', γ''
Ta	1.4	γ'
Ti	3.7	γ'
W	2	Grain Boundaries
Zr	0.1	Grain Boundaries

With regards to IN939, at the time of experiments there was only one other paper by Kanagarajah et.al [163] on this alloy as used in LPBF. Because of its novelty and lack of background in LPBF, it was determined as a good material with which to test the robustness of the machine learning algorithm. Table 3.3 provides a comparison between D10, D50 and D90 values for the IN939 Powder.

Powder was examined using the Inspect F50 and the Mastersizer. SEM images show good sphericity and very little in the way of either contamination or particles less than 15µm in diameter (figure 7.2)

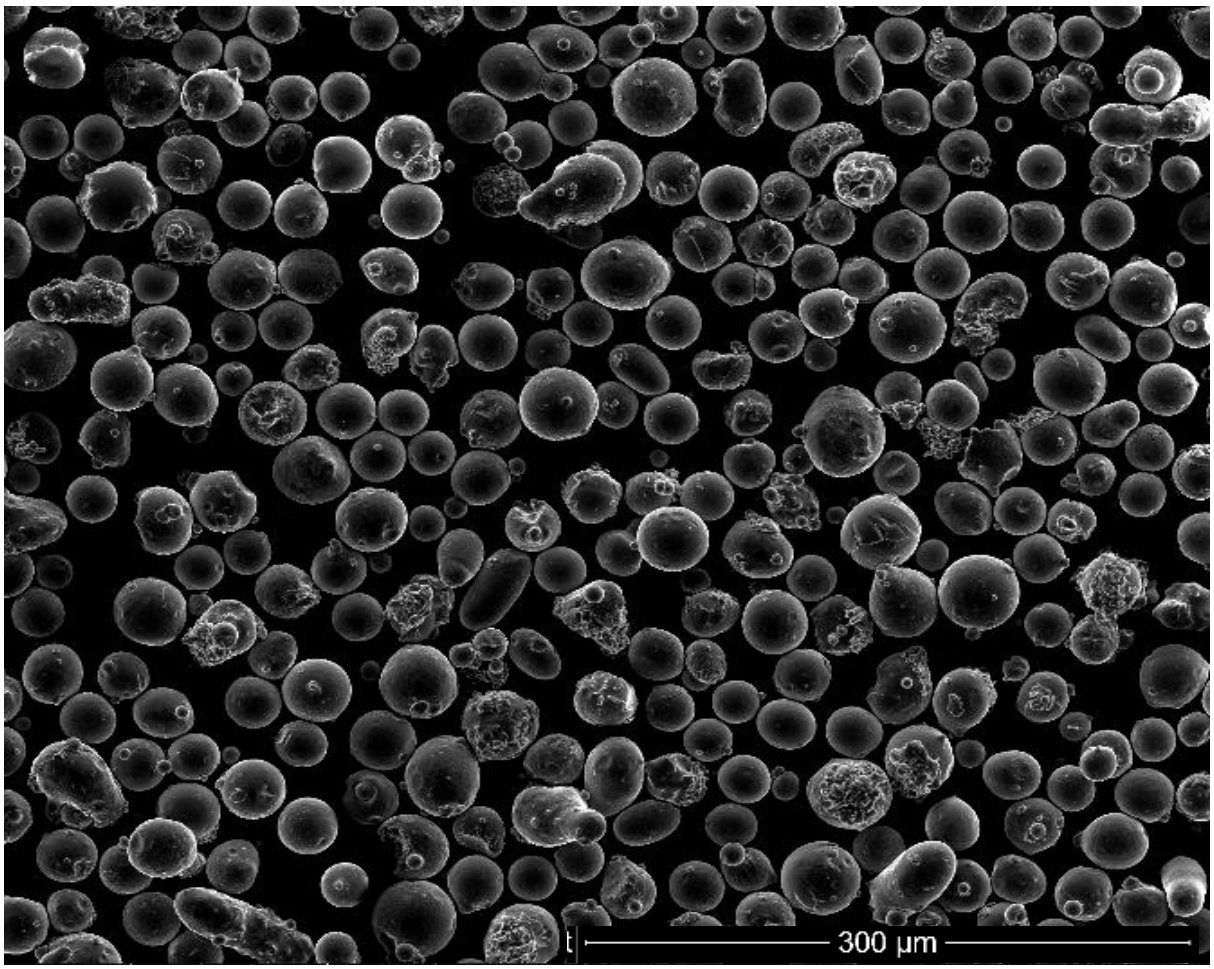

Figure 3.17: SEM micrograph of IN939 powder used in this study. This powder is highly uniform in terms of its size, making it ideal for use in the Aconity printers.

The PSD of the IN939 powder also showed the material's suitability for use in the Aconity Mini (figure 3.18).

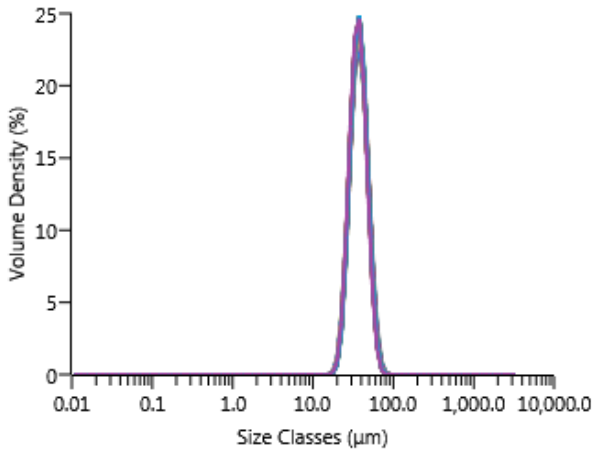

Figure 3.18 The PSD of the IN939 powder used in this study. The powder batch contains almost no subsize particles, meaning the flow of the powder should be suitable.

Table 3.4: IN939 average size distribution percentiles. This powder does not suffer from poor flowability and is acceptable for use in the Aconity systems.

Alloy	D 10	D 50	D90
IN939	25.8	34.7	47.7

3.3.4 Grinding, Polishing and Imaging Routes for Samples

Samples were mounted in Polyfast resin using a Buehler Simplimet 1000, then ground and polished using a Struers Tegramin-20. The mounted samples were 32mm in diameter. All samples examined in this study were polished using the following polishing route (table 3.5):

Table 3.5: The grinding and polishing route used in this study for CM247-LC.

Stage Number	Grit/Cloth Grade	Rotation (RPM)	Counter Rotation (RPM)	Force (Newtons)	Polishing Media	Time (Minutes)
1	220 Grit Polishing Pad	150	40	50	Water	16
2	500 Grit Polishing Pad	150	40	50	Water	8
3	1200 Grit Polishing Pad	150	40	50	Water	16
4	2000 Grit Polishing Pad	150	40	50	Water	8
5	Cashmere	150	40	35	1µm Diamond Suspension	2
6	MD-Chem	150	40	25	0.25µm Fumed Silica Suspension + water	5

Parts were then imaged using the Clemex Microscope to reveal microstructural features. Composite images were obtained using the mosaic function on the Clemex system, allowing the PC to stitch together multiple images to provide a single picture of a sample, which was used for almost every sample examined in this study. In order to investigate the microstructure through optical imaging, etching is also required as well as the standard grinding and polishing. Glyceregia was chosen as an etchant. This etchant must be mixed fresh and is composed of three parts glycerol, two parts hydrochloric acid and one part nitric acid. Hydrochloric acid is added slowly to glycerol during stirring to ensure a steady mixture. After this, nitric acid is slowly added during stirring as well. This mixture is then gently swabbed on using cotton wool dabs and continuously refreshed until the sample turns cloudy. Once this occurs, the reaction is halted by washing the sample in clean running water. The microstructure is then imaged again using the Clemex/Olympus microscope. In all micrographs in this thesis, the direction of build is from the bottom of the image to the top, unless otherwise stated.

3.3.5 ImageJ Analysis of Sample Images

One common objective in the experiments performed in this study was the determination of whether or not a produced sample was dense, or whether or not it contains defects. Whilst qualitatively this is a trivial exercise, a quantitative approach is necessary to provide an accurate assessment of the impact of parameter changes. To do this, ImageJ (FIJI) was used to analyse the total amount of defects within the imaged material.

The workflow for this process is relatively straightforward and provides a way of quantifying the density of a part. Firstly, samples are imaged using an optical microscope. Images produced can then be loaded into the ImageJ software and converted to 32-bit images. Once this is done, they can be processed using the "Threshold" function located in the "Adjust" menu. The threshold can be manually adjusted to ensure that all of the defects desired for analysis are included by changing the sliders in the pop-up window. Whilst this can be subjective and give variable results due to the adjustable slider, the difference between increments is so small that the change in reported porosity is minimal. The percentage of light and dark zones gives a value of density/porosity respectively (figure 3.19).

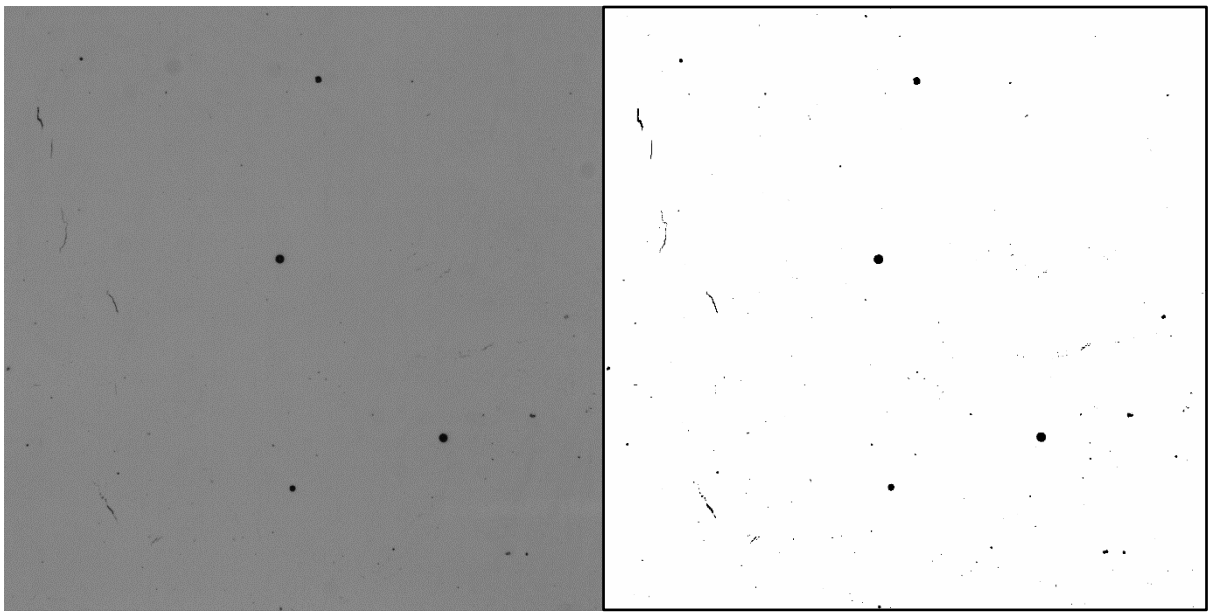

Figure 3.19: An example of a "thresholding" process. The original (left) image has been converted to a binary map (right), meaning that the percentage of dark pixels provides a value of density.

In this study, surface-connected cracks were not included in porosity measurements, as they usually arise from surface roughness and do not represent the alloy's standard behaviour.

3.3.6 Hardness Mapping

One relatively inexpensive and simple way to generate material property data is to perform hardness testing. By producing multiple indents on a sample's surface, it is possible to generate statistically significant data from a small number of metallographic samples. To do this, the samples in this study were tested using a Struers Durascan G5. This system allows for rapid automated testing numerous times on a polished surface.

According to ISO6507, indentations must be made at least 2.5 times the diameter of the indenter from the edge of the sample. Furthermore, indentations must be separated by this distance to avoid any work-hardening effects from previous indents [164]. In the case of this study, a separation of indents of 0.8mm was used to provide an 8x4 grid of indents across one half of a 5mm sample. As well as providing a good indication of average hardness across a sample, it also provides insight into the distribution of hardness across the surface throughout a sample and can illustrate whether or not there are any reductions in hardness closer to the surface. This is important for this study, as temperature variations near the edge of a laser scan can cause slower cooling rates, potentially affecting the microstructure and cracking behaviour, which is of great import for this study.

Once data points are acquired, they can be processed using Minitab by using the contour function. Minitab is a piece of statistical analysis software (similar in function to Microsoft Excel) that is very helpful when analysing data for a response-surface methodology. Data can be fed into the software and a surface contour map can be produced to illustrate a three-dimensional relationship in a two-dimensional graph.

Examples of contour maps can be seen both in the literature review of this study and later in several results sections. This is a quick and effective way to show how hardness can vary within a metal AM sample.

4. Additive Manufacture of CM247-LC

4.1 Introduction

This chapter explores alloy CM247-LC and how it behaves during LPBF. The intention of this chapter's work was to determine whether LPBF can be used to process high γ' nickel superalloys through existing parameter study methods. A central composite design of experiment parameter-based study was performed with a view to obtaining a standard set of parameters that can successfully produce metallographic samples with minimal present defects.

Once a parameter set for fully dense material was obtained, a combination of hardness tests and room-temperature hardness tests were performed to inform of the material's properties. Tests showed a high room temperature strength of up to 1250MPa UTS and an average hardness of 400HV1. However, failure of the material still occurs predominantly through cracking, evidenced by the cracking observed during hardness testing.

To characterise the behaviour of the material further, a pyrometer sensor was employed on the Aconity Mini to determine how a detected material response may be used to inform on the quality of the material produced. To that end, an examination of the optics in the Aconity Mini was performed in collaboration with the Electronic and Electrical Engineering department (EEE) in Sheffield. This examination discovered that the spot size of the pyrometer was very large relative to the size of the melt pool (around two orders of magnitude larger). Modifications were made to the optics in order to reduce the spot size of the pyrometer and provide a more accurate reading of temperature for the system. This was moderately successful, showing that the spot size was reduced to around 0.5mm from 10mm.

4.2 "Classic" Design of Experiment and Parametric Studies

Previous work performed by Y.Brif has demonstrated the ability of the Aconity Systems to print near-defect-free CM247-LC. Parameters used to produce the defect free samples are shown in table 4.1. Whilst the parameters used to produce this set of samples do not follow the procedure of experimental design as outlined in section 3.5, they do provide a wide range of energy densities, which as demonstrated by M.Thomas et.al [85], is an incredibly useful variable for AM parameter studies.

Table 4.1: The DOE used for the cubic CM247-LC test samples. All samples were manufactured with a layer thickness of 20μm and used a meander scan strategy that scanned from corners and rotated by 90° per layer.

Part Number	Power (W)	Scan Speed (mm/s)	Hatch Spacing (μm)	Energy Density (J/mm^3)
1	190	2000	17.5	271.43
2	190	2500	17.5	217.14
3	190	3000	17.5	180.95
4	190	2000	25	190.00
5	190	2500	25	152.00
6	190	3000	25	126.67
7	190	2000	35	135.71
8	190	2500	35	108.57
9	190	3000	35	90.48

In order to verify this work as a starting point for further testing, the experiment was repeated. Nine 5mm^3 samples were manufactured using the parameters shown in table 4.2. To determine the best parameters out of the set, a support structure was designed to provide a way of removing the manufactured components from the baseplate without needing to undergo costly and time-consuming wire EDM. A similar design is shown in figure 3.6. The pyramidal shape of the support is manufactured using the same parameters to allow for as much consistency in the design of the part as possible.

4.3 Data-Driven Methods for Experimental Design

The Aconity Mini's pyrometer serves to act as a very rapid (though qualitative) method of determining whether parameters are suitable during a build. If a component is overheating or not being sufficiently heated by the laser, this can be difficult to see simply by watching the process with the naked eye, particularly if the process is occurring behind the laser glass. Even large differences in parameter choice can be difficult to discern in this fashion. A more gradual overheating may not become apparent until several hours after the beginning of the process, by which time more material has been used and potentially wasted if this has had a deleterious effect on the powder.

Thermal emissions from the process are captured through use of the coaxially mounted pyrometer. When the laser melts the powder, thermal emissions can be collected if they travel back through the optical system (figure 3.4). In studies of novel materials, this can be used to determine within several layers of the beginning of the process whether a component part is overheating, or is not being heated sufficiently relative to the rest of the components in the layer. Alternatively, this pyrometer reading can be used as an indicator for energy density, with components often sporting similar temperature (in millivolts) readings within a build layer. An example of this can be seen below in figure 4.1 that pertains to the energies and parameters seen in table 4.1. In figure 4.1, the laser scan direction is from the bottom left corner towards the top right corner in each 5mm cube.

It is important to note that the "temperature" referred to in this chapter (and when referring to pyrometer readings) is not an absolute temperature, but an electronic signal produced from the thermal and near-infrared emissions detected by the pyrometer. It is referred to as temperature here simply for expedience. This method of data collection has limitations however. Each cube in figure 4.1 has a distinct "cold" bottom left corner. This is due to the way that the laser scan head directs its galvanometers. When the laser scan head is directed at a component, there is a brief pause before the scanning begins. The pyrometer is exposed at the beginning of each layer and remains continuously exposed until the end of the layer. Because of the continuous exposure, data is collected when the scan head remains stationary and the laser switches off. During this time, the material being observed is much cooler, so the average values of these regions is drastically reduced. This "cooling" of pyrometer data also occurs at the end of a component, as there is another brief pause before the scan head travels to the next part. Furthermore, cold lines (known as "flight" lines) can be seen between components. This is again an artefact created by the continuous exposure of the pyrometer during the moving of the scan head when the laser is switched off between individual parts.

The output of the pyrometer is determined by the collected data being averaged to provide a single output value for every dot on the colour map shown in figure 4.1. Data is not only collected from the melt pool, but also from material that has not yet been scanned by the laser. The laser performs hatching scans at 45° across the parts, rotating by 90° per layer. Furthermore, corners effectively act to drag the average down by being 75% comprised of material that is unaffected by the laser. Because of this, the average is lowered through the area of interest being flooded by values of zero. This is due to the spot size of the pyrometer being too large relative to the size of the melt pool, the effect being most prominent at the corners and edges because of the collection field of view's proximity to a change in thermodynamic regime (i.e. melted/high temperature material to cool powder). This mismatch in length scales between observer and target results in varying temperature values for certain regions of parts, mainly edge and corner regimes.

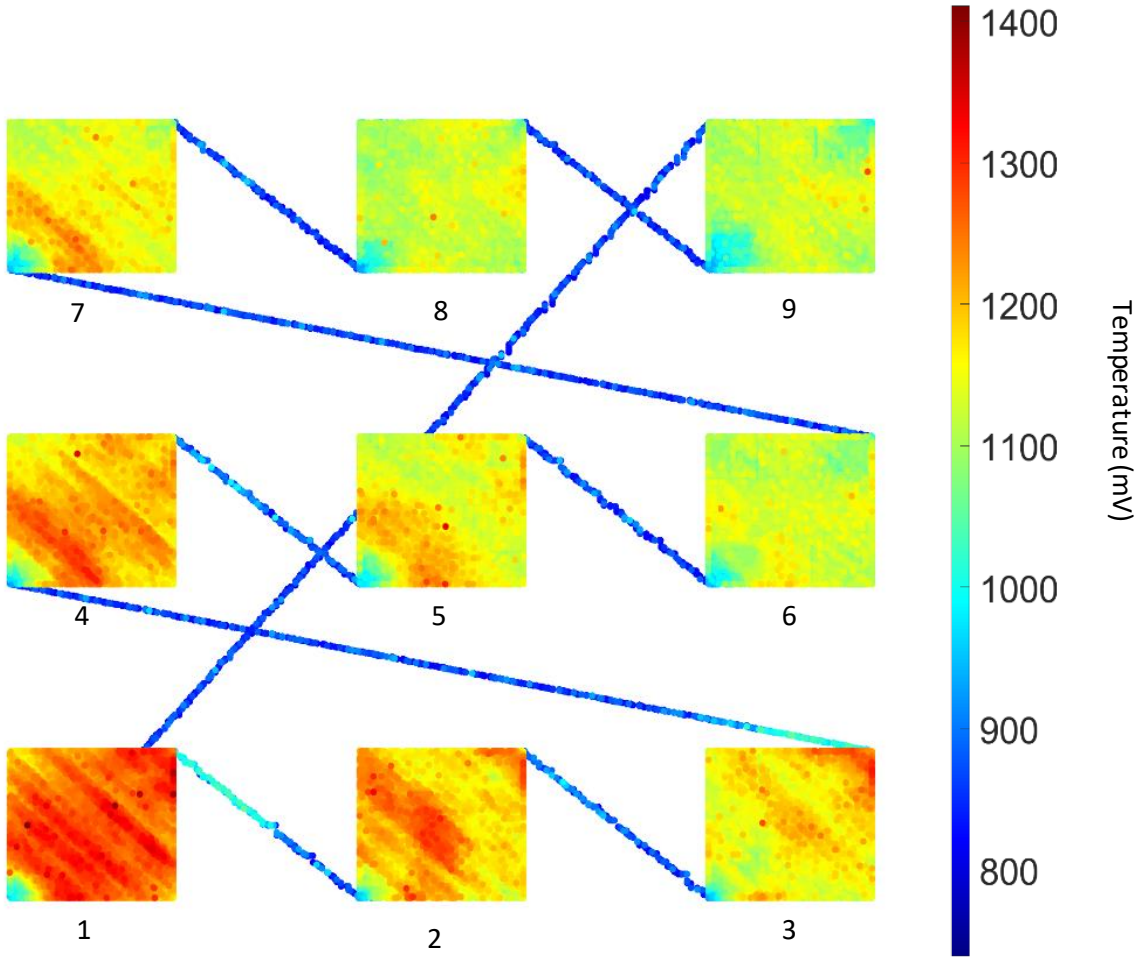

Figure 4.1: Raw pyrometer data from the Aconity Mini. This image shows the thermal emissions captured from across the 48th layer for the components built with parameters from table 4.1, numbered 1-9. The scale bar shows electronic temperature in mV. Scan direction is diagonally from the bottom left across each part individually, with a brief pause before lasing that results in data being collected for non-heated powder, producing a cold spot in the data.

Another reason for this colder appearing initial corner may be slightly affected by to laser ramp-up time. When activated, the laser power source does not immediately jump from 0 to the desired power, rather taking a discrete amount of time to reach the desired level. Because of this, an initial measurement at the very beginning of the layer may be lower than expected. However, this would only be a small fraction of the first scan and should not affect the entire corner, only the initial hatch.

By comparing the energies in table 4.1 and the pyrometer data in figure 4.1, it is possible to show a clear relationship between energy density input and observed average temperature (figure 4.2).

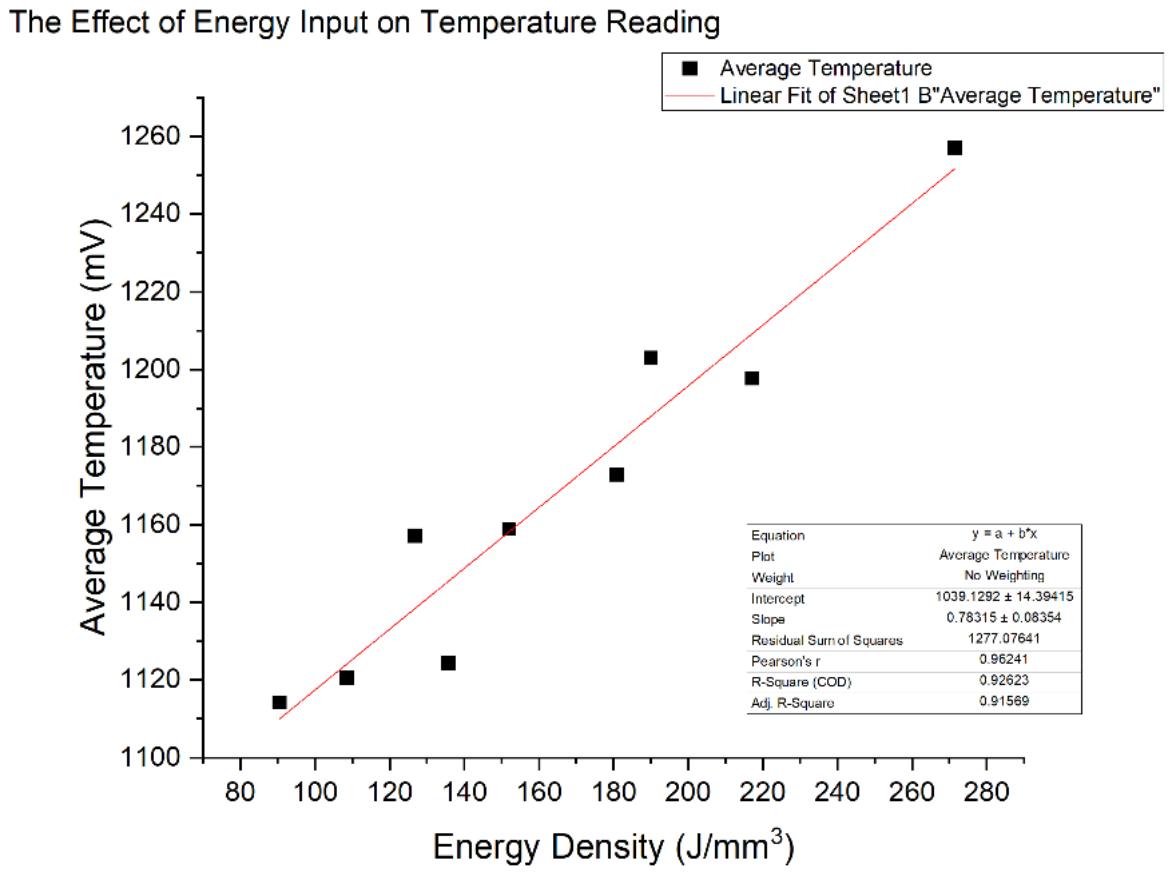

Figure 4.2: The plot of the pyrometer temperature and energy density in the LPBF process detailed in section 4.2.

Once components are manufactured, they can be sectioned, mounted, polished and imaged to provide further analysis. Many tools exist to analyse images that are taken from microscopes, which can be used to provide useful data.

Automatic analysis can be performed to identify defects within a micrograph, which can be further broken down into types of defects such as cracks, pores and LoF. This provides a qualitative look into the quality of the material, whether or not it is defect-free and presents the opportunity to examine the trends observed in the samples.

4.4 Results of Parameter Study – High Density

The initial repeats of the first DOE set manufactured successfully and parts were snapped straight off of the baseplate using a soft tap hammer. The thinner supporting struts were then removed through the use of an abrasive paper. The accepted density of CM247-LC is 8.54g/cm^3 [165]. To provide density measurements, the method used was to section, then grind and polish the samples in Bakelite resin. This is a very widespread method for metallographic sample preparation and is necessary to polish samples of the size in this study effectively as they are too small to polish by hand.

Whilst the density of parts manufactured from the parameters shown in table 4.1 were relatively high for this alloy, only components made using parameter sets 6,7, 8 and 9 were of interest for their relatively low defect densities (figure 4.3), particularly parameter set 9 (figure 4.4). This component showed minimal cracking and porosity visible with optical microscopy after polishing and etching (figure 4.5). Cracks are present in some samples, likely because of hot tearing as the material solidifies and shrinks under a restrictive force [77], [78], even in the most dense sample (figure 4.6). The best results in both initial and repeat experiments came from sample number 9 (190W power, 3mm/s scan speed, 35µm hatch spacing). Comparison of the material porosity to the average layer temperature is also shown (figures 4.7, 4.8). Sample 9 - the most dense sample – has the lowest average temperature of all the parts produced, reading as 1114mV on the pyrometer.

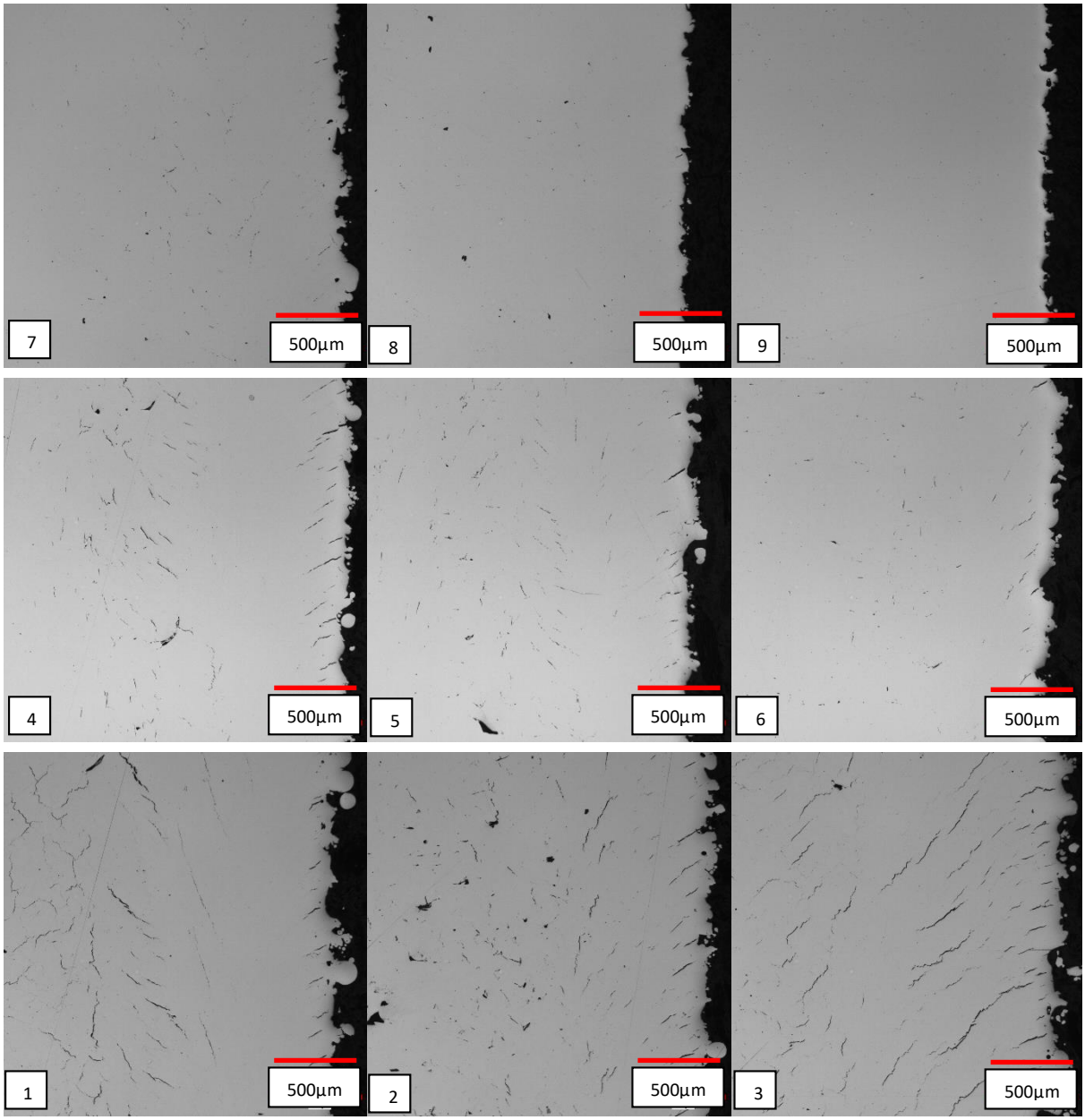

Figure 4.3: Representative optical micrographs of the sample quality for samples 1-9, in the same order as in figure 4.1. A clear improvement can be seen in the quality of the material in sample 9 relative to samples produced with other parameter sets. Images were taken in the same place on each sample for consistency.

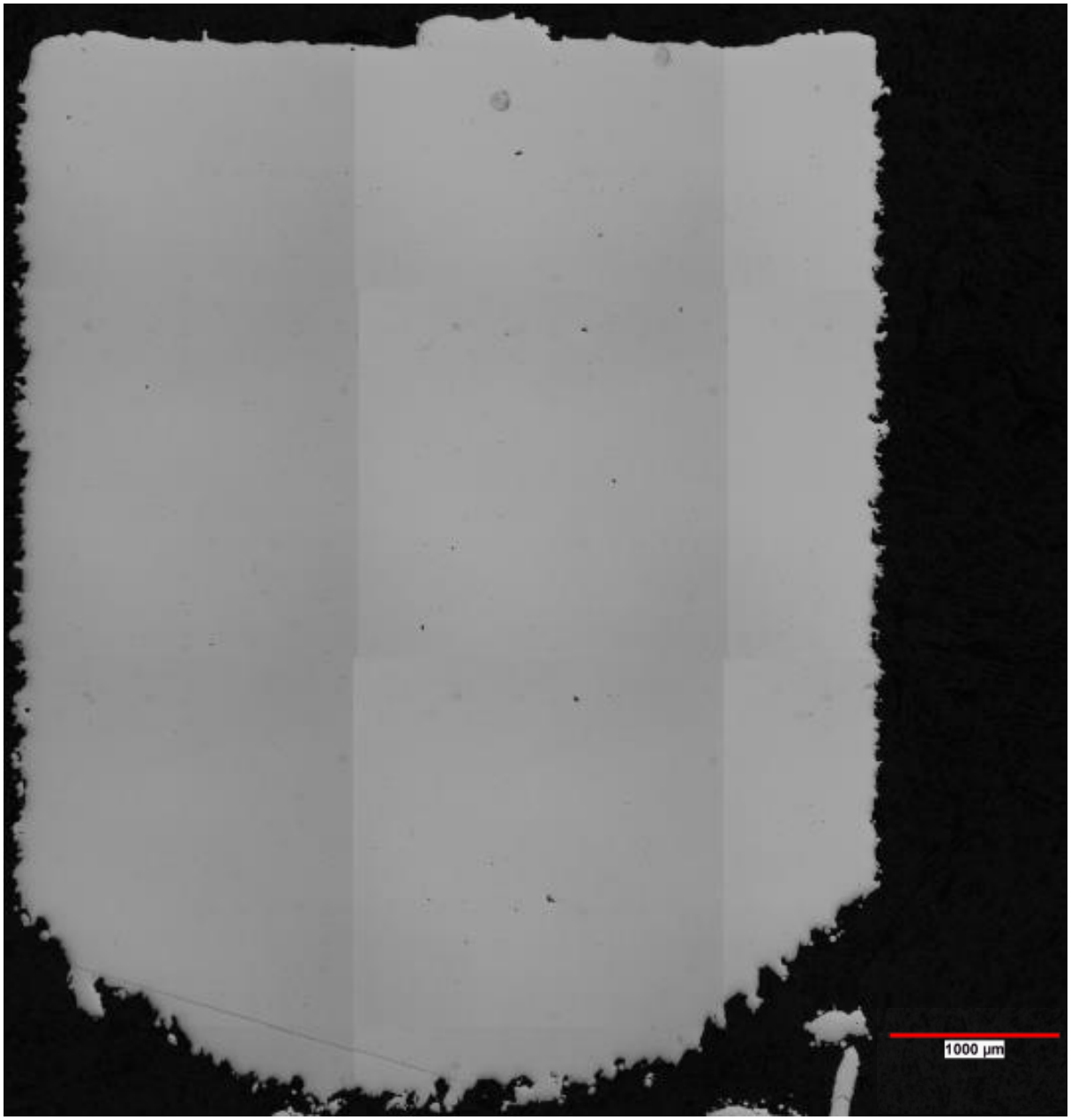

Figure 4.4: Optical micrograph of "ideal" CM247-LC before etching. Whilst small traces of gas porosity are still present, cracking appears to have been eliminated, though some may remain elsewhere in the sample.

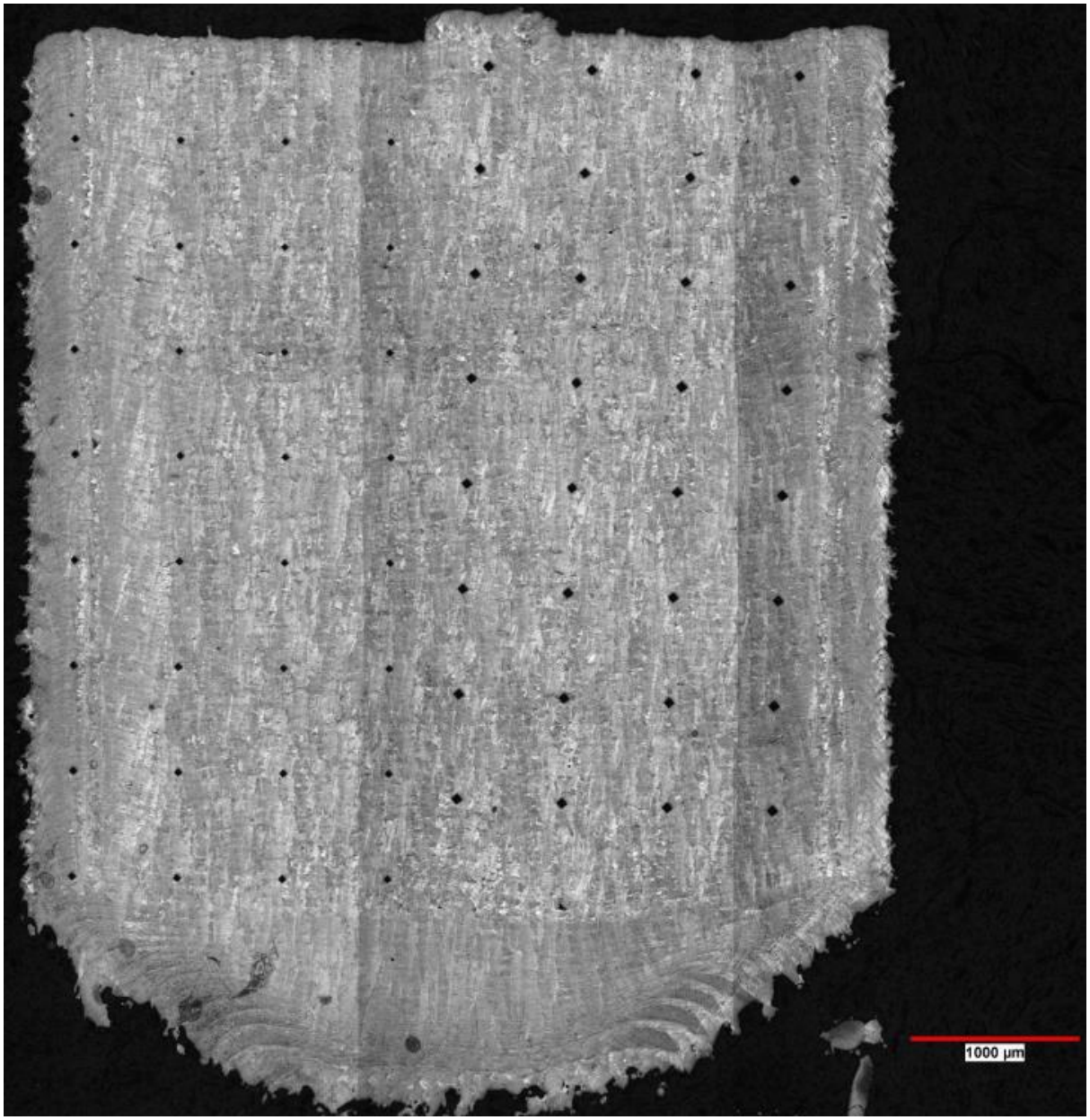

Figure 4.5: Optical micrograph showing an array of hardness indents performed on this etched sample.

Using ImageJ to analyse the images of the samples, trends can also be drawn to examine how the input parameters affect the material responses. Figure 4.7 shows the impact of the change in temperature on the produced porosity within the samples.

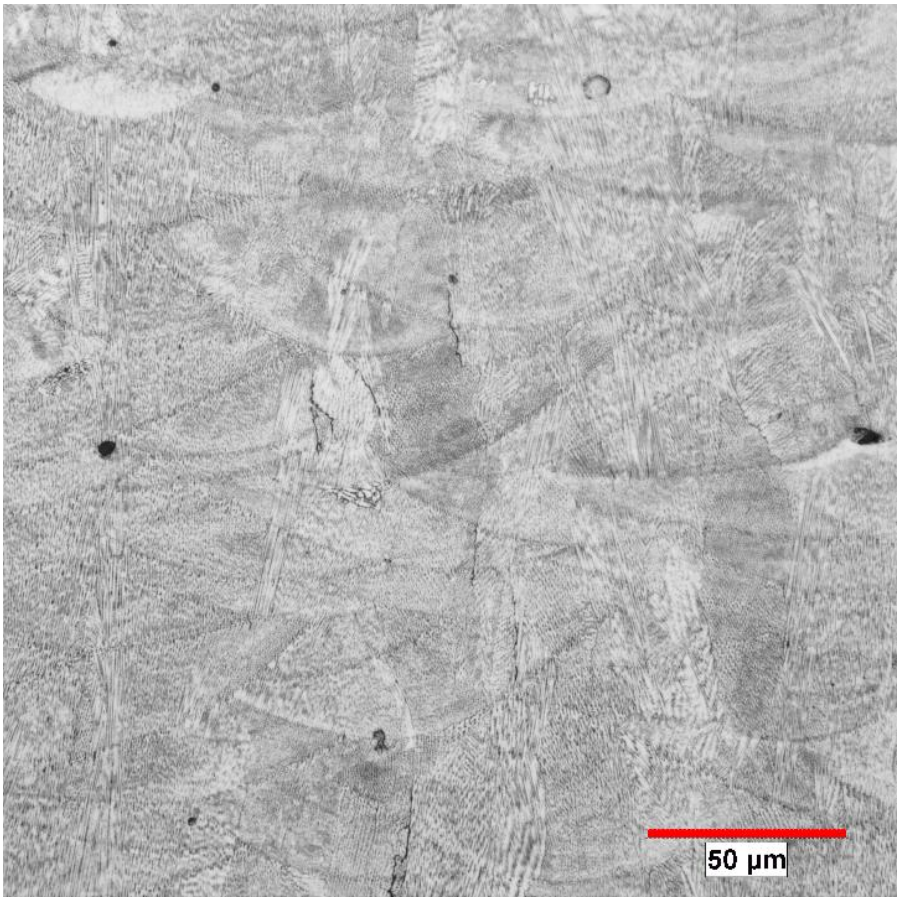

Figure 4.6: Optical micrograph of micro-cracks and porosity visible within sample 9. Cracks tend to form between grains of varying orientation and in the direction of building (upwards).

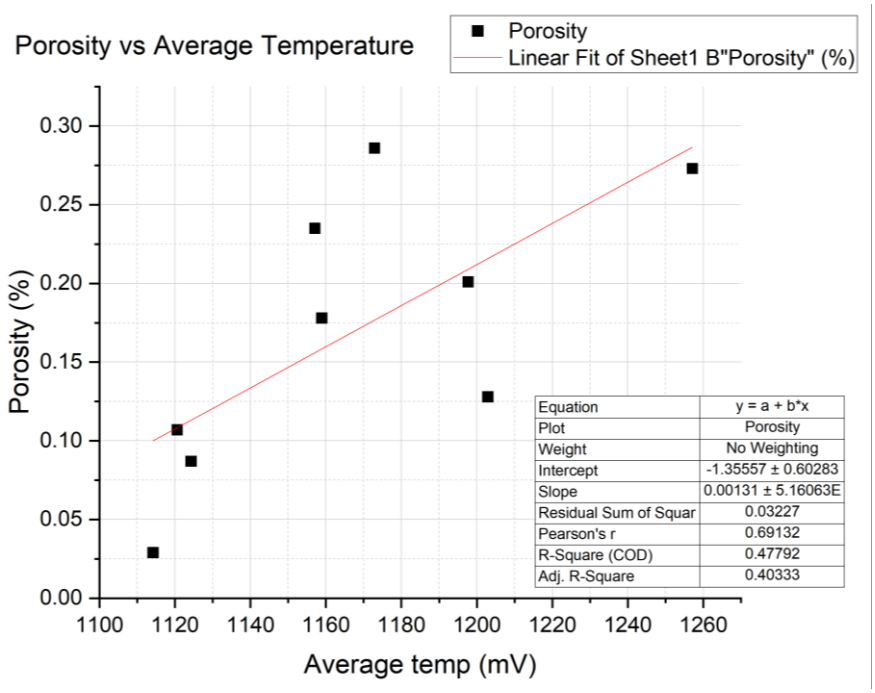

Figure 4.7: Plot of porosity values vs pyrometer temperature. A trend can be seen in this data, but more would be required to determine a true relationship.

In both of these instances, sample 9 is the lowest energy input and average temperature reading. The effect of hatch spacing and scan velocity on porosity and detected temperature is also examined and shown in figure 4.8.

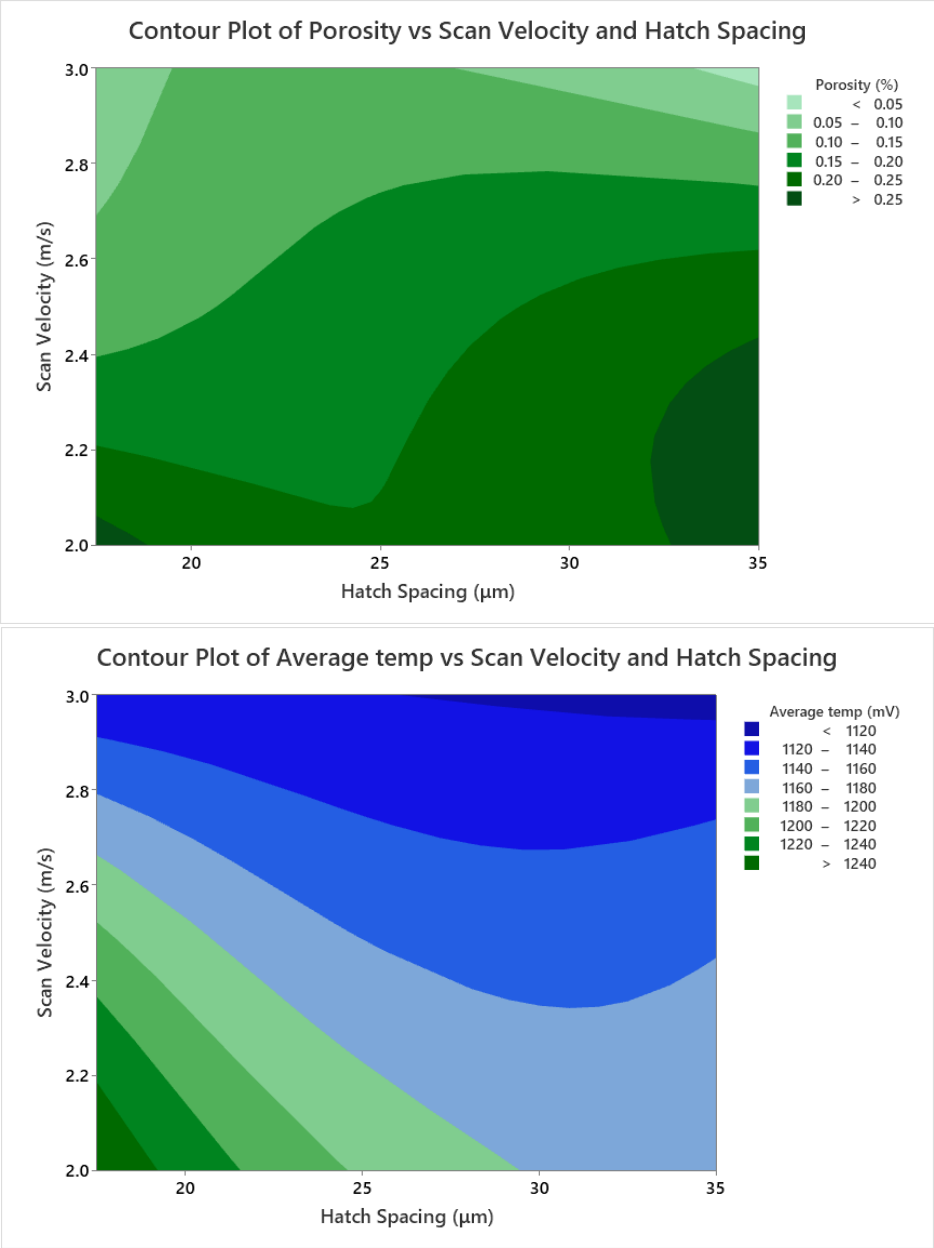

Figure 4.8: The relationship between laser parameters changed in this study and the resultant material porosity and detected temperature.

These two graphs together suggest that porosity is indeed dependent on the temperature of the material and that the material is overheating in the instance of the more porous samples due to the laser beam moving too slowly.

4.5 Hardness Mapping

The decision was made to perform property testing using a Durascan G5 to confirm the quality of the produced samples. The hardness of a material is usually correlative to its UTS, meaning that these tests should be representative of a material's ability to resist deformation at room temperature. It also means that very small samples can be produced, reducing the cost of each experiment.

Hardness tests were performed with a Vickers indenter, with a load of 1Kg (HV1). For each sample, an array of 8x4 points was produced across one-half of the sample's polished surface. This was done to determine whether the hardness changed as a function of position in the cross-section of the components and whether thermal effects at the edge of samples have any impact on the hardness of the material. Given that the powder bed often acts as an insulator, this is important to understanding whether this has an impact on the properties of thinner sections of material. Using only one half of the sample meant that further imaging could be performed if necessary, without the express need for further grinding and polishing to remove the hardness indents. Figure 4.9 shows the hardness map for sample 9.

The average hardness of all of the samples is 406.9HV1, comparable with other nickel alloys manufactured via LPBF. A noticeable trend in many of the hardness maps is the reduction in hardness towards the edge of the material, relative to the centre of the sample. This is particularly noticeable in figure 4.10. This reduction in effective hardness near the edge is likely due to surface stresses present in the material, which are often formed in LPBF. These large tensile stresses in the surface can result in a weaker surface, as less force is required to overcome the UTS of the material.

In the instance of the hardness maps, the build direction is upwards (or "north"). This reduction in hardness due to surface stresses can be seen in the micrographs of the material, where edge cracking occurs only in the outer shell of the material, with a depth of around 0.25mm into the material. It is possible that the surface roughness of the components acts as a stress raising feature. This would also explain another possible reason why shallow layer thicknesses tend to produce better results than thicker ones, as there is less material to act as a stress raiser to cause delamination between layers. The plots of all hardnesses are compared in figure 4.11 as boxplots.

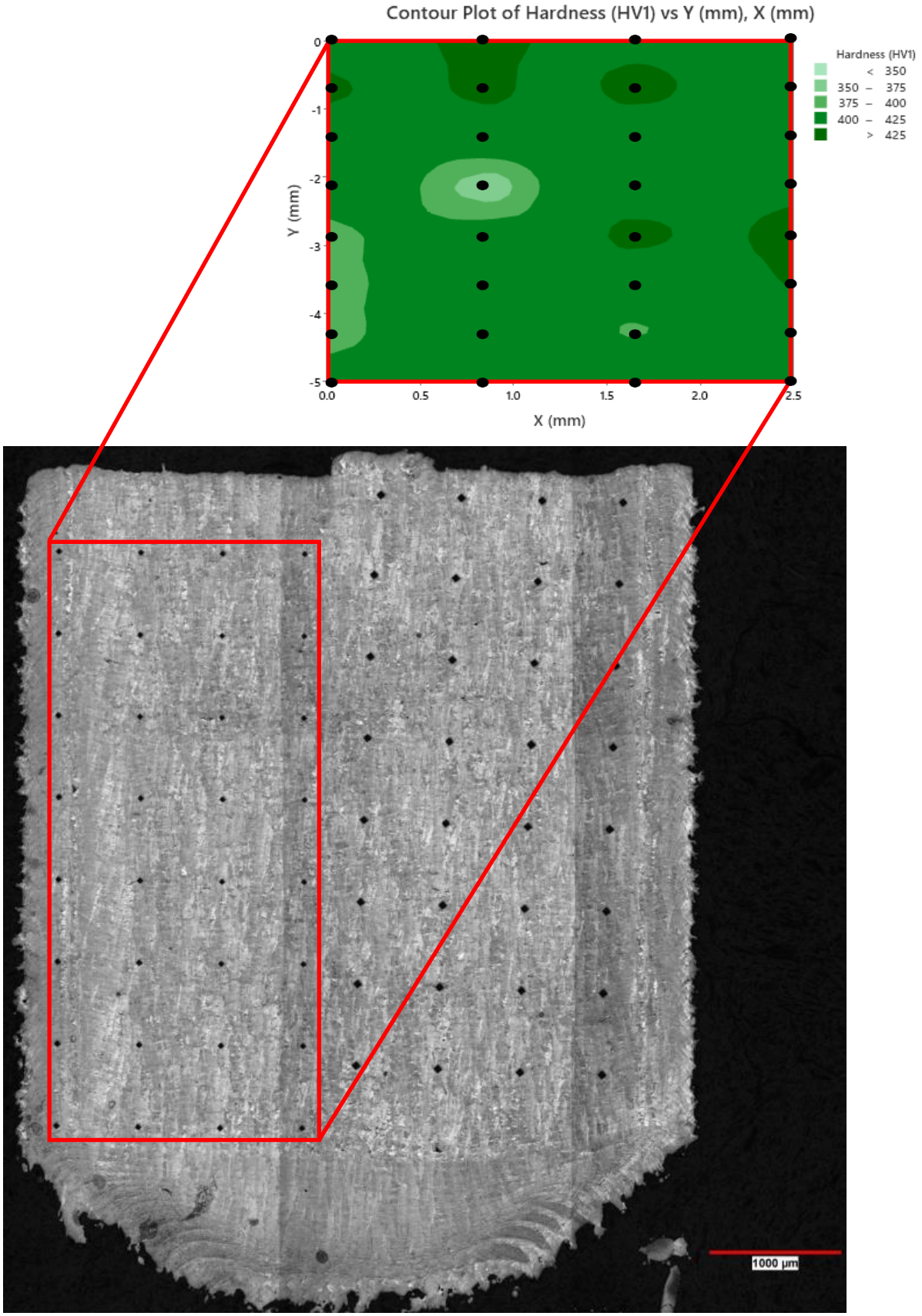

Figure 4.9: Hardness map of sample 9. This sample is one of the most consistent in terms of its hardness, with a very low standard deviation. The red zoom box denotes the location of testing on the sample, with points highlighted as black dots on the contour map.

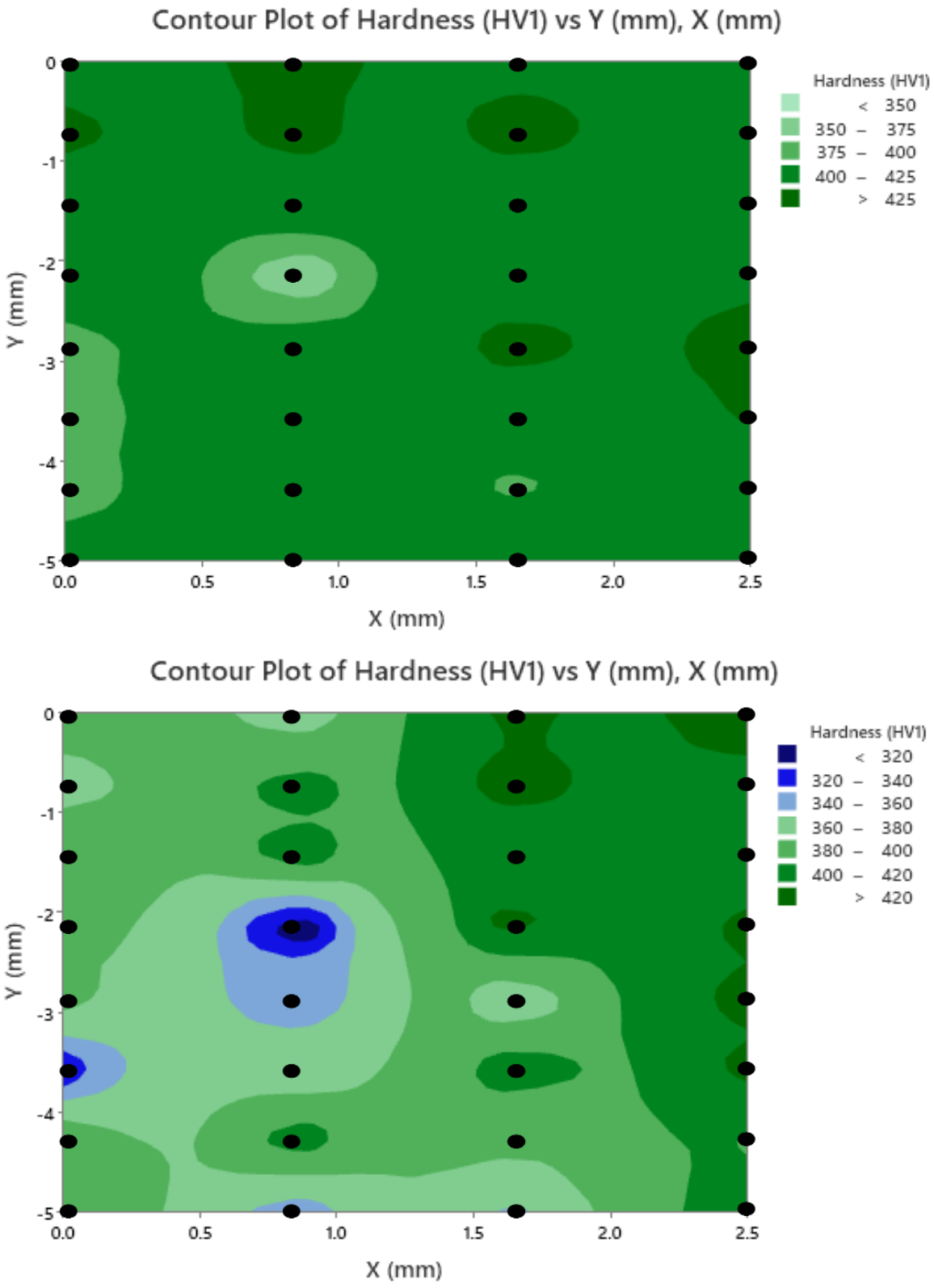

Figure 4.10: The hardness map of samples 9 (top) and 7 (bottom), demonstrating a trend with several components that the effective hardness of the material reduces with proximity to the surface.

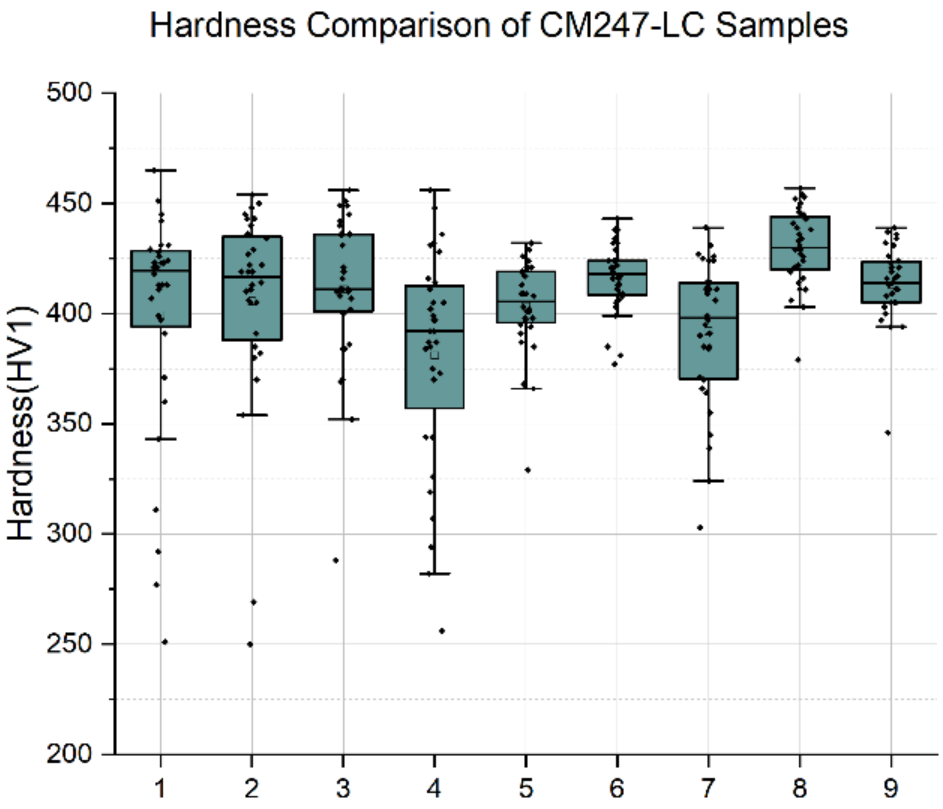

Figure 4.11: Comparisons of sample hardness from this study. Samples 6 and 9 are shown to be the most consistent. These samples utilise the scan velocity of 3m/s.

An indent that lands on a crack or subsurface defect often results in a very wide or misshapen indent, effectively reducing the observed hardness of that local region. Many cracks were observed to be caused by the indents of these tests, suggesting that the proximity to the edge may increase the susceptibility of the material to cracking. Examining pyrometer data for the same samples, the edges of the material appear to be overheating relative to the rest of the samples in many cases. Comparing the hardness data for each component allows one to draw trends with the pyrometer's response signal and examine how hardness varies with porosity (figure 4.12).

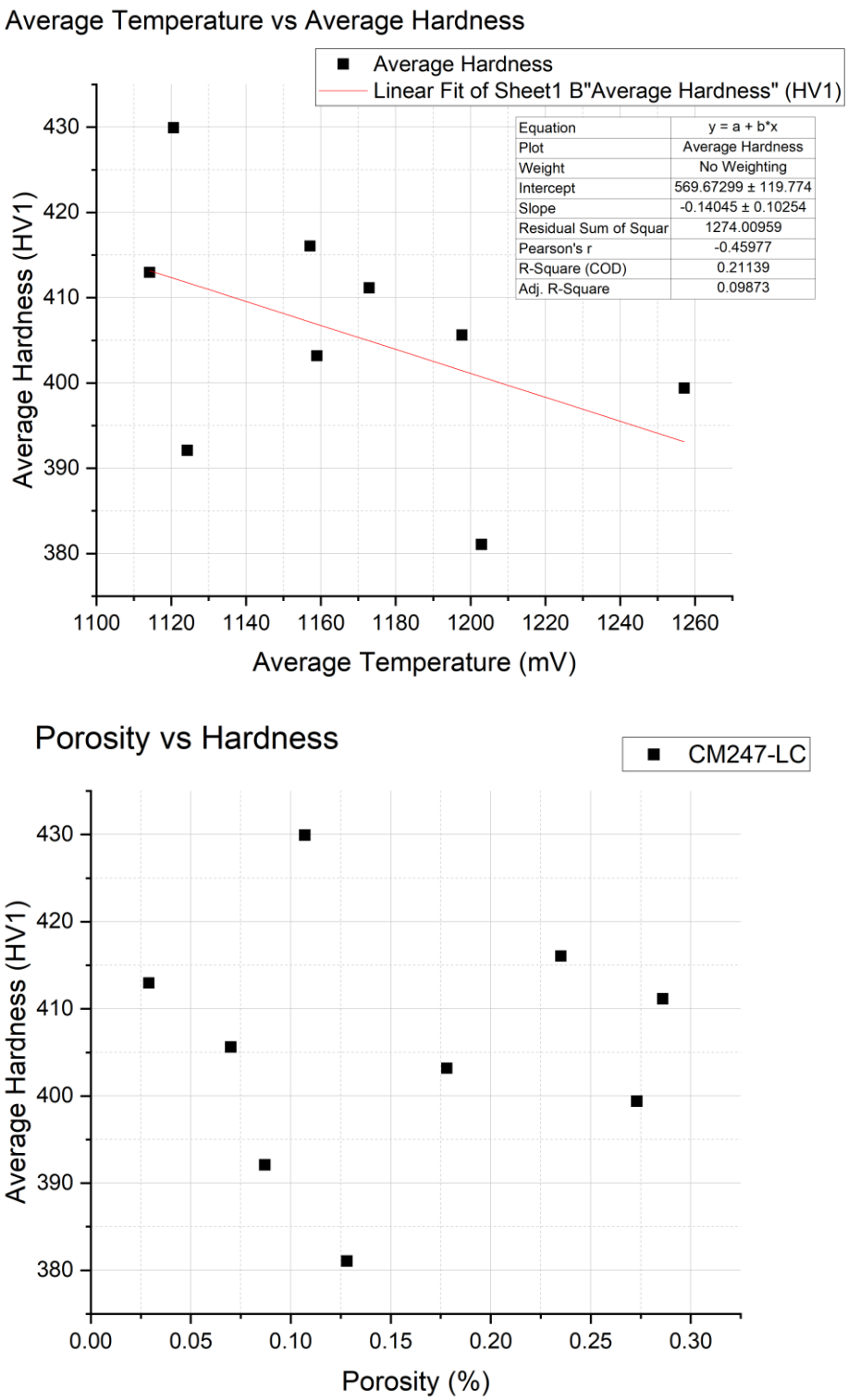

Figure 4.12: How average hardness is impacted by the detected temperature (top) and the resultant porosity (bottom). The average hardness is largely independent of porosity, though these samples have been designed with the aim of reducing porosity as much as possible and may be a local minima.

It is also possible to examine the dependency of material hardness on input parameters by plotting a contour graph, similar to that in figure 4.8. Figure 4.13 demonstrates this, showing that hardness is directly linked to the reading detected by the pyrometer and therefore to the input parameters also.

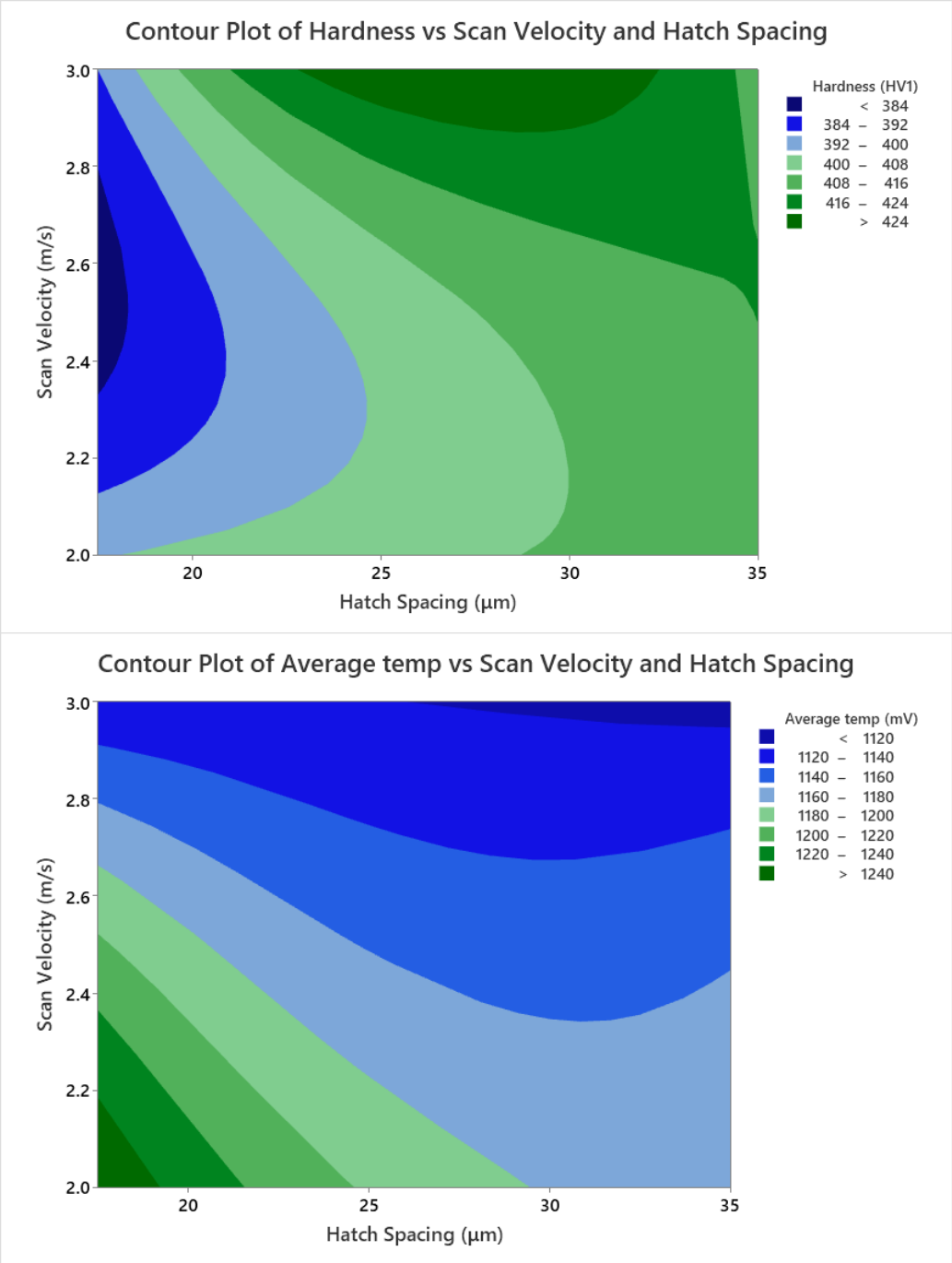

Figure 4.13: A comparison of the relationship between input parameters and material responses. These two graphs suggest that hardness is inversely proportional to the average pyrometer reading for a cube.

4.6 Tensile Tests

Whilst cube components can provide an important insight into the microstructure and density of a material produced by LPBF, as well as micro-hardness, they struggle to inform of the macro-scale properties of the material or more complex in-service components. To provide this information, six test pieces were manufactured from CM247-LC with the parameters used for cubic sample 9. These test pieces were bars measuring 10mm x10mm x75mm. These components were then removed from the build substrate via wire EDM and dispatched to Special Testing ltd. in Sheffield for tensile tests at room temperature. The bars of CM247-LC were machined and tested according to ASTM standard E8. This ensures that the tests are consistent and are comparable with other bodies of work and research. Figure 4.14 shows the UTS, 0.2% proof and elongation values for this set of tests.

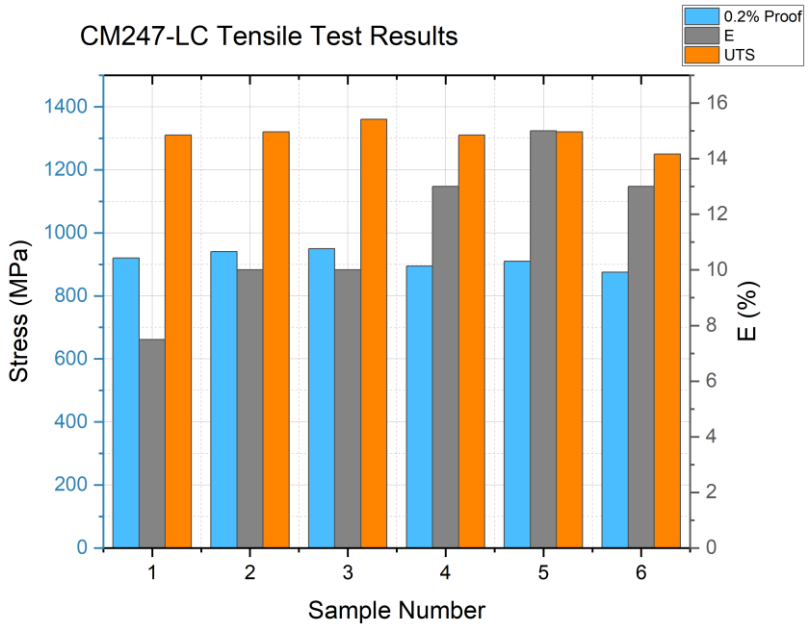

Figure 4.14: Tensile test results for CM247-LC manufactured using the Aconity Mini. All of these test pieces used the same laser parameters for their construction.

Due to the relatively low volume of powder available for manufacture of parts, vertical tensile tests were not performed in this study. While these values of UTS are very high, the variation between samples demonstrates that reproducibility is still a challenge for the LPBF process, even with idealised parameters sets. Even a relatively small change in the density of the material can result in significant changes in the macroscopic properties of components. This may explain the wide variation in elongation, which is often more dependent on the specific sample than the UTS or yield strength.

4.7 Comparison with Literature

4.7.1 Density and Defects

Beginning with the density micrographs of the material produced, a significantly higher density than reported in many other literature is achieved in this series of experiments. Examining work performed by Carter [99], [166] and Adegoke [80], [118] can provide some insight as to the reason for this higher level of densification in manufactured CM247-LC parts. Carter (as well as others) suggests that the use of energy density is a useful tool in determining processing windows. The specific type of energy density may vary however. In the case of Carter's work, this uses area energy density (J/mm^2) – a function of scan speed and hatch spacing. Given that the layer thickness of 20µm is consistent between both this work and Carter's study, results may be compared easily when examining energy density.

Given that so few cracks are present in the samples produced for this study, void content analysis is chosen for comparison instead. One may plot the results from this study against the same set of axes from Carter et.al's work. Figure 4.15 shows the relationship between area energy density and void area for both studies.

This study demonstrates similar levels of porosity for this range of energy levels, with voids being present only in very small quantities of the overall area of the sample. However, Carter et.al still report heavy cracking in many of their samples at these same energy levels – something that is not seen in this study.

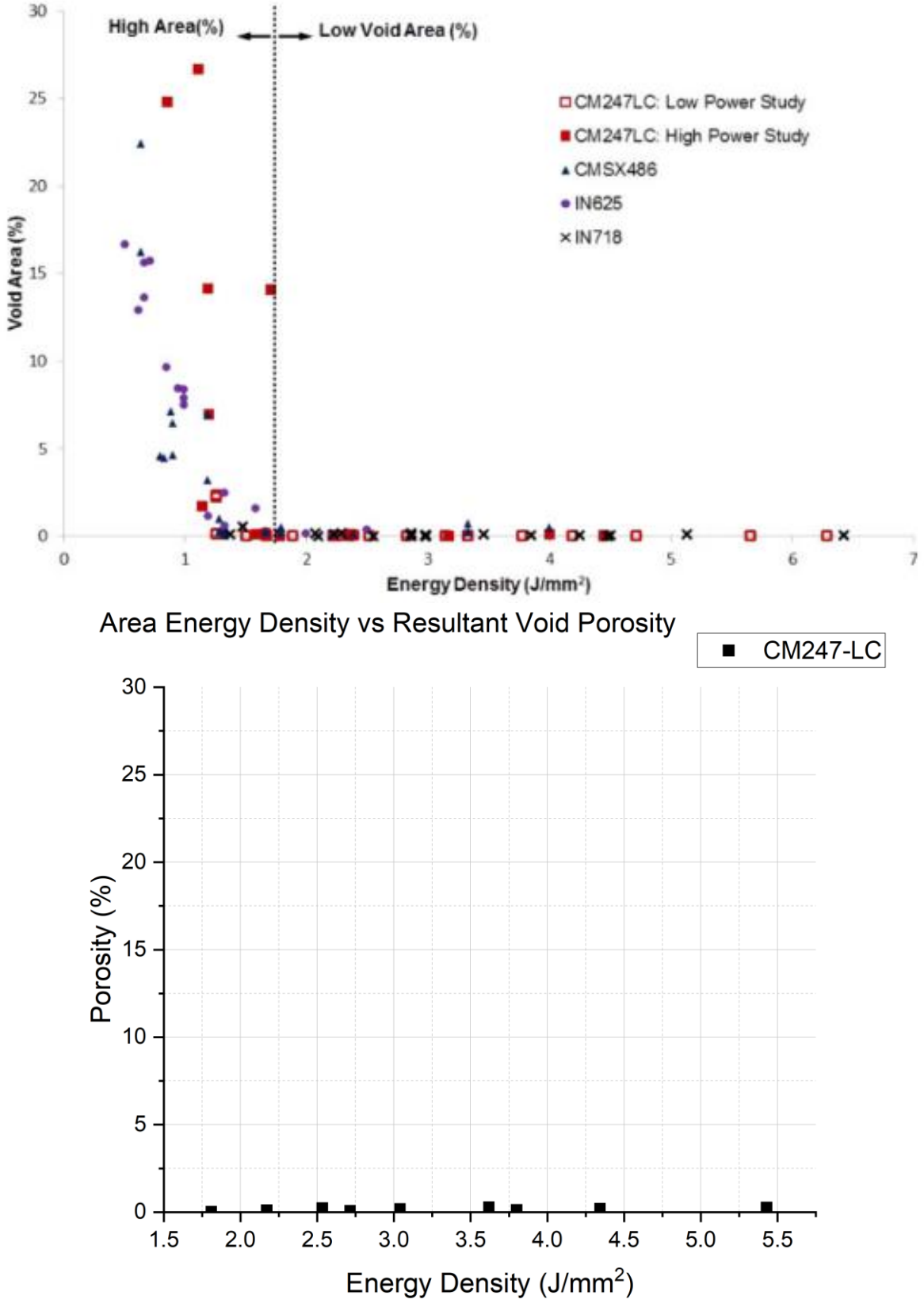

Figure 4.15: Comparison of void density plots for work by Carter (top) [166] *and this study (bottom). Data points have been plotted on the same scale to give context.*

Adegoke developed a model to predict the processing window of the CM247-LC alloy. Examining the windows suggested to be windows of minimal crack and void formation, the "ideal" parameters developed in this study sit outside of the region of predicted high density. Figure 4.16 shows the predicted processing windows suggested by Adegoke. Only two of the parameter sets used in the DOE described in table 4.2 can be effectively plotted on these graphs. In figures 4.16 and 4.17, they are denoted as points 6 and 9.

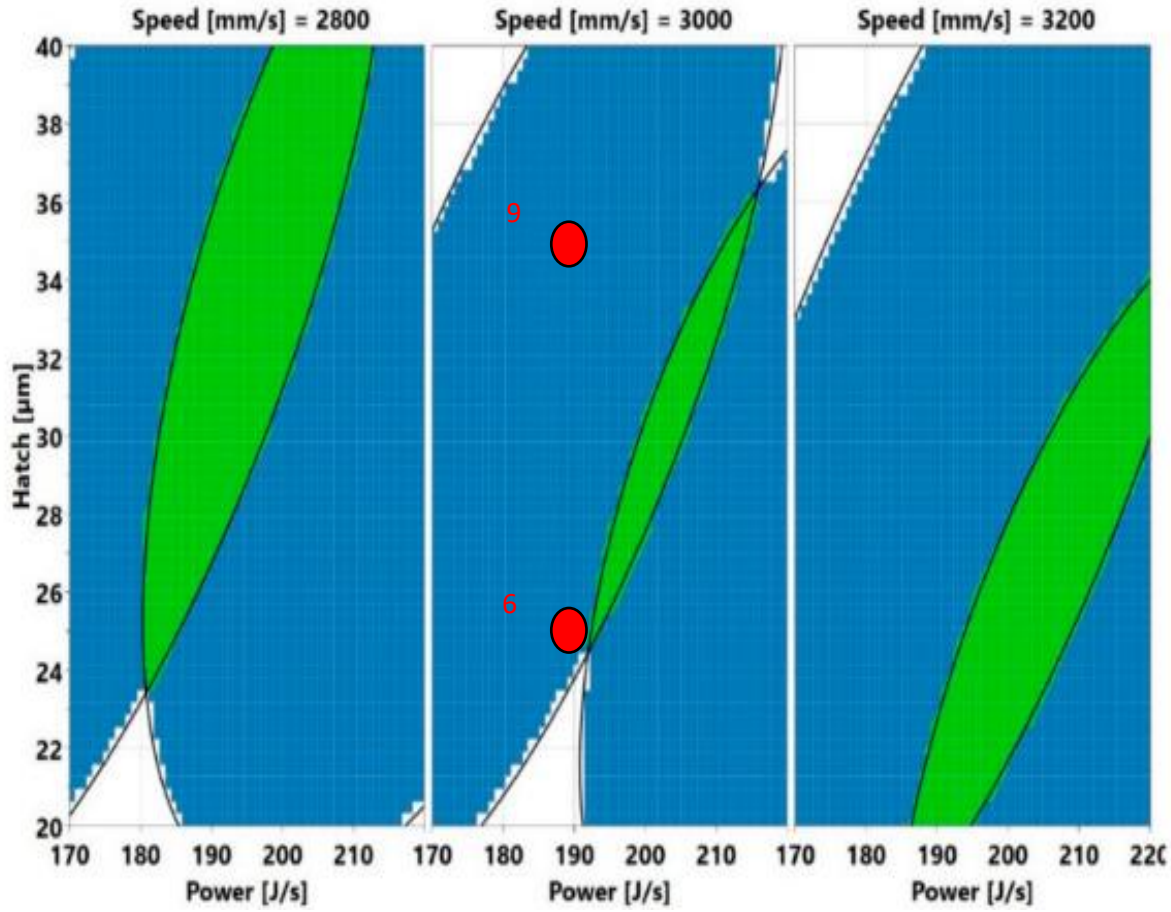

Figure 4.16: Plots proposed by Adegoke et.al. visualising processing windows for CM247-LC. The two red dots represent where data points from this study would sit relative to this information.

However, the point closer to the supposed "region of high densification" is actually a component that is less dense than the point that is further away. The lower point, cube 6, contains a higher concentration of voids despite its proximity to the green region. Examining the processing map prediction for cracking density, this does fit into the lowest region, sitting in the region of the lowest cracking level for this particular laser scanning speed.

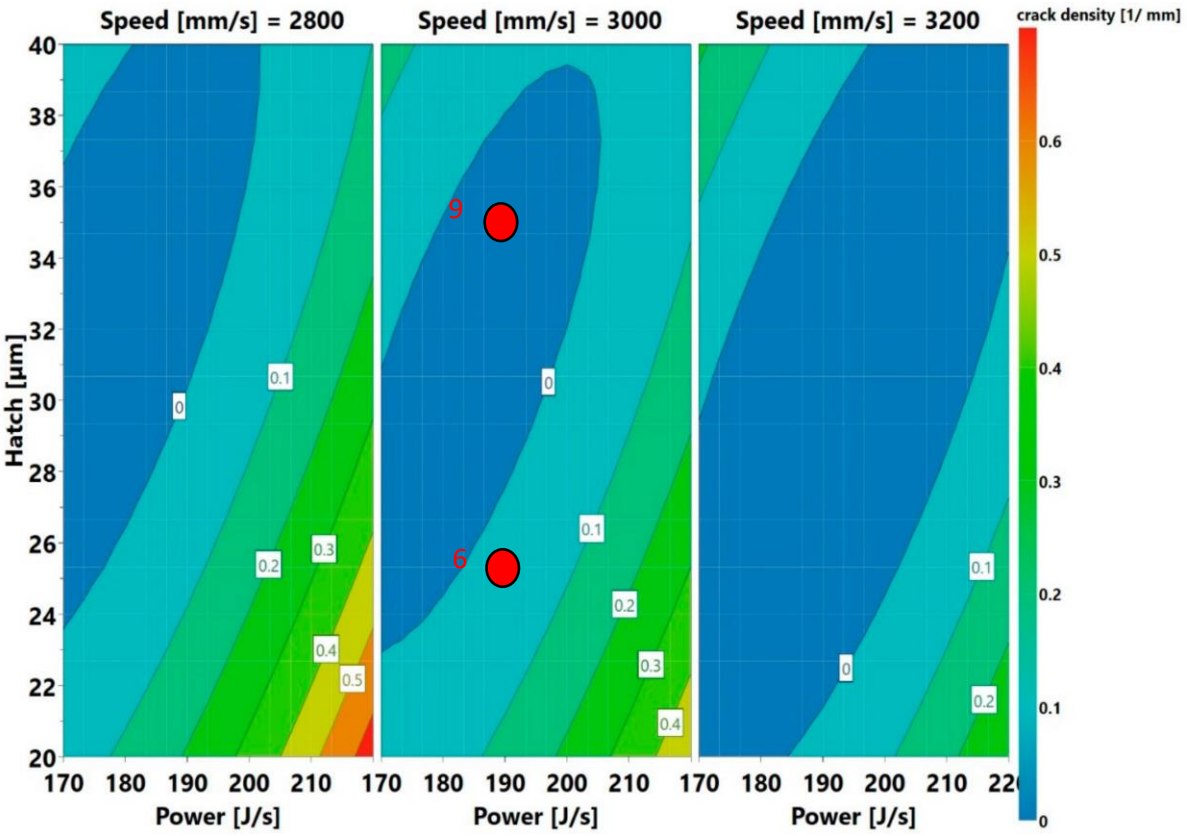

Figure 4.17: Graph of predicted crack density for CM247-LC produced by Adegoke et.al [118]. *The crack free CM247-LC produced here fits within the region of lowest predicted cracking.*

Point 6 lies within a slightly higher region of crack prediction, despite not showing any visible signs of cracking. Another point of note is the energy density of components manufactured in the two studies. The Adegoke et.al study presents a list of parameters chosen for testing, with energy density values provided for each cube. Table 4.5 shows the energy densities of the samples produced in this study. These energy densities can be compared with porosity values determined from the micrographs taken and can also be plotted (figure 4.18).

Table 4.5: Energy density values for each sample produced for this study.

Sample Number	Energy Density (J/mm^3)	Porosity (%)
1	271.43	0.27
2	217.14	0.2
3	180.95	0.13
4	190	0.28
5	152	0.18
6	126.67	0.23
7	135.71	0.08
8	108.57	0.11
9	90.48	0.03

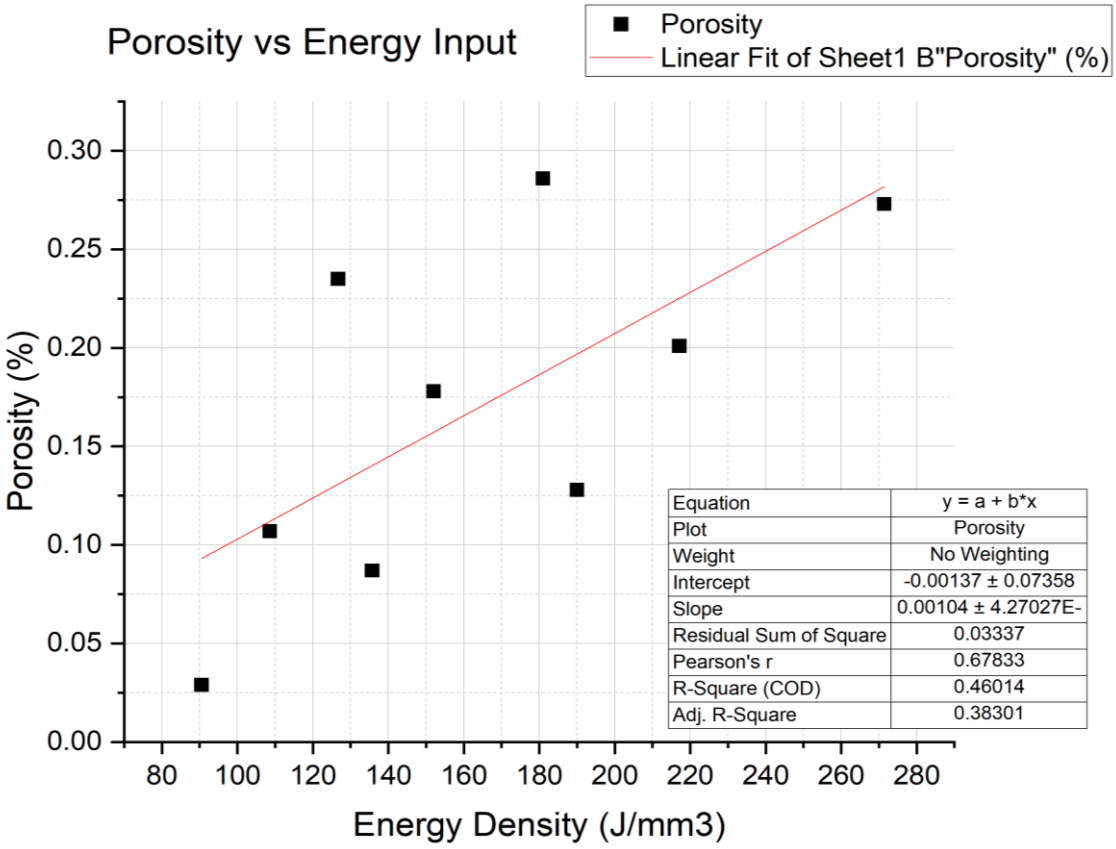

Figure 4.18: Porosity vs Energy Density for the samples produced in this study. A correlation is seen, suggesting that reducing the volumetric energy density input is better for CM247-LC.

A key difference between these two studies is the size of the component manufactured. In this study, 5mm cubes have been chosen for their simplicity and speed in manufacture. Adegoke's study uses 15mm cubes, which are 9x larger per layer to print. As detailed in chapter 2, component geometry has a significant effect on the quality of a component if the same laser parameters are used. This study also used an EOS M290, which is again a different printer with a different laser beam spot size of 100µm [167].

The normalised energy density of the different studies is also considered below in figure 4.19 with the energy densities in both this study and the study performed by Adegoke [118] shown.

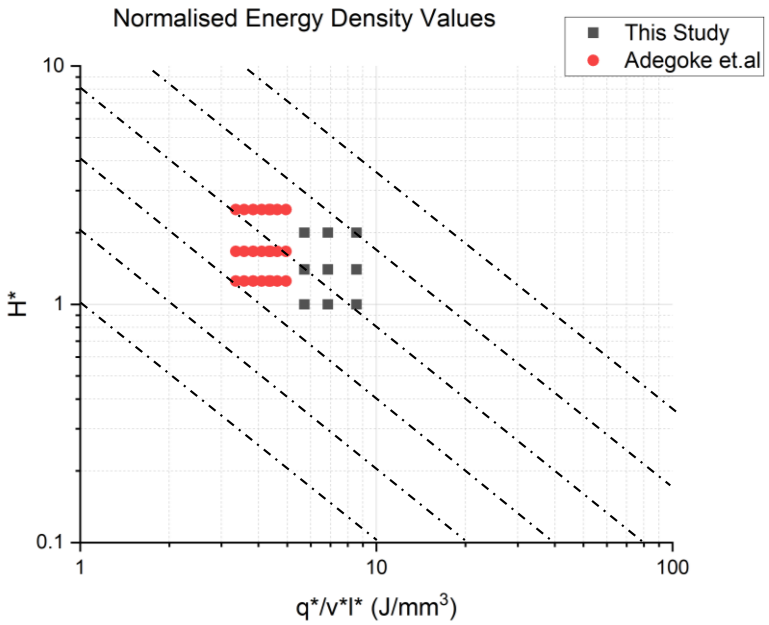

Figure 4.19: Normalised energy density processing map similar to Thomas et.al [85] *with data points for this and Adegoke's study* [118].

Whilst the normalised energy density values of Adegoke's work are close to the ideal level of energy found in this study, none are exactly the same. The closest in terms of density that they produce is their sample 28 (figure 4.120) [118]. This sample used parameters very close to the ones used in this study: 195W power, 3m/s scan speed, 30µm hatch spacing. Again, the main difference between the studies is the choice of machine and its spot size. Normalised hatch spacing takes into account the amount of overlap between melt pools produced by the relationship between beam spot size and hatch spacing.

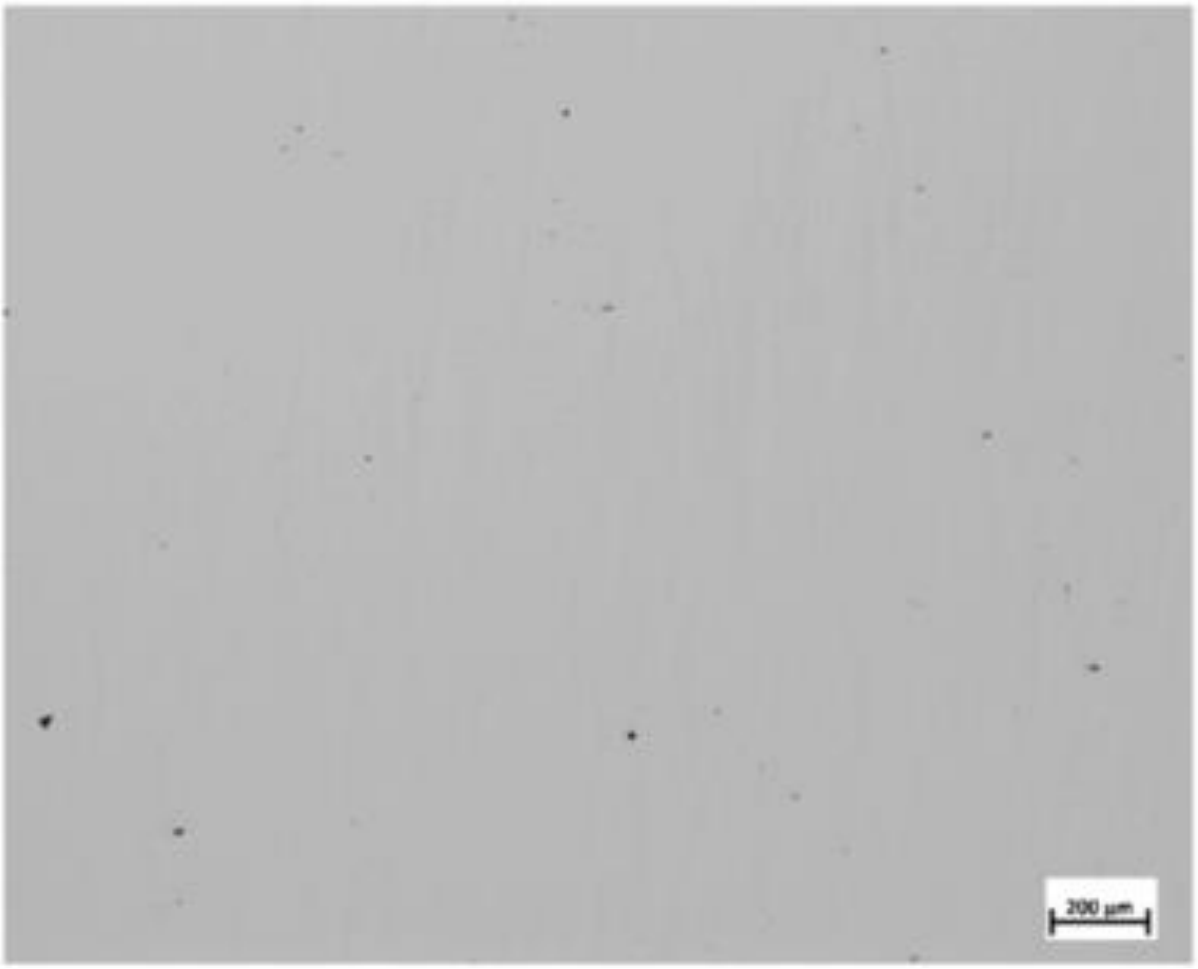

Figure 4.20: Optical Micrograph of CM247-LC produced on an EOS M290 with very similar parameters to this study [118]. *The final void content is 0.06%.*

When considering the normalised hatch spacing between the most dense results of the two studies, Adegoke's work shows a much higher level of overlap between melt pools. The wider beam is likely offsetting the slightly higher energy density of the beam, thus creating a similar final product. However, figure 4.19 does demonstrate that while the value of E^*_0 is similar, there is no graphical overlap between the two studies.

4.7.2 Tensile Strength

Comparing the tensile test results with other work from the literature, these components are significantly stronger than many previous attempts. Comparing several different studies with the average values from this body of work (figure 4.21), it is clear that the improved manufacturing parameter sets are showing a promising improvement in the physical properties of the material specimens. Other tensile specimens produced by Y.Brif on the same Aconity Mini printer are also included for comparison.

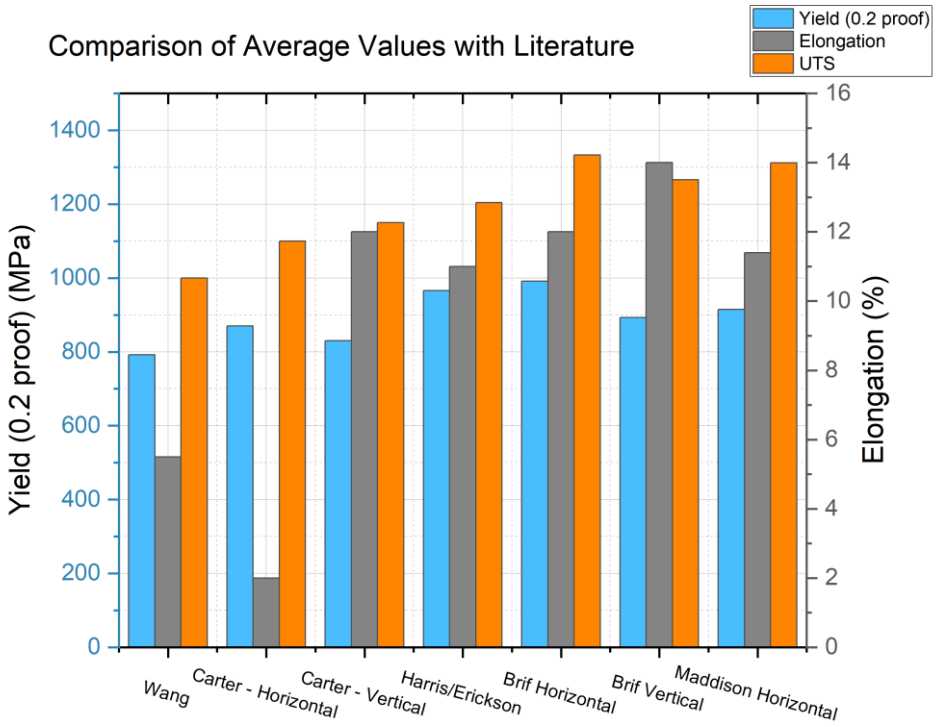

Figure 4.21: Comparison of average tensile test results from both this study and several others. The most comparable to this study is the results produced by Y.Brif, also on the Aconity Mini.

Whilst this study's material properties are not the highest of the ones shown in figure 4.21, they are the material properties of a near-fully dense set of components. This likely translates into greater UTS than most other studies, with the yield point being fairly similar across all studies.

4.8 Parameter and Machine Comparison

Every LPBF machine is different. Even between the Aconity Mini and Aconity Lab, there are significant differences in the operation and capabilities of the two. When compared to other systems, differences that are more fundamental become apparent, such as the types of laser used. The Renishaw's 200W laser uses a pulsed beam, exposing the laser for a short while, before moving on to the adjacent spot. Rather than using a measurement of scan velocity – as in the Aconity – the laser is instead characterised by two parameters; laser exposure time and point distance.

Whilst this appears to be a trivial difference, the effect on the way that the laser heats the material is profound. As demonstrated by Lyle [168], the pulsed laser does not produce a continuous weld track, instead producing a series of stationary melt pools that are produced so quickly they appear as a continuous line. This change in the morphology of the melted zone(s) may result in an increase in stress along the scanning direction, as solidification strain will occur at regular intervals between solidifying regions. This method of "stepping" the laser also increases the chance of misalignment when firing, particularly at higher resolutions [125].

In the Aconity LPBF systems, the laser also utilises an offset technique that alters the starting position of the laser at the beginning of each layer. This, along with a rotation in scan direction after each layer, helps to make the microstructure of the manufactured components more uniform and less prone to defects such as lack-of-fusion between laser tracks.

Another consideration to take into account in LPBF is the radius and intensity profile of the laser beam. The intensity profile is also referred to as the shape of the beam. The shape of the beam may also even provide a method for microstructural control. Work by Tumkur et.al [169]. has demonstrated the impact of changing from a Gaussian beam profile to a Bessel profile and how that can drastically alter the resultant microstructure seen in melted material.

Radius and profile can drastically alter how a material's microstructure are formed. In a recent nature paper by Morris Wang et.al, the beam radius is demonstrated to be critical in the formation of an extremely fine microstructure. This fine microstructure is responsible for the vastly improved properties seen between Concept and Fraunhofer machines in that particular study. Whilst this was for SS316L, it is likely that this is possible also for other material families, such as nickels. Returning to the study by Carter et.al [166] it is also worth noting that a concept M2 system was used for the manufacture of components. While the system uses a 400W laser, similarly to the Aconity Lab, the beam profile and radius is likely different to that of the Aconity Mini. Morris Wang et.al [170] suggest that the wider beam radius of the Fraunhofer machine (up to 207μm in this instance) was possibly responsible for this improvement in elongation, whereas using the Concept M2 (with a beam around 54μm),

there was a shift towards a higher strength material, characterised by a finer microstructure (figure 4.22). This effective change in the melt pool width will inevitably affect the cooling rate of the material and will therefore affect the solidification rate of the material.

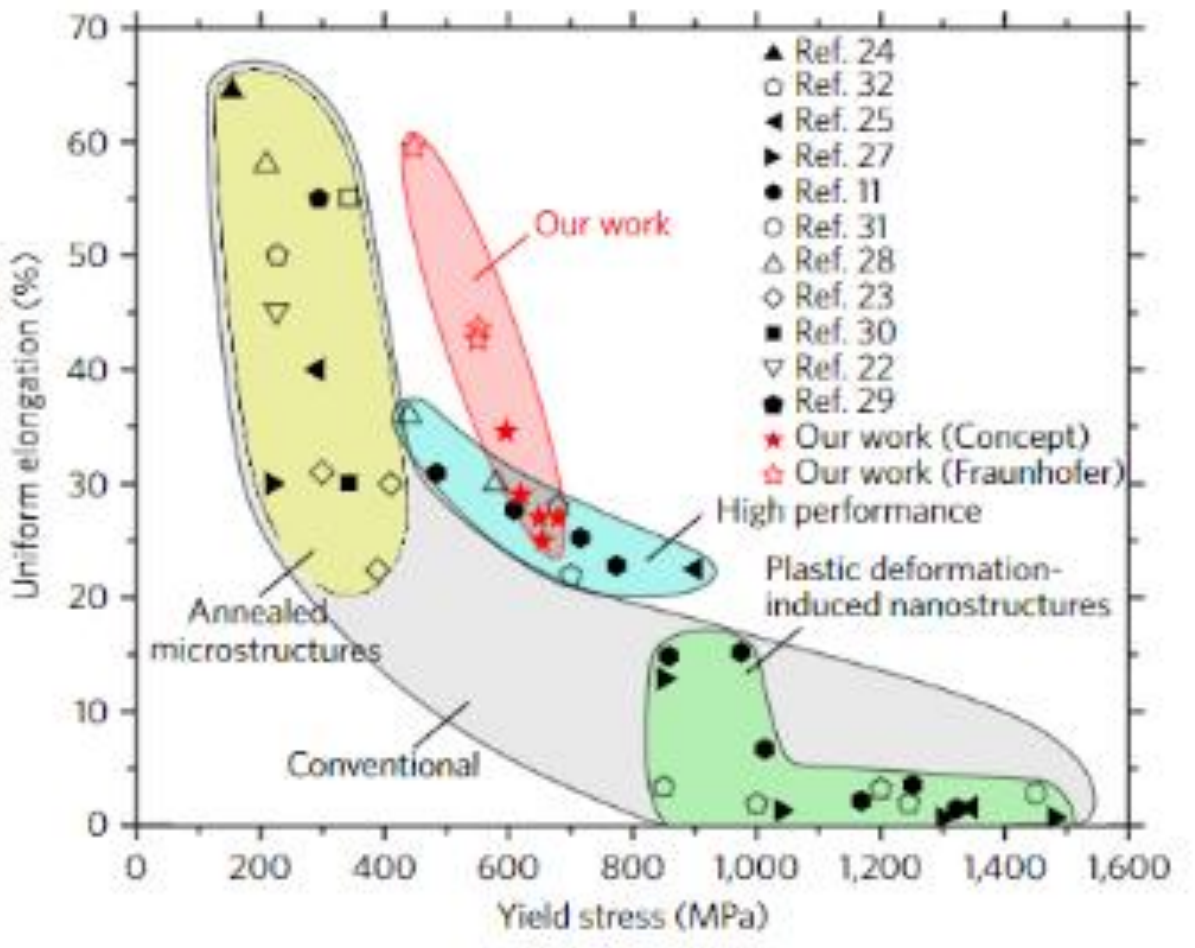

Figure 4.22: Example of the impact of beam size on final material properties from Morris-Wang et.al [170]. *This highlights how much of an impact the choice of LPBF printer can make. References in figure are from the source publication.*

Given that the Aconity systems use a spot size of approximately 70µm (figure 3.2) at the focus point, it is likely that this is a possible reason for the fine microstructure observed in the alloy. In the future, it may be worth investigating the impact of the beam radius on the alloy, using the laser's defocusing mechanism to widen the beam to similar levels to that seen with the Fraunhofer machine in the study by Wang et.al [170].

4.9 Pyrometer Spot Size Modification

The main disadvantage currently of the Aconity Mini's in-situ monitoring systems is the overwhelmingly basic design of the optical system. The lack of optical components within the system means that the field of view of the pyrometer is far larger than the melt pool itself.

The reason that this is a problem is due to the difference in size between the melt pool (the region of interest) and the full spot size. The melt pool is usually around 0.1-0.2mm in diameter, whereas the spot size of the pyrometer is around 10mm. this is a difference of nearly two orders of magnitude. Because the reading of the pyrometer is an average of all of the emissions signals in the field of view, a spot size to feature ratio of this scale results in the average value being dragged down greatly, meaning that some information is lost as to the real temperature of the melt pool . This means that the value provided by the pyrometer becomes unreliable at the edges of components, as seen in figure 4.23, because the cool powder influences the average temperature more than molten and recently melted material.

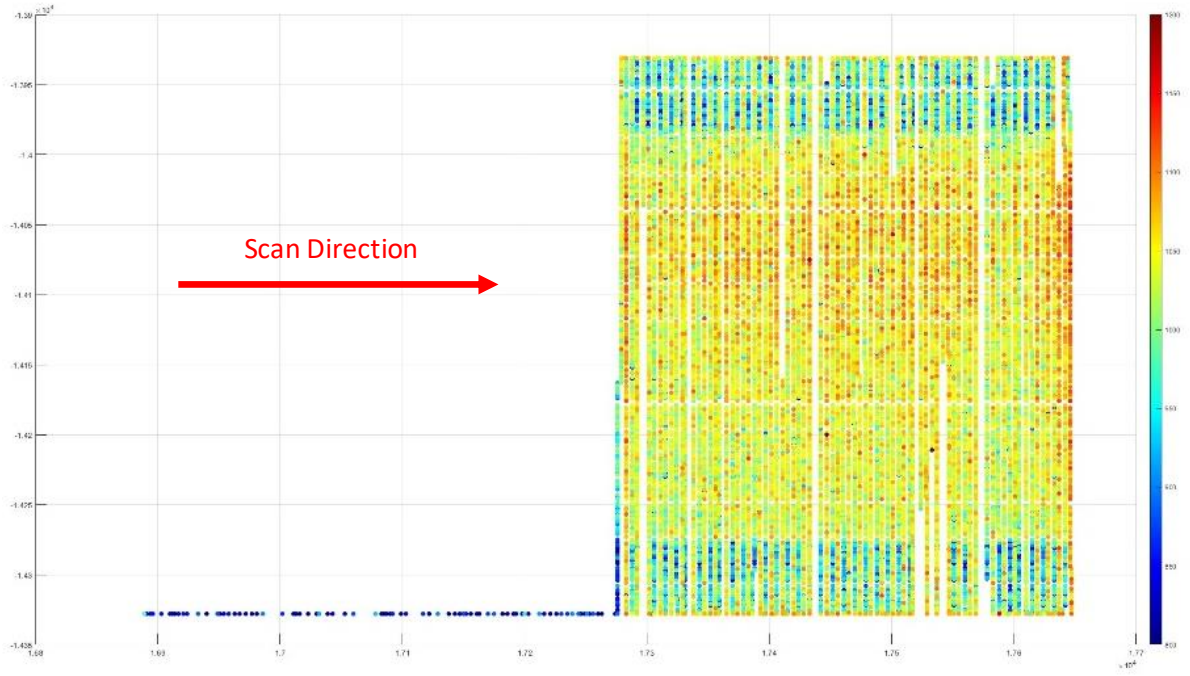

Figure 4.23: Pyrometer data from the Aconity Mini of a 5mm cube. The boundary effect of the pyrometer data can be seen here in the form of blue stripes at the top and bottom edges.

This presents a problem for the detection of hot zones in components, as they often occur at edges or corners. In complex components, this is seen where a large change in cross section occurs. This unwanted cold noise can effectively mask hot zones, presenting a problem for analysis. It was decided that the best method to rectify this problem was the installation of new optical components to reduce the spot size.

4.9.1 Spot Size Determination

In order to produce a suitable optical system capable of reducing the system's field of view to a more useful level, an estimation of the current spot size had to be performed. To do this, the Aconity Mini's chamber was detached and removed from its position beneath the laser scan head. A blackbody furnace was then placed beneath the scan head, in order to act as an illumination source for calibration. Figure 4.24 shows a picture of the setup.

Firstly, the signal emitted through the optical system was measured to provide a nominal value of intensity. A spectrometer was also used to determine the spectral throughput of the optics system to determine the transmission window. This is to ensure that the IRT is protected with an appropriate built-in filter, as the standard Aconity pyrometers are. Figure 4.25 shows the spectral throughput of the optical system.

A series of aperture plates were then placed between the furnace and scan head and optical system. The apertures start at 10mm and become progressively smaller, all the way to 0.25mm. As the radius of the aperture becomes comparable to the radius of the spot size, the observed signal intensity through the Aconity's optical system begins to be reduced. Once the signal drops below a particular threshold, the spot size has been reached.

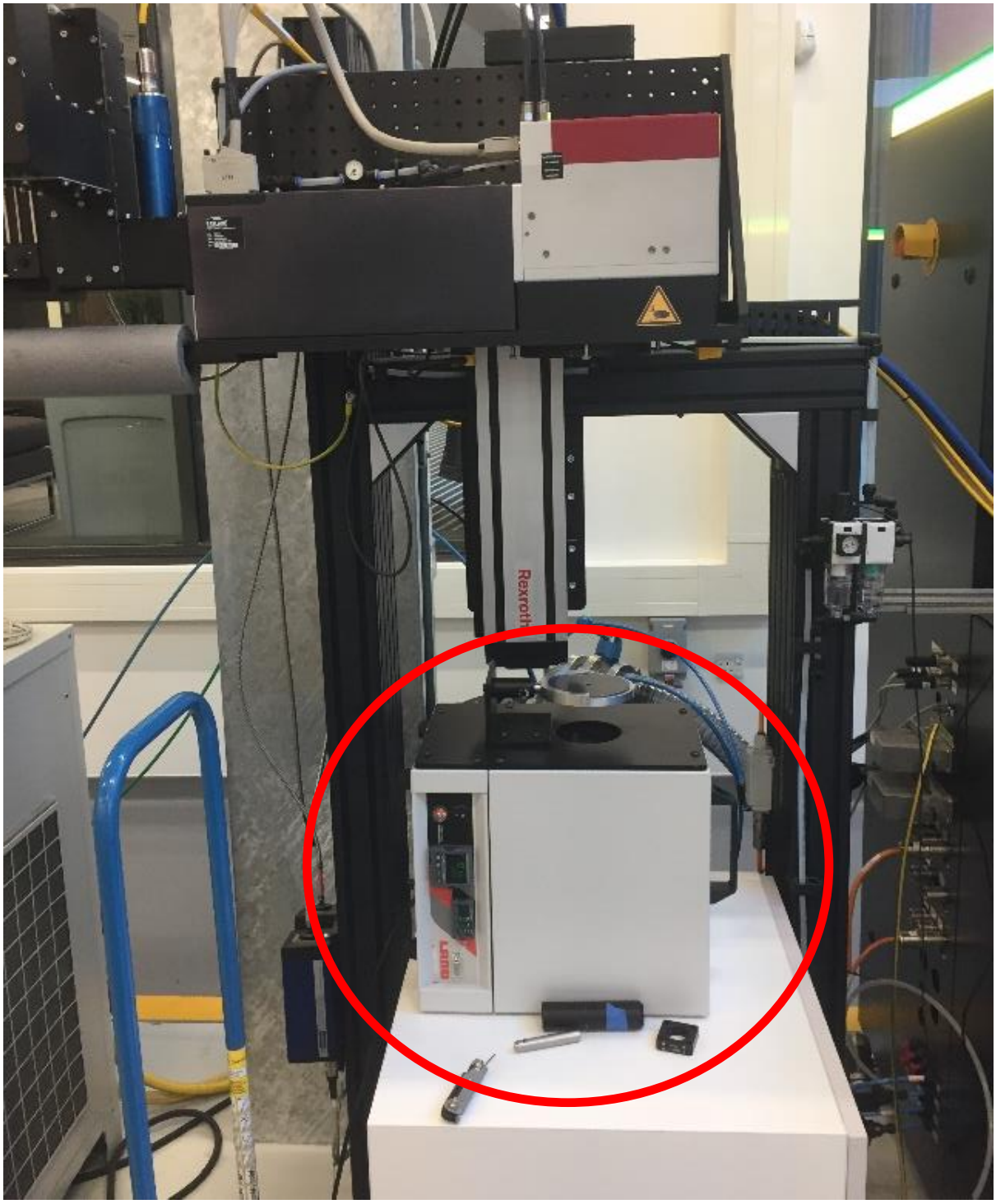

Figure 4.24: The blackbody furnace (circled) aligned with the Aconity Mini's scan head (squared). This allowed for a simulation of a large blackbody signal to be sent through the optics, to provide a method of determining the spot size.

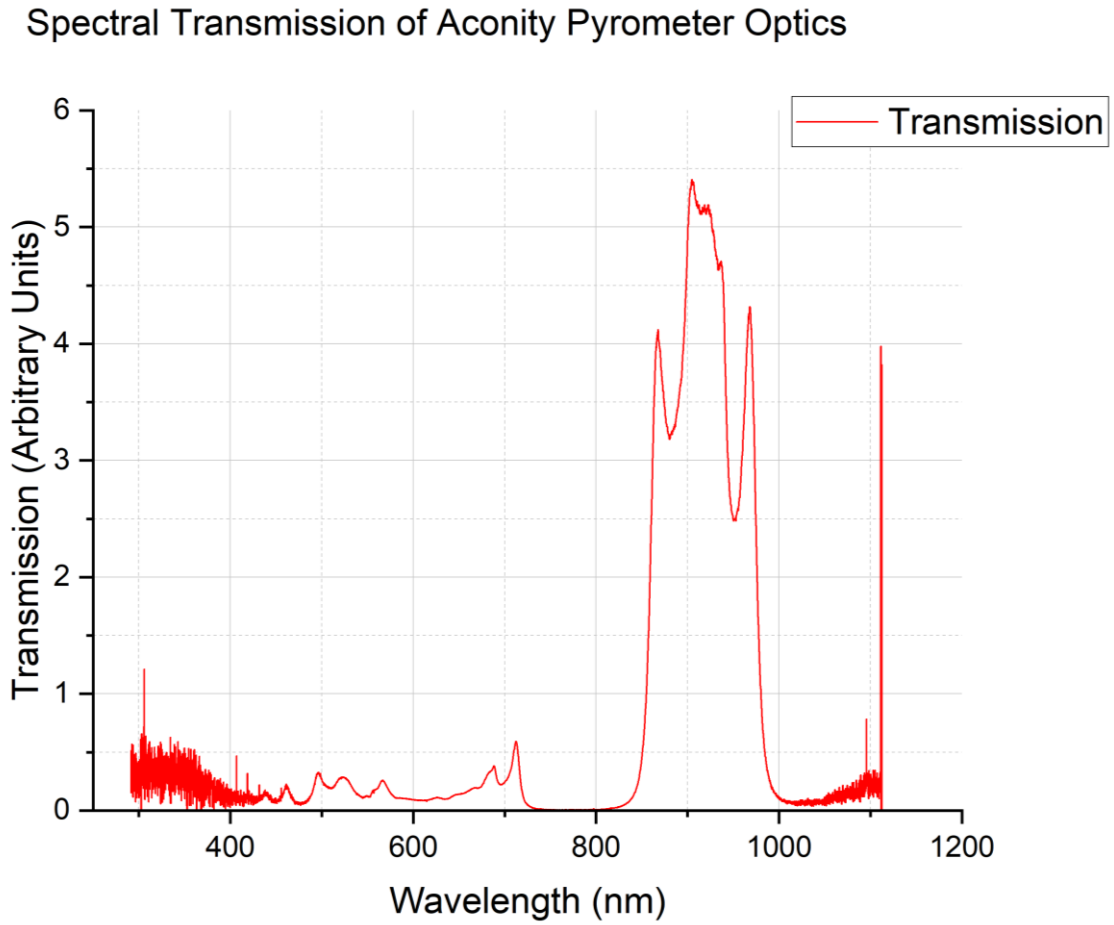

Figure 4.25: The spectral trasnsmission as determined using a thorlabs spectrometer. In this instance, the spectral range is likely to be 0.85-1μm, given the large peaks in this range.

This signal transmission line also provides a clue to the pyrometer's specific temperature detection range. Because the signal is allowed to pass between a range of 0.85 and 1.05μm wavelength, this means (according to the specifications of the pyrometer itself – see appendix A) that the temperature range is either 600°C-1600°C or 800°C-2300°C. Whilst this does not provide a definite scale for converting electronic reading to absolute temperature, it does provide a range of possible values that can be explored.

4.9.2 Altered Optics and Pyrometer

In order to rectify the problem encountered by the original optical system, the existing lens was removed. It was replaced with a more sophisticated set of components to better focus the signal and reduce the spot size of the pyrometer. The cable was then routed through a different pyrometer that uses a different gain circuit. The replacement of both components was trivial, as the components could easily be mounted within the existing Thorlabs framework. Figure 4.26 shows the comparison of the two optical systems.

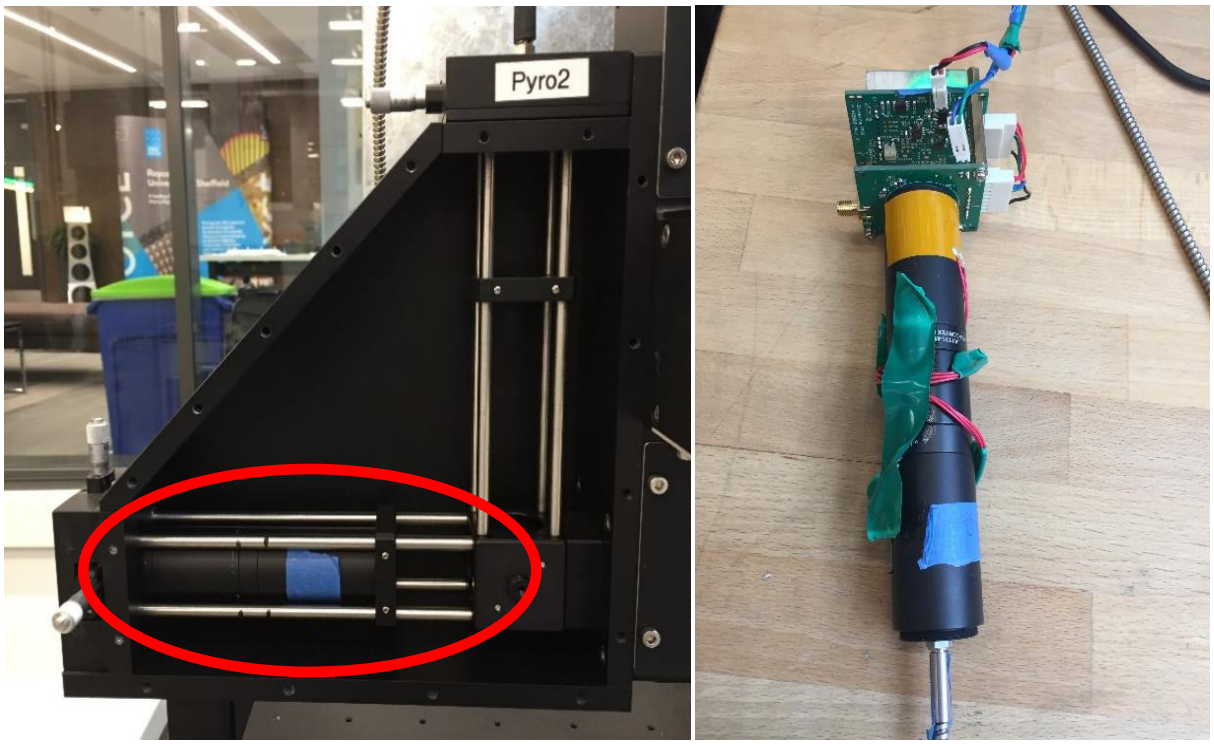

Figure 4.26: The installed optics on the horizontal axis (circled) and the original optics on the vertical axis (left image). The new pyrometer (right image).

To attempt to characterise the spot size, a more complex shape was produced with the Aconity Mini with the new optics installed. Apertures were placed down to 0.25mm, however after the 0.5mm aperture, it became increasingly difficult to properly align the optics and scan head to the signal source, due to the incredibly small signal. Eventually, the spot size was estimated to be less than 0.25mm in size.

To examine the effect of the altered optics on the data produced by the pyrometer, a build was performed to test the impact of the reduced spot size. Figure 4.27 shows images produced from data collected from the two different optical systems.

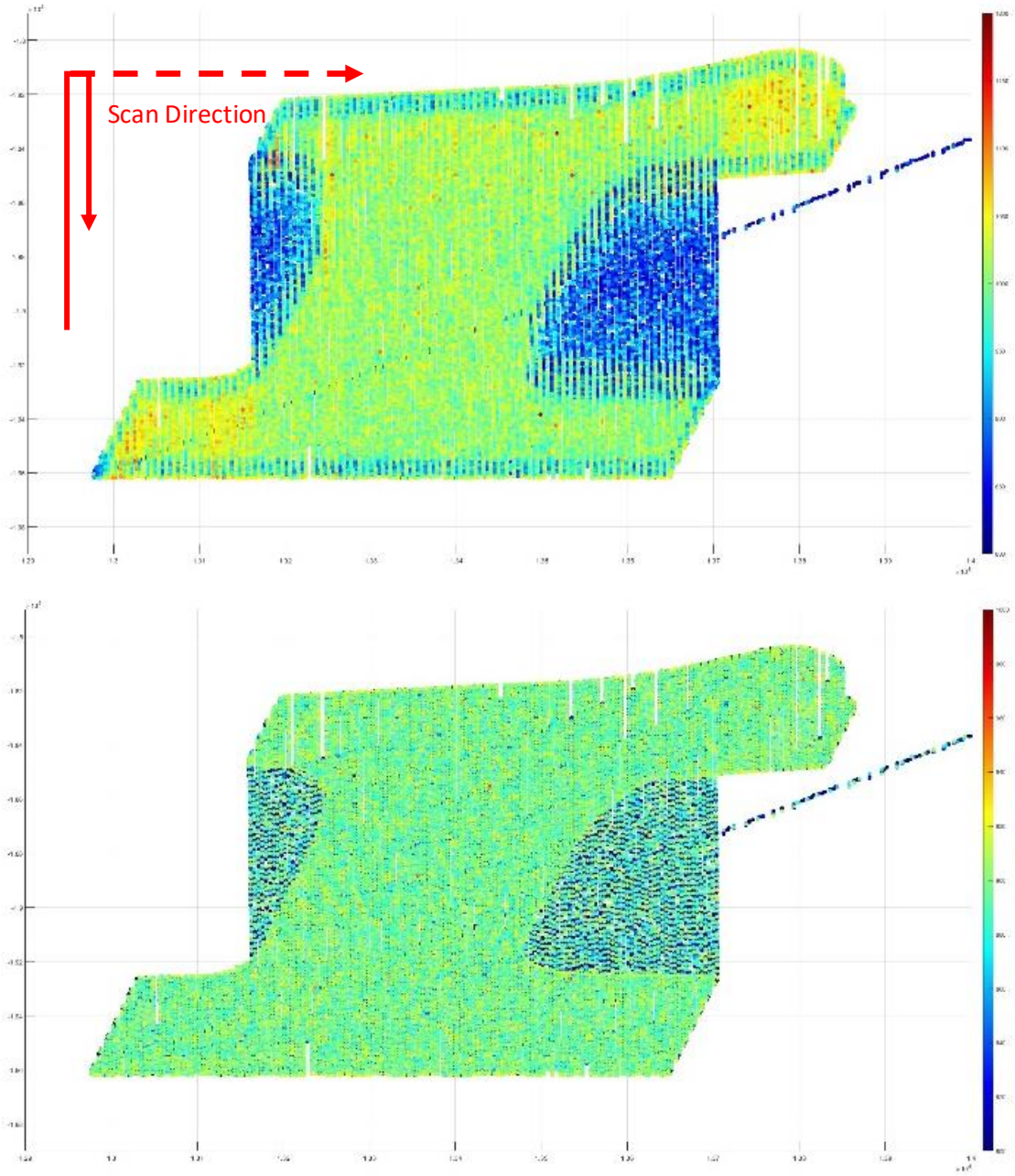

Figure 4.27: A direct comparison of the two optical systems. The image on the left is with the original Aconity optics, the image on the right uses the modified optics. The scan direction shows the the scan meander (solid line) and the general direction of travel (dotted line).

Immediately noticeable is the lack of a clear and distinct "border region" at the edge of the component. This proves that the spot size has been reduced sufficiently to acquire accurate data

from the build process. Furthermore, an estimation of the spot size can be provided by examining the data from the two optical systems. However, a similar problem now occurs with the data, in that the data is so precise, it is almost impossible to discern the actual spot size, as the feature of the data has been entirely removed. This also means that the resolution of the pyrometer data is far more refined, resulting in much more accurate data, particularly in the edge of the manufactured component.

Examining the data from these graphical plots can provide details into the trends present in the maps of the temperature. Through Matlab, a simple output of intensity values and how regularly they are detected can be turned into a histogram. Between the two optical systems, the range of the signal intensity is the same, but the raw values are shifted slightly (figure 4.28). This is due to the lower gain setting on the amplifier circuit of the altered pyrometer producing a lower signal. The effect on the temperature profile is profound, resulting in a clearer and more smoothed signal overall. The percentile lines also help to demonstrate that the range of values is still very similar, suggesting that the signal is indeed real and not caused by another source.

In both data streams, the hot edge effect often seen in LPBF is visible, though it is not consistent in the original Aconity optics and is often occluded by the noisy data (figure 4.27). However, the modified optics provide a much more clean and consistent reading for this common feature, with the elevated temperature reading visible at the edges where the laser turns.

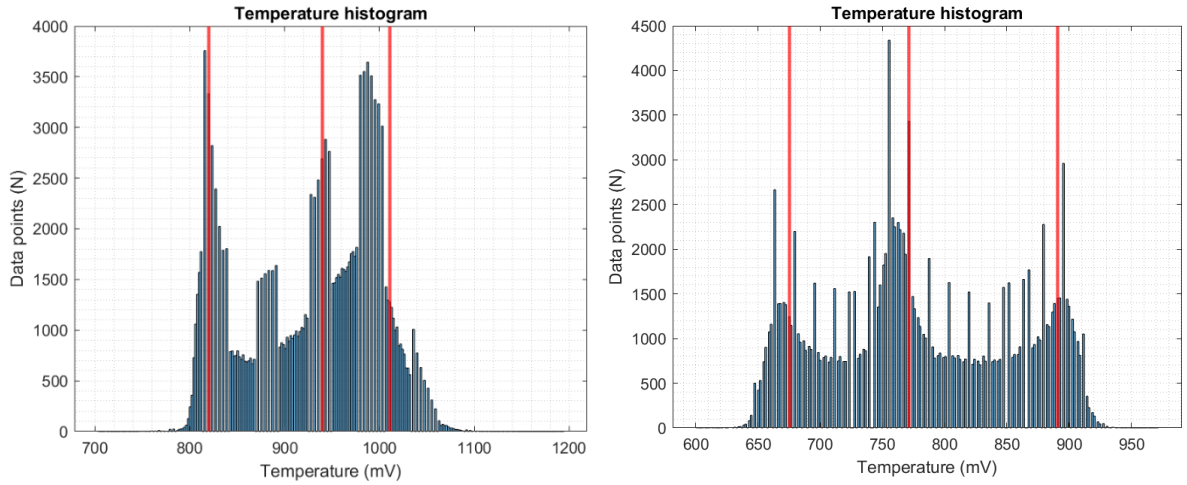

Figure 4.28: The difference between data produced by the original optics (left) and the modified optics (right). Red lines denote the D10, D50 and D90 values of the distributions.

Also noticeable is the reduction in signal amplitude when viewed using the modified optics. Whilst this may appear to be a problem, it is due to the alternative pyrometer being set to produce a smaller signal. This was done to ensure that damage could not be done to the FPGA board within the Aconity, as this has been a problem in previous work.

This impact on the shape of the data distribution appears to be due to the resolution of the spot size, with more discernible hot and cold regions present. However, due to the small signal from the limited gain function, the signal-to-noise ratio of the data is far higher, as can be seen in figure 4.29, where the seemingly even data still contains individual data points that are significantly hotter or colder than the average.

The effect of the baseplate in the initial layers of the build is also no longer visible in the data from the modified optics, providing more evidence that the spot size has been drastically reduced (figure 4.29).

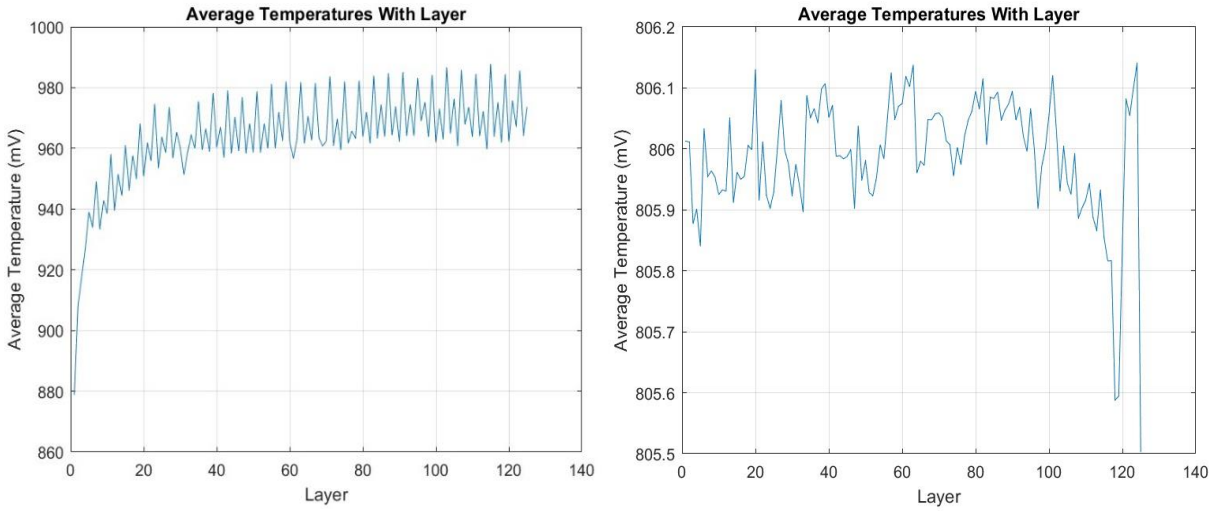

Figure 4.29: The average temperature readings obtained by both the standard Aconity optics (left) and the modified optics (right) for the same component. A near-total reduction in temperature variation is observed, suggesting that the reading is much more precise. However, the optics are likely absorbing some signal, resulting in a seemingly lower reading.

The reduction in both the average temperature and its variation is likely due to the large reduction in spot size. Given that the spot size is now comparable to the size of the melt pool, the reading is more representative in terms of its variation. The direct readings that make up the average are lower, though this is likely due to the effect of the gain mechanism in the IRT of the modified system.

4.10 Summary

CM247-LC has been shown to be printable to a high material quality, both for hardness tests and for tensile testing coupons. The processing window has been highlighted in an energy density sense but also for a temperature response on the Aconity Mini's pyrometer system. An improvement in the tensile strength of the material has been noted in the horizontal as-built condition, reaching beyond 1250MPa. Whilst the micro-hardness of the material remains high, it is highly variable, demonstrating the problems that can arise with the consistency of LPBF-printed components.

Crack formation has been significantly reduced in most samples, with very few highly elongated defects being present in samples. Some samples contain almost no visible cracks, though some small cracks may remain that are not visible in the micrographs. Voids overwhelmingly consist of those produced by gas porosity, which then becomes a question of powder quality rather than processing parameters. The overall density of the material produced remains very high and sits well with models and calculations from other studies. This success suggests that the processing window of the alloy may not be as small as some other studies (such as work done by Adegoke) suggest.

The installation of new optics into the pyrometer system has also paved the way for a more accurate analysis the temperatures on a melt pool scale. The boundary effect observed in pyrometer data has now been rectified, though challenges remain to ensure that the signal received is properly calibrated. This system has also demonstrated that the average temperature and temperature profile on the melt pool scale is highly consistent for a single-parameter build, regardless of geometry. The determination of the spectral transmission range also provides crucial information that will be invaluable for the creation of more in-situ monitoring systems that utilise the co-axial mounting optics.

5. In-Situ Heat Treatment of CM247-LC

5.1 Introduction

This chapter details the investigation of the possibility of inducing property changes and reducing defect formation using in-situ heat treatment techniques. The primary goal of this work was to evaluate whether the as-built material quality of CM247-LC could be improved using a pre-heated build substrate and whether laser rescanning produces a visible impact within the material.

Several sets of cubic test pieces were manufactured with varying parameter sets to evaluate the impact of the use of the pre-heated substrate on final build quality. Laser parameters and bed temperature were determined using a melt pool model developed by Freeman [89]. To qualify the impact of using the heated bed, hardness tests were used, allowing small samples to provide a direct comparison between this and the previous chapter's results for the same size components. This was in addition to the use of metallographic preparation, etching and microscopy to investigate the unusual microstructures present within the samples caused by the effective heat treatment of the samples in-situ. Hardness values are compared with and without substrate heating, providing a striking demonstration of the value of this technology.

The possibility of utilising a thermal camera during the operation of the heated bed to examine possible phase changes is also explored. This initial analysis may provide insight into whether a different microstructure or phase is forming due to the lower cooling rates experienced during the use of the heated bed.

Finally, the impact of the absorptivity of the material was examined to demonstrate the impact that this value can have on simulations of melt pools and how this affects predictive models for parameter selection. This was performed using an adapted methodology from Trapp et.al [113] to provide in-situ absorptivity measurements of a "close to real" system during laser melting of powder material on an already-manufactured layer.

5.2 Part Layer Rescanning

One proposed form of in-situ heat treatment is the use of laser rescans. This process involves using the laser to make one or more secondary passes over the material that has already been melted or sintered by the laser, or as a "pre-sintering" pass similar to the operation of certain EBM systems (such as an Arcam). This is intended to promote material consolidation and stress relief through grain boundary growth and realignment, in a similar fashion to traditional forms of heat treatment.

There are two main problems with part rescanning in LPBF. The first is the very high thermal conductivity of metals. This property means that components cool very rapidly, due to the build substrate acting as a heat sink. Because of this, it is difficult to try to maintain a temperature using the laser over more than one component at a time, especially as the galvanometers in LPBF systems struggle to move quickly enough to maintain a temperature across multiple components or larger build areas.

This is achievable on an EBM system [48], as the electrons are controlled by the fluctuations of a magnetic field, so can be controlled and directed much faster. In Arcam systems, a preheat option is available with this technique, where the electron beam passes over the target area, before then passing the more intense beam over to melt the desired part.

The second problem with rescanning is ensuring that the rescan does not melt the material. When materials undergo stress relief via heat treatment, the temperature must not exceed the melting point of the material. If this occurs, existing material grains are lost, meaning that when solidification occurs, the material will return to the same state it was in before rescanning, making the endeavour pointless. Because of this "balancing act" between the two phenomena of melting and rapid solidification, it is difficult to make this process work effectively.

To examine this, cylindrical components were designed and built in the Aconity Lab. Two experiments were designed to examine the effect of using pre and post-scan strategies on the density and quality of parts manufactured in this way. Both experiments used a series of nested components in NetFabb, in order to tell the system to make a second pass with the laser with different parameters.

The "ideal" parameters described in table 4.2 were then used again, but had a rescan pass immediately afterwards. A power of 100W, speed of 3000mm/s and hatch space of 35µm was used. This meant that a weaker pass would occur after the main melt, with a view to relieving stress and promoting better component consolidation. Using a similar laser power would be likely to melt the material and cause re-solidification, defeating the objective of the process. Components that underwent a post-scanning procedure were fully fabricated; likely due to the

presence of a solid structure from the first stronger laser pass. Despite this however, there is minimal evidence of the laser pass having any effect on the defect density of the material, as shown in figure 5.1.

This lack of impact on the material will be revisited and discussed further in chapter 8. It is likely however, that the incident laser has either been largely reflected (thus having minimal effect) or has not delivered enough heat to have an effect on the microstructure. Because of this, the microstructure of the printed component will be nearly identical to that of one without rescans, as the solidification will be very similar.

Due to the laser's very small spot size and area of effect and given that the bulk metal is highly conductive, only a very small region will be reheated during the rescan at any one time. In addition, the time that the heating will take place is very small, as the heat is very rapidly conducted away. Because of this, the effect on the defect density of the material is minimal.

The tiny fraction of a second that the heat is imparted for is not sufficient to promote any noticeable consolidation. This is different to a heat treatment procedure, where the elevated temperature may last for several hours before quenching. The rapid cooling of the material - which may induce thermal stresses, particularly if the material is not fully solid immediately after the rescan - will also offset any stress relief or relaxation. Finally, the lack of external pressure (such as in HIP) means that there is little driving force for pore and defect closure. The only instance when this may occur is when laser shock peening the material, however this would be a physical interaction rather than a thermal one. This procedure would also be difficult to perform in-situ in LPBF, as the process requires a transparent overlay at the surface of the material, in order to confine the plasma produced by the laser.

Figure 5.1: Representative micrograph of cracked CM247-LC after a rescan build. Minimal effect was observed on the material from the rescanning.

Without this overlay, physical peening effects do not produce any level of compressive force in the material and produces only a small thermal effect. This small thermal effect would require hours of exposure to heat an entire component without inducing melting and would need the heat source to move very rapidly across the whole build volume. This is possible in EBM but not in LPBF. Because of this, the ability of the laser to perform effective heat treatment throughout the samples produced in this fashion is inefficient at best, at worst actively hindering the processing of the alloy.

5.3 Aconity Induction Pre-Heated Build Substrate

An alternative method of control in AM processing involves adjusting the build substrate temperature. Because of the presence of extremely high thermal gradients arising from the relatively cool substrate and the high thermal input of the laser, an undercooling effect is often seen in LPBF. This usually manifests in the form of dendrites or very small cells and grains, which are indicative of a very rapid temperature drop in the material. This resultant microstructure is ideal for strengthening, particularly for applications such as turbine blades where the forces on the component are predominantly in a single direction. However, for components where ductility or workability are important properties, this microstructure can present a problem.

The heated bed in the Aconity Lab (figure 3.6) provides a method of reducing the thermal gradient in the system by raising the temperature of the bed through joule heating and subsequent conduction. This effectively slows the cooling of the metal. In certain steels (such as 17-4PH), allowing the microstructure more time to change and stabilise, rather than "locking in" a metastable state can make the difference between a martensitic or austenitic final product, which can result in wildly different properties. In the case of 17-4PH, this change of properties is exhibited as magnetism [160]. According to Aconity3D, the substrate is capable of reaching temperatures up to 1200°C.

Due to the ease of which they can be changed, the laser power, scan velocity, hatch spacing and beam radius are historically the most commonly used to determine ideal parameters for materials in LPBF. Specific heat, density and melting temperature are material specific and can only be changed by altering the material composition. Ambient temperature in LPBF has previously been limited to around 250°C. However with the Aconity Lab's heated substrate, the temperature may be increased to up to 1200°C. This presents a unique opportunity to explore a new experimental space within the field of AM, as at this temperature, the alloy may potentially undergo in-situ recrystallization, as well as stress relief.

5.3.1 Energy Density Equivalence

Utilising Thomas et.al's equation for the normalised energy density input (equation 2.6). It is possible to calculate the ambient temperature change required to deliver an equivalent energy input equal to that of the "ideal" parameters described in chapter 4. There are several terms in this equation that are controllable variables. Table 5.1 shows the values considered for this study.

Table 5.1: The two parameter sets used in this study to produce equivalent energy density input to the produced samples. The first is at room temperature, the second is at 700°C but with a layer thickness that is doubled.

Q (W)	V (mm/s)	L (m)	H (m)	A	Rb (m)	T0 (°C)	E*0 (J/mm^3)
190	3	0.00002	0.000035	0.6	0.000035	323	5.71229423
190	3	0.00004	0.000035	0.6	0.000035	973	5.71229423

Utilising an ambient temperature of 700°C (973K) results in exactly twice as much energy delivered to the sample during melting as at 50°C (323K). Because the laser heats the substrate upon contact at room temperature, it is likely that most LPBF processes will not actually cool fully to room temperature between layers. The ambient heat produced by the laser exposure can be felt if the chamber is opened immediately after the building process has finished, as the build plate is often warm to the touch.

To further test this methodology, a further test was designed to explore how energy density input can be influenced using the heated bed. Rather than controlling the input energy density to quite such a degree as was demonstrated in table 5.1, the experimental space around the value of 5.71 J/mm^3 was explored further by changing laser power and speed. Table 5.2 shows the set of parameters used to produce similar levels of normalised energy input. Whilst not identical, this will demonstrate whether energy density approximations are applicable when taking ambient temperature into account when designing parameters for component production. As well as these tabled parameters, the values of density, melting point and specific heat are utilised. These are constants that are material specific and so must be used for accurate predictions for the behaviour of CM247-LC alloy.

Table 5.2: The parameter sets used to produce similar energy density input values to that of chapter 4's ideal parameters.

Q (W)	V (mm/s)	L (m)	H (m)	A	Rb (m)	T0 (°C)	E*0 (J/mm^3)
75	2.5	2.00E-05	3.50E-05	0.6	3.50E-05	973	5.411647163
100	2.5	2.00E-05	3.50E-05	0.6	3.50E-05	973	7.215529551
125	2.5	2.00E-05	3.50E-05	0.6	3.50E-05	973	9.019411939
75	3	2.00E-05	3.50E-05	0.6	3.50E-05	973	4.50970597
100	3	2.00E-05	3.50E-05	0.6	3.50E-05	973	6.012941293
125	3	2.00E-05	3.50E-05	0.6	3.50E-05	973	7.516176616
75	3.5	2.00E-05	3.50E-05	0.6	3.50E-05	973	3.86546226
100	3.5	2.00E-05	3.50E-05	0.6	3.50E-05	973	5.15394968
125	3.5	2.00E-05	3.50E-05	0.6	3.50E-05	973	6.442437099

5.3.2 Melt Pool Modelling

A model produced by Freeman et. al. [89] was employed to investigate how changing the ambient temperature of the system would affect the shape and size of the melt pool produced by the laser. The models itself uses the Rosenthal equation to predict how a moving "point" heat source affects surrounding material. Hypothetically, this would allow for the melt pool size and shape to be kept similar, whilst producing a thermal gradient that is much more amenable, in order to investigate the effect of cooling rate on defect density. CM247-LC was simulated at room temperature, and 700°C with varying laser powers and velocities, in order to attempt to predict melt pool shapes. Displayed below (figure 5.2) are the melt pool shapes produced from parameters given in table 5.1:

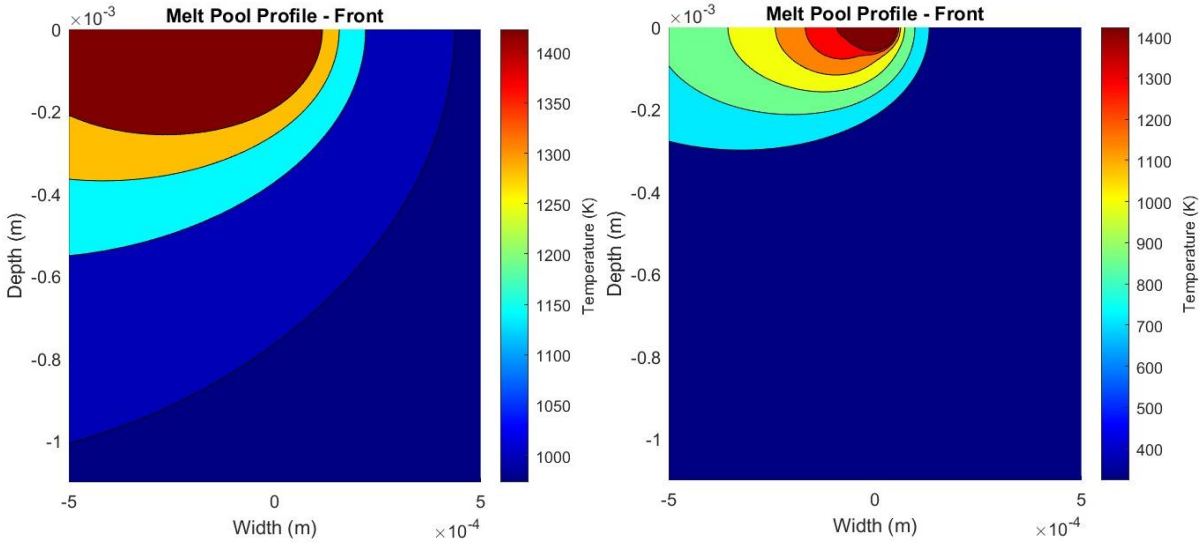

Figure 5.2: Comparison of predicted melt pools. The increase in predicted melt pool size between the regimes (rows 1 and 2 of table 5.1, respectively) suggests that the manufacture of the material will produce far larger melted regions.

The melt pool geometry of the two different scenarios is wildly different, suggesting that the ambient temperature can greatly increase the sensitivity of the material to the laser. The size of the predicted penetration of the melt zone for the elevated temperature suggests that this larger region of melted material will be as large as the HAZ of the room temperature parameters. This larger melt pool means that the cooling rate of the material will be significantly reduced. Because of this, the microstructure will likely be more evolved than in normal LPBF material, with greater levels of segregation and carbide formation present. This may be detrimental to the formation of components, as carbides and segregation often cause problems in similar welding processes.

A comparison of the reduced power laser parameters was also performed (figure 5.3) using values from table 5.2. These parameters predict similar melt pools to the elevated temperature prediction in figure 5.2. The radius of the HAZ is very similar between the two experiments, however the size of the fully molten region is much smaller for these reduced power parameters, especially for the lowest energy input set.

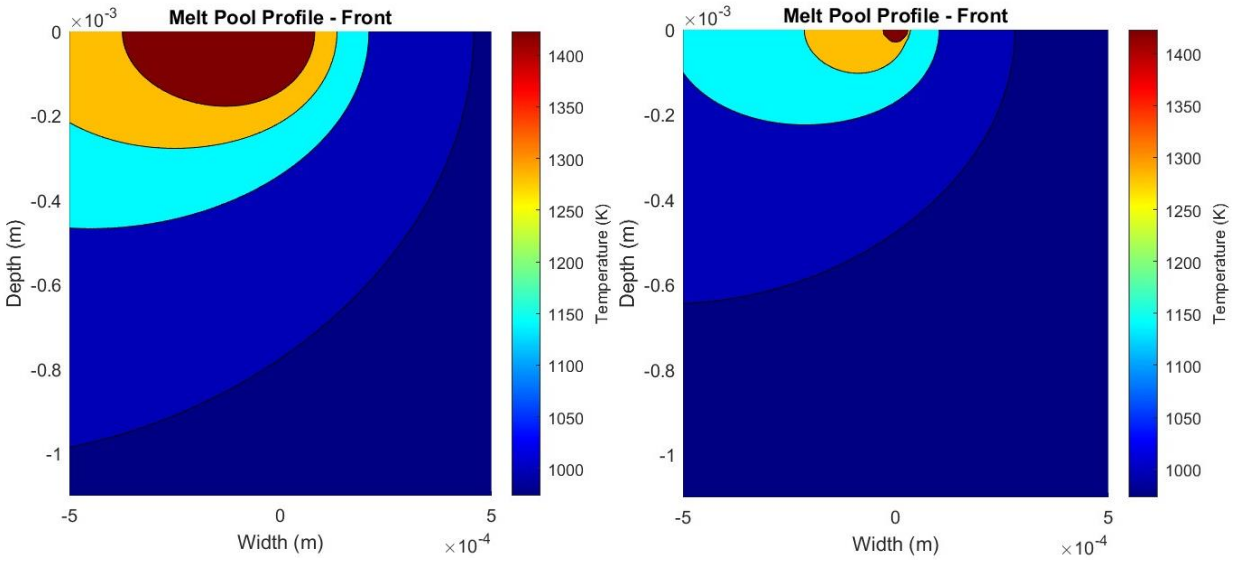

Figure 5.3: The predicted melt pool of the highest (left, Q=125W, V=2.5m/s) and lowest (right, Q=75W, V=3.5m/s) energy density melt pool in the set of reduced power samples.

Of these reduced power samples, the closest ones to the ideal normalised energy density value (5.71J/mm^3) are samples 1 and 5, which have values of 5.41 and 6.01 respectively.

5.3.3 Experimental Procedure – Heated Bed Characterisation

It is likely that whilst the preheating system is capable of generating temperatures around 1200°C at its heating element, there are likely losses when the heating element is in contact with the substrate and the powder. To determine the full extent of the losses in the system, a thermocouple array designed for a Renishaw 125 (figure 5.4a) was employed on the Aconity Lab. The array attaches using standard fittings (figure 5.4b) that are common to both Renishaw and Aconity printers.

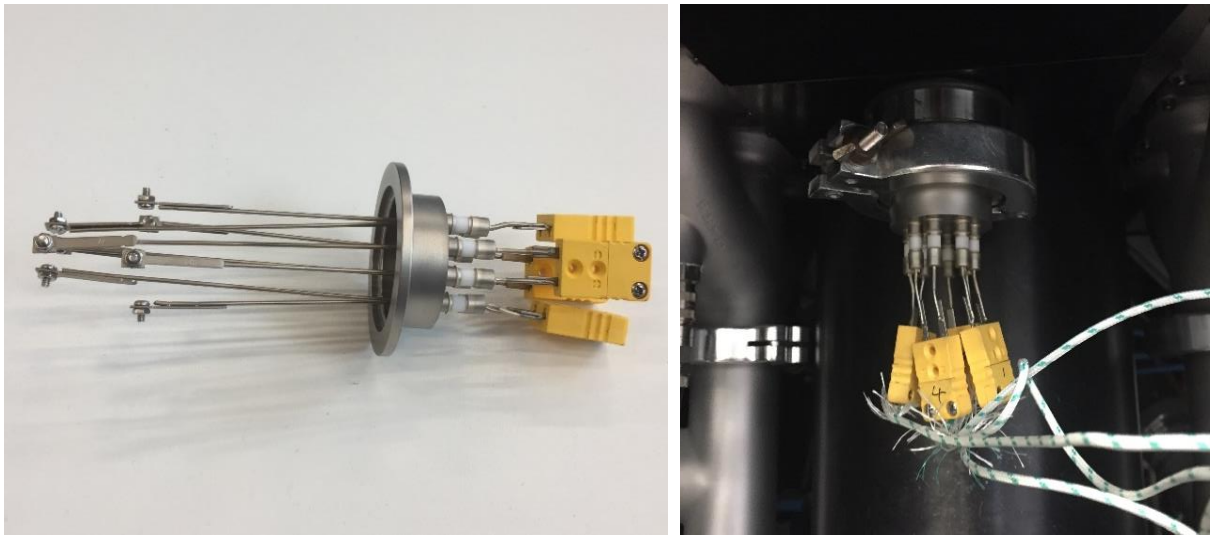

Figure 5.4: a). The thermocouple array used to pass a signal from inside the chamber without compromising the internal atmosphere. b). The standard fitting port that the array attaches to which are common to both Renishaw and Aconity printers. In this instance, the port attaches through the overflow trap port (figure 3.7, C)

Thermocouple wires were attached to the fitting before being passed through the port and placed in contact with the heated substrate. Multiple thermocouples are used in this experimental design to provide comparisons across the top surface, in order to examine variation in temperature/thermal retention due to plate geometry. A picologger was used to collect data from the thermocouple probes, allowing for direct capture and collection of temperature data. Figure 5.4 shows the overflow canister removed and replaced with the thermocouple array, which is attached to the picologger.

This data was then corroborated with the target temperature and the temperature of the heating element itself, in order to determine the loss of heat at higher temperatures from the build substrate. This test was repeated with a powder bed present, in order to provide a representative

result for in-situ temperature monitoring. A total of four thermocouples can be fed through simultaneously.

The first is placed at the centre of the plate's surface. The second then sits halfway between the centre and the edge of the baseplate, to check for temperature variation within the layer. The third probe sits at the edge of the plate, to examine how the "corner" of the baseplate behaves at the elevated temperatures. The fourth thermocouple was placed in the centre of the powder bed, to investigate the effect of the raised temperature on the powder.

Once the thermocouples were placed, the temperature of the heating element was set to increase to 1200°C (figure 5.5). Whilst this was happening, the temperature data was collected by a Pico Technology data logger and used to generate a graph of temperatures. This data was then exported in the form of a .csv file and further manipulated using either Matlab or Excel.

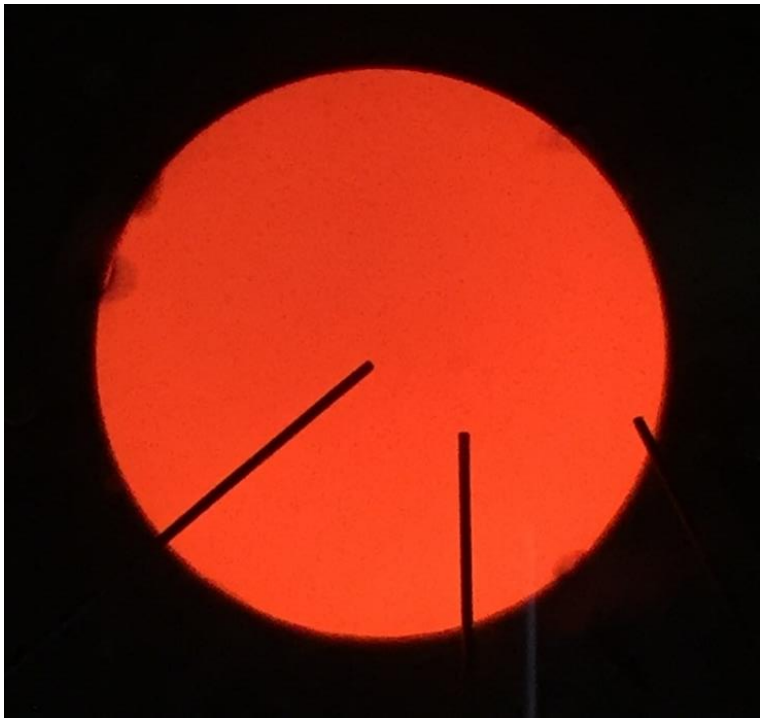

Figure 5.5: Top-down view of the heated substrate with thermocouples. This image was taken when the temperature of the heated substrate had peaked during the test with powder. Inconsistencies can be seen around the edge due to slight perturbations in the powder bed.

As well as the data from the fed-through thermocouples, the data from the control thermocouple can also be collected by accessing the machine logs on the Aconity PC. This and the collected data can then be placed side-by-side on a graph to demonstrate the extent of the losses in the heated bed system, which can be seen in figure 5.6.

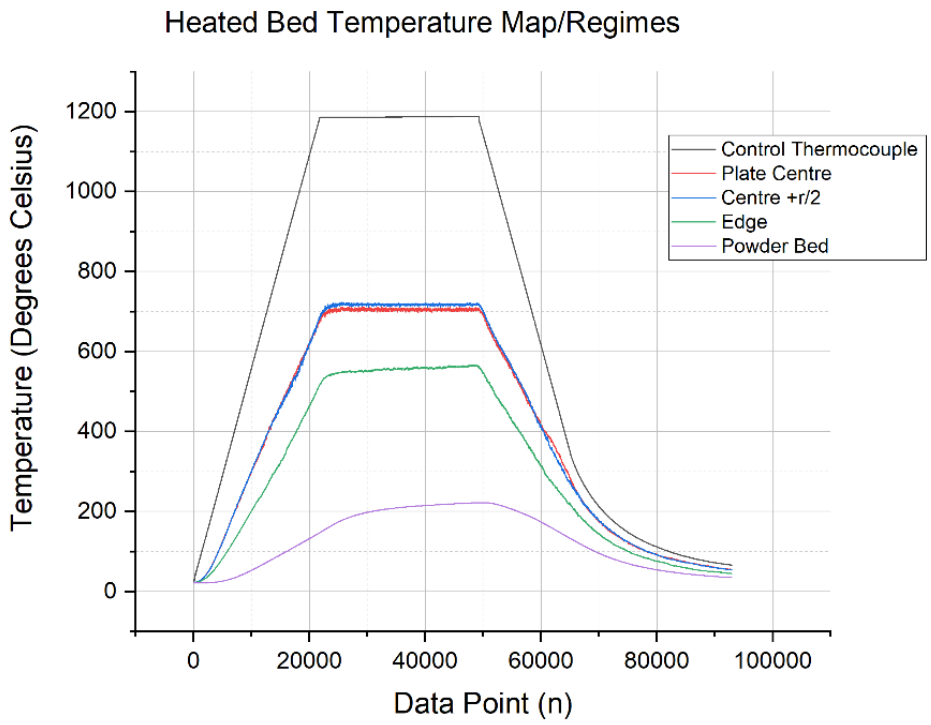

Figure 5.6: A graph of temperatures at various points in the heated bed. The blue line denotes the temperature halfway between the centre of the plate and the edge.

As can be seen in figure 5.6, the heated substrate does not achieve its full temperature, only reaching approximately 700°C even after a further soak time of 20 minutes recommended by Aconity3D. It is also worth noting that the heating element's top surface did not quite reach the desired temperature, instead stopping around 20°C shy of this at 1180°C. There is also a variation in the temperature profile of the heated bed, with a lower retention of heat at the edge. This is due to conduction effects from the surrounding powder, as the edge of the baseplate acts as a corner with two surfaces that the heat can escape from via conduction. This change in temperature distribution across the baseplate is due to the powder acting as a heat sink, increasing the heat loss through conduction at the edges of the baseplate. The powder used in this characterisation trial was CM247-LC.

While 700°C is not close to the expected 1200°C, it is still higher than most LPBF systems can achieve with a heated substrate. Furthermore, rather than causing an in-situ recrystallization effect, this temperature is more likely to result in a form of stress relief common at this temperature for nickel superalloy heat treatment. It is important to note that while the thermocouples were held in contact, they were not fully welded to the sample, which may impact on the final detected temperature. Furthermore, when gas flow is initiated during a build, the movement of cool clean gas across the build volume causes the detected temperature to drop by a further 100°C.

5.3.4 Experimental Procedure – Heated Bed 3D Printing

In order to reach the temperature of 700°C, the induction unit must slowly ramp its heat up from room temperature. This is done at a rate of 13.333°C per minute, as any more rapid can damage the coils or cause too rapid an expansion of the water used for cooling. Due to the large disparity between the target temperature of the heating element and the actual temperature of the substrate, the target was set at 1200°C. As seen in figure 5.6, this results in an actual temperature of ~700°C. The time for ramp up to this temperature is 90 minutes. The system is then allowed to soak for a further 20 minutes to ensure that the bed is heated more evenly. To ensure that the baseplate's temperature profile did not impact on the material's temperature, all samples were concentrated closer to the centre of the plate.

As soon as the building process was completed, the cooling process began. Again, the cooling rate is limited to 13.333°C to avoid damaging the induction heater coil (this is advised by Aconity3D). This means that as well as heating during the build time, there is also the effect of the heat during the cooling time to consider as well, during which the material is still undergoing thermal processing in-situ. As well as this, once the heating element reaches ~300°C, the cooling rate drops, likely due to the insulating effect of the powder. In total, the material spends approximately two and a half hours cooling back to room temperature before it can be removed from the chamber. Removal earlier than this presents a fire hazard, due to the presence of the metal powder. This is in addition to the time it is held at 700°C during the build process.

This process was then repeated for samples using parameters from both table 5.1 and 5.2. In addition, parameters from table 4.2 were built to determine whether similar effects are seen in similar parameters, not just the identical energy density input. Three builds were performed. One with nine 5mm cubes using the room temperature parameters from table 4.2, one with 9 cubes using the reduced parameter sets from table 5.2. Finally, a build of nine 5x5x10mm samples was printed using the elevated temperature parameters from table 5.1 The increased height was intended to provide more material for study.

5.3.5 Results of Heated Bed Trials

5.3.5.1 Defects and Microstructure

All of the components with parameters from table 5.1 built successfully. These components were mounted and polished in an identical fashion to the previous chapters' experiments. These components contained high levels of defects, with both cracking and porosity present in most samples.

Components built with room temperature parameters (table 4.1) were less successful. Seven of the test pieces manufactured with the heated substrate were cancelled before reaching full height because they were swelling above the powder layer. All of these components were bulging at the centre of their top surface, possibly due to the local surface tension across the top layer of the part during the longer cooling time. The two lowest energy parameters (components 6 and 9) were the only two to build to full height.

Several of these components contained major inclusions (figure 5.7), where the material had not fully consolidated. This may be a result of the increased surface tension. If the top surface was pulling upwards, it may have caused a void to form beneath the top layers. All samples contained some sort of major defect or had to be stopped during the build because of the swelling.

Microstructurally however, these samples contain vastly different material to components built in standard operation mode. Etching the samples with glyceregia in the same fashion as described in section 3 reveals a more evolved microstructure, with grains growing in a more even fashion to the standard columnar grains (figure 5.8). In the well formed regions of material, defect density is extremely low, including at the edges of the material.

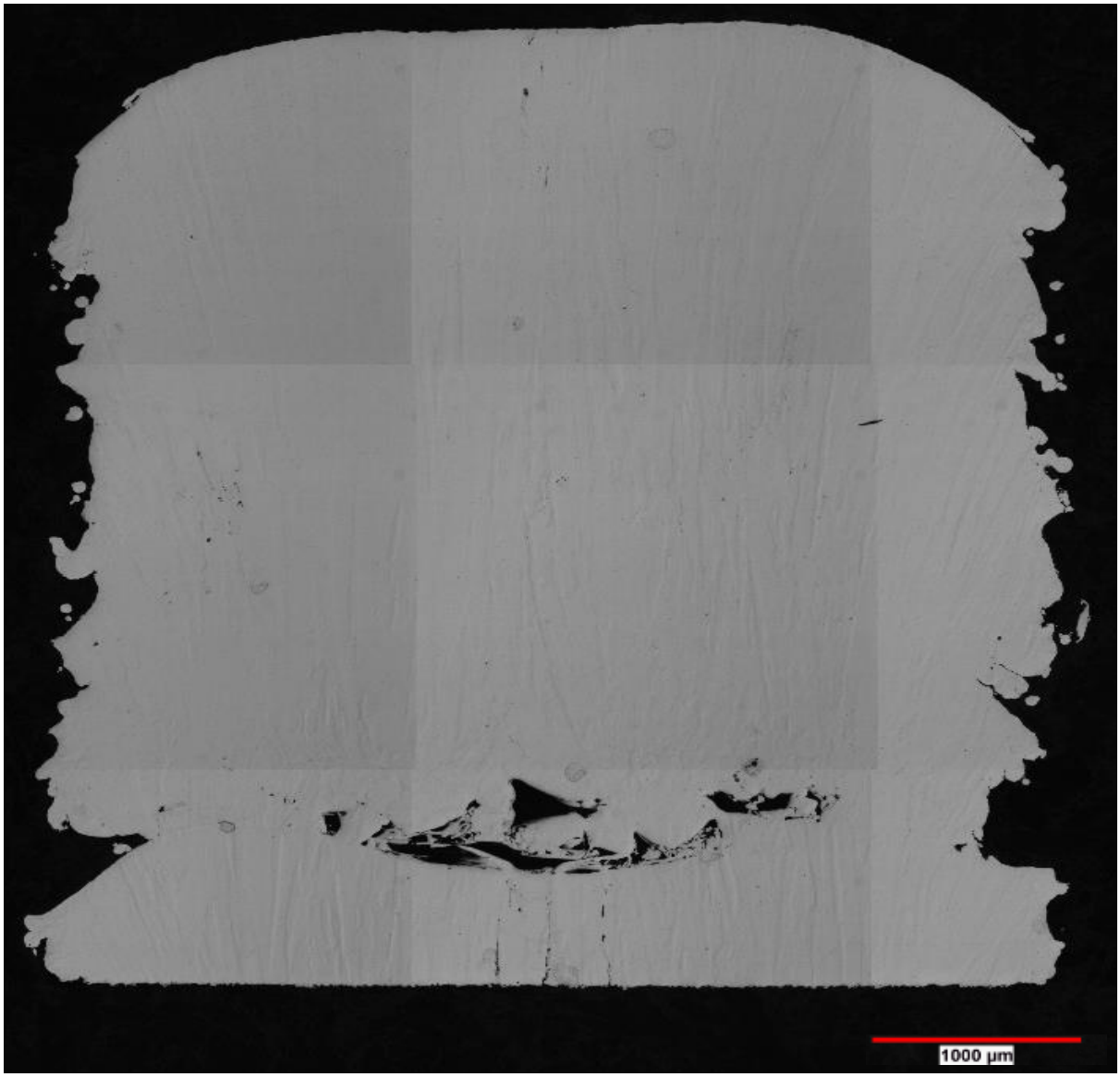

Figure 5.7: Optical micrograph of heated bed sample 9. The inclusion at the bottom of the sample is likely due to swelling at the beginning of the build process.

Other regions of material are visible with vastly different microstructures to those normally encountered in LPBF. Dendrites are observed with much larger arm spacings than normally seen, and carbides have evolved far more because of the slower cooling times. These carbides typically form during solidification, beginning around 1400°C. Because the cooling rate is vastly reduced with the heated bed, carbides have far longer to segregate from the bulk material. Normally in LPBF, the cooling rate is so high that this is not often possible except at the edges of samples. The classic cell structure seen in LPBF material is still present in the microstructure, with carbides also interspersed between them as well. Most noticeable throughout all heated bed samples is the abscence of melt pool structures commonly seen in etched LPBF samples. It is likely that the slower solidification of the alloy coupled with the

effective heat treatment of the alloy will have dissolved this microstructure, however this has not affected the larger layer by layer microstructure, which is still visible in the etched samples (figure 5.9).

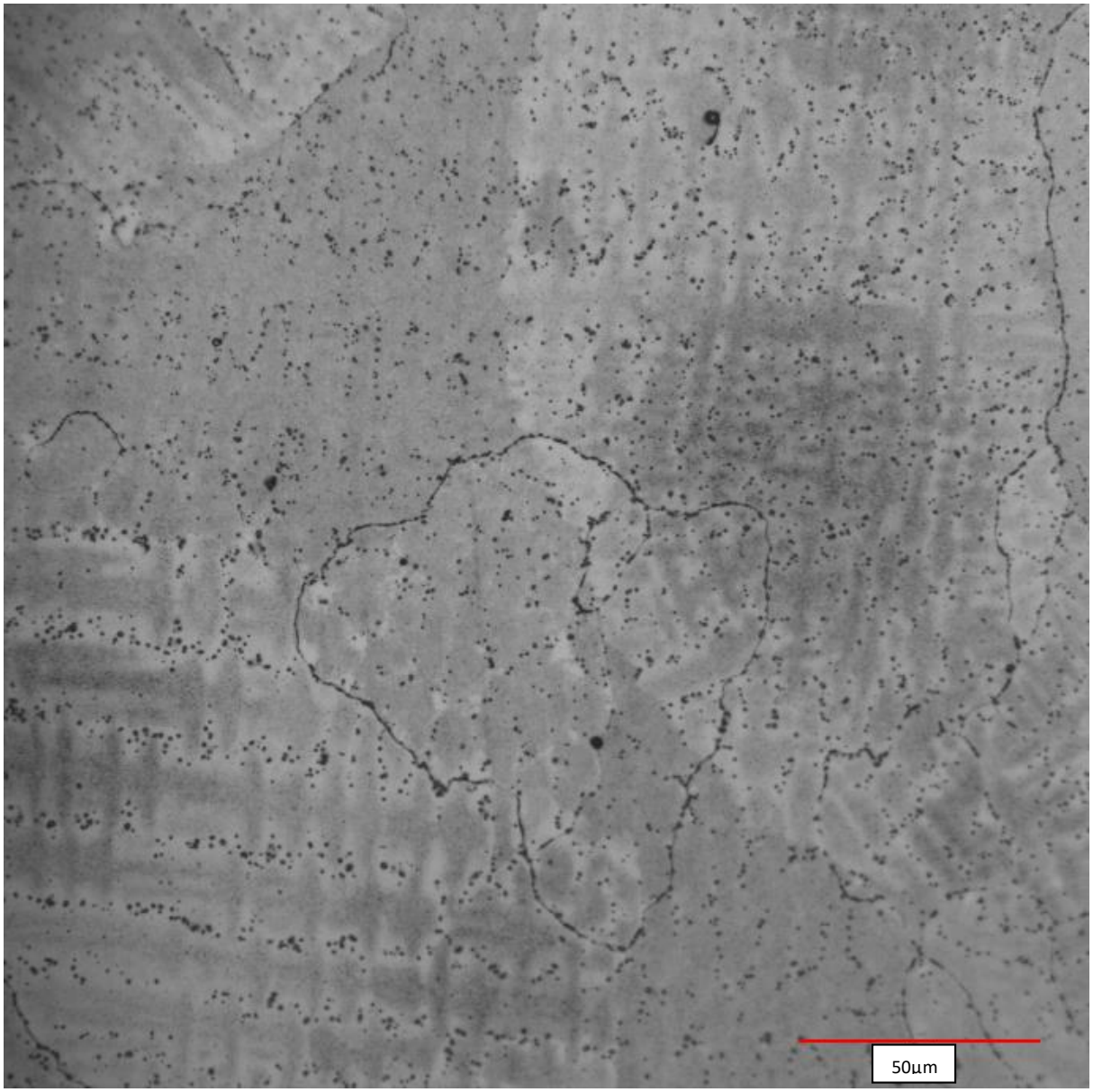

Figure 5.8: Optical micrographs of etched material produced in LPBF in conjunction with the heated bed. More evolved dendritic microstructures are visible as a result of the longer cooling times experienced by the material.

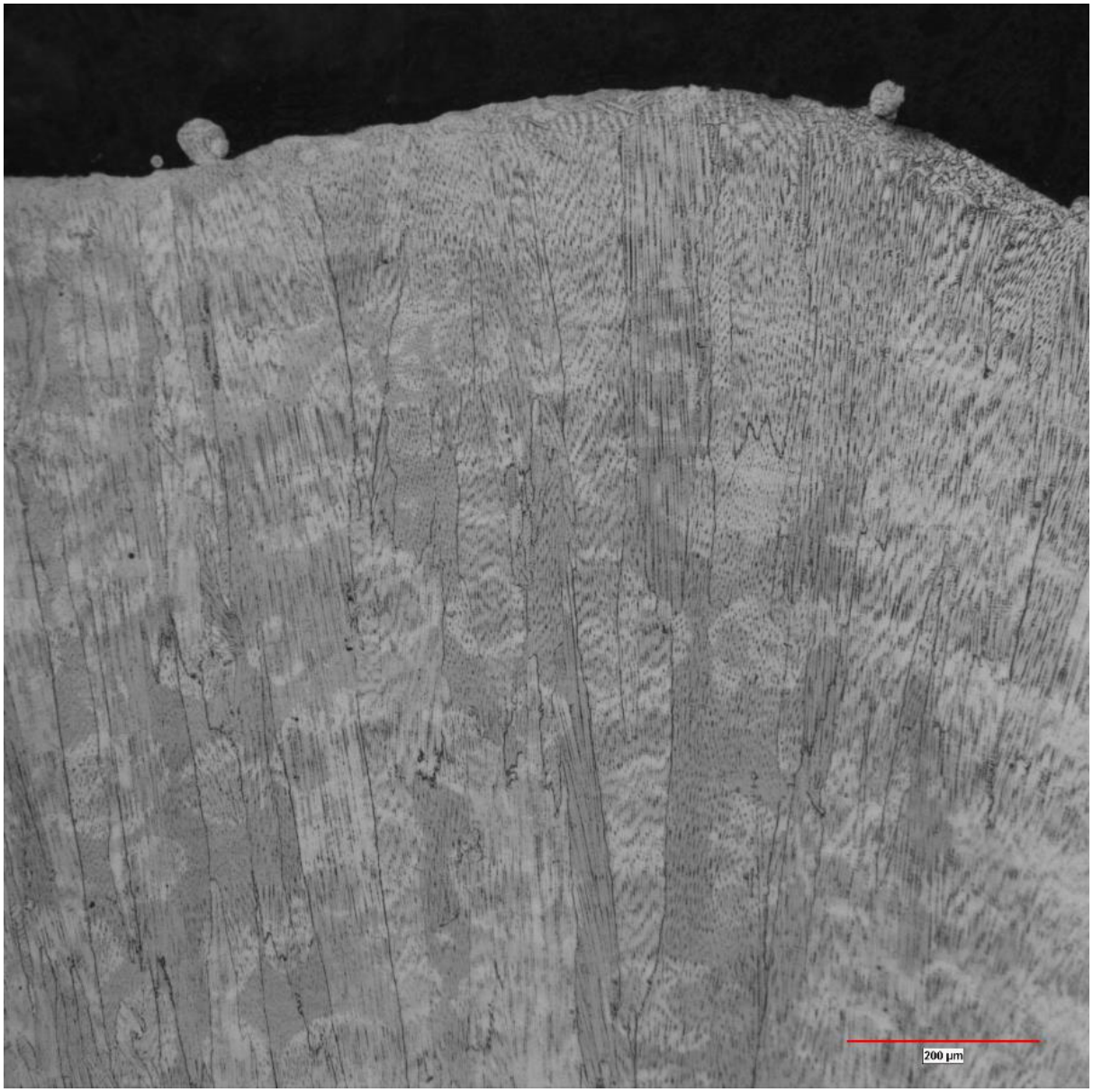

Figure 5.9: Optical micrograph of CM247-LC produced on the heated bed. The layer-by-layer microstructure synonymous with AM components is still visible, despite the absence of visible melt pool shapes.

These samples also exhibit a lack of inter-grain misorientation and thus have a significantly reduced level of cracking. Grains are far larger than in standard LPBF, with some visible columnar grains being several millimetres in length, likely a by-product of the slower cooling rate. Finally, despite these samples being heavily affected by voids (mostly lack of fusion due to poor spreading), there are very few cracks present in the material; the high temperature gradients responsible for hot tearing no longer exist. Couple that with the size of the predicted melt pools and there is a very slow rate of solidification in the material.

Examining the porosity of the samples produced through the reduced power parameter settings, the relationships between input parameters and material outcome can be determined. Figure 5.10 shows the relationships between porosity and normalised energy density.

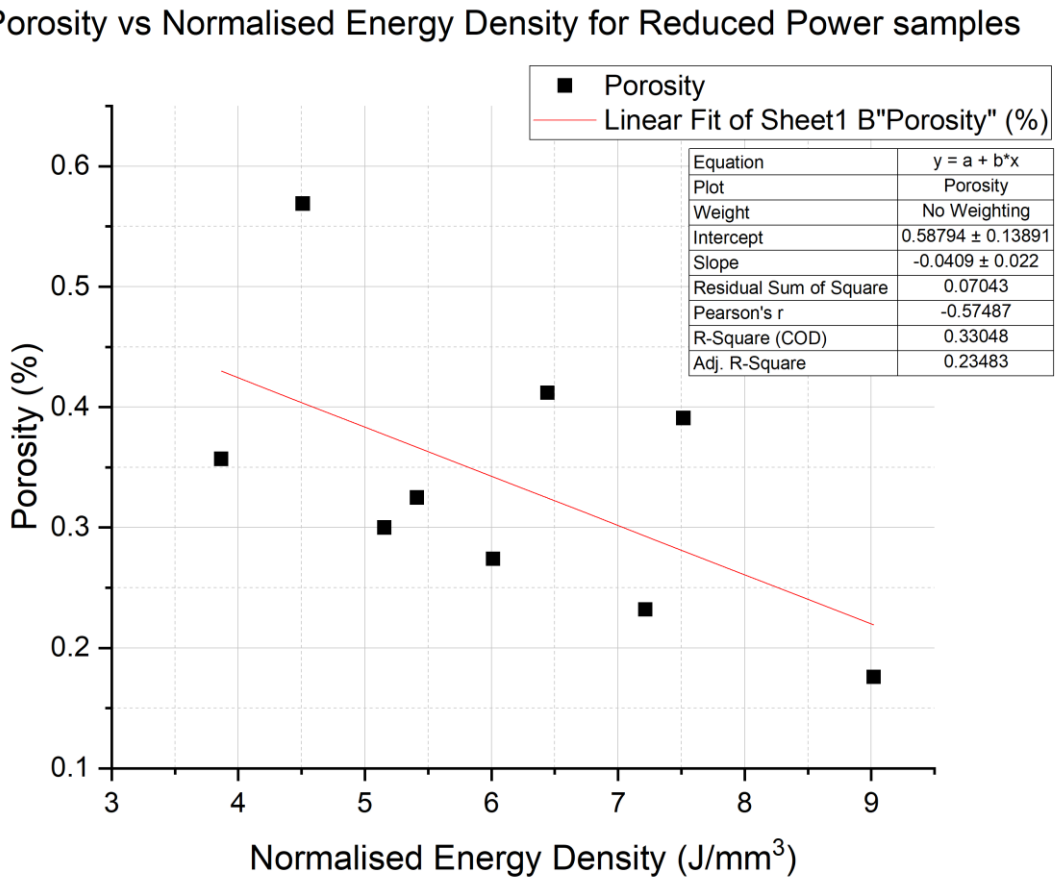

Figure 5.10: The effect of increasing normalised energy density on material porosity.

Even at the lowest level of porosity, cracking is still widespread (figure 5.11). In etched samples, the material is heavily cracked. LoF is also present in the samples.

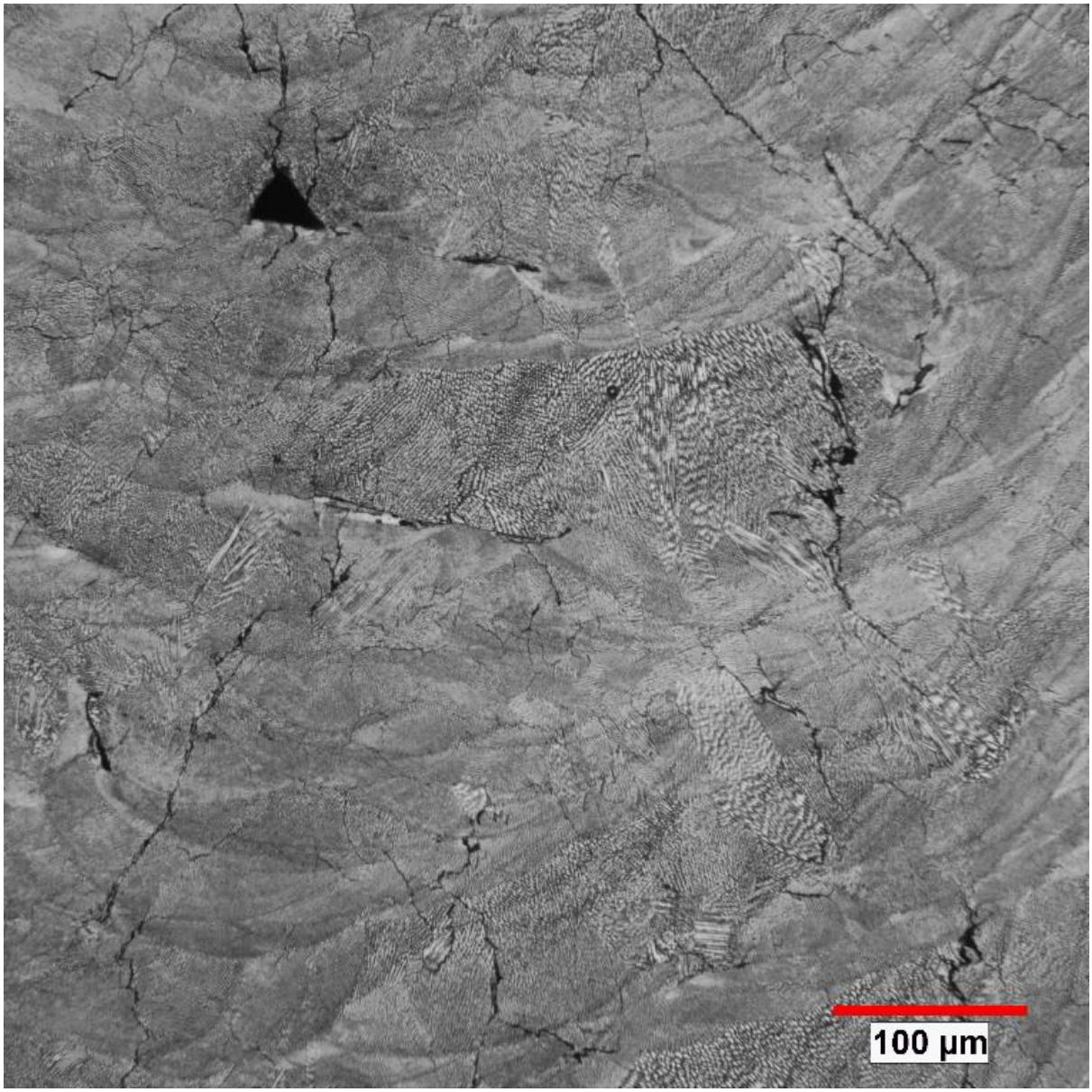

Figure 5.11: Optical Micrograph of reduced power CM247-LC. The presence of cracks running both vertically and horizontally suggests several different cracking mechanisms are at work here.

This pairing of defect types suggests that the energy imparted to the material is insufficient. In CM247-LC, these defects are commonly seen at lower normalised energy densities, often below 2 J/mm^3. If the energy density of these parameters is considered at room temperature, then the energy imparted to the material is around this level, ranging from 1.93-4.51 J/mm^3, which is lower than the "ideal" level of 5.71 J/mm^3.

In comparisons to other literature, Hagedorn et.al demonstrated the use of pre-heated substrates to produce similar refractory carbides in MAR-M-247, however these carbides were formed as a result of in-situ heat treatment after the completion of the build, rather than during it (figure 5.12). Furthermore, this study used a much higher temperature of 1200°C to effectively age-harden the material after the creation of the components.

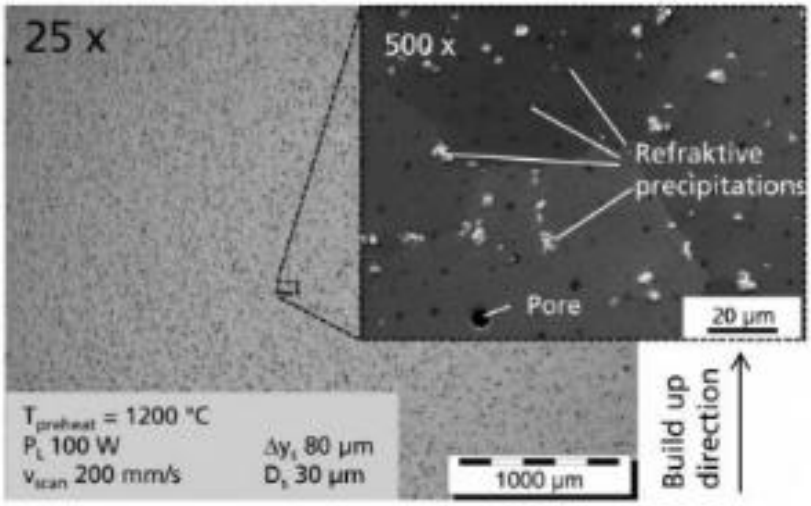

Figure 5.12: Precipitation hardening in MAR-M-247 [171]. *While the carbides are similar in size, the processing route is not comparable to this study.*

The samples' lack of cracking is also surprising, given that CM247-LC's usual response to heat treatment is to crack on cooling. However, many post-processing routes for this alloy involve heating beyond the level required to induce precipitation.

For in-situ heating of the plate, one must often turn to EBM, where the beam's rapid speeds can be used to induce a pre-heating effect to the powder. This differs from the Aconity's heated bed, as it is the powder in the bed itself being heated, rather than the substrate and the subsequent deposition. Lee et.al demonstrate the ability of EBM and part orientation to be capable of controlling the crack susceptibility of the alloy [172]. However, this again involves the use of temperatures in excess of 1000°C, which is far higher than the current study.

5.3.5.2 Hardness Mapping

Comparing hardness values of the samples to those produced in standard operation mode showed a major increase in the material's hardness, in spite of the defects clearly present. Figure 5.13 shows box plots comparing the samples produced with the heated bed to those produced without it. Again, this was done primarily to determine whether the hardness changed as a function of position in the cross-section of the components and to compare how different processing methods and techniques affect properties – in this case, investigating how the heated bed affects hardness.

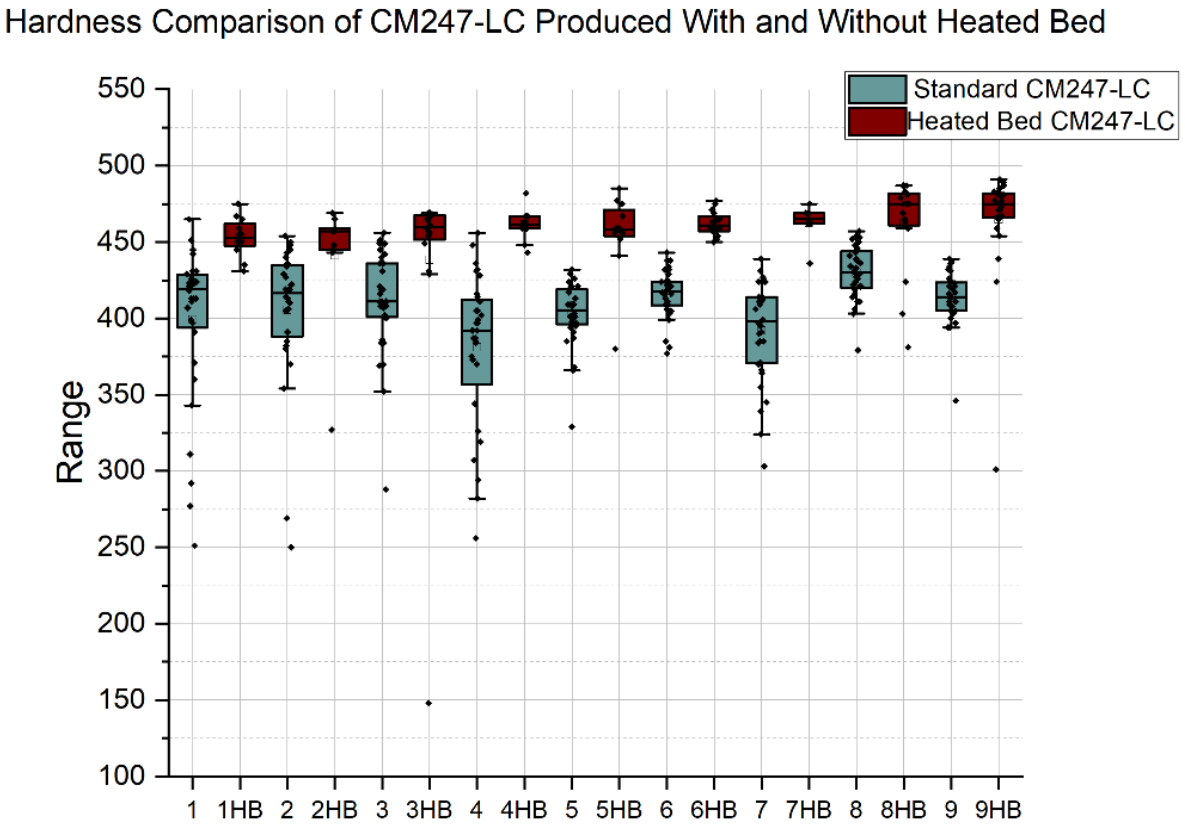

Figure 5.13: Comparison of Hardness values produced by identical parameters both with and without the presence of the pre-heated substrate.

This graph shows the impact on the hardness caused by the heated bed. Both the maximum and average hardnesses of the material have been improved. The spread of the hardness values appears to be lower, however it is worth remembering that most of the heated bed samples were not built as tall and therefore did not have as many hardness indentations.

The sample with the highest hardness is sample 9. This improvement in hardness is certainly a result of age-hardening. In total, the material spent approximately three hours at an elevated temperature both during and after printing. In addition, the impact of the laser on lower layers will have been more pronounced, as this elevated ambient temperature will have resulted in a far lower cooling rate and retention of heat, meaning that the impact of the laser will have been greatly enhanced from a heat treatment perspective.

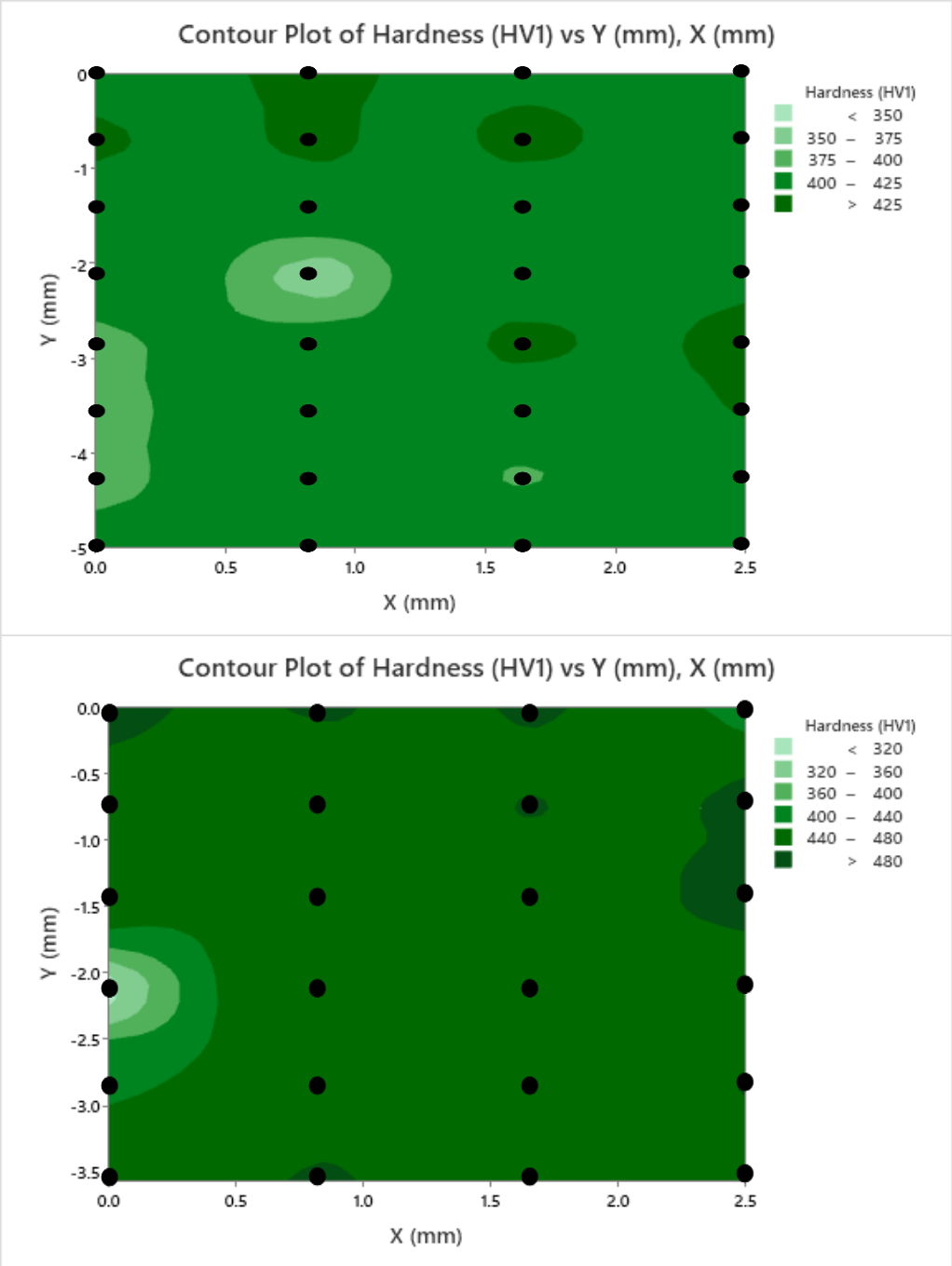

Figure 5.14: Hardness plot of a 5mm cube sample produced without (top) and with (bottom) the heated bed. The presence of the heated bed drastically improves consistency.

However, this seemingly improved material hardness is present in samples that did not build very well. Only two of the samples built in this way successfully built to the full 5mm height. During building, the heat of the substrate caused poorer spreading, as the expansion of the heating element, substrate and the powder together meant that the level of the plate would raise slightly. Many indents have been performed on material that is more evolved through the in-situ heat treatment (figure 5.15), which is widespread throughout the material.

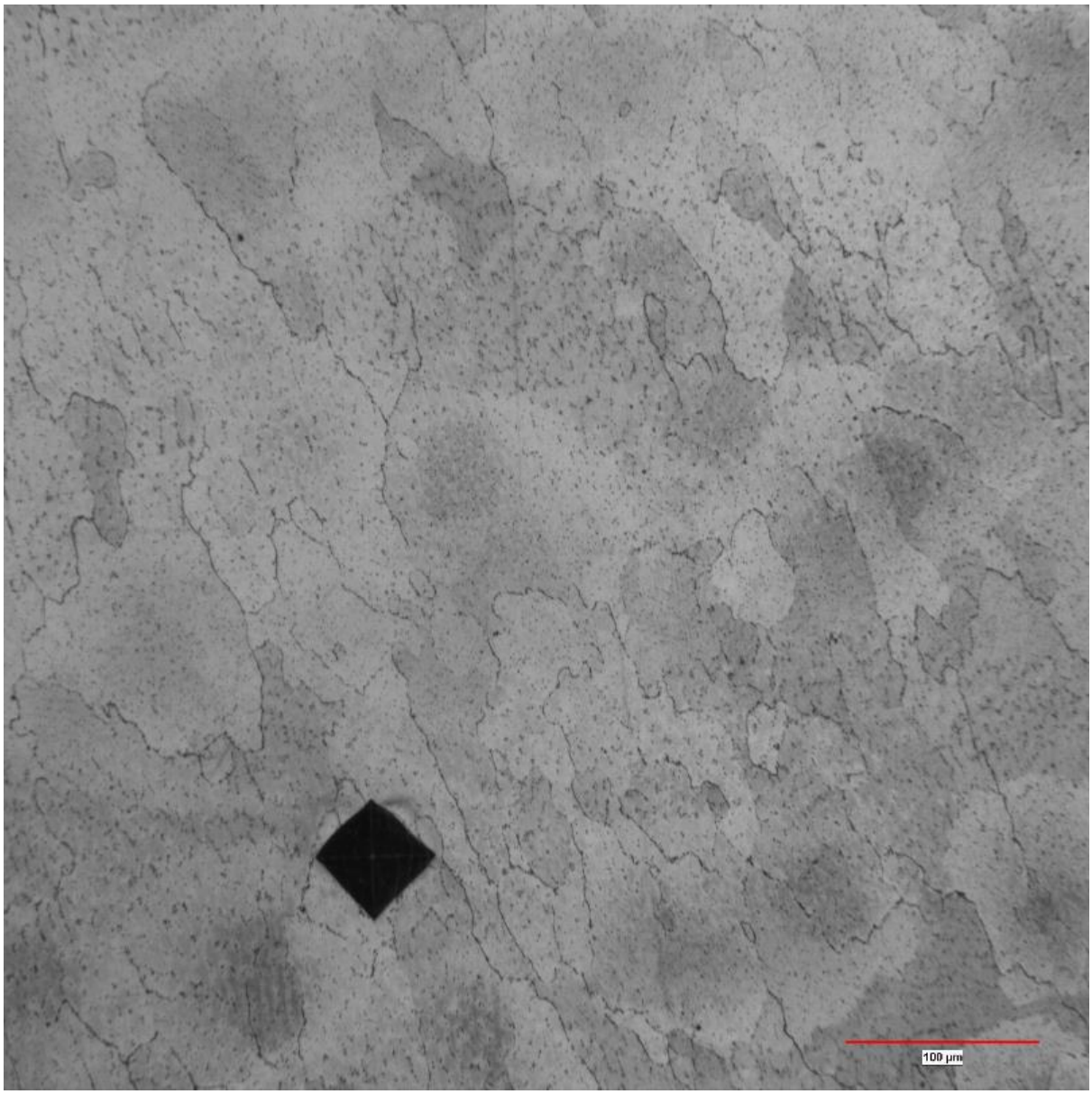

Figure 5.15: Optical micrograph showing a hardness indent in the heated bed CM247-LC alloy. The increased hardness is likely a product of the close-to-equiaxed grain structure visible here.

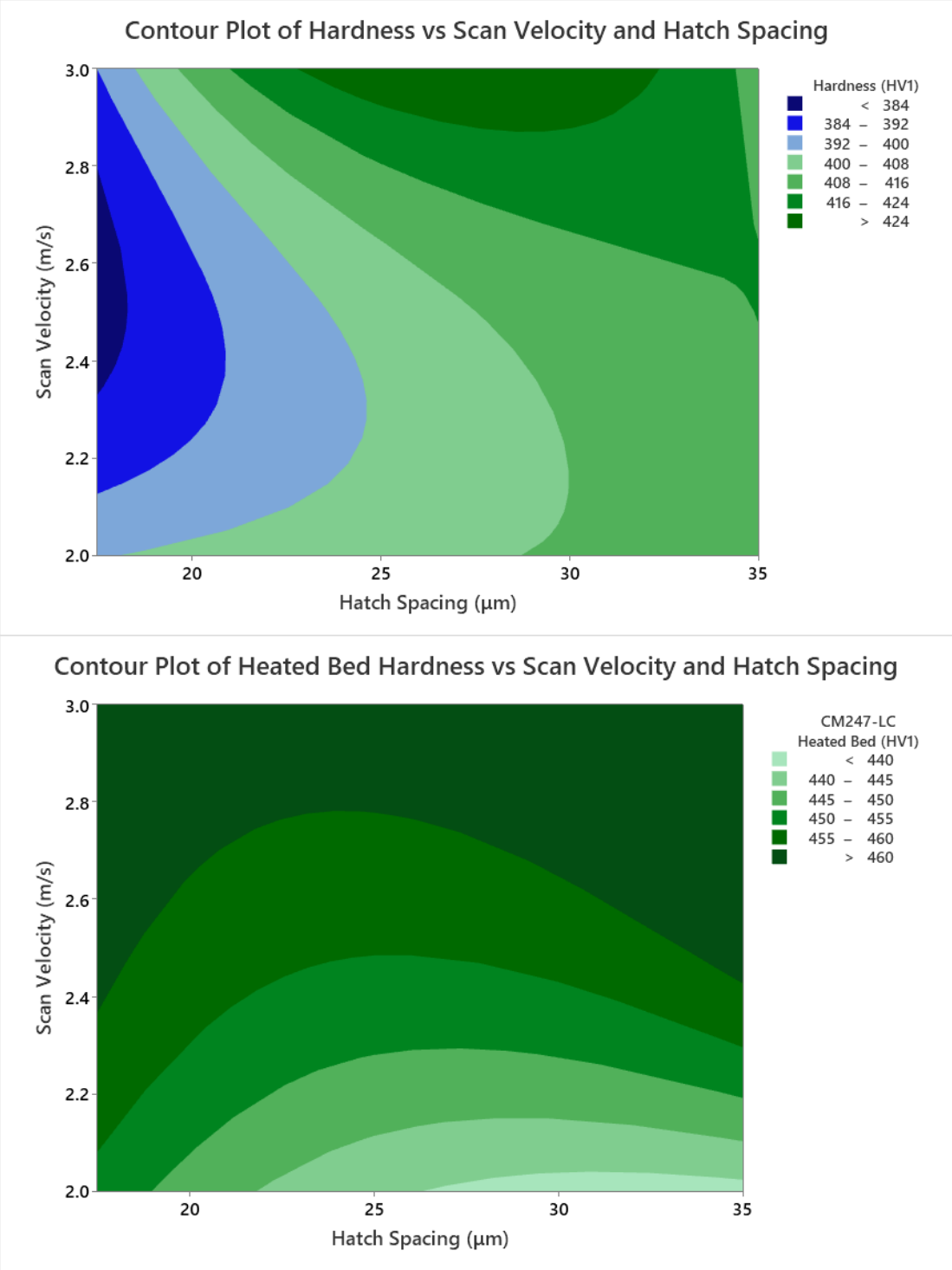

Figure 5.16: The impact on hardness relative to variable processing window of changing the substrate temperature. The room temperature hardness (left) and the elevated temperature hardness (right).

A key part of this study is to examine how the hardness of the material changes with respect to the parameter space under the varying process conditions. Figure 5.16 shows the impact of changing the ambient temperature on the average hardnesses of samples with respect to processing space.

This graph (figure 5.16, right) shows a complete change in the behaviour of the material in this particular processing space and a totally different dependence on hatch spacing. The hardness of the material still drastically improves with extremely high scanning speeds however, suggesting that a more rapid and uniform heating is superior to slower moving melt pools.

Analysis of a taller 10mm tall sample suggests that a hardening effect is occurring throughout the material, even with greater numbers of hardness indents (figure 5.17). This suggests that the material's quality is indeed improved through use of the heated bed for this parameter space.

The taller 10mm high build also contained a far more evolved microstructure (figure 5.17), as opposed to the samples built without the heated bed. Grains are more pronounced and the shape of the melt pools is no longer visible – as with other heated bed samples. In the case of the taller builds, the total heating time from the start to end of the build was approximately 3 hours, with two further hours of cooling under argon. This longer heating time may explain the slight difference between the hardness of the cubes and the taller build – grains may be slightly larger, resulting in softer material (figure 5.19).

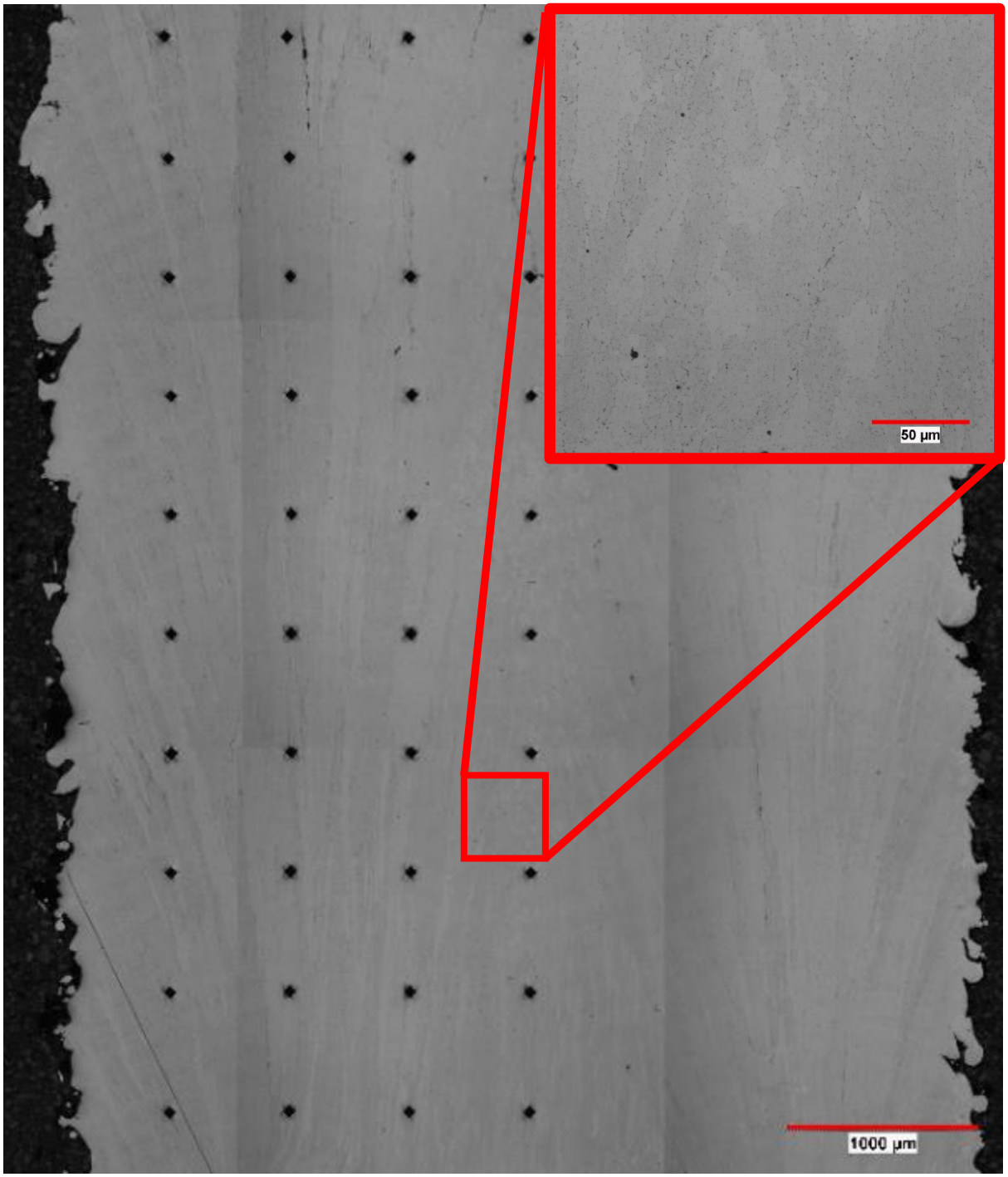

Figure 5.17: Optical micrograph of longer grains produced in the heated bed build (main image). Smaller equiaxed grains are also visible towards the centre of the sample (inset), suggesting a drastically different style of heating.

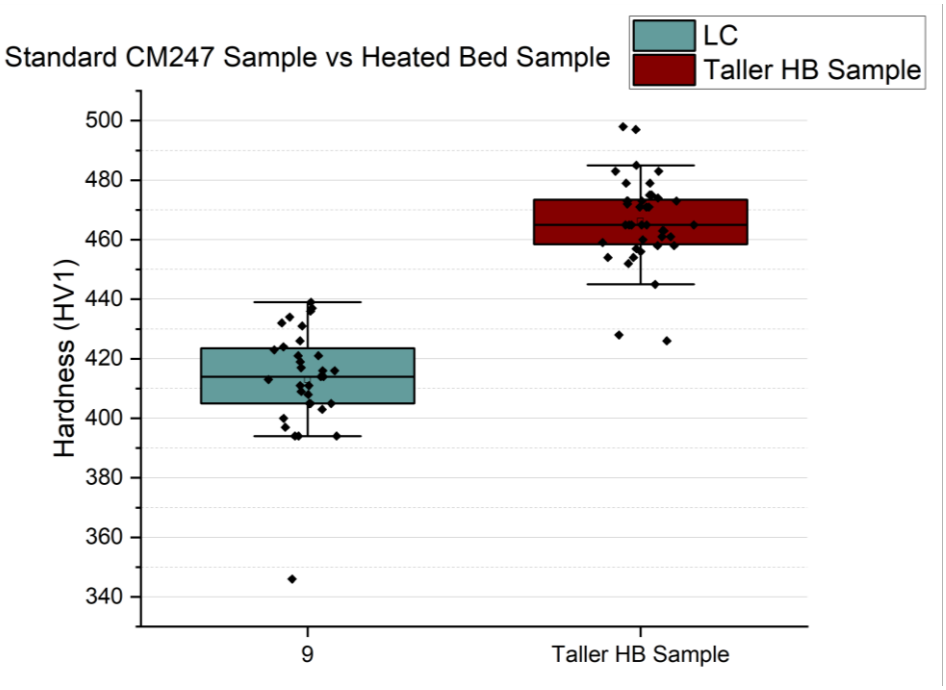

Figure 5.18: Direct comparison of identical sample parameters with and without the heated bed. The taller HB sample built up to 10mm and could therefore have more indents performed to test the consistency of the material.

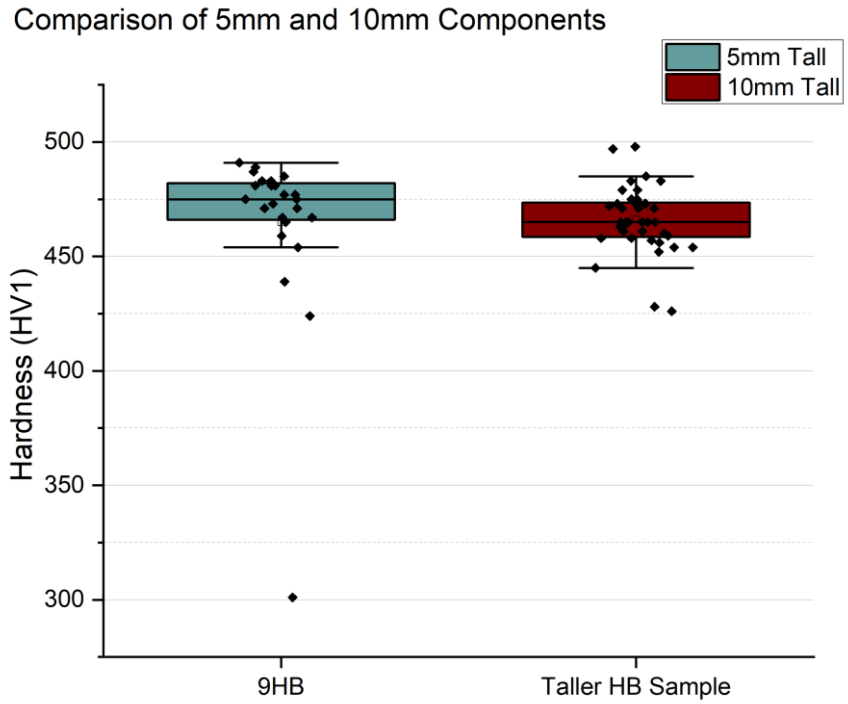

Figure 5.19: The difference in hardness between 5mm and 10mm tall samples. The taller samples underwent a longer in-situ heat treatment time and have much larger grains, suggesting that there may be a "sweet spot" for the heat treatment time.

Samples were produced using the heated bed and reduced laser energy density. These samples used parameters determined by a combination of the melt pool model designed by Freeman [89] and equation 2.6 from Thomas et.al [85]. Figure 5.20 compares these with the ones manufactured with the standard parameters used in chapter 4.

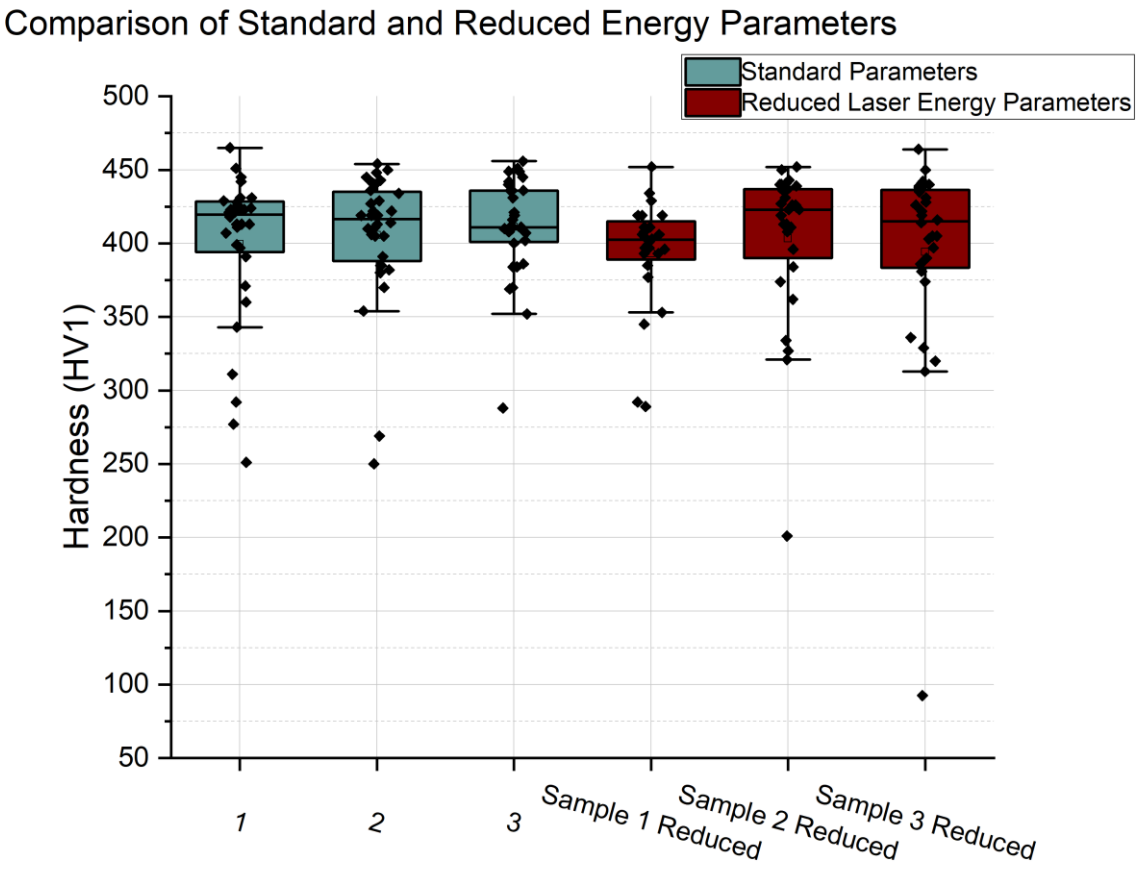

Figure 5.20: A comparison of hardnesses between samples produced by standard high-density parameters from chapter 4 (without the heated bed) and those with identical normalised energy density input created using lower laser powers.

The reduced parameters have not had quite the same impact on the hardness levels of the material. These samples are seemingly more prone to cracking and weakness, with a lower average hardness and greater variation in hardness overall compared to heated bed parameters. The reduced parameter samples produced on the heated bed have strikingly similar properties to those produced with the "ideal parameters" described in chapter 4. This is likely due to the similar normalised energy density input values determined from equation 2.6 that were applied to the Freeman model. A similar set of average and peak hardness values are observed in these samples, suggesting that the use of the pre-heat substrate in conjunction with the normalised energy density equation from M.Thomas et.al [85] can produce similar properties. The range

of hardness in the alloy is slightly increased, but still comparable. However, the alloy manufactured in this fashion remains prone to cracking and defect production, as micrographs demonstrate (figure 5.21). Given that the melt pool microstructure is not visible in the produced material, it is not possible to validate the melt pool model for elevated temperature processing in this instance.

A repeating pattern can be seen in figure 5.21. This pattern repeats every 4 layers of height, due to the rotating scan strategy (45°, + 90° per layer). Because the rotation affects the direction that the cell structure grows, the etched samples change colour depending on the specific scan direction. Every four layers, a lighter band is seen as cells reach a particular orientation relative to the surface. This is repeated every 160µm (on average) throughout the material. Whilst the melt reaches more than 4 layers deep, the increment of heat is still going up by 40µm per layer.

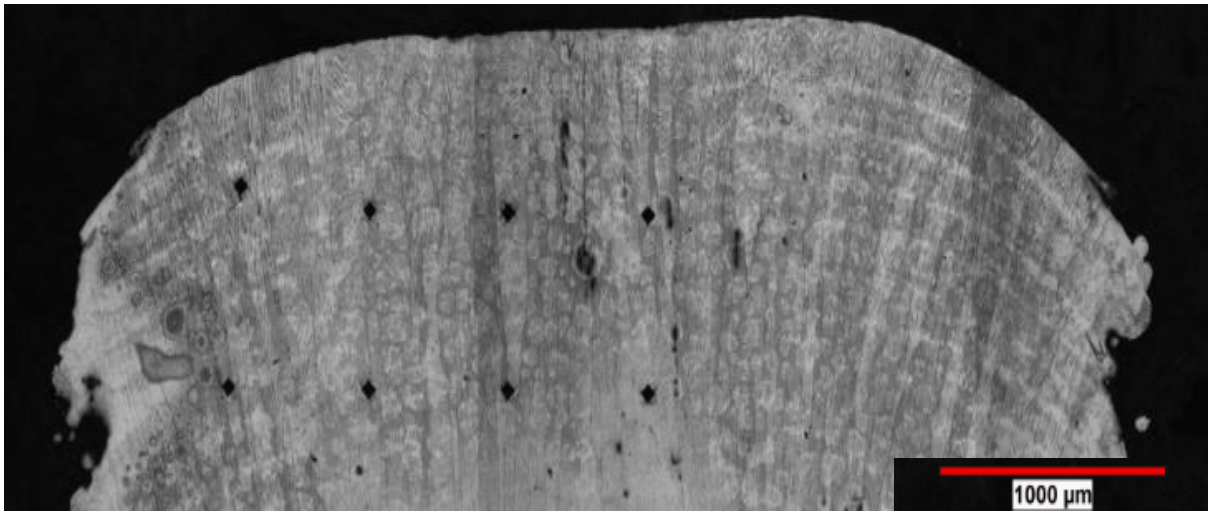

Figure 5.21: Optical micrograph of CM247-LC produced using the heated bed with room temperature parameters. Lighter and darker bands of material can be seen throughout, produced by the growth direction of cells within this microstructure.

Considering the depth of the predicted melt pool (figure 5.2), this is predicted to reach to between 220 and 240µm in depth. This means that the penetration depth of the melt would be 5.5-6 times the layer thickness. Comparing this to the melt pool produced for the same energy at room temperature (with a layer thickness of 20µm) the penetration is only 3 times the layer thickness. This can be seen in figure 5.21, with the top layer ranging approximately 200-240µm, as the final layers have not been re-melted or re-heated, thus the pattern is not repeated in the top layers. This top layer thickness provides some evidence of accuracy in the melt pool model.

5.4 Scaling and Drawbacks

Whilst the result of the heated bed builds are promising and demonstrate that LPBF at elevated ambient temperatures is possible, there are some problems to be solved before this can be adopted by industrial scale systems. The first obstacle relates to scaling itself. Because of the size of components and build chambers that industrial products require to be efficient, the induction heater in its current form will be wholly inadequate. The heating system is designed to rapidly heat a relatively small metal object. In the case of industrial scale printers, their build volumes are many times larger than that of the Aconity Lab's. The larger the build substrate, the greater the amount of energy required to heat it evenly. More coils would be required, but these could also interact with one another, making a multi coil heating system challenging from a design perspective. Higher energy inputs would need to be very carefully controlled to avoid overheating. In the Aconity, the temperature is controlled by a water cooling jacket, but in a larger component, the effect of this at the centre of the plate will be limited, meaning that a far more extreme temperature gradient could be observed than that demonstrated in chapter 5.

Another obstacle is that the heating is directional, meaning that larger components will see a reduced effect from the heating element as one moves further from it. Whilst this is not a problem for the current research-scale activities being performed currently, if this is to become an industry-adopted technology, more even and thorough methods of heating will be required. Furthermore, to allow for the microstructural control available in methods such as DS casting, the temperature must be rapidly controllable throughout the component. A large heat source at one end is not an ideal situation.

Another problem arises from the lack of egress routes for the component upon build completion. Because powder ignites at high temperatures, the build chamber cannot be opened until the interior has cooled sufficiently to mitigate this risk. An internal glove box and airlock is a possible solution, however this is still risky as the object may still be hot enough to glow. Upon contact with the air, any powder still stuck to the component could ignite once it has been removed from the chamber. Because of this limitation, heat treatment techniques such as quenching cannot be performed on components that have been produced through this high-temperature LPBF on the Aconity Lab.

In terms of thermal expansion of components during this process, another problem arises during component manufacture because of the change in height of the powder layer. Linear thermal expansion can be determined through use of the following equation:

$$\Delta L = \alpha_l L \Delta T \qquad \text{(Equation 5.1)}$$

Where L is the length of the object, α_l is the linear coefficient of thermal expansion and T is the change in temperature of an object. However, this is for a linear expansion rather than a volumetric one. The volumetric thermal expansion can be approximated as follows:

$$\alpha_v \approx 3\alpha_l \qquad \text{(Equation 5.2)}$$

When the heated substrate has its temperature raised, the expansion of the substrate and heating element can be estimated using this equation. Because the two are different materials, different coefficients are required. The normal height of these two parts is 20mm. With expansion at 700°C, this becomes 20.33mm – an increase of 330µm. For a process that relies on precision in layer height between 20µm and 40µm, this is a problem. This causes the build plate to become raised above the initial powder bed, requiring further careful adjustments to correct for. Each layer of nickel powder is also susceptible to the effect of expansion. Over the course of several tens of layers, the effect of this begins to become significant, meaning that components built with this system will always suffer from "swelling" during the build.

This can be initially offset by lowering the build volume by this amount and re-dosing, however the powder and the consolidated material will still expand relative to material at room temperature. Every subsequent layer will expand by around 3%. This explains why, after around 50 layers, many of the components were swelling above the powder bed, to the point where the wiper blade was being damaged and powder was not spreading properly. At this height, the extra height added to the deposited material makes it effectively unable to spread powder to the top of the material. This lack of new material then causes the laser to pass over already consolidated material, resulting in further unnecessary heating.

In the case of the pre-heated substrate, it may also be thermal expansion that is responsible for the improvement in material quality. With a standard operation or rescan strategy, the laser heats only a very small region to close to the melting temperature at any one time. Because of this, the material expands and contracts very rapidly and throughout the entire material. The heat of the laser in the top surface also caused both tensile (initially) and compressive (on cooling) stresses to be induced into the material. With the higher ambient temperature from the heated bed, this effect is lessened. Furthermore, when the material is finally allowed to cool to room temperature, the force of its contraction on the internal structure will increase the hardness of the material and may result in a small level of consolidation. This also means that there is likely a recovery effect during the cooling phase, as the material still has energy to relieve some of its internal stresses. This likely explains why the material has not cracked as heavily on fabrication and may explain the seemingly lower frequency of cracks suffered during hardness indentation testing.

5.5 In-Situ Absorptivity Measurements

5.5.1 Premise

Work by J.Trapp et.al [113] suggests using sensors implanted directly into a 3D printing system. A probe, such as a thermocouple, may be used to acquire temperature data directly from conduction from a powder bed melt, rather than as a thermal emission. From this, a temperature change can be recorded as the laser passes close to the thermocouple. By taking into account the material of the powder bed and the laser parameters, it is possible to estimate the absorptivity (A_{eff}) of the material being examined. Beginning with the equation 5.3:

$$A_{eff} = \frac{E_H}{E_L} = \frac{\int_{T_0}^{T_1} mC_p(T)\,dT}{(l/v)P} \qquad \text{(Equation 5.3)}$$

Where E_H is the energy necessary to heat the sample from starting temperature T_0 to final temperature T_1 and E_L is the energy input from the laser. The mass of the disc including powder is denoted by m, P and v are the power and velocity of the laser and l is the length of the laser scan track. $C_p(T)$ is the specific heat of the material at a particular temperature T, given by the following relationship:

$$C_p = C_{p0}(1 + \alpha T) \qquad \text{(Equation 5.4)}$$

Where C_{p0} is the specific thermal heat of a material at 0°C and α is the temperature coefficient of C_p. Expansion of the integral, gives the following equation:

$$A_{eff} = \frac{E_H}{E_L} = \frac{mC_p(T_1 - T_0)}{(l/v)P} \qquad \text{(Equation 5.5)}$$

For simplicity of experiments initially, the l/v term in equation 5.5 is replaced with a value of exposure time, t_e, resulting in equation 5.6:

$$A_{eff} = \frac{E_H}{E_L} = \frac{mC_p(T_1 - T_0)}{t_e P} \qquad \text{(Equation 5.6)}$$

This substitution retains the equivalent dimensional parameters and allows for simpler experiments that only require a short laser pulse rather than a weld track.

5.5.2 Proof of Concept – IN718 Absorptivity Measurements

Taking the Trapp paper as an inspiration, a similar experimental setup was designed for the Aconity Mini system. An alumina refractory stand (figure 5.22) has been obtained to act as a sample mount. This material is ideal as a target, as it should shield the thermocouple from any unwanted thermal effects from the surrounding area, as well as being a non-metallic surface that will not bond to a material that is placed in close proximity during a laser firing.

In order to connect the thermocouple into the Aconity Mini's chamber, a method of allowing a cable into the system without compromising on laser safety or on the inert atmosphere had to be created. The previously described thermocouple array designed for a Renishaw 125 was used (figure 5.4a), as the fittings are standard and can be repurposed (figure 5.4b). In order to reduce complexity, the array was inserted into the chamber by the overflow cavity at the rear of the machine. This does not influence operation, as the amount of powder being used does not require a wiper recoat to take place, thus the overflow system is surplus to requirement.

The other requirement for the system is a powder reservoir made from the same material as the powder. This was designed from the schematic in the Trapp paper, but in this experiment was produced from IN718, rather than 316L stainless steel. This is essential for the absorptivity measurement to be of a single material. These "powder cups" (figure 5.22) were additively manufactured on the Aconity Mini prior to this experimental trial, with supports to allow for a fast production turnaround. This meant that the cups required only an hour to manufacture and remove from the substrate. The cups consist of a 10mm diameter disc of thickness 1mm, with a 0.1mm depth "lip" around the edge to restrain the powder (as in the work by Trapp [115]).

IN718 was chosen for its relative ease in processing (as opposed to other nickel superalloys) and to avoid repeating directly the experiment performed by Trapp.

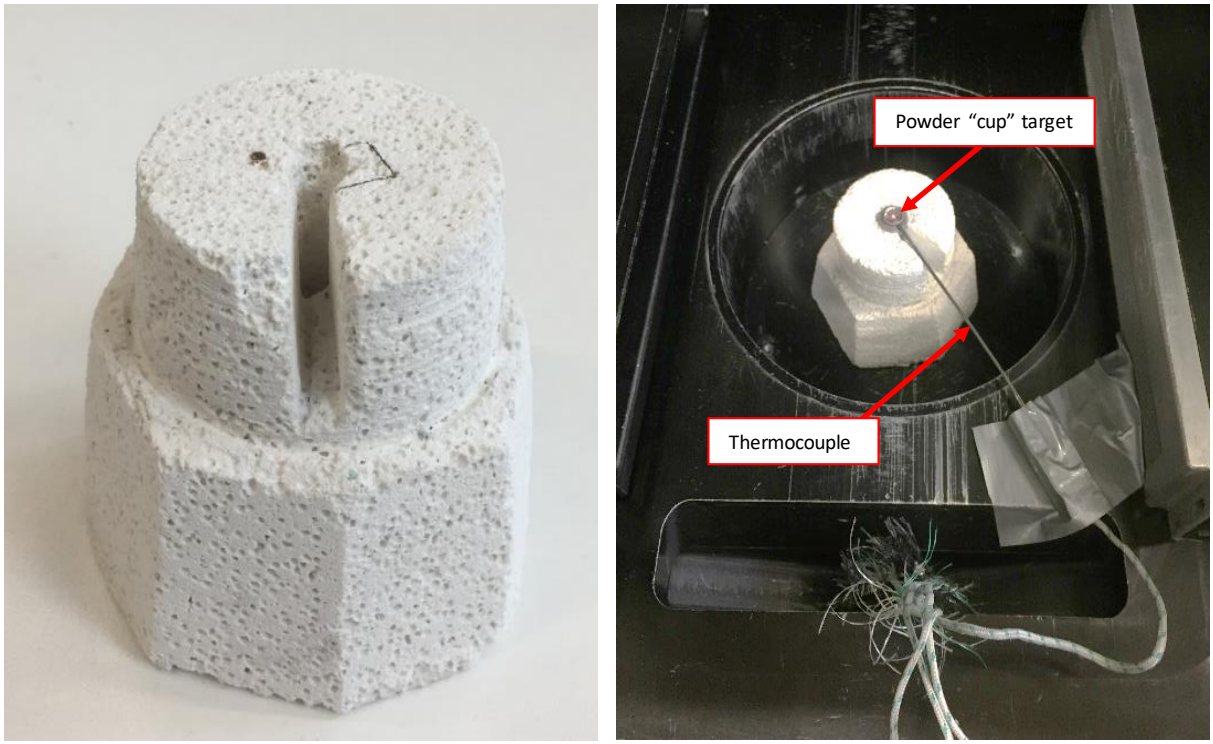

Figure 5.22: a).The alumina stand used to position targets on top of thermocouples. b). The stand in-situ with the target cup inside the Aconity Lab. The stand is placed within the build volume inside the chamber, with the thermocouples fed through the overflow trap.

A standard K-type thermocouple can be connected to the array and connected to the underside of the powder cup. A small amount of powder is then placed into the cup with a spatula, and a razor blade is used to scrape off the excess powder to ensure a flat level. Once the powder sample and thermocouple are both in placed and fixed, the build volume is lowered to bring the powder into the focal plane of the laser. This ensures that the melt pool generated is representative of a real melt pool that would be observed in the LPBF process. Figure 5.23 shows the full final setup of the experimental apparatus.

Once this is complete, the chamber is sealed and the atmosphere is rendered inert. The picologger system is then connected to the thermocouple array, providing a real-time data feed in the picolog software for the temperature at the underside of the powder cup. A short laser pulse of 100W for 0.1 second is delivered to the centre of the cup. This melts the powder present in the cup and causes a temperature rise within the system, as can be seen in figure 5.24.

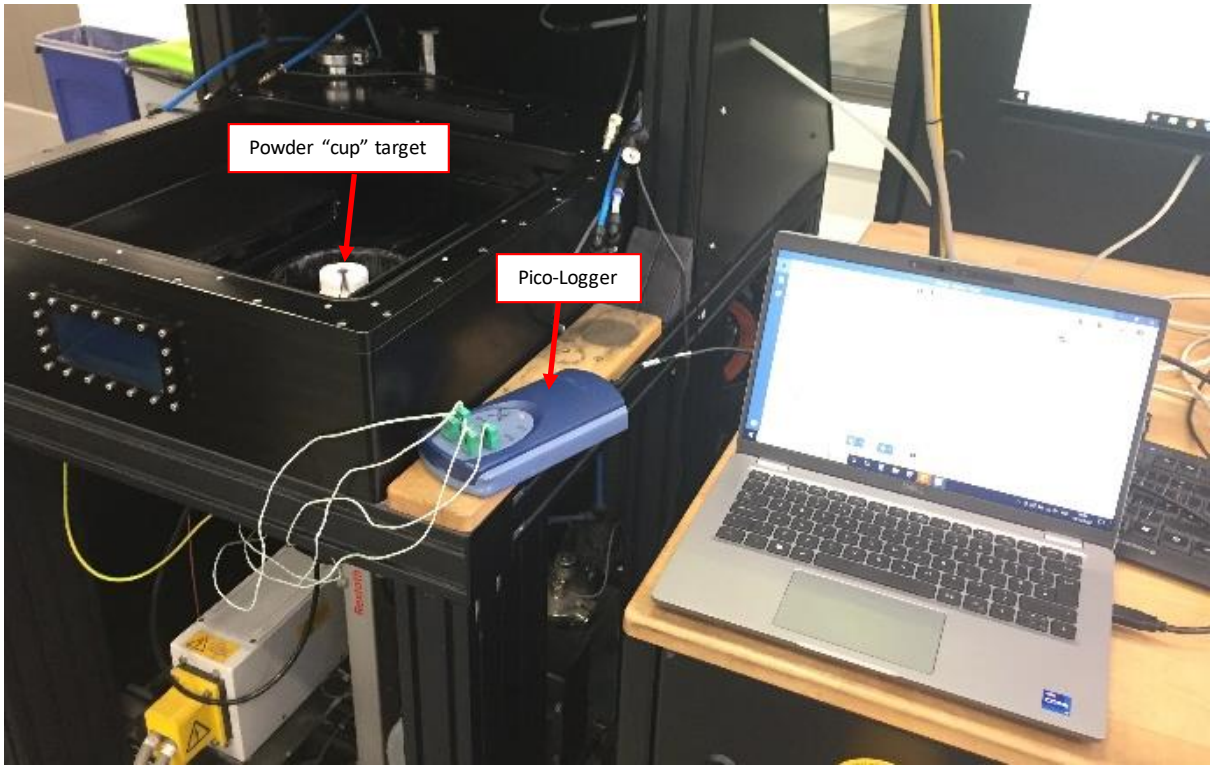

Figure 5.23: The final setup of the thermocouple array system to provide data from the Aconity system. The thermocouple leads to a picologger, which stores data on the PC.

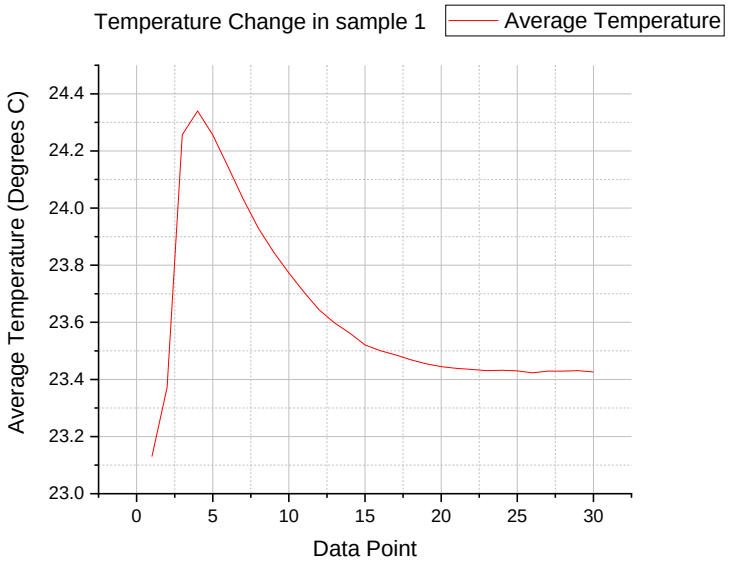

Figure 5.24: Temperature change detected at the thermocouple. This low-resolution initial test was recorded at 1Hz, meaning that each data point represents one second of time passing.

This was repeated several times. The number of functional powder cups that were produced limited the number of repetitions. In this case, four were available in total, with the curves of each test shown in figure 5.25.

This curve is generated by plotting each of the data files produced in OriginPro. The change in temperature can be determined from these data sets and used in equation 5.6 to provide an estimated value for Absorptivity. Once a temperature change has been determined, the absorptivity can be estimated by using equation 5.6. In the instances shown above in figure 5.25, the absorptivity estimated from each is summarised in table 5.3.

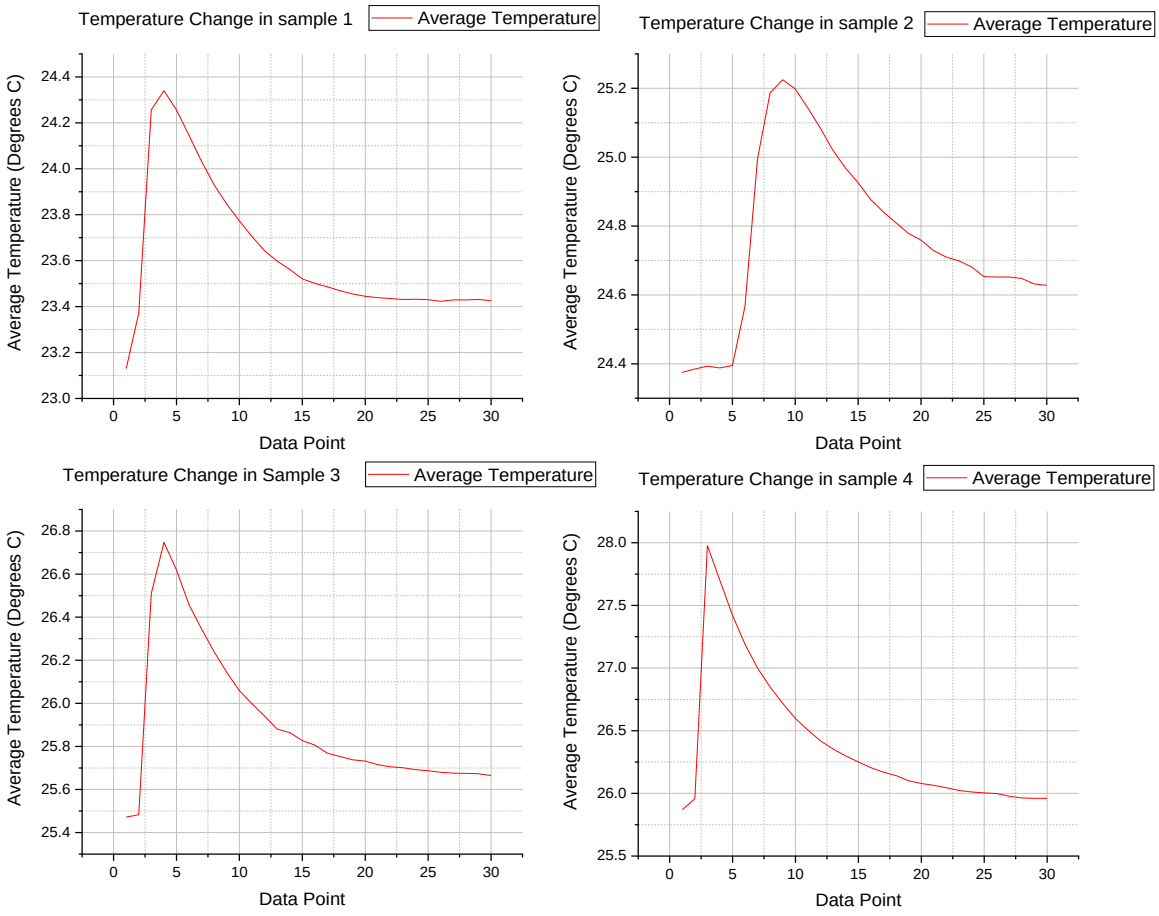

Figure 5.25: Temperature changes recorded for four different powder cups. The baseline temperature increases with each subsequent measurement, which is caused by handling of the thermocouple between each experiment.

Table 5.3: Calculated absorptivity values for IN718 produced by data acquired in this study.

Trace Number	Estimated Absorptivity
1	0.206
2	0.145
3	0.204
4	0.358

5.5.3 Experimental Procedure and Results – CM247-LC

With a proof-of-concept completed for the in-situ measurements, CM247-LC was used instead of IN718 to provide a more relevant data set for this study. Cups were manufactured from CM247-LC to provide a larger sample size. Laser power and dwell time was varied with each laser exposure to provide a wider range of data points and to reveal further trends in the data. The parameters used for these components was identical to those used by Trapp[113] in order to provide a more accurate comparison between materials.

Initially, the effect of varying power and dwell time was used to examine the change in absorptivity. Table 5.4 details the initial parameters chosen for this experiment. The observed temperature changes for the CM247-LC targets are shown in figure 5.26.

Table 5.4: Parameters used in the initial CM247-LC target study. High dwell times often resulted in unreliable results due to laser boring.

Sample Number	Laser Power (W)	Dwell Time (ms)	Target Mass (g)
1	50	100	0.4
2	50	500	0.5
3	50	50	0.5
4	100	100	0.5
5	100	500	0.4
6	100	50	0.6
7	150	100	0.5
8	150	500	0.5
9	150	50	0.5

Because of the tendency of these higher energy laser pulses to penetrate the target cups, further experiments used shorter exposure times. Samples 5 and 8 suffered significant laser incidence due to the high energy density used during their tests. Because of this, they are discounted from further analysis, as they are not representative, nor reliable for absorptivity measurements.

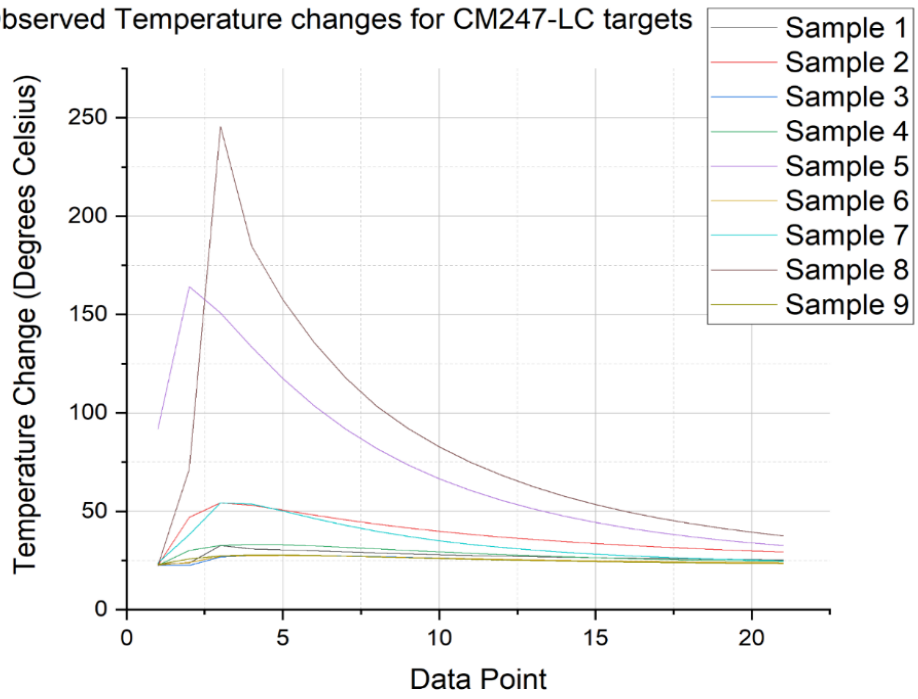

Figure 5.26: Observed temperature changes from initial experiments with CM247-LC targets. Samples 5 and 8 show extremely high temperatures due to laser incidence on the thermocouple after boring through the target.

By extracting values for the temperature change from the data traces, equation 5.6 was used to calculate the absorptivity values for each of the targets. These are shown below in table 5.5:

Table 5.5: Effective Absorptivity values for stationary beam CM247-LC targets.

Sample Number	Effective Absorptivity
1	0.32
2	0.27
3	0.44
4	0.23
5	0.48
6	0.25
7	0.43
8	0.64
9	0.14

These absorptivity values were then plotted against the values of input energy determined by the power input and the exposure time (figure 5.27).

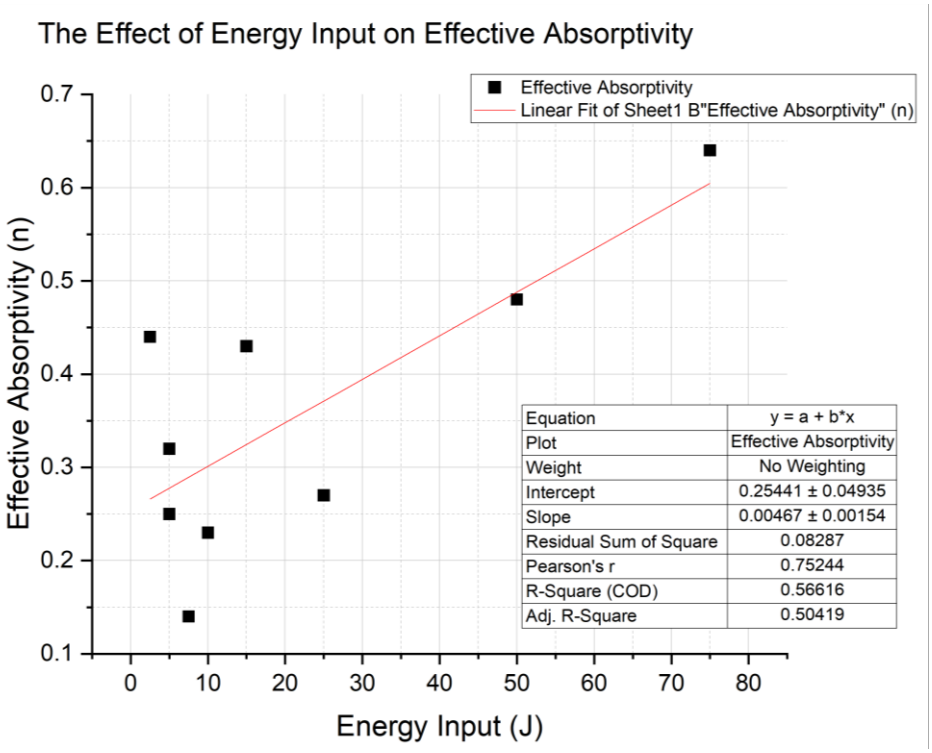

Figure 5.27: The effect of increasing energy input on the absorptivity of the material for a stationary beam.

In order to provide a direct comparison with the work performed by Trapp et.al, further tests were performed using track welds across the target plates. In this instance, absorptivity was calculated using equation 5.5. To provide a more direct comparison, the same parameters used by Trapp were investigated for CM247-LC. This included line scans at 100, 500 and 1500mm/s with powers ranging from 50 to 390W. The results of this for a target with powder are shown below in figure 5.28:

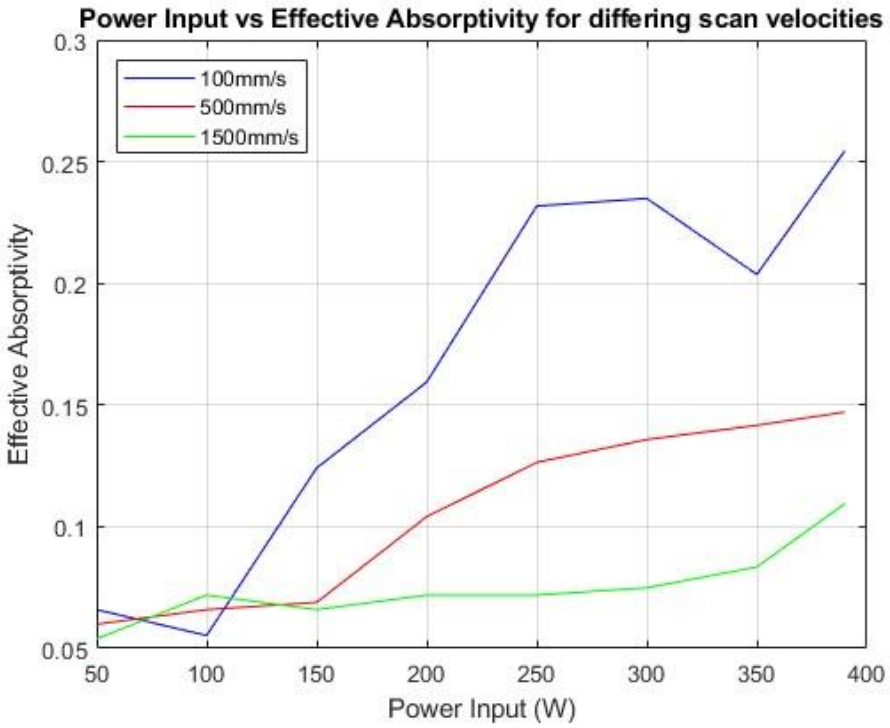

Figure 5.28: The effect of laser power and scan velocity on the absorptivity of CM247-LC. As a general trend, the more energy imparted, the greater the effective absorptivity of the target material.

Having a moving beam provides a more accurate representation of the LPBF process and is much less likely to result in the laser boring straight through the target material, due to the greater volume of material that the energy is dispersed into. This graph shows that absorptivity changes significantly depending on the chosen parameters of the laser.

An examination of the effect of the powder layer was also included by doing a series of varying power laser tracks at 100mm/s, without powder layers present (figure 5.29).

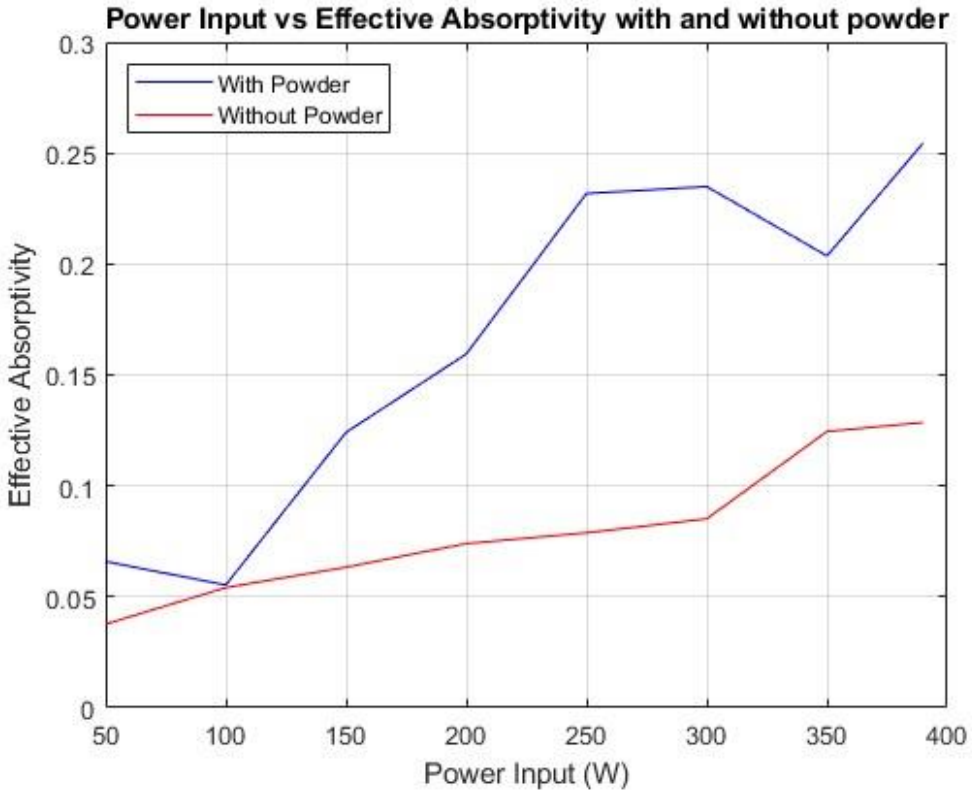

Figure 5.29: How the presence of powder affects the absorptivity measurement recorded.

Plotting the energy input of the three data sets from figure 5.29 provides an insight into the effect of scan velocity on the absorptivity of CM247-LC. Figure 5.30 shows a graph of energy input against the measured effective absorptivity. The general trend for each data set (and indeed all data points collated) is that the effective absorptivity increases with the energy input.

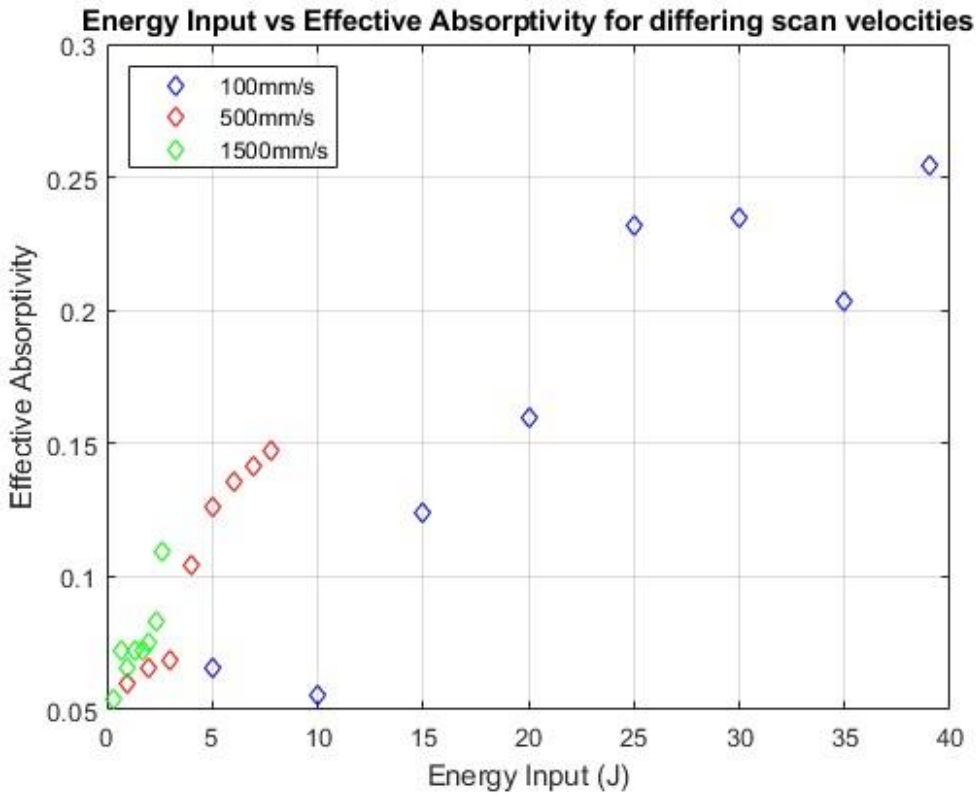

Figure 5.30: How overall laser energy input affects the effective absorptivity.

For each of the three data sets shown, there is a clear correlation between energy input and absorptivity. However, the effect of scan velocity appears to be more of a "scaling" factor. Each data set begins with a very low absorptivity before ramping up as the power increases. Each curve then begins to plateau, similar to a cumulative frequency graph. What this suggests is that there is a critical threshold of energy input where energy is absorbed more effectively – likely when the material passes through its solidus and begins to undergo phase transformations.

This phenomenon of increasing absorptivity as the material melts also helps to demonstrate why part rescanning is not likely to work for CM247-LC. As explained in section 5.2 the laser rescan must not melt the target material. However, as shown by this study and others (Trapp, Sainte-Catherine), a lack of powder produces a far lower absorptivity in the material than if powder is present. This means that in order to have an effect on the material, enough energy must be supplied to begin some form of phase transformation, thus making the process of rescanning largely ineffective.

5.5.4 Comparison to Similar Studies

Trapp et.al use SS316L in a similar experimental setup to perform their experiments. Figure 5.31 shows a side-by-side comparison of the absorptivity values obtained in their study and this one.

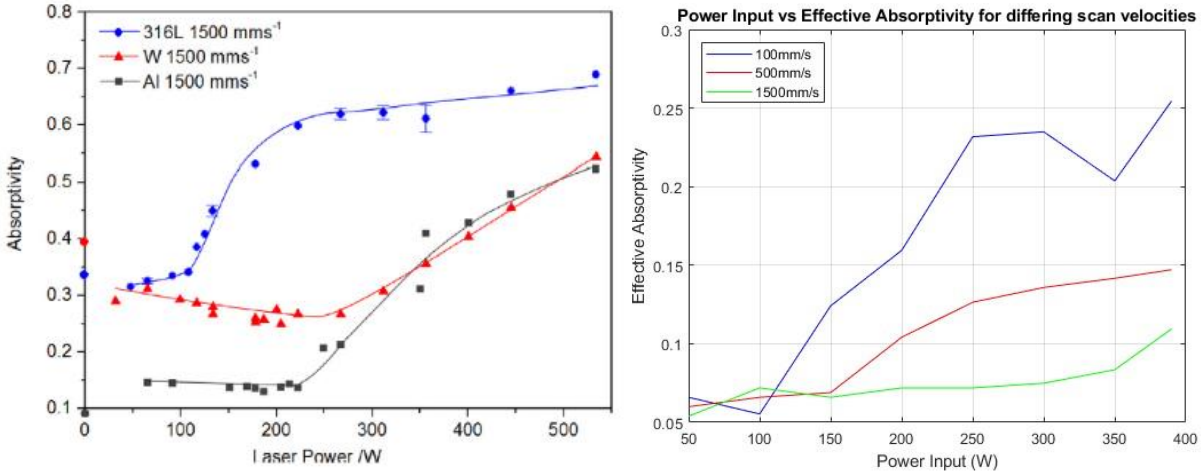

Figure 5.31: Comparing the two sets of curves, some similar trends can be seen, such as an increase in absorptivity after 100W. Values are different, but this is likely due to the nature of the specific equipment, powder and targets used [113].

Similar trends between studies are also observed in experiments examining the difference between powder and non-powder laser scans (figure 5.32).

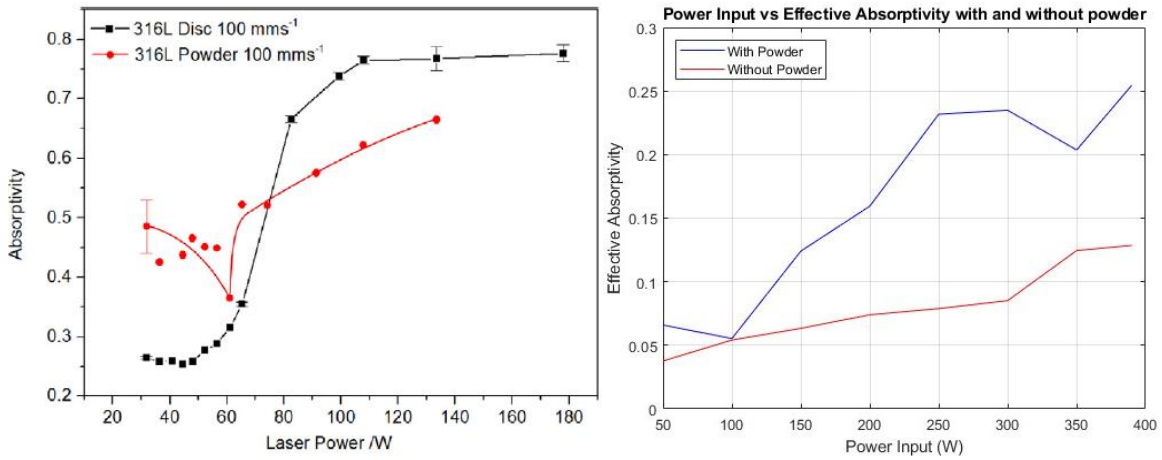

Figure 5.32: Similar trends are seen in comparisons of scans performed with and without powder present. The work by Trapp [113] *(left) shows a dip at around 60W with powder, however this may not have been noticeable in this study (right) due to the increments of power used.*

Another study performed by Sainte-Catherine et.al (figure 5.33) [173] demonstrates the measurement of absorptivity using a Nd:YAG laser of a very similar wavelength to that used on the Aconity systems. This study also utilises IN718 as a target material for absorptivity calculations. Comparing this results of this piece of work and the one by Sainte-Catherine shows similar results to the stationary beam work, with absorptivity rapidly increasing until a tipping point is reached and the laser bores straight through the material.

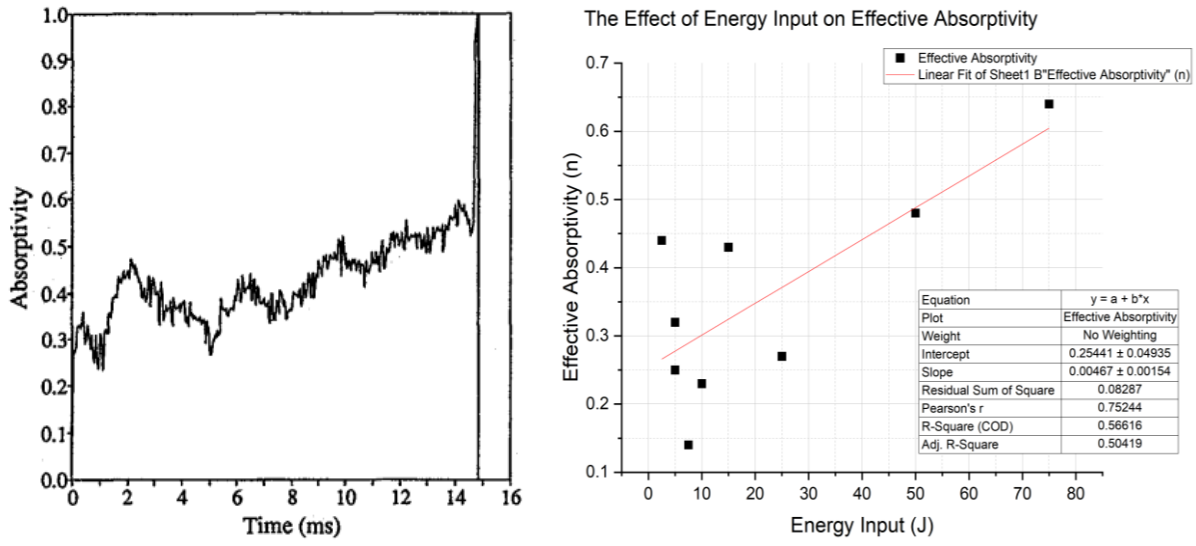

Figure 5.33: Work by Sainte-Catherine et.al [173] *(left) and this study (right) on stationary beam absorptivity. Whilst longer times were used for this study, the work by Sainte-Catherine utilises higher power levels. Furthermore, while the x-axis utilises different units, they are largely interchangeable, as the energy is a function of both dwell time and energy.*

The impact of this tipping point phenomenon could be seen in samples 5 and 8, with absorptivity at 0.48 and 0.64 respectively. The effect of this can be seen in figure 5.33, where the temperatures of these two samples spikes much higher than other samples. Whilst neither of the samples were fully melted, they did result in a light bonding of the target to the thermocouple.

5.5.5 The Impact of Changing Absorptivity

This series of experiments also suggests that expected absorptivity for the material in-situ is significantly lower than expected. With a peak of around 0.28 for absorptivity (at a very high energy density input), the realistic absorptivity of the material in-situ and in a realistic environment is likely to be far lower. Examining the data obtained from a "representative" track speed of 1500mm/s, values do not exceed around 0.07 unless a significant amount of power is used to offset the reduction in energy density. This is further supported by graph 5.30, which shows all of the points taken and highlights the importance of scan speed. It also has a major impact on the melt pool modelling shown in section 5.2, as absorptivity is taken into account when determining the shape of the melt pool, as shown in figure 5.34.

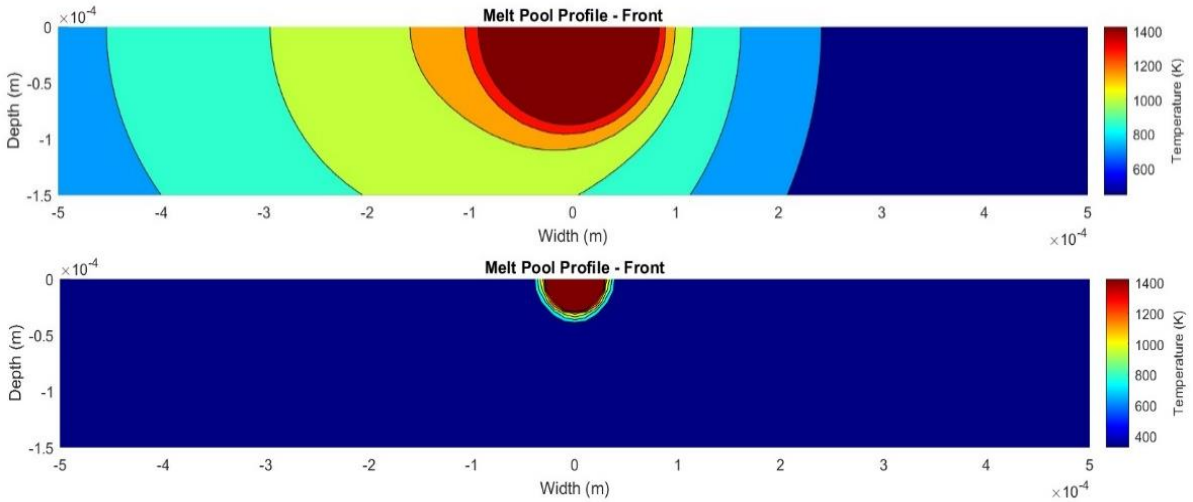

Figure 5.34: The impact of changing absorptivity on the size of a modelled melt pool. The top image utilises a scan speed of 100mm/s and a power of 150W, with an absorptivity of 0.5. The bottom image uses the same parameters but uses a measured absorptivity value of 0.125.

At absorptivity values <0.1, the melt pool model begins to break down, suggesting that the use of this model at the beginning of this chapter to predict suitable parameters was likely inaccurate. By changing the thickness of the layer of powder held by these target components, it may also be possible to simulate how absorptivity changes when building components that contain overhanging geometries. Ultimately, the similarities observed between this work and two other studies demonstrates that this method is capable of producing valid data, despite its simplicity. Furthermore, the use of targets produced by LPBF from CM247-LC for the absorptivity analysis of CM247-LC is also highly novel, potentially demonstrating a method for material characterisation for further understanding of powder-based processes.

5.6 In-Situ Thermal Imaging

5.6.1 Premise

While the pyrometers mounted to the Aconity Mini are capable of collecting vast quantities of thermal emission data, they are limited by several factors. Firstly, their field of view is very narrow. While this is desirable for determining the physics of very small phenomena such as melt pools, it is not a suitable method for examining an area the size of a build substrate. Secondly, the pyrometers collect data snapshots from an area as the laser beam moves, with each sample being an average value over an area. Unfortunately, the spot size is significantly (10x+) larger than the size of the melt pool. This means that the average temperature is often far cooler than the melt pool itself, so a lot of information is lost.

Work done by N.Boone et.al. [14] with a high-speed thermal imaging camera on an Arcam A2 system has shown that it is possible to correlate thermal data with defects that are generated in components produced by AM processes. However, this was performed on an older EBM system rather than an LPBF printer. The same camera used for the work performed by Boone et.al. was removed from the Arcam A2, due to retirement of the SLM equipment. The Aconity Lab was then fitted with this camera using the top window port next to the laser sheath. In collaboration with members of EEE at the University of Sheffield, a series of modifications to the Aconity Lab were performed (figure 5.35).

Firstly, a boroscope was designed for the system to provide a better angle of observation, as well as allowing optics to be installed. Due to the relatively small chamber however, a second modification had to be performed to raise the chamber lid by 50mm, in order for the boroscope housing to fit into the chamber without the wiper rake crashing into it. This is visible in figure 5.35 as the spacer/raiser beneath the lid of the Aconity.

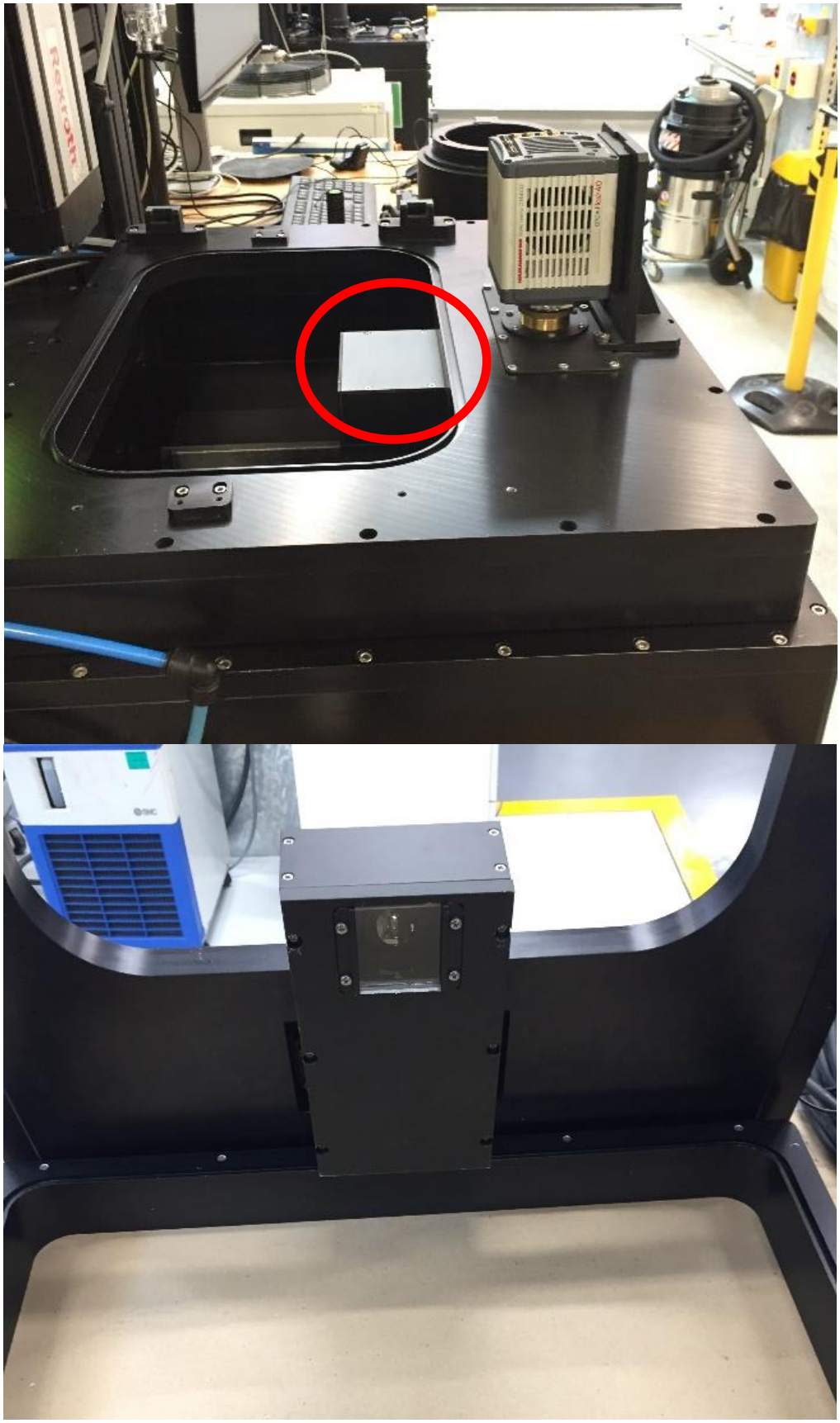

Figure 5.35: The Aconity thermal camera mount (top) and boroscope (bottom). This design allows for a better view of the pre-heated substrate's build volume.

5.6.2 Experimental Work

As part of a set of experiments to calibrate the thermal camera, a series of small tiles were produced in conjunction with the induction-heated substrate. One of the materials chosen to manufacture these tiles from was CM247-LC. Taking the work performed previously by Stanger et.al. - using high-speed imaging to monitor solidifying material in-situ in a Renishaw 125 - as a starting point, a similar experiment was devised to examine the effect of the heated substrate on the cooling rate of the material, also in-situ. The data this would provide would effectively inform as to the cooling rate of the bulk material in a more "representative" scenario.

To examine this, six 10mmx20mm tiles made from CM247-LC were manufactured and observed in-situ using the thermal camera. The temperature of the heated substrate was kept at room temperature for several millimetres of build height, in order to provide a representative material base for the cooling rate observation experiments. Once a suitable "steady state" block of material was produced, the build process was paused and the temperature was raised by 200°C (according to the Aconity control thermocouple).

Once the substrate had been left at the target temperature for 20 minutes, the build was "resumed" for a single layer, with the thermal camera acquiring data for the one of the parts, before running out of RAM and having to pause to process and save the images that were collected. Once the part had completed, the process was paused again and the temperature was raised by a further 200°C. The experiment was then repeated at 200°C intervals until 1200°C was reached (the maximum safe temperature of the heating element). In order to provide a more simplified data set but still be "representative" of the LPBF process, the parameters of the final layer's line scans were changed to have greater spacing and slower speed, in order to be able to discern them more clearly.

5.6.3 Analysis of Thermal Data

Data captured is in the form of a series of images that can be stacked or processed by software such as ImageJ. As explained in section 2.6, it is possible to monitor the raw intensity value of the obtained images throughout the process and collect them to show how the material cools throughout the entire build. This cooling curve can also be used to identify certain phase changes, where a change in the gradient of the radiance curve can be observed. Figure 5.36 shows a typical image obtained by the thermal camera during this experiment, as well as some initial processing steps performed in ImageJ to provide useful data:

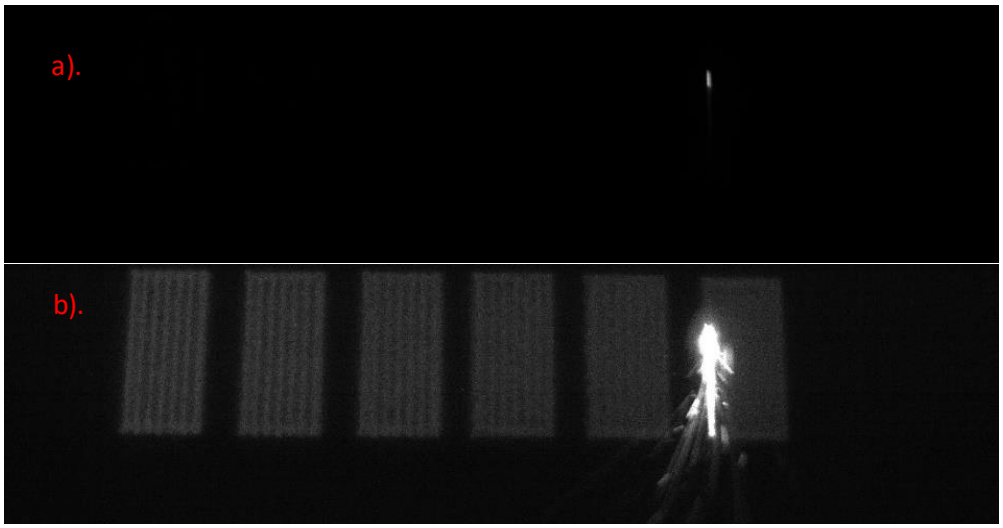

Figure 5.36: a). A raw and b). contrast enhanced scan track in CM247-LC observed using the high-speed thermal camera.

The camera was calibrated to "see" emissions most clearly at around 1700°C. This does mean that in some of the initial images taken, the very centre of the melt pool is saturated in the image, meaning that there is some information lost. By performing a plot profile along each scan line, it is possible to see both the "melt pool" and its tail in each image displayed as a graph, which also provides a set of data points. The graph shows the intensity with changing position along the line, which can be converted into an actual temperature by multiplying by a factor of the pixel's intensity divided by 256. This can then be fitted to the calibrated scale, which begins around 550 as determined by the characterisation of the heated bed in chapter 5. Unfortunately, there is still some image blur, which can is observed in raw images in the form of a "smear" of the melt pool.

Examining the cooling curves of the data from the camera also demonstrates the complex and often chaotic nature of LPBF. Many regions can be seen in images to contain fragments of spatter from the process. These hot lumps of material often settle behind the trail of the powder and can interfere with the cooling of the material, potentially imparting more thermal energy into its local region, as shown below in figure 5.37.

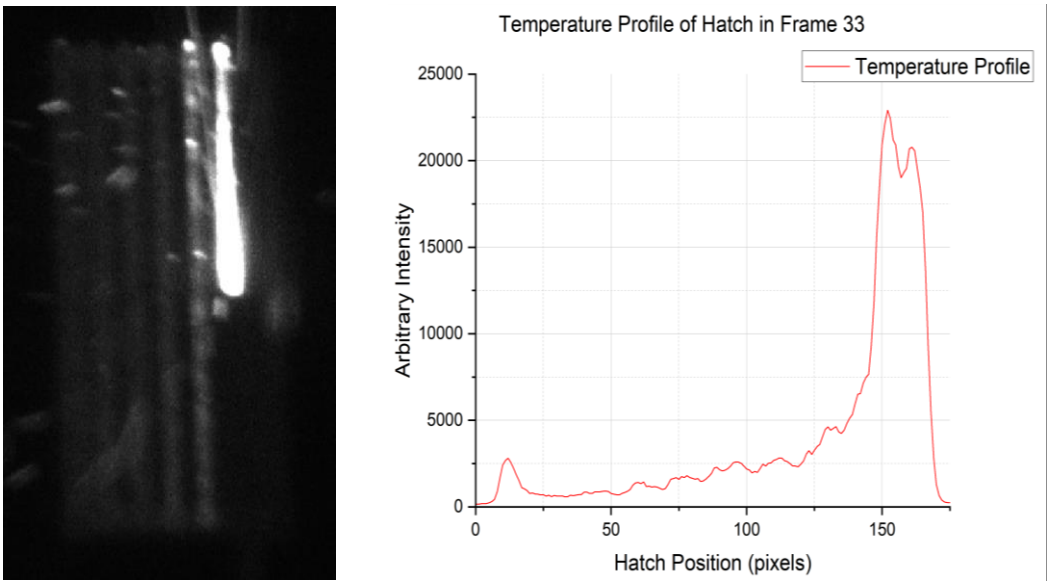

Figure 5.37: Contrast-enhanced image of frame 33. The temperature profile runs along the hatch from the trail to the melt pool head. This shows a region of elevated temperature, visible in the image as an edge region, where the rate of cooling drastically reduces.

This edge effect is likely due to the edge effect from powder insulation and the slowing of the laser as it turns. Small pieces of spatter can also be seen within the image, often characterised in the temperature profile as the rather bumpy cooling trail.

This project is in relatively early stages. The primary goal now is to calibrate the system to provide a "true" temperature, as all of the intensity values provided are in arbitrary units. Equations 2.7 or 2.8 could be used, however the value of emissivity in this case (for CM247-LC in a powder form) is unknown and must be determined before attempting to estimate temperature.

5.7 Summary

This chapter has examined the possibility of in-situ heat treatment within the LPBF process, with a view to improving the final material quality of CM247-LC alloy components. Through the use of a pre-heated substrate, the produced alloy has been shown to be vastly improved, with an increase in hardness of 12.4% on average, solely from use of the heated substrate. This improvement is likely due to segregation strengthening in the alloy, as more evolved microstructures with more prominent carbides are visible. However it may also be (at least partly) attributed to a relieving of internal stresses from the relatively slow cooling rate of the material. This in-situ elevated temperature processing appears to be a relatively novel technique for CM247-LC in LPBF, as most instances of the use of this type of technology appear to involve using heated substrates to perform heat treatment after the build process. Examination of response-surface diagrams also points to the hardness of the material being closely tied to the speed of the laser scan, suggesting that this directly influences how the material solidifies.

The use of the normalised energy density equation produced by Thomas et.al [85] has shown to be effective at predicting processing windows for room temperature processing. However, LPBF processing at this elevated ambient temperature is not well documented and its scalability limits it from being truly useful in industry with currently commercially available technology. Because of this, there is disparity in predictions of how the input energy density from the laser will affect the final product. Using lower powers and speeds with a higher ambient temperature but identical input energy is not sufficient for predicting the final material outcome, with many of these samples suffering from cracking on fabrication.

The absorptivity experiments demonstrate the importance of the material absorptivity during LPBF. Of particular note is the reduction of around 50% in absorptivity when no powder is present. Furthermore, the absorptivity of the material changes, depending on the specific laser parameters. This demonstrates that absorptivity is not simply a constant material property, but is a more dynamic phenomenon that is highly variable and may have a significant effect on how the material behaves at different points of the process.

In situ high-speed thermal imaging has been set up for the Aconity Lab, providing a window into material behaviours, both during the melting process and during cooling. Examining the change in radiance over the cooling process reveals the change in rate of optical spectra emissions, likely a result of a phase change. This method of monitoring is also capable of tracking spatter and temperature profile over the course of milliseconds, possibly providing a method of further control methods.

6. Crack Susceptibility and Alloy Design

6.1 Introduction

This chapter details the use of both modelling and experimental methods to determine the impact of changing hafnium content within the CM247-LC alloy system, when produced by LPBF. Thermo-calc models were used to investigate the crack susceptibility and solidification behaviours of CM247-LC with different levels of hafnium present. This was intended to determine whether hafnium plays a role in the heavy cracking normally observed during processing of this particular alloy. This has been suggested in several recent articles as a potential source of cracking for this alloy. Hardness tests and porosity measurements derived from optical micrographs are used to provide a response-surface examination of the impact of changing hafnium levels on the crack behaviour of the alloy.

6.1.1 The Clyne-Davies Crack Sensitivity Model

Clyne and Davies proposed a relatively simple method of predicting crack sensitivity in an alloy system [67]. Summarised in the following equation:

$$C_{CS} = \frac{t_{is}}{t_{lf}} \qquad \text{(Equation 6.1)}$$

Where C_{CS} is the coefficient of crack sensitivity, t_{is} is the time spent in the interdendritic separation regime and t_{lf} is the time spent in the liquid feeding regime.

Assuming a constant rate of cooling, it is possible to reduce this to the ratio between the temperature ranges of the two regimes. The interdendritic separation regime is the range between 1% and 10% liquid, whereas the liquid feeding regime is the range between 10% and 60% liquid. Thus, equation 3.1 becomes:

$$C_{CS} = \frac{(T_{10\%} - T_{1\%})}{(T_{60\%} - T_{10\%})} \qquad \text{(Equation 6.2)}$$

By then using the Thermo-Calc data obtained from the graph in figure 6.1 in this equation, it is possible to obtain an indicator of how likely the material is to crack, purely based on its solidification curve.

To illustrate this, compositional data for CM247-LC (table 2.1) and several other alloys were used in Thermo-Calc to illustrate the concept. Figure 6.1 shows the comparison of several nickel superalloys based on their gamma-prime content and their subsequent crack susceptibility (according to the Clyne-Davies model). Figure 6.2 illustrates the Scheil solidification curve for CM247-LC. The equivalent for each material was generated to provide data for figure 6.1, utilising their common compositions to do so. All Scheil curves were generated in the most recent version of Thermo-Calc using Nickel database TCNI8 v8.2.

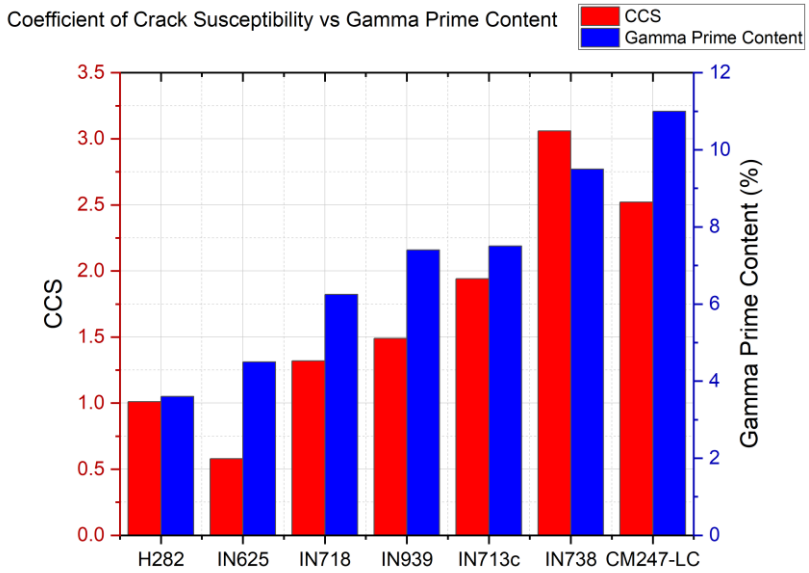

Figure 6.1: Coefficients of crack susceptibility as determined using the Clyne-Davies method, plotted alongside the gamma-prime content for each alloy. The length of solidification regimes for each material was calculated using Thermo-Calc software.

Particularly noticeable in the Scheil solidification simulation (figure 6.2) is the presence of a "step" at around 1330K. This indicates a relatively sudden reduction in the fraction of liquid in the solidifying solution. Examining the phase when this occurs, it is when the majority of carbides begin to form within the alloy. This is also noted when examining the phase diagram of the alloy (figure 6.3) as this also shows the same carbides beginning to form at this temperature.

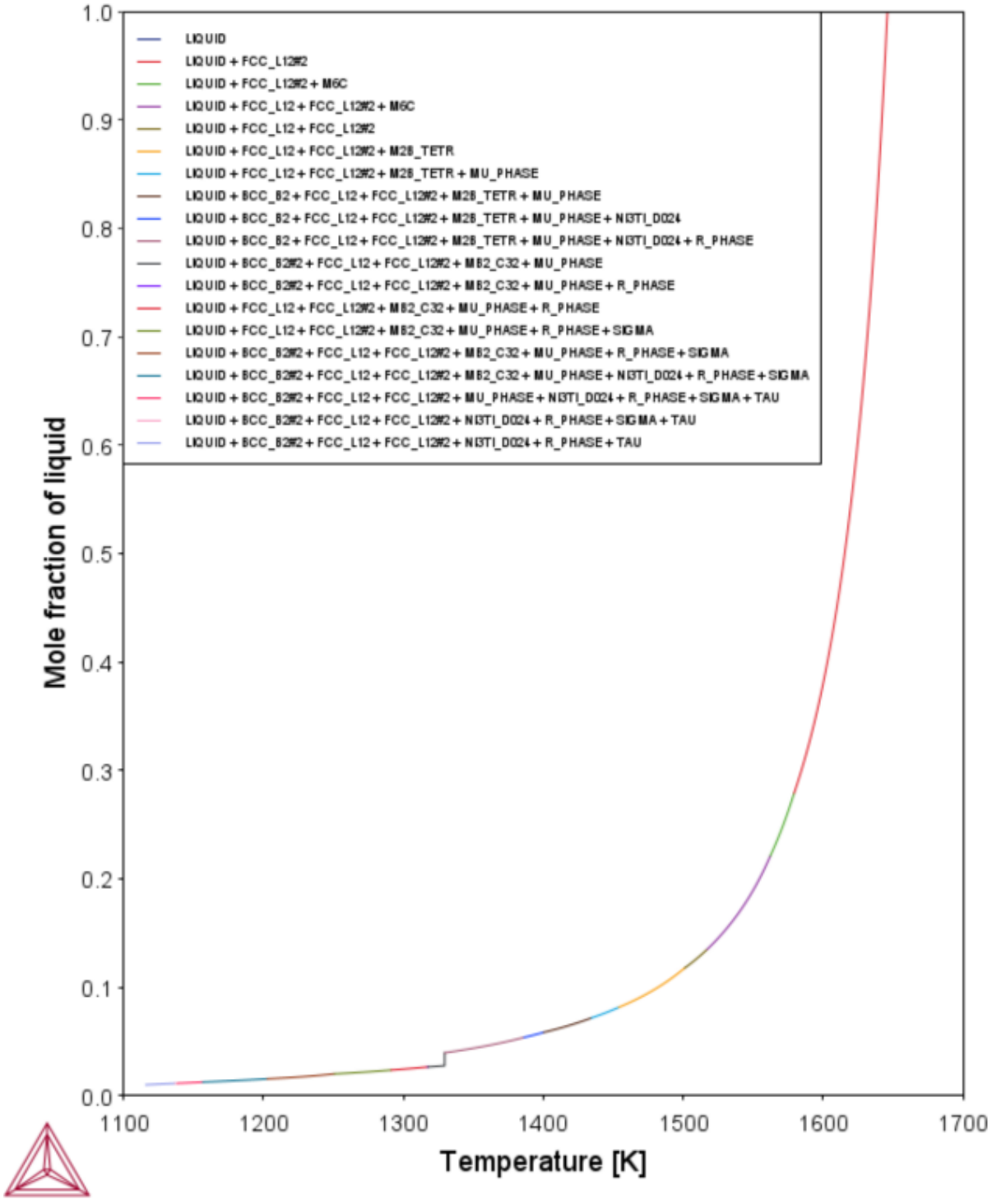

Figure 6.2: Thermo-Calc Scheil solidification curve for nominal CM247-LC. This curve demonstrates the very large solidification window for CM247-LC, a reason for cracking in the material due to the length of time spent in the "mushy zone".

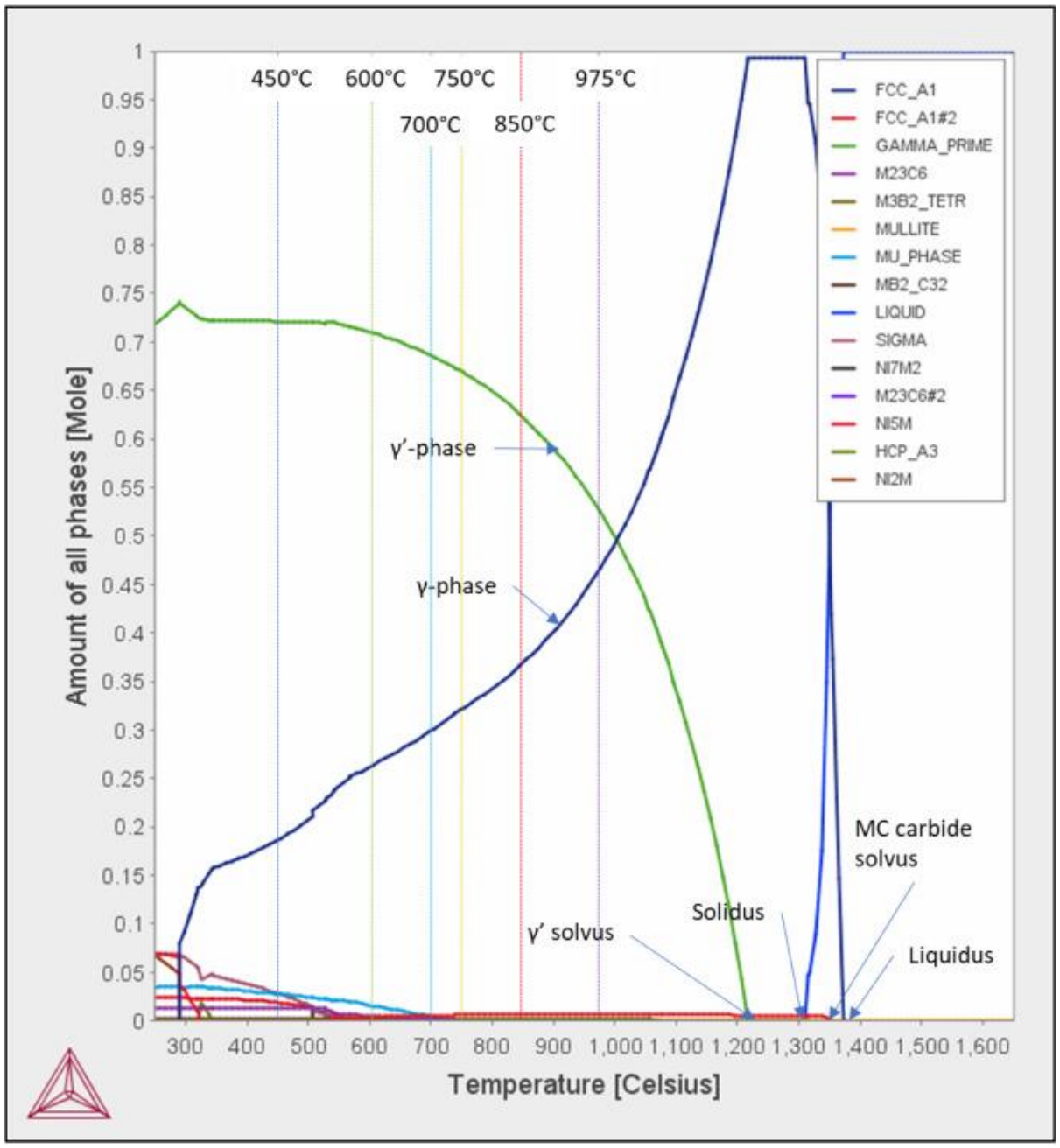

Figure 6.3: Annotated phase diagram produced by M.Atallah et.al. [66]. *The MC carbide solvus is located at around the same temperature as the liquid fraction "step" seen in Scheil simulations in this study. Any slight difference is likely due to batch-to-batch variation in the composition of the CM247-LC alloy.*

6.1.2 Solute Trapping

Cracks are often highly prevalent in CM247-LC due to the unique composition of the alloy itself and the interactions between constituent elements. An explanation to why the cracking in this alloy is so severe can be formed from examining the processes that occur during solidification. During LPBF, the processed material layers are repeatedly melted and solidified in very short timescales - often on the scale of microseconds. In this instance, solute trapping becomes of particular interest because of its implications on AM as a whole. When a complex alloy system such as CM247-LC is in a liquid state, atoms can diffuse easily, as in any other liquid metal system. When solidification begins, it becomes harder and harder for atoms to diffuse as more of the material becomes solid, due to the energy required to pass through already nucleated material. If solidification front velocity exceeds the diffusion speed (as is often the case in AM because of the rapid solidification rate), then solute atoms can be prevented from diffusing, effectively becoming "trapped" within the solid material, in a more homogenous structure.

If diffusing atoms are trapped within the bulk material rather than being allowed to segregate, the cracks observed throughout the material should be reduced. Segregation of particular materials such as boron or zircon to grain boundaries is often sufficient to provide a site for solidification crack formation and propagation, caused by the formation and presence of liquid films between dendrite arms. As segregation occurs during this solidification, the concentration of solute atoms will increase at the grain boundaries. As the quantity of liquid material drops, this will result in the interdendritic region becoming extremely high in solute content.

6.2 Additive Manufacture of Hafnium-Free CM247-LC

With the publishing of several papers that have highlighted the role of hafnium in the CM247-LC system, it is apparent that whilst the grain boundary strengthening effect of the hafnium is desirable - particularly for creep-resistance - it often acts as a source of cracking within the fabricated material. A variant of CM247-LC that contains 0% hafnium was obtained from Sandvik Osprey, in order to investigate the extent to which the element causes cracking during LPBF processing.

Hafnium is sometimes added to nickel superalloys to impart high-temperature strength. This imparts a high level of creep resistance, which is highly desirable for turbine applications. During processing, hafnium tends to the grain boundaries within the bulk material. This is the source of the high temperature strengthening mechanism, which is desirable, but also acts to induce a significant level of cracking during processing. Because of the significant interest in literature on the effect of hafnium in CM247-LC, a set of experiments were devised in order to determine the extent of hafnium's impact on ease of processing. In order to maintain consistency, the same set of parameters were used as in table 4.2. In order to change hafnium content, a modified CM247-LC composition was obtained from Sandvik Osprey. This composition replaces the hafnium content with base nickel, providing a composition of CM247 with 0% hafnium content. This alloy is referred to as CM247-NHf in this study. The Scheil curve for this altered composition is shown below in figure 6.3.

Figure 6.4 suggests that the complete removal of hafnium may only have a marginal effect on cracking within the alloy. In addition, removing hafnium – a grain boundary strengthener – may have a deleterious effect on the strength of the alloy, particularly at higher temperatures.

It was decided that despite the potential increase in cracking within the alloy presented in figure 6.4, it would be worth determining whether or not a "sweet spot" exists between 0% and 1.4% hafnium content. This would likely be characterised by a slight loss in measured properties but also a reduction in cracking. This is possibly what is seen in figure 6.4, where a trough exists between the two crack susceptibility peaks.

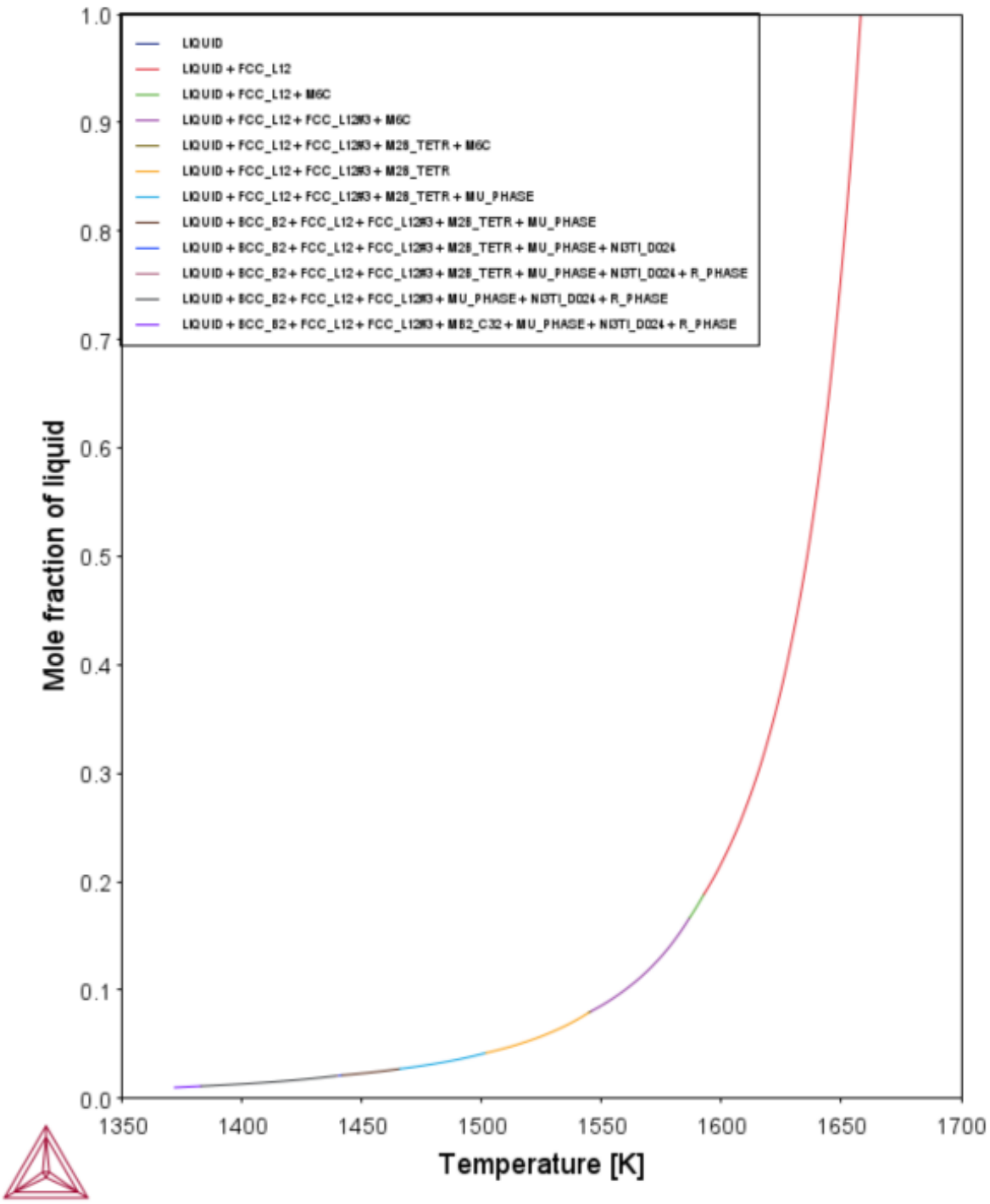

Figure 6.3: Scheil solidification curve for CM247-NHf. This altered alloy has a much shorter solidification window than its parent CM247-LC.

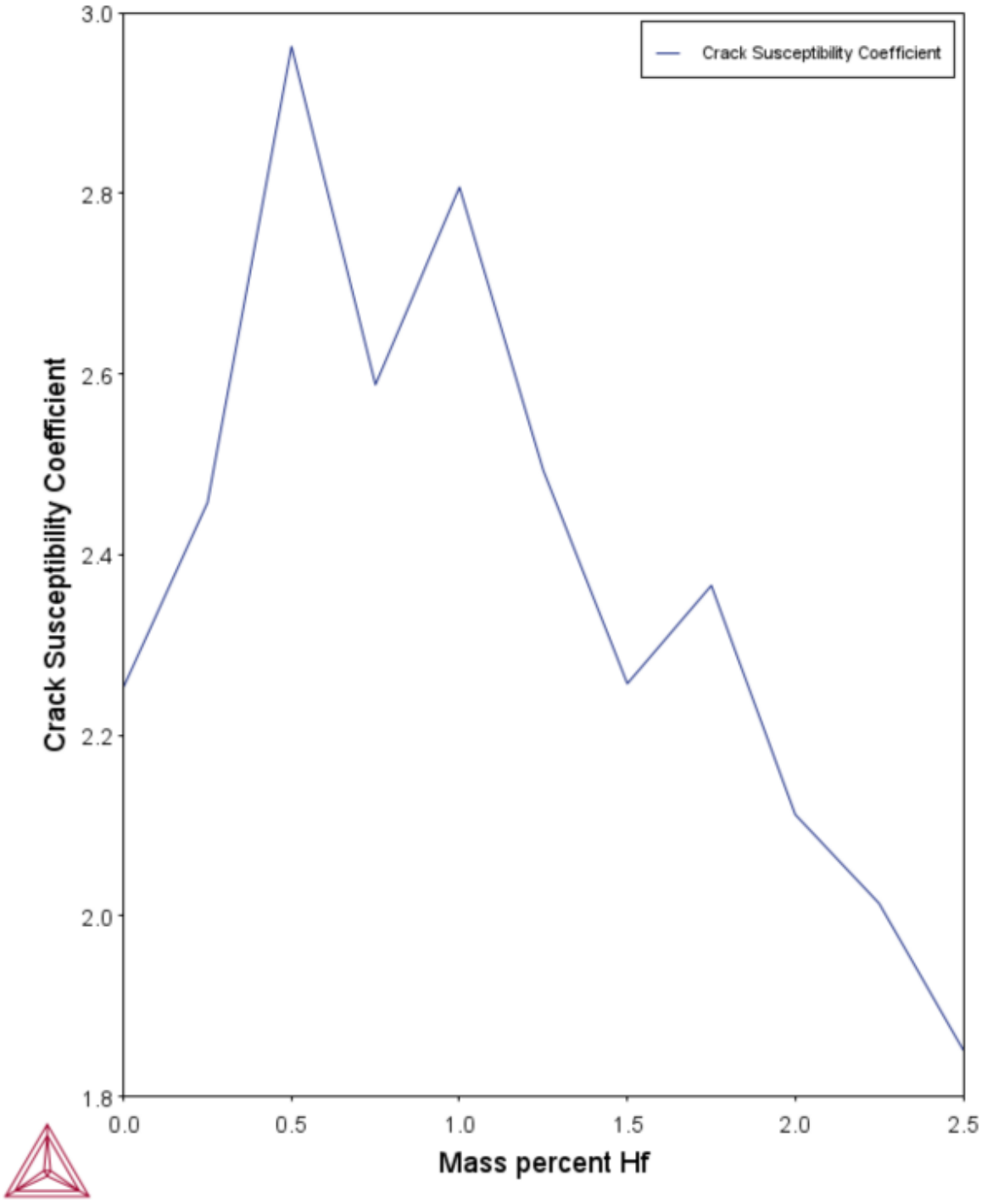

Figure 6.4: Thermo-Calc simulated coefficients of crack susceptibility for varying levels of hafnium in the CM247-LC alloy.

The two alloy powders (CM247-LC and CM247-NHf) were mixed to provide equal amounts of 0.5% hafnium and 1% hafnium concentration powder, in order to determine the effect of this elemental addition when altered. These specific alloy compositions are not pre-alloyed powders, rather they are simply the two variants (CM247-LC and CM247-NHf) mixed in a ratio to produce 0.5 and 1% Hf content. This mixing of powders for use in LPBF is referred to as in-situ alloying, which has been shown to be capable of producing comparable results to pre-alloyed powders. To provide further insight into the cracking behaviour of the two "new" alloys, the Clyne-Davies crack susceptibility coefficient was also calculated for both of these compositions. The Scheil curves of the CM247 variants are shown in figures 6.5 and 6.6.

The experiment described in chapter 4 was repeated for both of these mixed alloy compositions, to provide another clear comparison for analysis. 3Kg of both of the two mixed compositions were produced. In order to provide a scientific comparison between the two variants of CM247, an identical experiment to the one described in chapter 4 was used. The only difference would be the change in alloy composition.

With Scheil curves for each of the alloy variants obtained, the coefficients of crack susceptibility could be determined for each of the examined variants. Figure 6.7 shows the impact of reducing the hafnium content on the comparison between CCS and γ' content. As expected, the relationship between CCS and γ' level remains consistent, though there appears to be a drop-off in the predicted cracking susceptibility below 0.5% hafnium content, likely as a result of removing this common carbide former.

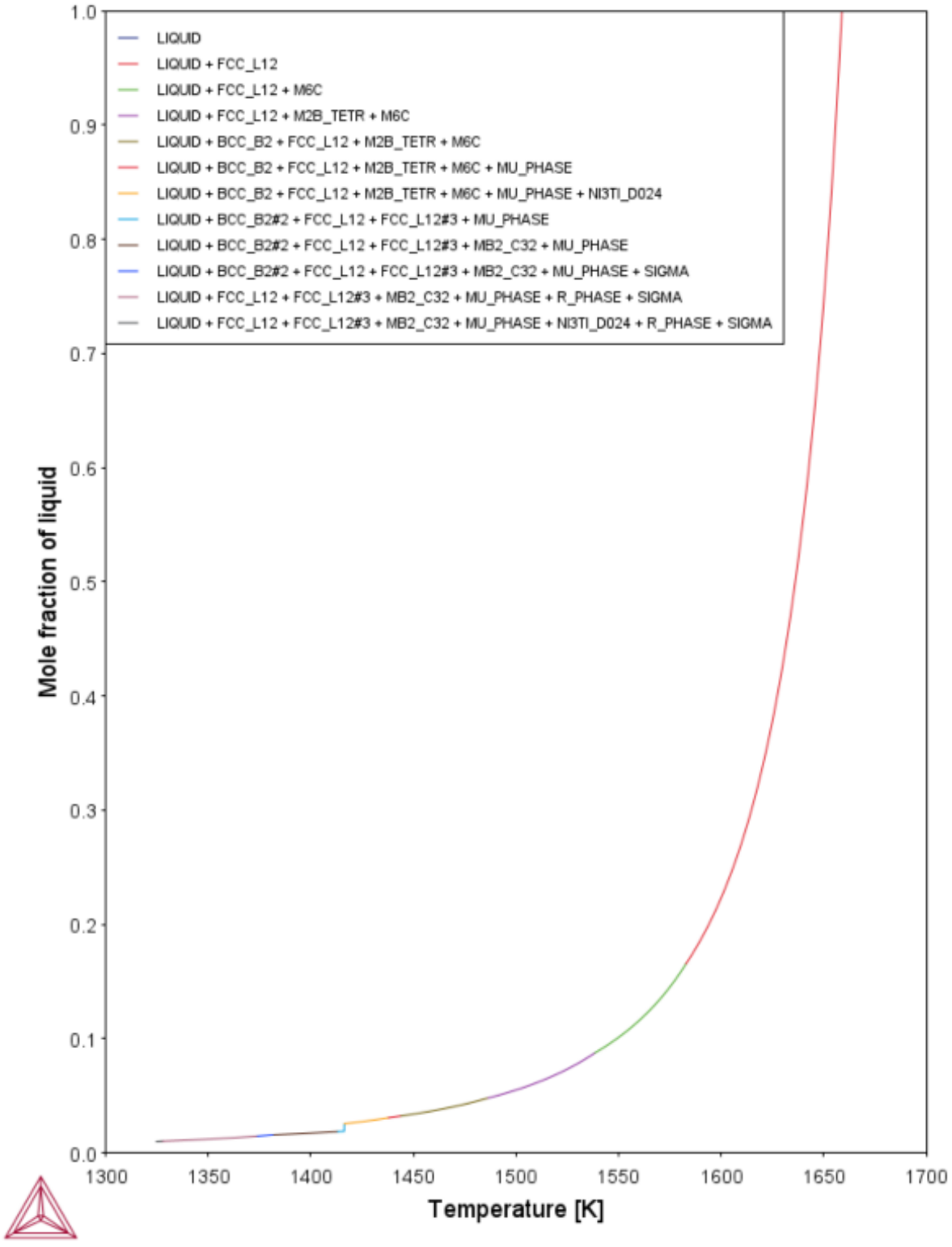

Figure 6.5: Scheil solidification curve for 0.5% hafnium CM247. The "step" seen previously has returned, but has shifted position and is less pronounced.

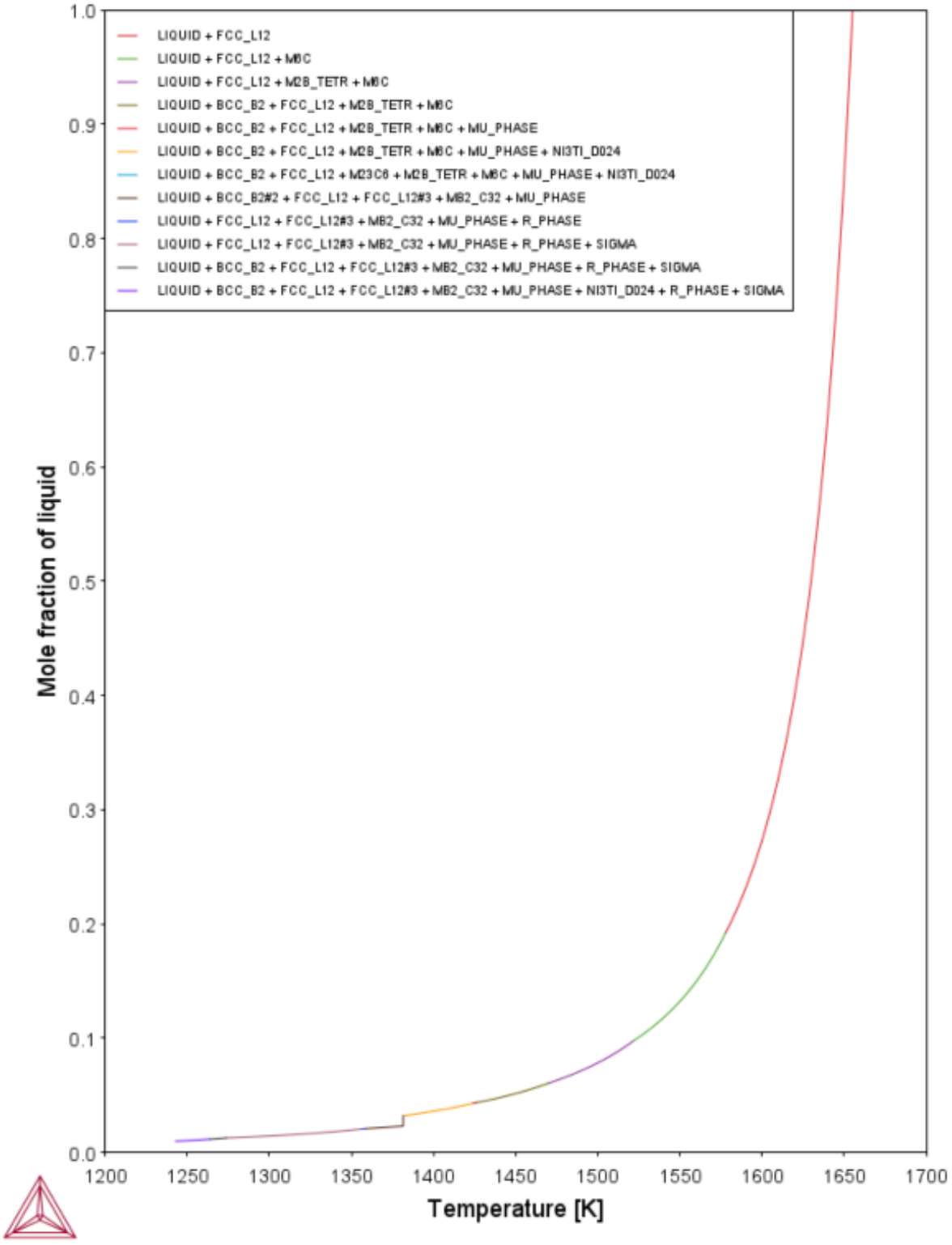

Figure 6.6: Scheil solidification curve for 1% hafnium CM247. The "step" is now more pronounced, suggesting that this rapid change may be largely due to hafnium content.

With Scheil curves for each of the alloy variants obtained, the coefficients of crack susceptibility could be determined for each of the examined variants. Figure 6.7 shows the impact of reducing the hafnium content on the comparison between CCS and γ' content. As expected, the relationship between CCS and γ' level remains consistent, though there appears to be a drop-off in the predicted cracking susceptibility below 0.5% hafnium content, likely as a result of removing this common carbide former.

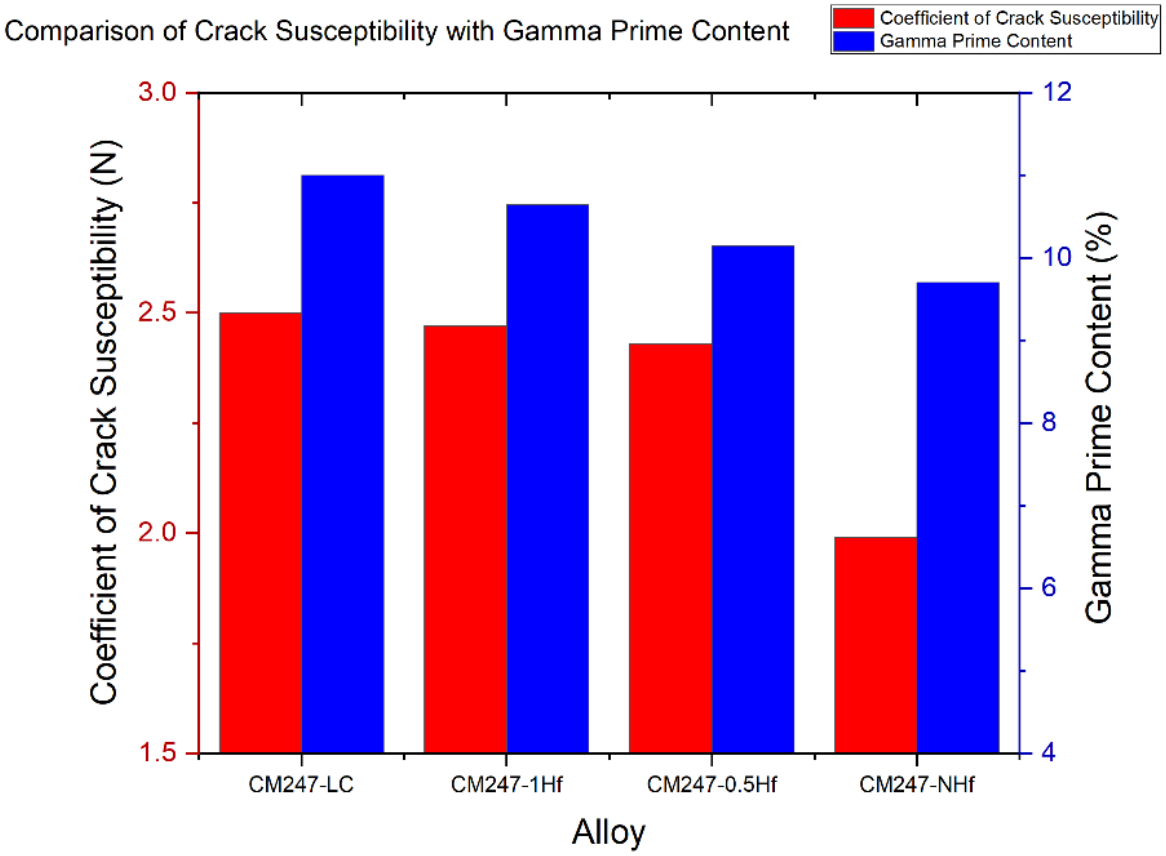

Figure 6.7: Comparison of gamma-prime content with Clyne-Davies cracking susceptibility. A drastic reduction in cracking is seen on the total removal of hafnium, though this is likely to drastically reduce the material performance in testing.

6.2.1 LPBF of CM247 Variants

The methodology of part manufacture described in chapter 4 was repeated for the altered composition material. Identical parameters and part geometries were also used for the experiment (see table 4.2) to provide a direct comparison between alloy variants. Figures 6.10 and 6.11 show representative micrographs of the 9 cubes manufactured in this study. When initially examined, the material appeared to be heavily cracked. However, further grinding and polishing removed these defects, revealing a bulk material that is largely defect-free.

The reason for this change in defect density can be identified by looking close to the edges in each sample. Surface cracks can be seen at the sides of the components that were imaged, suggesting that the edge of the material is undergoing some form of solidification cracking. This "edge cracking" is also observed in the samples of CM247-LC shown in chapter 4. This edge cracking is likely liquation cracking, which is often observed in welding as a type of crack that runs through to the edge of a sample. It is possible that the removal of hafnium has led to an increased susceptibility to hot tearing and liquation cracking, as the hafnium acts as a grain boundary strengthener at elevated temperatures. Without this strengthening agent, the material will be far more susceptible to defect generation during the final stages of solidification.

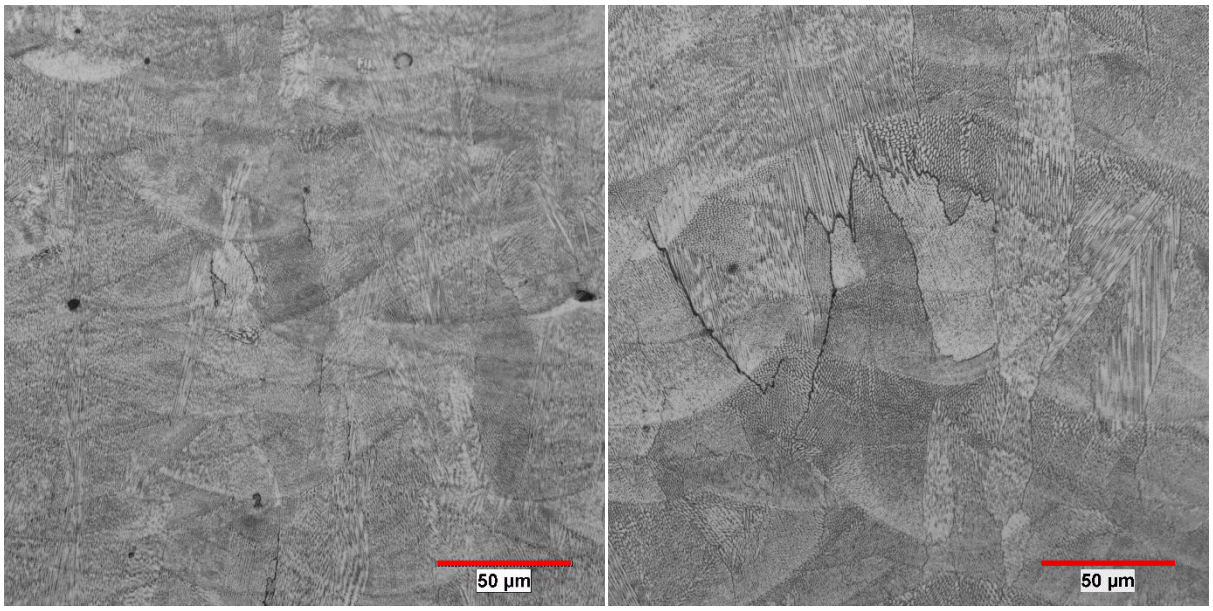

Figure 6.10: Optical micrographs of CM247-LC (left) and CM247-NHf (right) built using identical machine parameters. Cracks are more pronounced than voids in the hafnium-free material, but are still relatively low in number.

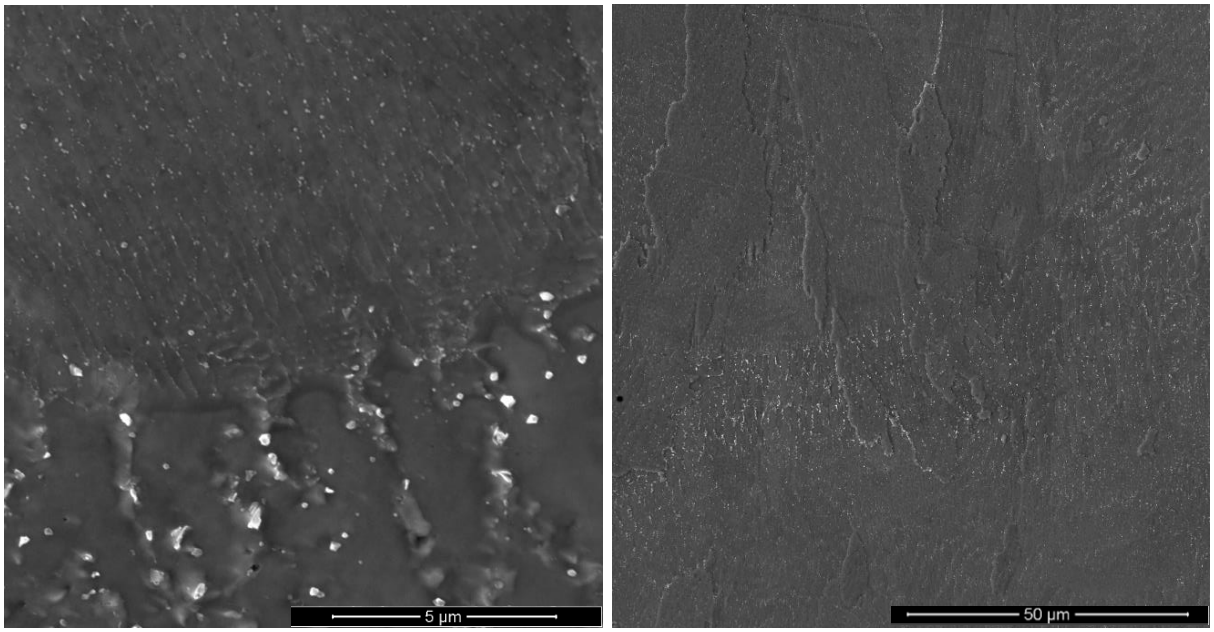

Figure 6.11: SEM Micrographs of CM247-NHf. Cell microstructures can be seen throughout the material, with melt pool and heat boundaries also visible throughout the material.

Figure 6.12 shows a full mosaic micrograph of a heavily cracked sample produced from CM247-0.5Hf. Cracking is mostly prevalent in the edge regions of the sample, with the centre bulk being more well formed (though still containing porosity). This suggests that solidification rate plays a major role in the crack susceptibility of the alloys.

Figure 6.12: Heavily cracked CM247-0.5Hf material. Cracking is concentrated at the edges and overhangs, where the solidification would likely be slower.

6.2.2 Comparison of the Alloy Variants

Of particular interest is the results for CM247-NHf. 50% of the samples that were made from the hafnium free variant reportedly failed by ductile fracture, whereas 100% of hafnium-containing tensile tests done prior to this had failed by brittle fracture. The elongation demonstrated here is significantly higher than for previous studies. The values shown on the graph are averages (table 6.1) , but the highest elongation recorded for the hafnium-free material was 21%. In addition, this elongation occurs with only a minor (~0.5%) reduction in 0.2% proof stress and tensile strength relative to normal CM247-LC.

The results obtained from the CM247-LC and CM247-NHf tensile tests performed by Special Steels are shown below (figure 6.13).

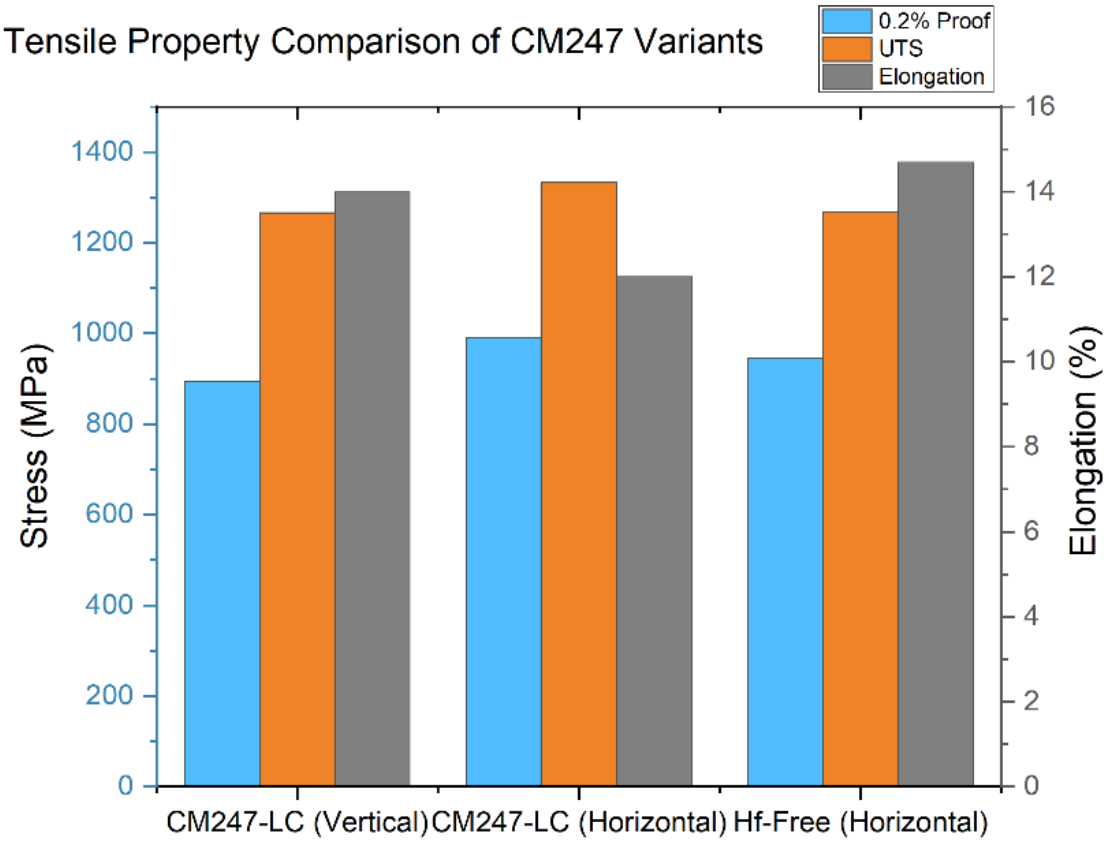

Figure 6.13: Comparison graph of average CM247 tensile properties produced via LPBF in Sheffield. This includes data obtained by both Yevgeni Brif and this study.

Whilst there is a 5% drop in both UTS and the 0.2% proof stress due to the removal of hafnium, the properties of the Hf-free variant are still comparable with the original.

Table 6.1: Average values of the tensile strengths displayed in figure 6.13. Whilst a minor reduction in tensile strength is observed, the properties of the room-temperature hafnium-free material remain comparable to normal CM247-LC.

Material	0.2% Proof (Mpa)	UTS (Mpa)	E (%)
CM247-LC (Vertical)	893	1266	14
CM247-LC (Horizontal)	991	1333	12
Hf-Free (Horizontal)	945	1267	14.7

A closer inspection of the hafnium-free material shows the columnar grain structure endemic to LPBF processed materials similar to CM247-LC.

Due to the relatively small amount of powder available for builds, the two other compositions of CM247 (0.45% and 0.9% Hf) did not have tensile bars manufactured. Instead, further cubes were manufactured to determine the cracking, porosity hardness levels of the materials. These cubes used the same parameters as the hafnium free and standard composition tests, to provide consistent comparisons throughout the process. In addition to the parameters, the hardness testing method was kept consistent to that used in previous chapters in order to provide effective comparisons. A grid of 8x4 points was used, with indents performed on each of these points to provide a hardness value.

Hafnium-free and reduced hafnium compositions see a reduced hardness towards the edge of the material, likely due to the increased tendency of the material to crack in this region. However, the variation in the actual hardness values between the four different compositions varies considerably.

Comparing the standard CM247-LC alloy hardness to those of the modified compositions, a reduction in average hardness is noted across all samples (figure 6.14). The reduction in hardness is minimal – 0.6% - for 1% Hf content, but is far more pronounced for the 0.5% Hf and Hf-free compositions as hardness is reduced by 6% and 5% respectively. Considering the predicted crack susceptibility as determined by the Thermo-Calc model the peak of crack susceptibility is expected to be reached at around 0.5% Hf content. Given that cracks can cause hardness test values to be reduced by increasing indent size, this is likely the case for this level of hafnium content within the CM247-LC alloy. Given that hafnium acts as a grain boundary strengthener, providing a method of dislocation pinning, it is likely that this is responsible for the drop in material property.

For the other sets of samples however, the Thermo-Calc model is not quite as agreeable. The hardness level of the 1% Hf alloy is nearly unchanged from the base composition. While this may be attributed to the potential inconsistency of in-situ alloying, there would be more variation expected if this was the case. Instead, the material produced from the 1% hafnium batch is highly consistent, with very little variation in the average hardness of samples.

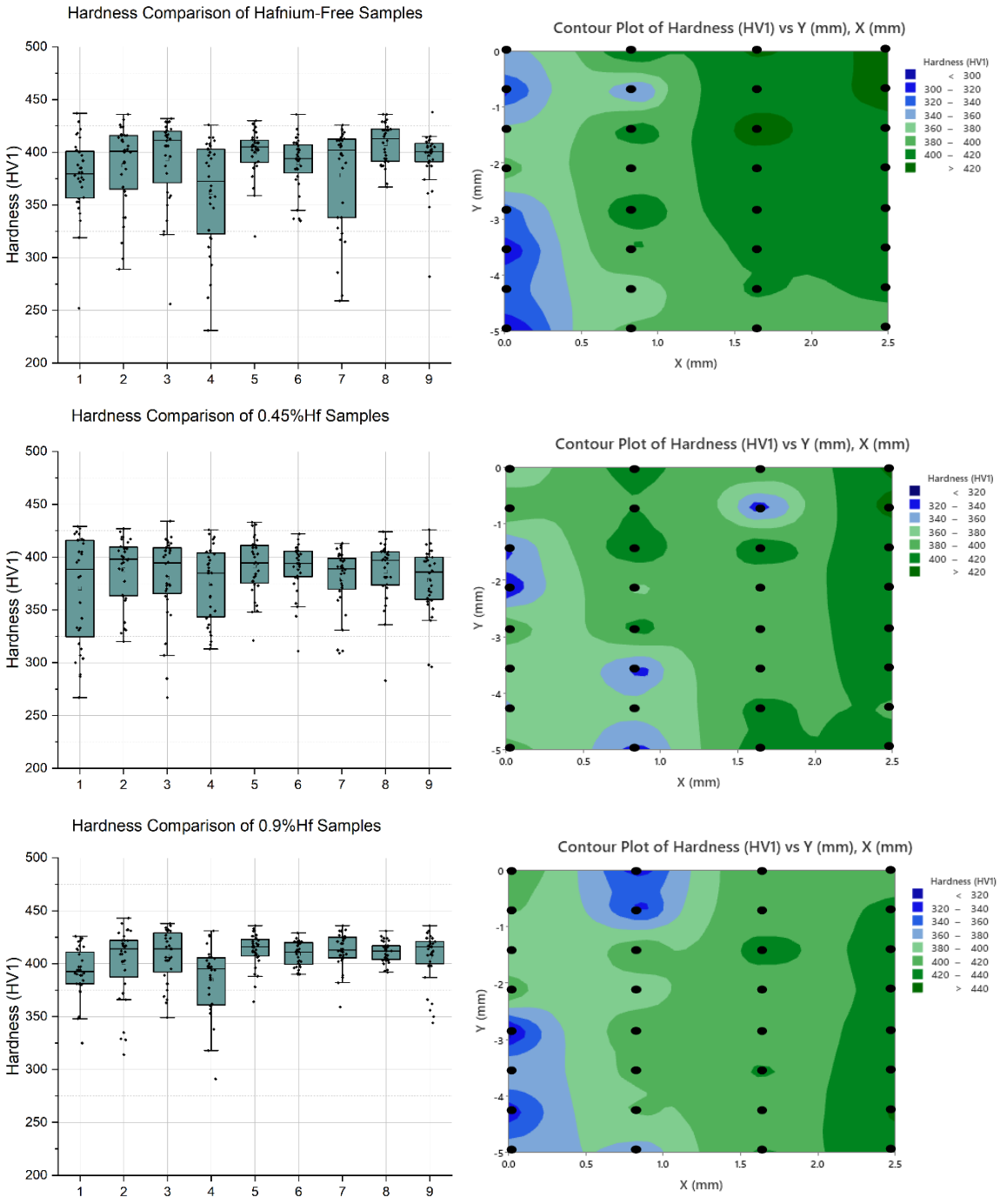

Figure 6.14: Hardness values and plotted maps of representative samples produced via LPBF. Similarly to the CM247-LC samples, all of the modified compositions suffer from a reduction in hardness closer to the edge of the material.

Because of this change in the likelihood of cracking, it is possible that this causes the effective strength of the material (and thus the hardness) changes depending on the hafnium content of the material. Figure 6.15 shows a comparison of the four alloy variants and how their average hardness values vary.

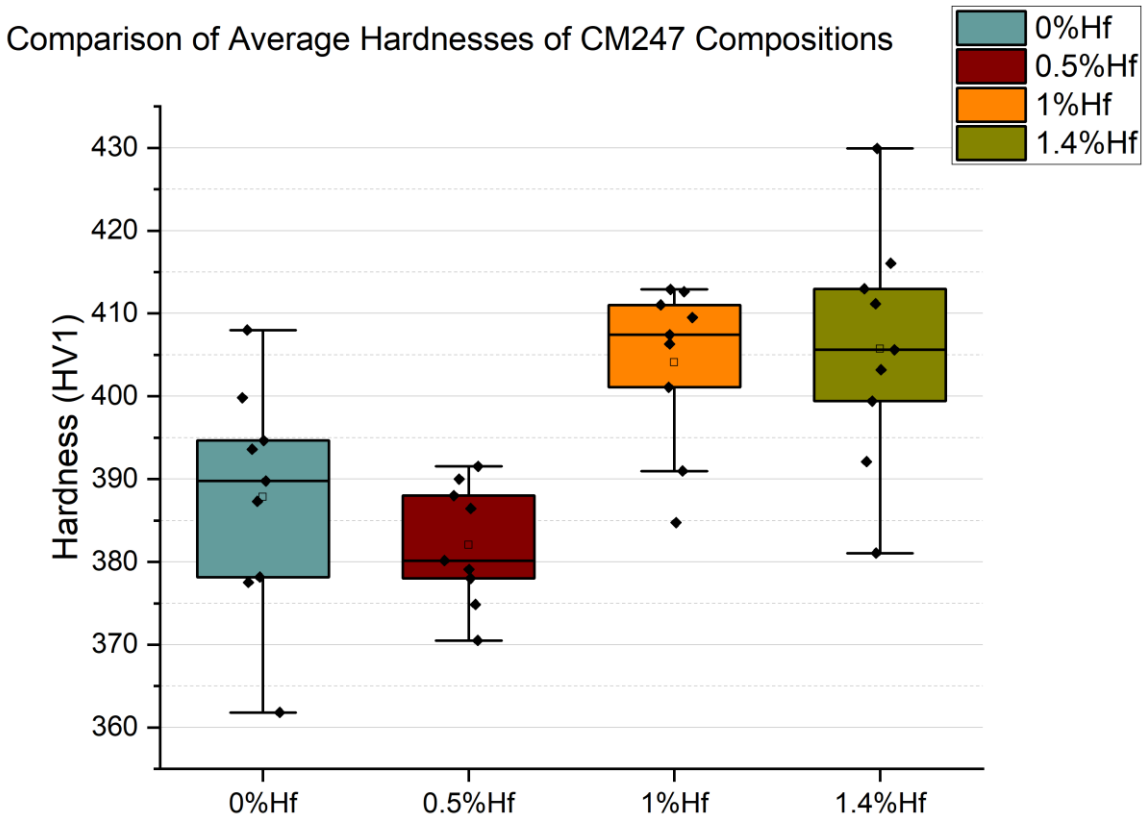

Figure 6.15: A comparison of the average hardness values of the four CM247 variants examined in this study. Whilst the reduction in hafnium reduces the overall performance of the alloy, a small reduction (to 1%) may result in a more consistent final material product.

From this set of boxplots, the following conclusions may be drawn. Firstly, a small reduction in hafnium to around 1% makes the material more consistent in terms of its material properties. This is surprising from the perspective of the Thermo-calc model, as this predicts an increase in crack susceptibility, which would be marked by a drop in material properties. Whilst there is a slight drop in the maximum hardness of the material, the lowest average value is higher than its counterpart in CM247-LC.

Secondly, whilst a small reduction to 1% in the hafnium content may improve consistency, removing more serves to significantly weaken the alloy. This can also be seen in micrographs, with the lower hafnium samples containing more defects. By this logic, there is a significant drop-off in material properties between 1% and 0.5% hafnium content in this alloy (figure 6.16). This makes sense – hafnium is a grain boundary strengthener and lower amounts will prevent that strengthening effect from being as pronounced.

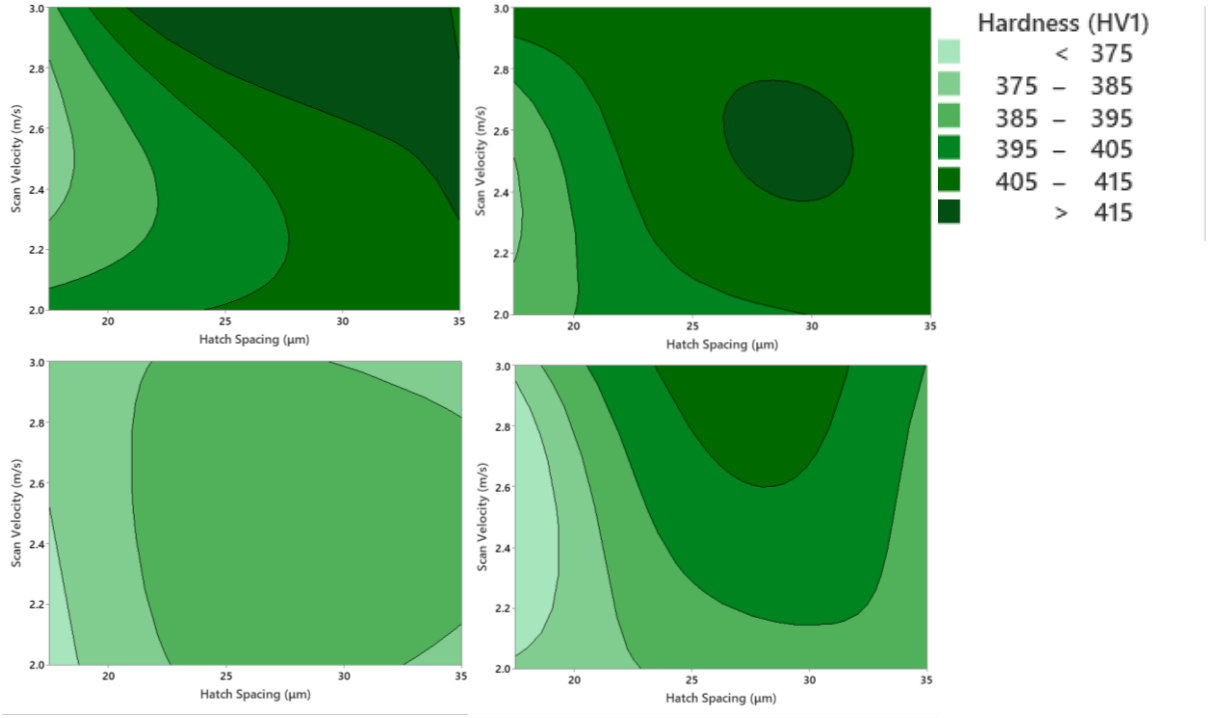

Figure 6.16: The change in hardness relative to processing window for each of the four alloy compositions. Clockwise from top left – CM247-LC, CM247-1Hf, CM247-NHf and CM247-0.5Hf.

6.3 Cooling Rate Analysis

As expected, the removal of hafnium reduces the material's resistance to deformation quite considerably – likely as a consequence of removing (or reducing) one of the primary grain-boundary strengtheners in the alloy's composition. Once the level of hafnium drops below 0.9%, a significant drop in hardness is noted. However, up to this point, it seems that the cracking predicted by the Thermo-Calc model has failed to appear. Afterwards however, there is a significant increase in the level of cracking present in the material.

This is particularly noticeable at the edges of samples, where cracking is far more prevalent. It is possible that because the external surfaces are not constrained by other material, they can relieve their stress through cracking and movement of material. However, this may not be possible in the bulk, as the material remains in a state of compression and cannot easily deform to accommodate this. During solidification and cooling, the edge of the sample retains its heat due to the insulating effect of the powder. Because of this, it solidifies and cools at a different rate to the bulk material. This means that the level of segregation within these two regimes of material will be different.

This edge cracking can be seen in modified compositions during sample polishing. If ground from the edge of the sample, rather than from a central sectioning, the samples appear heavily cracked (figure 6.17). This normally results in around 0.3-0.5mm being removed during grinding. However, if an extended grinding procedure is subsequently employed to remove around 0.5mm more material, subsequent micrographs (figure 6.18) show a distinct reduction in cracking density, suggesting that reaching more "steady state" bulk material gives a more representative view of the material, whereas the edge of the samples is heavily cracked.

Another explanation for this change in material behaviour is the change in temperature profile near to the edge of samples. Because the laser has to turn when it reaches the edge of the sample during a meander scan strategy, the laser spends a longer time near to the edge of the material due to a change in directional component of the velocity. In addition to this, powder is around 33% empty space because of its packing fraction. This empty space acts as an insulator, preventing heat from escaping as quickly than through the already consolidated layers. Because of these effects, the edges and corners of LPBF-produced samples are often overheated and swollen. This can also be seen in the pyrometer readings, where the edge is hotter than the bulk.

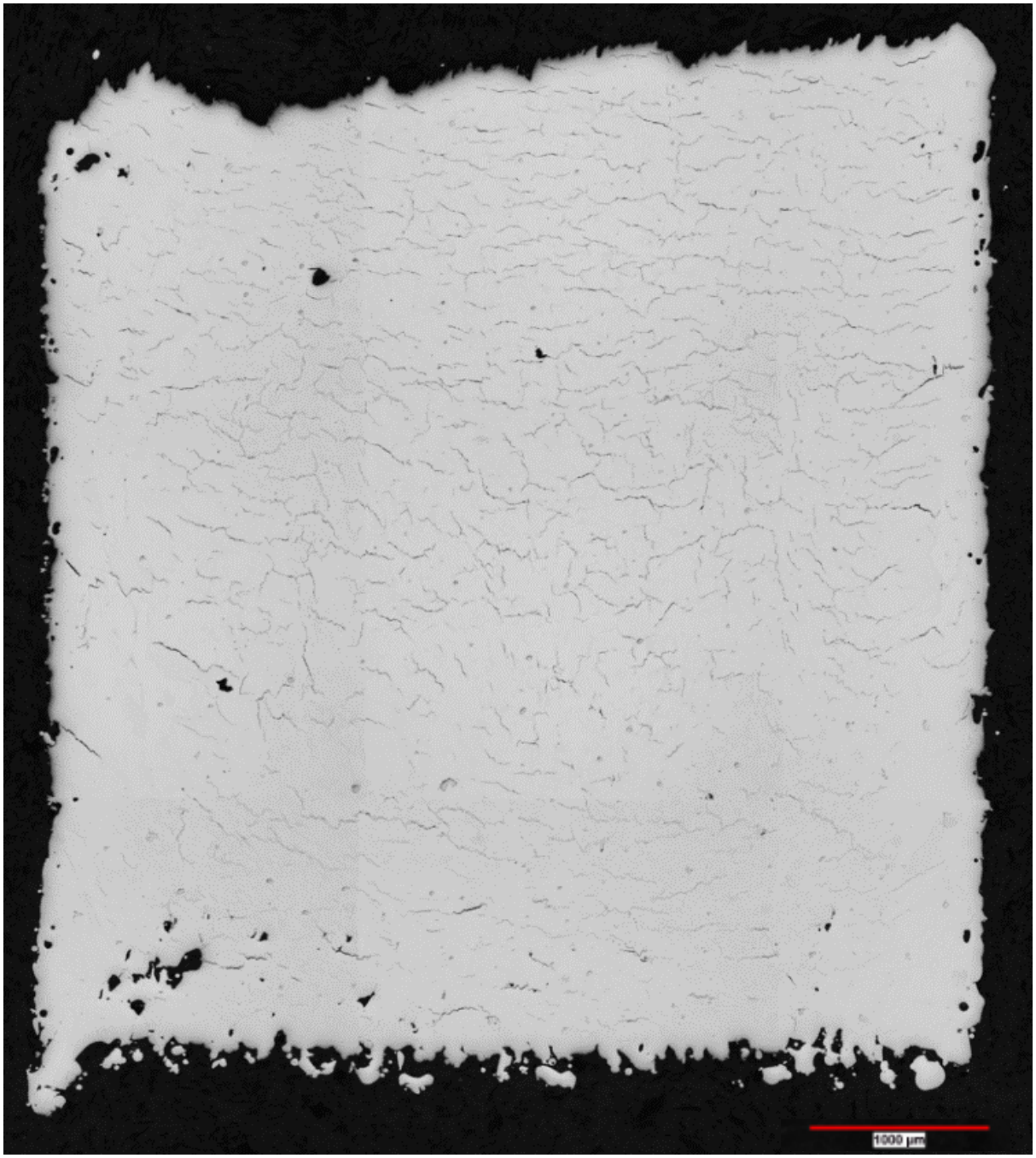

Figure 6.17: Cracking in CM247-NHf is observed across the entire 5mm sample when ground from the edge.

The bulk material solidifies very rapidly, producing a very even and fine microstructure. Lots of very small grains are produced, with little segregation. At the edges, the longer solidification time means that slightly larger grains are formed, with more segregation of elements. As more layers are deposited and remelted, the material's grains grow slightly and more segregation occurs, however the same rule applies – large grains and more segregation near to the edge of the material.

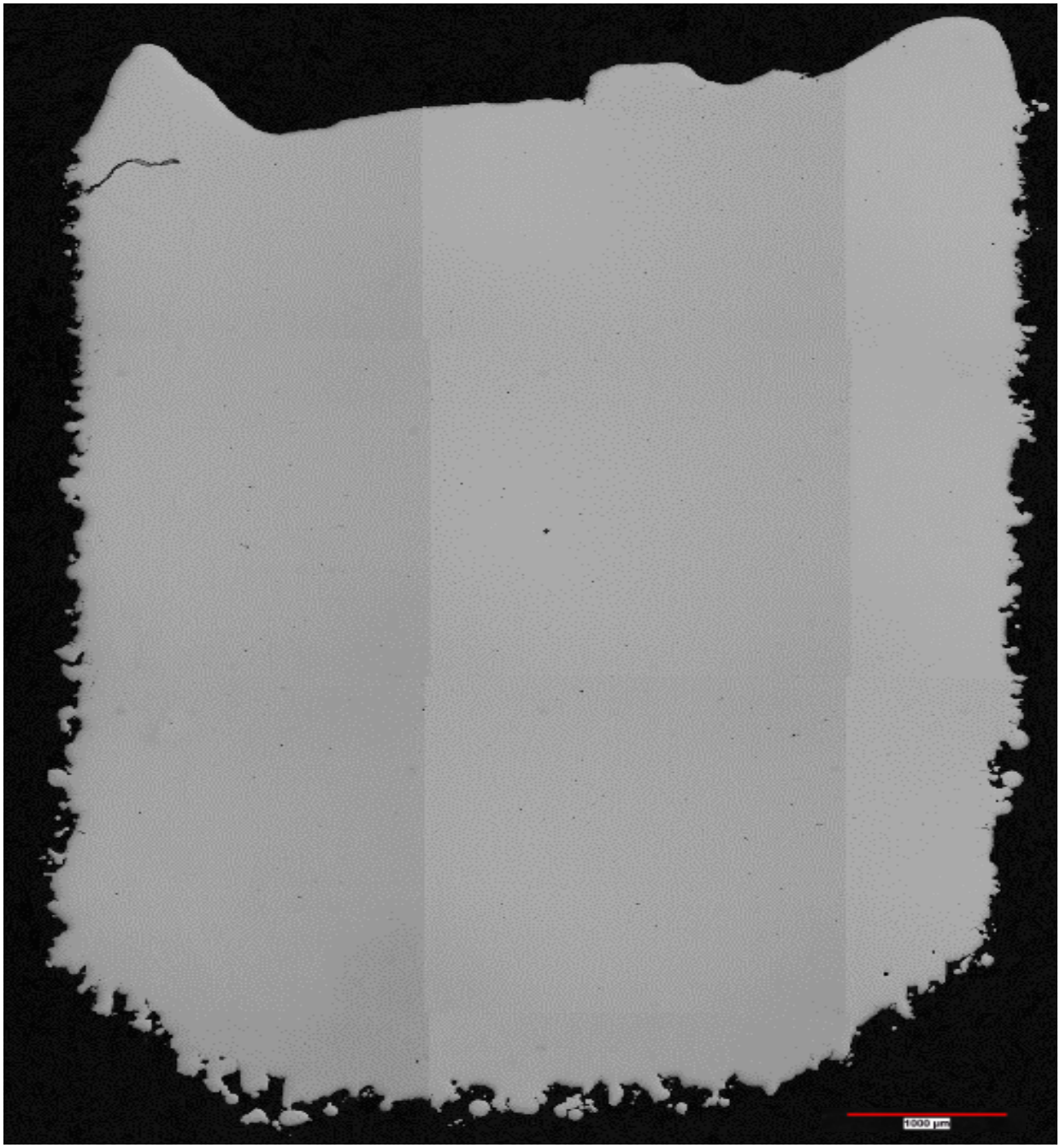

Figure 6.18: Cracks are removed when further surface grinding is performed to remove more material and reach a more "steady state" bulk material (right) that contains far fewer defects.

More segregation will mean that grain boundary strengthening is greater, but larger grains means that the amount of grain boundaries is reduced. To begin with, the grain size dominates the material properties, as per the Hall-Petch equation. As the grains grow however, they become more susceptible to dislocation movement. Because the edges have had effectively more heat for longer, their grains are larger. This results in a material that is more susceptible to deformation, resulting in a reduced hardness near to the edge of the material.

Furthermore, the increased susceptibility to deformation via dislocation movement means that intragranular cracking is much more likely to occur. This, coupled with the naturally high stresses seen at component edges in LPBF [174], means that the edge of the parts is far more likely to crack – which can be seen in the micrographs in section 6.17.

Reducing the amount of hafnium present will therefore have a minimal impact on the fine grain structure in the centre of the components, as this will still be strong due to the size of the grains (Hall-Petch) and the lack of Hafnium segregation to the grain boundaries from rapid solidification will be largely unchanged. In the more segregated form of the material near to the edges however, the level of hafnium will be much higher in the grain boundaries, which will produce a far higher level of grain boundary strengthening. At this scale, this is the primary source of strength in the material. Thus, removing the hafnium catastrophically reduces the ability of the material (with this level of segregation and grain size) to resist deformation.

Laser scan velocity primarily affects the depth of melt pools, as faster moving beams effectively have less time to impart their energy into the material. A slower moving beam would be more likely to keyhole through the powder and into the layers of already-solidified material below. In terms of energy density, this suggests that the removal of hafnium shifts the processing window into requiring a greater amount of energy. If building parts with these "ideal" processing windows, this means that the melt pools of material with hafnium will be smaller than the melt pools in material without hafnium and will therefore have a faster cooling rate, at least in the direction of travel. Cooling rate towards the centre of the melt pool will remain largely unchanged. This can be simulated through the use of the Freeman model, by calculating the cooling rates both parallel and perpendicular to the direction of travel. In all simulated instances for the processing conditions, cooling rates lie between 10^4 and 10^8m/s, suggesting rapid solidification in all cases. Table 6.2 shows how the cooling rates vary for different scan velocities used in this study.

Table 6.2: Processing parameters used in this study and their resultant cooling rates in m/s.

Scan Velocity (m/s)	G (base, m/s)	Tdot (base m/s)	G (tail m/s)	Tdot (tail m/s)
2	2.50E+08	6.80E+06	1.00E+06	2.00E+06
2	2.50E+08	6.80E+06	1.00E+06	2.00E+06
2	2.50E+08	6.80E+06	1.00E+06	2.00E+06
2.5	2.30E+08	1.70E+07	1.00E+06	2.60E+06
2.5	2.30E+08	1.70E+07	1.00E+06	2.60E+06
2.5	2.30E+08	1.70E+07	1.00E+06	2.60E+06
3	2.10E+08	2.60E+07	1.10E+06	3.20E+06
3	2.10E+08	2.60E+07	1.10E+06	3.20E+06
3	2.10E+08	2.60E+07	1.10E+06	3.20E+06

Unfortunately, the freeman model does not accurately predict the change in cooling rate at the edges or corners of parts, as the main assumption in this model (for cooling rate calculations) is that the solidification front velocity is equal to the scan velocity. This is not the case at the edge of a component during a meander hatch, as the proximity of the next hatch to the cooling/solidifying previous hatch will cause a retention of heat. This retention of heat will reduce the cooling rate of the material and will likely result in a much different microstructure and material properties. This can be observed in many of the micrographs in this study, as the edges often consist of a different microstructure (figure 6.18). In this instance, the cell microstructure at the edge of the component is far larger than at the centre, likely due to the reduction in cooling rate, allowing more time for solidification and evolution of the microstructure. At the edge of this sample, the cells have a spacing of 6.5μm, whereas at the centre, the cells are around 10x smaller, at 0.66μm. A similar scale effect can be seen in overhangs in the support structure of components built in this study.

With regards to the 0.5% and 1% hafnium variants, both contain higher levels of defects than the parent CM247-LC alloy, but these defects are different in their morphology and regularity between alloy compositions. SEM micrographs highlight this and can potentially reveal the underlying causes. Defects also vary in morphology by their position within the sample. Particularly at the edges of samples, cracks are extremely heavily focused. Figure 6.19 shows microstructures and cracking at the edge of samples for each alternative alloy composition.

At the edges of samples, cracks run at a ~30-45° angle from the build direction, towards the edge of the sample. This is explained by the changing scan directions with each new hatch. This change in direction causes the solidification front of the melt pool to change direction, meaning that the direction of solidification will also change. Crack morphology can also provide valuable insights into the behaviour of the material. Given that the majority of cracks in the micrographs above have propagated straight through the material, the main cause of cracking is likely solid state, due to a buildup of residual stresses during solidification. However, the ends of the cracks are highly irregular, suggesting that there is also an element of solidification cracking present. It is possible that during the longer solidification time experienced by the edge material, the stresses produced by the change in solidification direction causes a cracking in the liquid film region. If this occurs in two regions, then on solidification, stresses may cause a crack to propagate between these regions of liquation cracking.

The very presence of these small regions of liquid-induced cracking in the edges and not in the centre bulk of the samples suggests that the solidification rate is wildly different between the two regions. Indeed, rapid solidification should result in zero solidification cracks, as this defect requires at least some level of elemental segregation to produce a liquid film, which is a requirement for the process of solidification cracking.

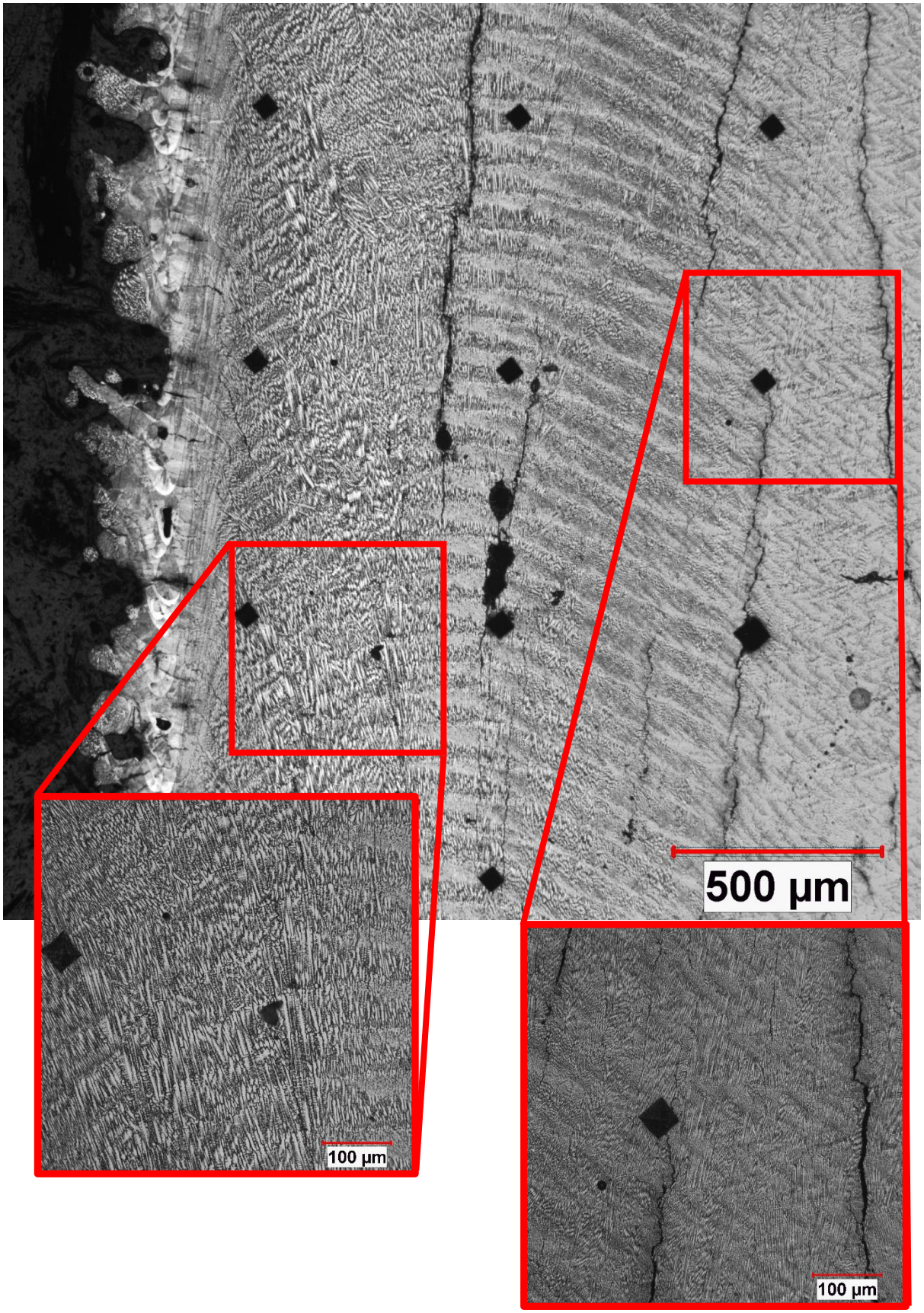

Figure 6.18: An example of how microstructure can change drastically within a layer due to edge effects. This is a sample from work done in chapter 5, using reduced power parameters with the heated bed. A drastically larger solidification cell size is seen near the edges.

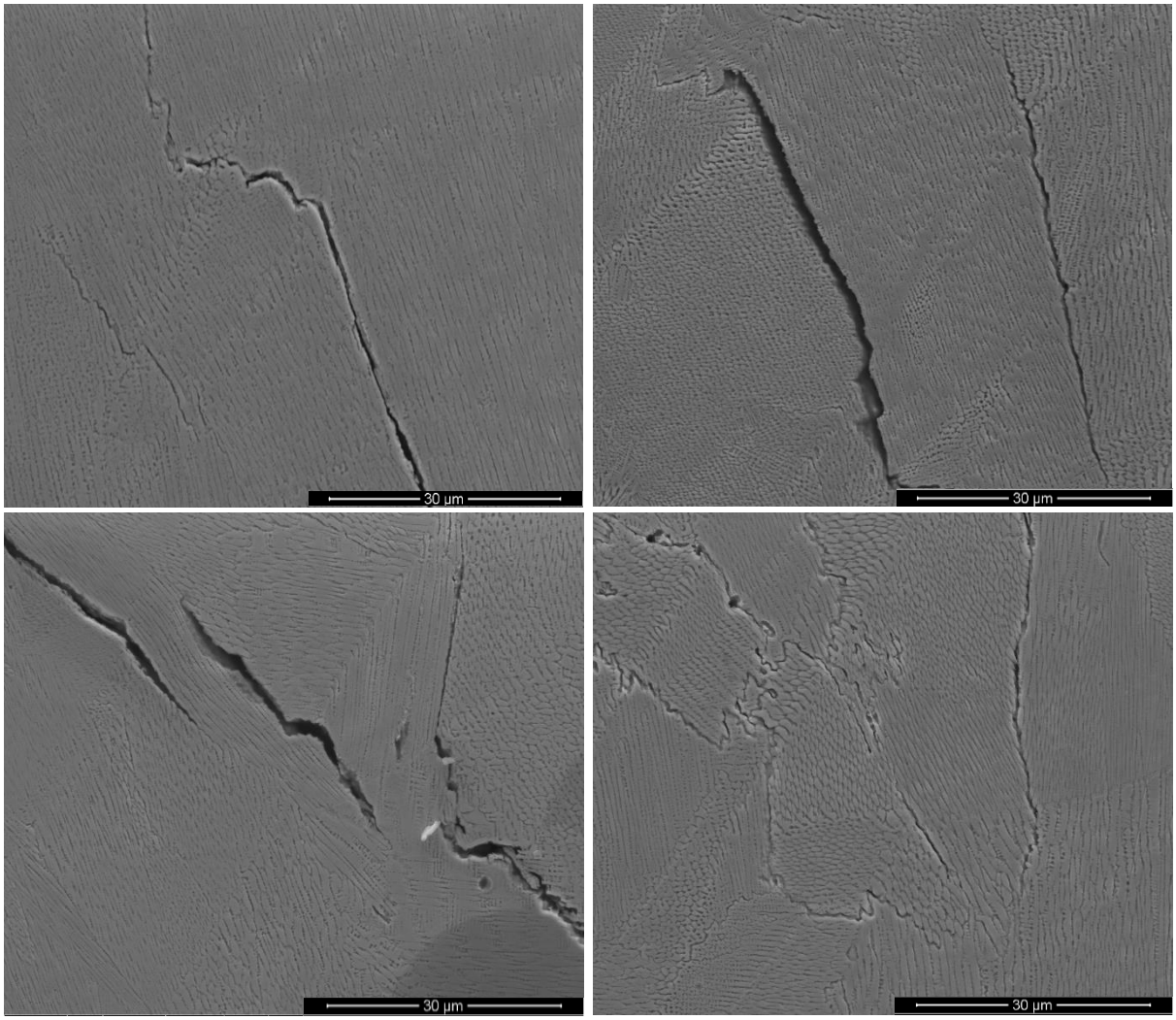

Figure 6.19: SEM micrographs of cracks and microstructures at the edges of samples containing different levels of hafnium content. Clockwise from top left: CM247-LC, CM247-1Hf, CM247-0.5Hf, CM247-NHf. Notably, cracking is still present in all samples.

If these cracks are indeed being caused (or at least initiated) by liquid film cracking, then this would suggest that the edges of the material are far slower to cool.

Samples with 0.5% hafnium content were the most heavily cracked, with many twisted and complex crack propagation paths present in the defects. This is almost certainly indicative of a form of liquid film cracking, however it is difficult to determine whether it is liquation or solidification cracking. Both of these causes could be exacerbated by the presence of an edge or corner region, as this increases the amount of heat being trapped in the local region and causes the laser to change direction. Given that solidification cracking is dependent on the length of time for solidification, it is likely that this is indeed the root cause.

This can be confirmed by examining the spacing of the cell structures visible in the SEM micrographs. Using ImageJ, it is possible to determine the size of the cell structures in the material. With these SEM micrographs, the sizes of cells was found to vary between the two regions of material for all samples, with larger cells in the edge material.

Using the Freeman melt pool model for the conditions of processing detailed in table 4.2, the values of $\dot{T}$ can be determined and then used to determine values for the primary dendrite arm spacing in the material. Whilst this equation was determined through empirical evidence from examination of the solidification of IN718, it should bear at least some resemblance for CM247-LC.

Using equation 2.2, the values of $\dot{T}$ were in the range of $2.6x10^7 – 2x10^6$ $°Cs^{-1}$. These values were then used to find the range of PDAS values, which came to 0.17-0.64μm. For bulk material at the centre of the samples in this study, this is in very good agreement (figure 6.19) however for the material at the edge of the samples, this is less accurate, with some cell spacings being as large as 1.5μm.

To examine whether this larger cell structure has a significantly different cooling rate, equation 2.2 can be rearranged to give the following (equation 6.1):

$$\left(\frac{(97\pm5)}{\lambda_1}\right)^{1/0.36\pm0.01} = \dot{T} \qquad \text{(Equation 6.1)}$$

In terms of cooling rate, this gives a very different range for the edge regions of material. In these regimes, the cooling rate ranges from $1.84x10^5 – 7.24x10^4$ $°Cs^{-1}$. Comparing the two ranges, the cooling rate is between 11 and 359 times faster in the bulk than in the edge of the material.

Whilst even the lowest value of cooling rate is still well above the threshold for solute trapping (i.e. it does still happen) this dramatically different cooling rate will undoubtedly have a major impact on the stresses within the material. This variation in cooling rate is shown in pyrometer data obtained from builds as a "crust" around the edge of the component (figure 6.20). Whilst it is impossible to determine the actual temperature from the pyrometer (due to not having an emissivity value for the material – more on that in chapters 7 and 8), it does confirm the presence of a hotter region around the edge of the component – similar to a contour effect. It is likely then that stresses that arise between these two regions will create a strain effect between the two regimes – hence the cracking occurs in the border region between the two.

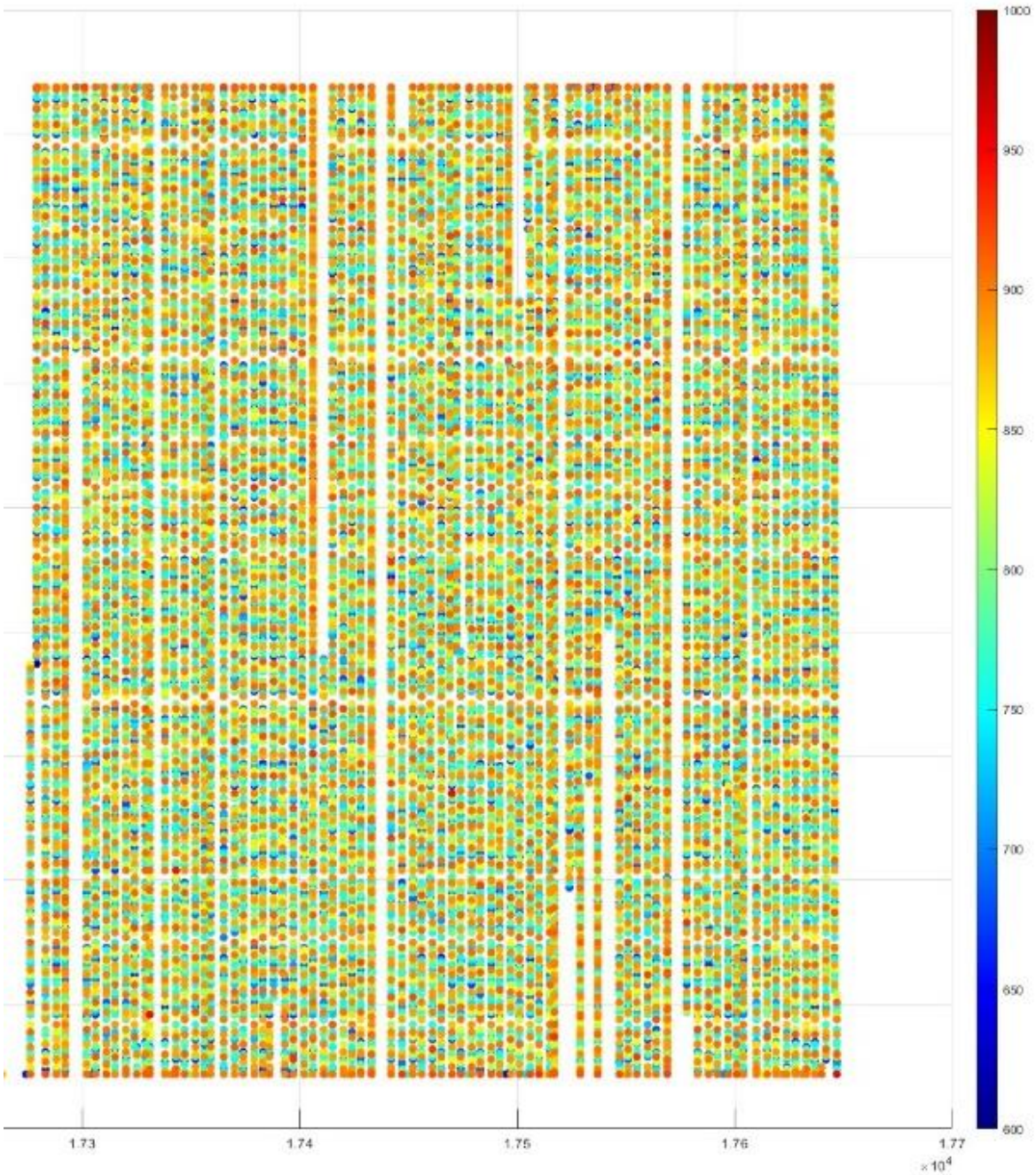

Figure 6.20: Pyrometer data obtained on the Aconity Mini from a 5mm cube sample. The scanning direction is from left to right, meaning that the laser meander turns at the top and bottom edges of the sample, resulting in a hotter observed border. The gaps in the data are due to inconsistencies in galvanometer positioning and data writing performed by the on-board FPGA in the Aconity Mini.

While this explains the reason for more cracking in the edge material, it does not explain why the removal of hafnium alters the crack behaviour of the alloy. In order to determine this the porosity of samples of each alloy must be examined to determine how the processing window

is changing with the decreasing hafnium content. Figure 6.21 shows how the porosity of samples plotted against the processing parameters for samples made from each alloy composition.

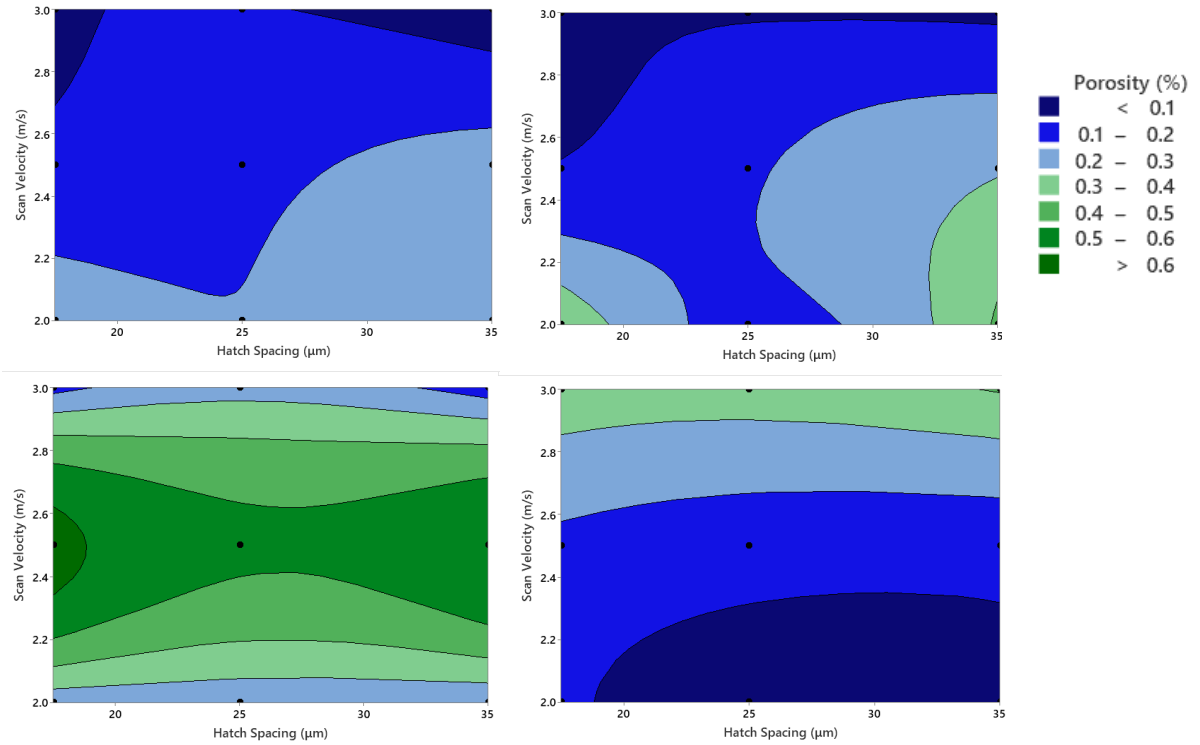

Figure 6.21: The change in porosity behaviour in the same processing window for each composition of the alloy. Clockwise from top left – CM247-LC, CM247-1Hf, CM247-0.5Hf, CM247-NHf.

6.4 The Impact of Hafnium Removal

As figure 6.21 shows, the removal of hafnium appears to alter significantly the processing window of the alloy system. Of particular interest is the 0.5% alloy system, whose levels of porosity appear to have been made largely independent of hatch spacing, with very clear bands of porosity occurring with changing levels of scan velocity. This suggests that the overlap of the beam has little impact on the defect behaviour of the alloy. Completely removing hafnium from the alloy system appears to simplify the processing window. Considering the change in processing window across all four conditions, hatch spacing appears (in this window at least) appears to play a relatively minor role in porosity generation, whereas the scan velocity appears to have a much greater effect. Considering this parameter, the region of lowest porosity appears to shift with each increment of hafnium reduction to a slower and slower laser scan velocity.

Laser scan velocity primarily affects the depth of the melt pool. Given that the change in hafnium seems to produce a greater response from changing the scan velocity, it makes sense that the defect density is directly tied to melt pool depth. The largest change in the processing window occurs between 1% and 0.5% hafnium. Until hafnium is entirely removed, hatch spacing appears to play little role between varying hafnium contents in determining the ideal processing window. With the removal of hafnium, the material requires deeper and deeper melt pools to prevent cracking. As the heat from the laser increases, the size of the HAZ would logically increase as well. If liquation cracking were to blame for the cracking in the material, it would surely become worse with an increasing HAZ size, as more material would undergo melting simultaneously. If solidification cracking were to blame, the same problem would occur, as solidification would be slower and the alloy would spend longer in the “mushy zone”.

If neither of the aforementioned types of cracking are responsible, others must be considered. Strain age cracking is unlikely to be the cause, as this normally only occurs during heat treatment cycles. Ductility Dip Cracking [175] has been noted to have similar effects to that of creep, in that it causes grain boundary sliding effects [176]. This is very important to note, as the primary role of hafnium in the CM247-LC alloy is to act as a grain boundary strengthener that prevents sliding and improves the creep resistance of the alloy [13], [16].

With this in mind, it is likely then that DDC is the primary reason in these samples for the increased level of cracking. The processing window requires a slower beam to prevent cracks as the hafnium cannot prevent grain boundary sliding and must therefore spend longer solidifying to relieve its internal stresses.

Griffiths et.al [13], [16] performed a similar trial to this with both CM247-LC and CM247-NHf. In the instance of both, defects were still present in both alloy variants. Figure 6.22 shows an updated version of figure 4.18, with the two conditions from Griffith's work added in as well. Again, whilst the normalised energy densities involved in this study are similar, they do not share any overlap with the work done by Griffiths et.al.

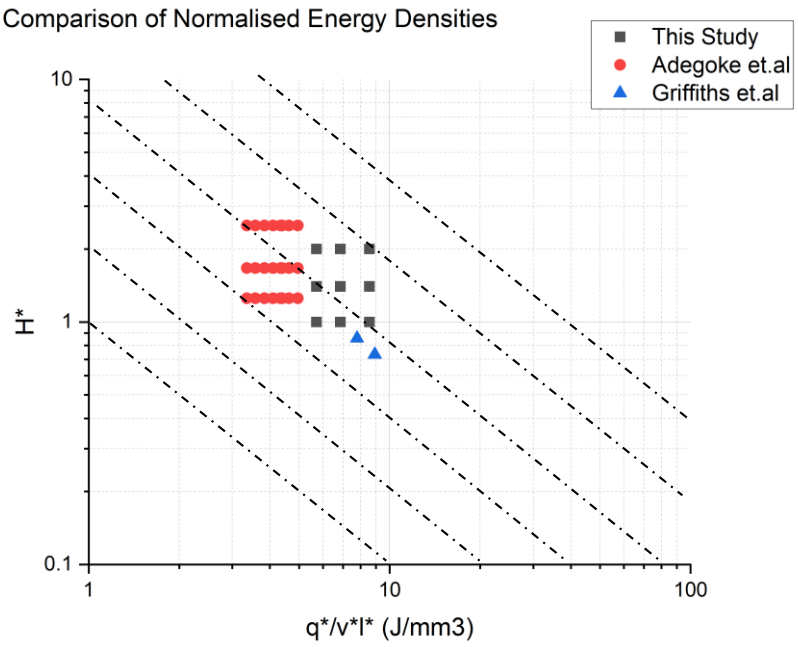

Figure 6.22 Comparison of normalised energy densities of several studies examined within this body of work.

Again, normalised energy is described by equation 2.6, repeated below:

$$\frac{q^*}{v^* l^* h^*} = \left[\frac{Aq}{(2lvr_b)}\right]\left[\frac{1}{(\rho C_p(T_m - T_0)}\right] \qquad \text{(Equation 2.6)}$$

Where A is the absorptivity of the material, q is the laser power, l is the layer thickness, v is the scan velocity, r_b is the beam radius, ρ is the density of the material and C_p is the specific heat of the material. T_m and T_0 are the melting temperature of the material and the ambient temperature of the powder, respectively. It is important to note that while the composition of the alloys being examined in this study will have similar specific heat and densities to that of nominal composition CM247-LC alloy, they will not be identical. However this impact is likely to be minimal.

Similarly to the work performed by Griffiths et.al, this study's hafnium-free samples show little to no cracking in the bulk material. In this study, this appears to be independent of process parameters, suggesting that the removal of hafnium does suppress the effect of strain-age cracking. However, the material contains a greater level of porosity. On examination, this porosity appears to be exacerbated in the lower energy samples, suggesting that the cause of these defects is lack-of-fusion due to insufficient energy input and there appears to be a greater level of gas porosity in the samples with hatch spacings of 35µm.

6.5 Summary

The impact of changing the content of hafnium in the CM247-LC alloy composition has been investigated through both simulation and experimental verification. Several different crack susceptibility models have been explored to determine which closest approaches reality.

Verification of these models has been performed by mixing standard CM247-LC alloy with a depleted hafnium version of the material. By mixing specific amounts of the two alloys together, alloys close to CM247-LC with different hafnium content can be produced through in-situ alloying in the Aconity LPBF printers. The change in hafnium content alters the defects produced during printing with identical parameters, highlighting the importance of specific elemental additions in complex alloys. In this instance, it is shown that the removal of hafnium from CM247-LC reduces the scan velocity of the beam required to produce higher-density components.

An examination of the crack behaviour of these alloys has also been undertaken, with a moderate agreement with models. It has been determined that the removal of hafnium results in the loss of grain boundary pinning effects seen by nickel superalloys. Ductility Dip Cracking is the likely cause of the increased cracking seen in the low-hafnium content material.

7. In-Situ Monitoring and Control in AM

7.1 Introduction

This chapter follows a study performed with the Aconity Mini to determine if live process control is possible with LPBF systems and how allowing an Advanced Neural Network (ANN) model to control the process yields variable results.

An in-situ control system developed in part by Lyle [168] was employed to determine if direct control of laser parameters by an ANN could influence the final material quality of parts produced via LPBF. Two materials were chosen for this study – CM247-LC and IN939. CM247-LC has an identified processing window with much pyrometry data available to provide an expected response (as detailed in both earlier chapters). IN939 has never been printed on either of the Aconity Systems in Sheffield before, making this a relatively unknown alloy system to work with. Further to this, there is very little literature on the processing window of IN939 in LPBF, making it a highly novel material to examine.

Once samples were manufactured, they were sectioned and polished for optical microscopy. Dense samples underwent hardness testing to provide information on both the material behaviour and the consistency of samples produced using an inherently variable process. The intention of this work was to determine if changing parameters according to a model's suggestions during a build caused major changes between different sets of samples.

As a final experiment to demonstrate the importance of controlling other parameters, tiles manufactured from IN939 with varying hatch spacings were analysed using both metallographic preparation and with a 3D scanner. Surface roughness is extremely important both during a build and in the post-processing sense. The use of a portable 3D scanner was investigated to determine whether or not integration into the Aconity systems was viable.

7.2 Code Overview and Workflow

Lyle [168] details the creation and testing of an advanced neural network (ANN) model to be applied to LPBF. This model analyses pyrometer data from previous layers in the build using a supercluster in the University of Sheffield's ACSE department (sharc) to generate a set of neural networks (one for each component in the build). This system utilises a surface-response optimised solution methodology (similar to that used in a traditional DOE) [85]. By comparing the average temperature across the surfaces of parts with a target temperature that the user sets, the program determines what laser power and scan speed should be used for the next layer, and then repeats this for each layer of the build (figure 7.1).

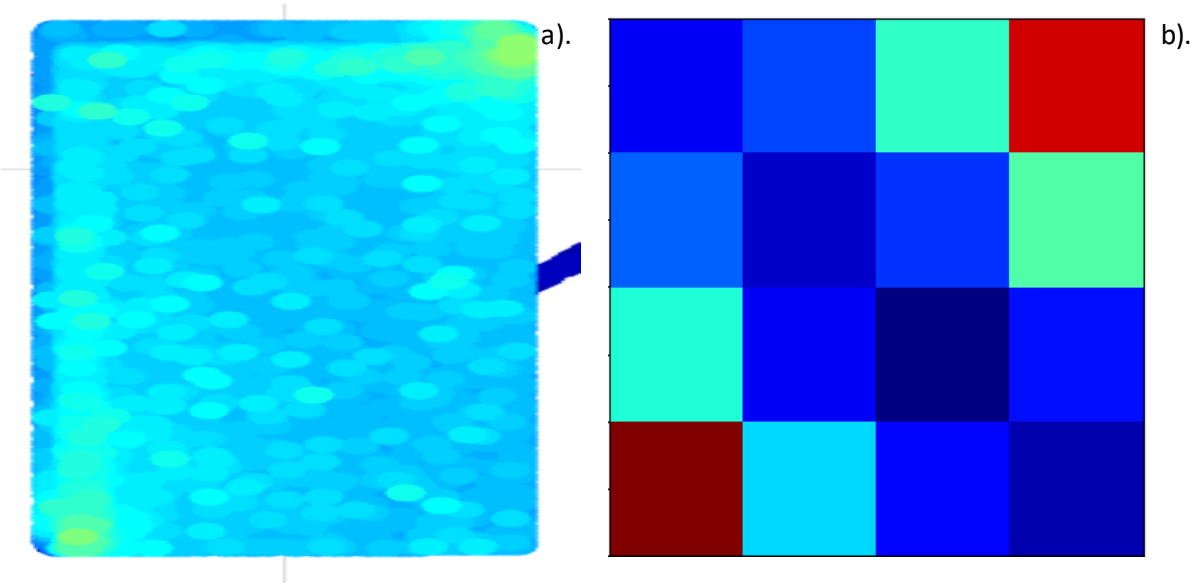

Figure 7.1:a). A direct representation of the pyrometer data produced via matlab from the electronic temperature data. b). The control system averages the pyrometer data across the object in question, in order for a simplified calculation of parameter choice. The red squares denote where hotspots are likely occurring.

The neural network uses a linear regression model to predict which laser parameters will produce the closest layer temperature to the target value in mV. The system uses a tolerance of ±40mV to determine whether the algorithm receives a reward or not. This "rewarding" is a feedback system to inform the algorithm whether it is succeeding or not, allowing the algorithm to be more effective in its pursuing of parameters. The algorithm eventually settles into a local minimum, where it has self-optimised for the target temperature, proceeding to maintain effectively (within a tolerance that is set by the user) the layer temperature at a consistent level.

This in turn drastically reduces the defect density in the produced components, as it significantly reduces hot or cold spots in the layers. The "temperature" that the Aconity Mini's pyrometers detect and output is an electronic reading produced by the pyrometer. Every point of data in the pyrometer's data set is the average value of all of the data collected in the pyrometer's field of view at that time. The effective rate of sampling is variable as it is tied to the speed of the movement of the laser galvanometers. The pyrometer's field of view is coaxial to the laser, meaning that data is always from the melt pool and the surrounding area.

The intention of using temperature as a measure of material response is twofold. Firstly, it is a relatively easy response to measure, as it can be measured by coaxial sensors that detect emissions from the region immediately near to the melt pool. The data can be easily manipulated and analysed as it is written as a .csv file, which can be opened in matlab, python or even excel. Secondly, the temperature at which a material begins to emit radiation is fixed, meaning that cooling from a particular radiance temperature should give a consistent microstructure and thus consistent properties. This runs counter to the rather stoichiometric nature of the LPBF process, which can never be identically repeated due to the discrete nature of the powder particles.

Any number of cubes can be manufactured using this method, but more cubes means a greater amount of computational loading on both the local PC and the supercluster. Whilst the supercluster can deal with the increased loading, the local PC struggles to cope with the data transfer if any more than around 20 cubes are produced. This is also exacerbated by the size of the components as well – i.e. a 10mm cube is 8x larger than a 5mm cube. Furthermore, there is no physical direct connection between the local PC and the supercluster – the data must be sent wirelessly. This unfortunately means that a far longer time is required for the data to be read at both ends.

As well as the cubes that are being manufactured with the control algorithm, at least one cube must be built before the rest of the parts in a layer. The reason for this is twofold. Firstly, the cube acts as a control cube, showing how the material reacts when the parameters do not change from their base starting point of 120W and 1125mm/s. Secondly, due to the way that the Aconity Mini interacts with the control algorithm, the first cube is produced before the data from the supercluster is read. This only occurs after the first part has been completed for that layer. When the machine pauses to read and apply new parameters, the pyrometer does not stop recording, meaning that much of the data for the first cube is simply junk data and serves no purpose. Around 10x as much data is generated by this first component, as the delay is long due to the amount of data being read. This makes it useless for the machine learning code. To combat this, the first cube is always a non-controlled cube, to prevent incorrect data from being used and affecting the control system. The algorithm is also capable of performing repeats of a particular measurement.

The biggest challenge by far facing the AM process is the time it takes for new materials and part geometries to go from the designing stage to full production. Very often, complex parts will have features that do not lend themselves to the AM process, such as thin wiry sections (such as lattices) overhangs and sharp corners, which both tend to overheat. Because of this, the use of a single parameter set is not ideal, because what may produce a dense result for a large thick section of material may overheat a very thin lattice that is part of the same component where the material does not have as much of a heat sink effect. One solution to this problem is to split components down into their constituent sections and provide a different parameter set for each. However, this is extremely time-consuming and is not realistic for components that have extremely high complexity. This also drastically increases the file size of components.

Currently, an LPBF build maintains the same set of laser parameters for each component throughout the entire build. Whilst this can work well for simple shapes such as blocks, complex shapes with changing geometries can suffer from overheating or insufficient heating at thin or thicker sections respectively. Because of this, it is desirable to obtain a method for controlling the temperature of each layer, which is what the automatic control system is designed to do.

The automatic control code's workflow is detailed below in figure 7.2. The system runs in python, which allows for easier integration into the Aconity's operation. This python code analyses layer temperature data from the pyrometers and sends it to a supercluster (ACSE). This supercluster consists of a set of advanced neural networks – one for each part – that analyse the data provided and use linear regression models to determine the next layer's laser power and scan speed. By doing this, it is possible to exert a great degree of control over the defect density of a component and greatly reduces the frequency of build failures.

The control system examines the pyrometer data obtained by the Aconity Mini during layer production. On a part-by-part basis, the data is sectioned and divided into a set of cells (see figure 7.1). Dividing and averaging into sub-parts makes the ANN-driven computation much faster, as fewer data points are then carried over for its analysis.

Cubes may also be grouped and analysed in sets. This action connects neural nodes together, allowing data to be shared across the linear regression calculations for components within a group, which can further alter their behaviour. This results in set-to set variation, but cubes within each set can be very similar and consistent.

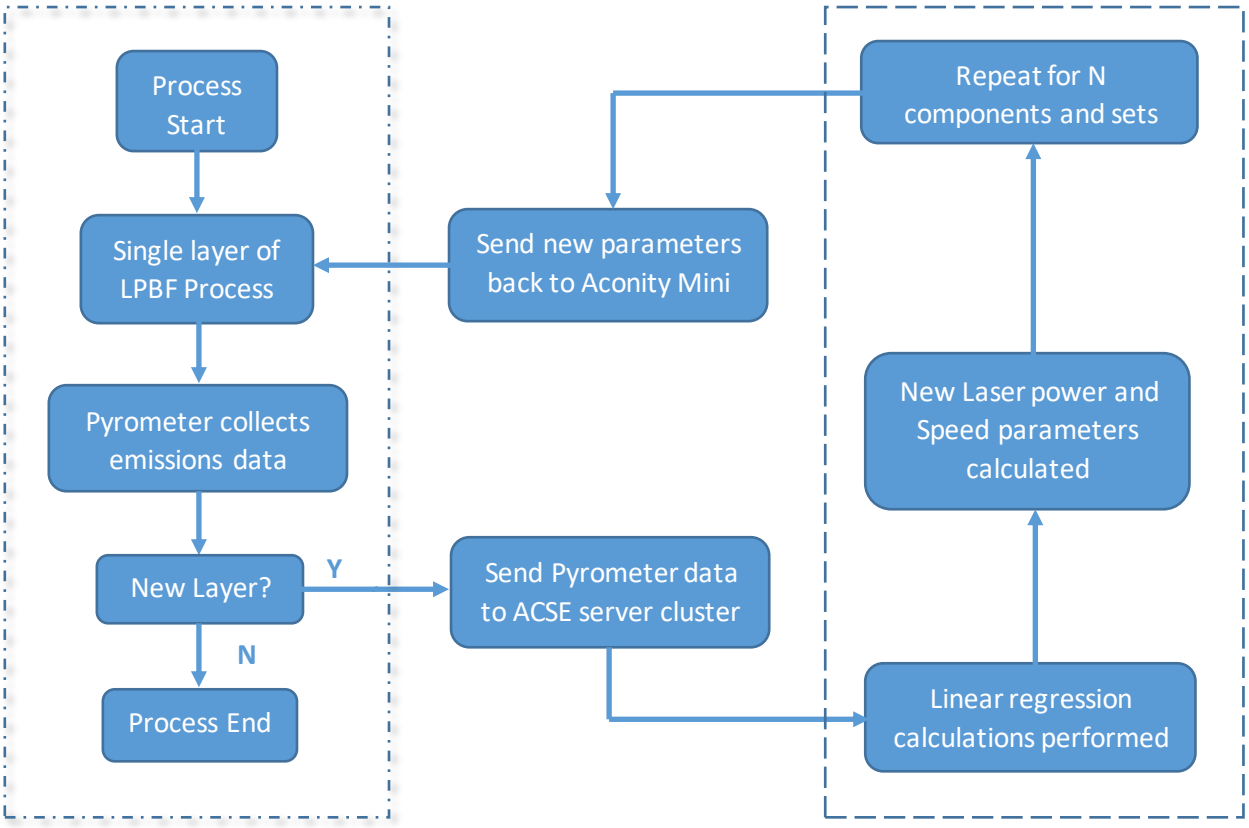

Figure 7.2: A flow chart to illustrate the steps involved with the operation of the control algorithm. The two dashed boxes denote the processes that occur locally on the Aconity (left) and those that are performed by the advanced neural network (right).

Challenges still exist in the implementation of this system however. The first is the application of the algorithm to complex, non-cubic shapes. When the pyrometer splits data into sections in order to average the values across regions, it does so into either square or rectangular shapes. This can cause problems for irregularly shaped components such as a lattice, or at edges and corners, as a significant proportion of this section of the component is empty space. When the area containing this feature is averaged, this relatively cool area can bring the average temperature down, potentially causing problems as the program attempts to the compensate by increasing the energy input. This can cause hot corners to get even hotter and can damage or destroy delicate features like those found in lattices.

The second challenge faced for this algorithm is mid-layer control. Currently, due to how build files are produced, it is difficult to effectively split a single layer into sections to be controlled differently by the machine-learning program. This is detailed further in chapter 6. In short, while in-situ control can reliably influence the quality of bulk material, corners and edges will still suffer from overheating due to rotations in hatching strategy and the insulating effect of powder. Ideally, the algorithm would be able to use different parameters in different sections

of a build. Currently, it is limited to interlayer control only, which limits the ultimate effectiveness of the control system. A hardware upgrade to the Aconity laser scan-head is required before this can be implemented.

The final obstacle to progress and arguably the most important is the local computational limitations of the Aconity Mini PC and the quantity of data that the pyrometers produce. Whilst the PC is adequate for operation and handling of pyrometry data, the machine learning calculations cannot be performed locally. Instead, data must be sent to the ACSE server cluster. This presents a problem, as packing and sending, then opening and reading such a vast quantity of data wirelessly takes time. The data also has to be returned via the same method, which further exacerbates the problem. This transfer of data causes the build to pause after each layer, which chronically slows the build process. Builds can take 4-5 times as long due to this pause for data transfer. This pause makes the algorithm unsuitable for industrial application in its current state, as even a small change in thermal history in a part can affect the lifespan of a product. In addition to this, the memory of the local PC is relatively small compared to the large quantity of data that is produced per build. Data is often in the order of hundreds of gigabytes in size, making storage a problem. This data must be regularly wiped, otherwise the Aconity PC will pause the build, as it is designed by the manufacturers to do. In the case of a control algorithm build, this can cause a crash as the system encounters an unforeseen stop.

The system analyses the 16 square regions in the averaged plot before calculating the RMSE (root mean square error) of the distribution. This is a similar calculation to standard deviation but is designed instead to be a comparison of predicted temperature to actual temperature. The standard deviation of each layer is also calculated.

7.3 Experimental Procedure

A plan to test the robustness of the system was carried out, consisting of several builds with different materials. The chosen materials were CM247-LC and IN939. These materials represent a range of industrial alloys relevant to this project, each being chosen for a different reason. CM247-LC was chosen for its relevance to this project and the interest surrounding it industrially and IN939 was chosen for its relative novelty in LPBF processing.

For each material, a target temperature in millivolts (as the pyrometer produces an electrical signal) was required, in order to tell the control algorithm what to aim for when calculating the laser power and speed. This was determined for the materials by examining the pyrometer data of previous builds that were successful and produced parts that were of high density. For CM247-LC, this was set at 1040mV. For IN939 this was set at 1000mV. Laser power and speed begin at 120W and 1125mm/s respectively, as these are "middle of the road parameters" that are compatible with other alloys, if not ideal. Hatch spacing was chosen to be 35µm for both alloys. This hatch spacing is compatible with CM247-LC (as shown in chapter 4), but for IN939 the "ideal" hatch spacing is completely unknown.

As well as the data that can be obtained from the micrographs of manufactured components, it is also possible to glean a significant amount of data from the machine learning system. By analysing the chosen laser powers and velocities across the layers of the build, it is possible to determine whether the system is succeeding in determining a method for maintaining as consistent a temperature as possible (figure 14). In this case, a tolerance of 40mV is used as a range for "positive" feedback.

There are two operational modes for the control algorithm. The first produces a neural network for each component, analyses the data for each cube individually and builds a model based on that data alone. The system uses a simple linear regression model to build a picture of how the LPBF process works, aiming for the target temperature and controlling the input power and speed. Every part has a slightly different data set and thus behaves differently.

The second mode is slightly different. Instead of keeping the data separate for every cube, the other operational creates "sets" of cubes, where data is shared between each of the individual models within each set. By doing this, the cubes have a larger data set to draw on when calculating their parameters. Whilst this is slightly more computationally taxing, for a supercluster it is not a large change and the amount of data transmitted between the supercluster and the host PC remains the same as for the other operational mode.

7.3.1 CM247-LC Results

A total of 17 10x10x5mm test pieces were produced through the control algorithm on the Aconity Mini. While all of the components finished the manufacturing process and built to the full height, they all suffered from significant levels of cracking and porosity (figure 7.3).

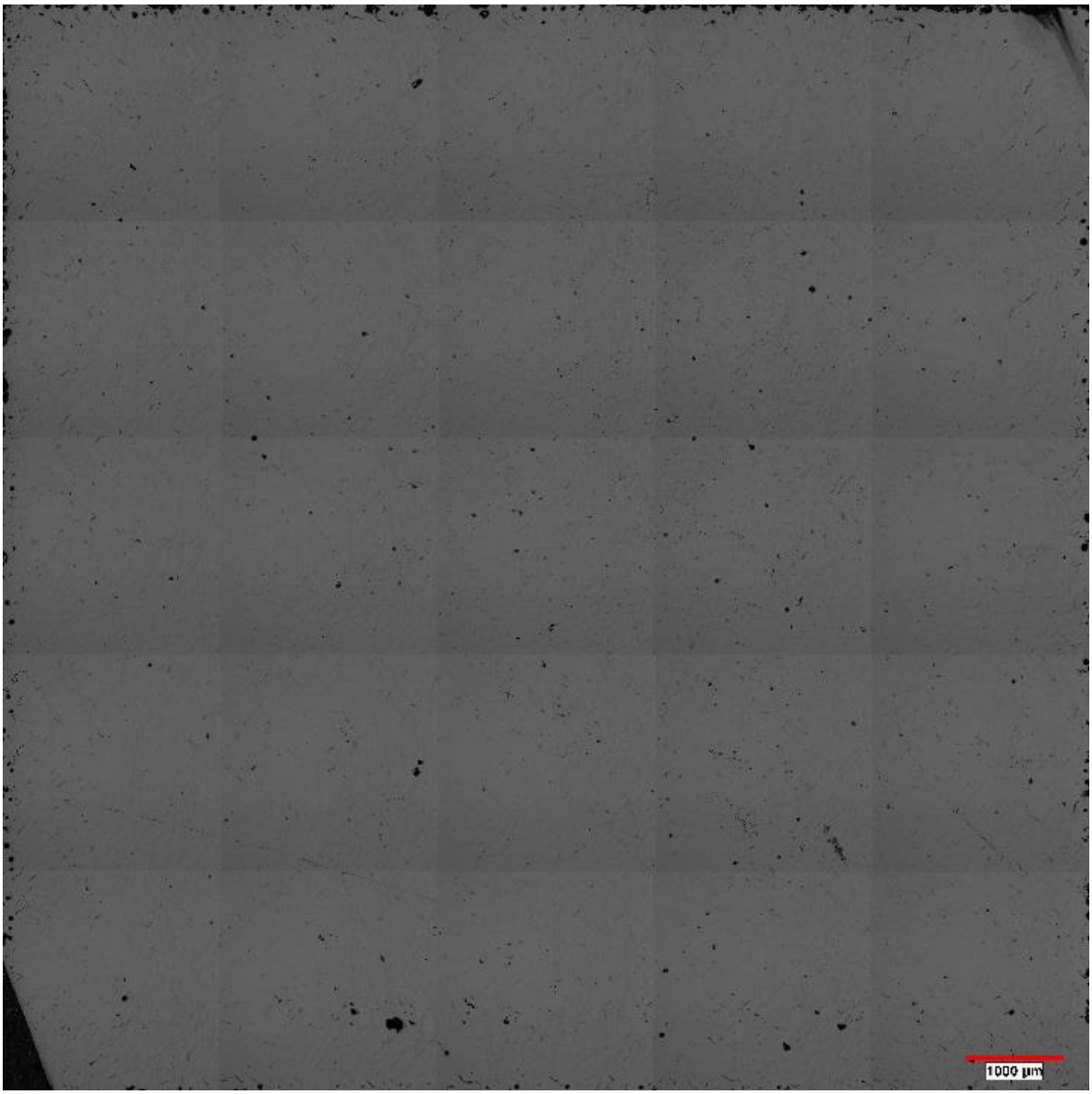

Figure 7.3: A representative X-Y plane (top down, build direction towards reader) micrograph of the CM247-LC manufactured via machine learning assisted LPBF. Both cracking and keyholing are present in the CM247 samples, suggesting that the target temperature may have been too high or too low.

Starting parameters chosen were the same as used in previous experiments with the closed loop control system on the Aconity Mini. A starting point of 120W laser power and 1125mm/s scan velocity, together with a 1000mV pyrometer temperature target was selected as an arbitrary starting point. A hatch spacing of 35µm was also used, along with a 30µm layer thickness, to provide consistency between this and the previous CM247-LC machine learning experiment.

20 5x5x5mm cubes were manufactured in total, with the first two of these cubes built to act as the control and redundancy components. Other than the starting parameters and target temperature, the conditions of the machine learning code were identical to those used in the CM247-LC experiment in the previous chapter. These cubes were not grouped in sets – instead being analysed and controlled individually.

7.3.2 IN939 Results

All 20 of the cubes were successfully fabricated, with varying degrees of porosity and component quality. The first two components, built to accommodate the inefficiency of the data handling of the code and as control options, suffered from large amounts of cracking. Cracks in these samples can be seen throughout the entire sample and distinct unevenness can be seen at the top of the component, suggesting that swelling may have also been occurring and further compounding the deleterious effects of incorrect parameters with those of poor powder spread. Most cracks are aligned with the build direction and once the components were etched, the cracking was particularly noticeable around grain boundaries. Examination of other components revealed not only cracking, but also keyholing voids that arise when the laser energy is too high and creates melt pool instabilities. All of the samples manufactured in this experiment show at least some level of defects, but there is a large variation in the defect types and densities across the set.

Figure 7.4 shows the data from the component that contains the fewest defects and its corresponding graphs. Figure 7.5 shows a micrograph of the cube in question.

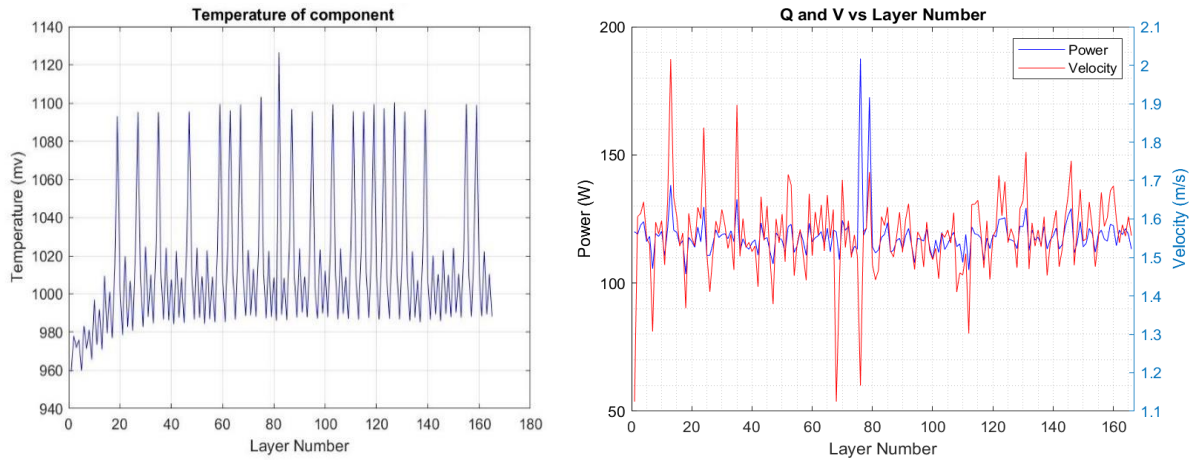

Figure 7.4: The layer temperatures (left) and input parameters (right) of an IN939 sample (group five, sample 2) with high density. The system tries to keep the temperature at the set-point of 1000mV and whilst it does spike at some layers, it always returns to within 40mV of the target.

These represent a range that is commonly explored in traditional LPBF parameter optimisation strategies. The cubes were monitored and controlled in 6 sets of 3 (plus the two precursor cubes that were not controlled). The precursor cubes were very heavily cracked (figure 7.5). Cube sets were compared to examine the different outcomes of the automatic control system.

Initial examination shows clear differences between each set of samples. Particularly sample set number 2. This set was far more heavily defected than the other sets of cubes, showing major lack of fusion defects through all of the samples (figure 7.7). Other sets were very consistently manufactured, with far fewer defects visible (figure 7.6).

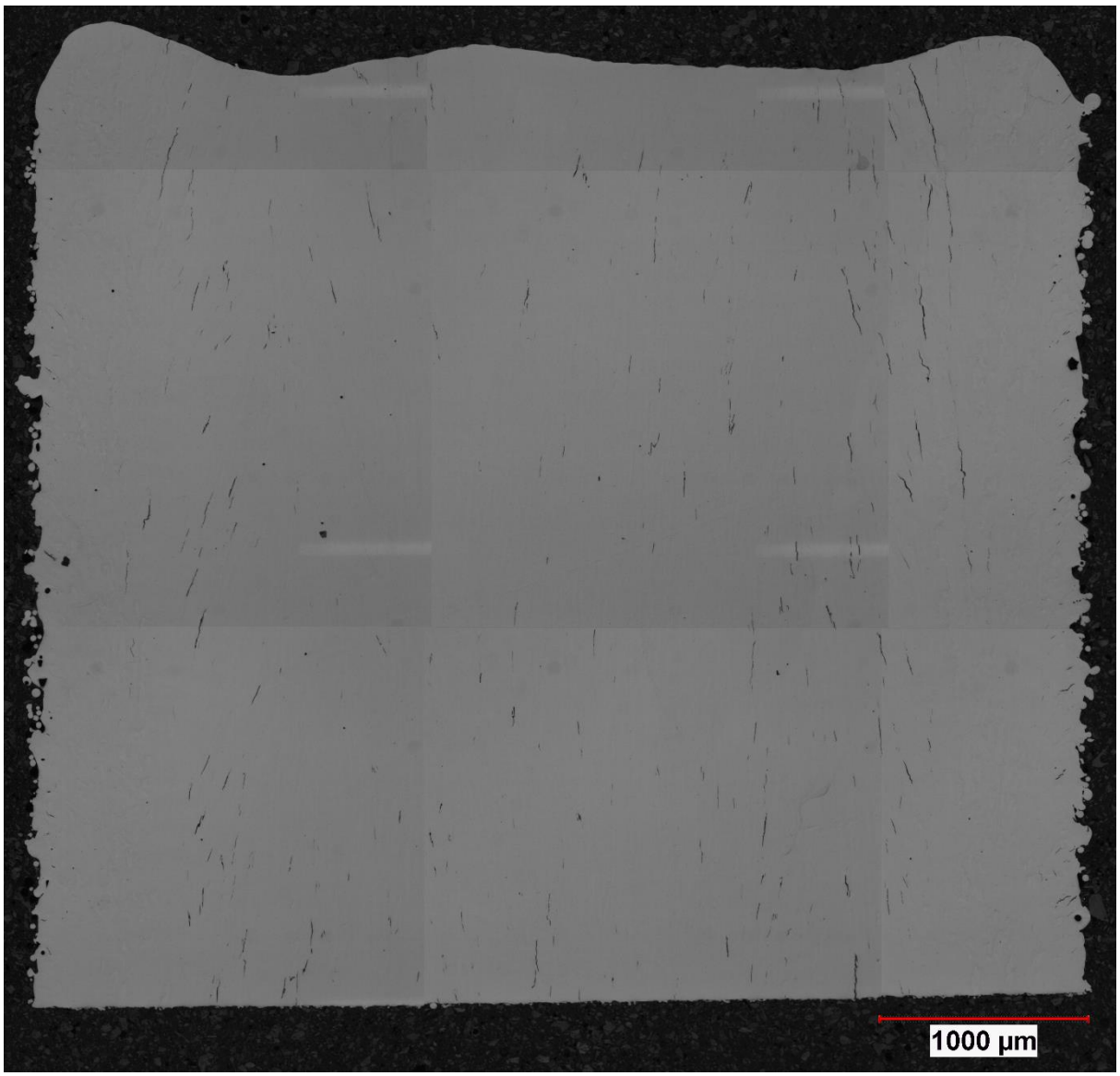

Figure 7.5: A precursor control cube built with a single set of parameters (120W, 1.125m/s). Cracks still travel along the build direction and are highly pronounced in this instance.

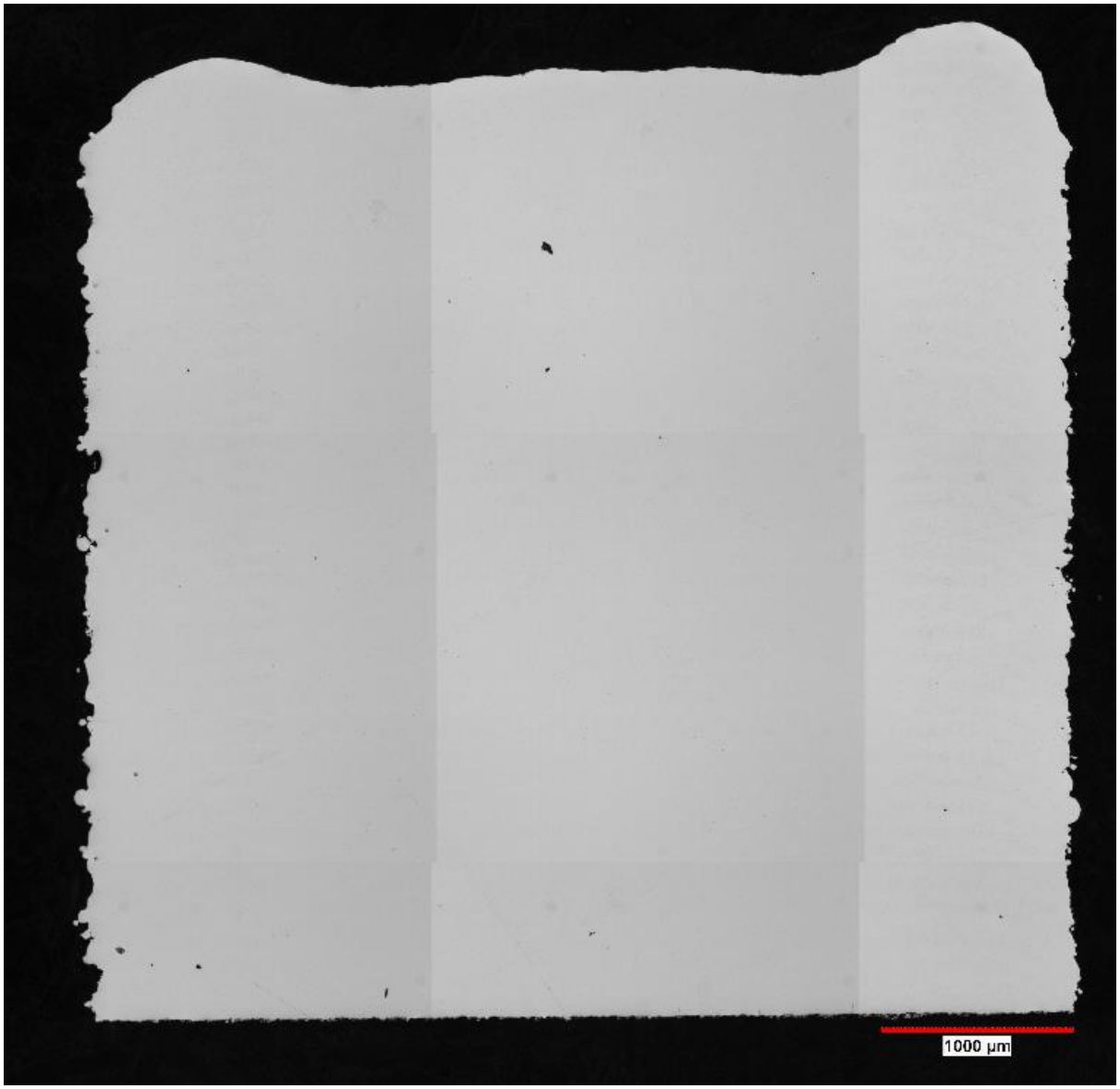

Figure 7.6: Example of machine learning-assisted component produced on the Aconity Mini from IN939. This sample is from set 5, which is one of the more densely built set of cubes.

A comparison of cubes from the different sets and their corresponding powers/speeds is shown below in figures 7.7 and 7.8.

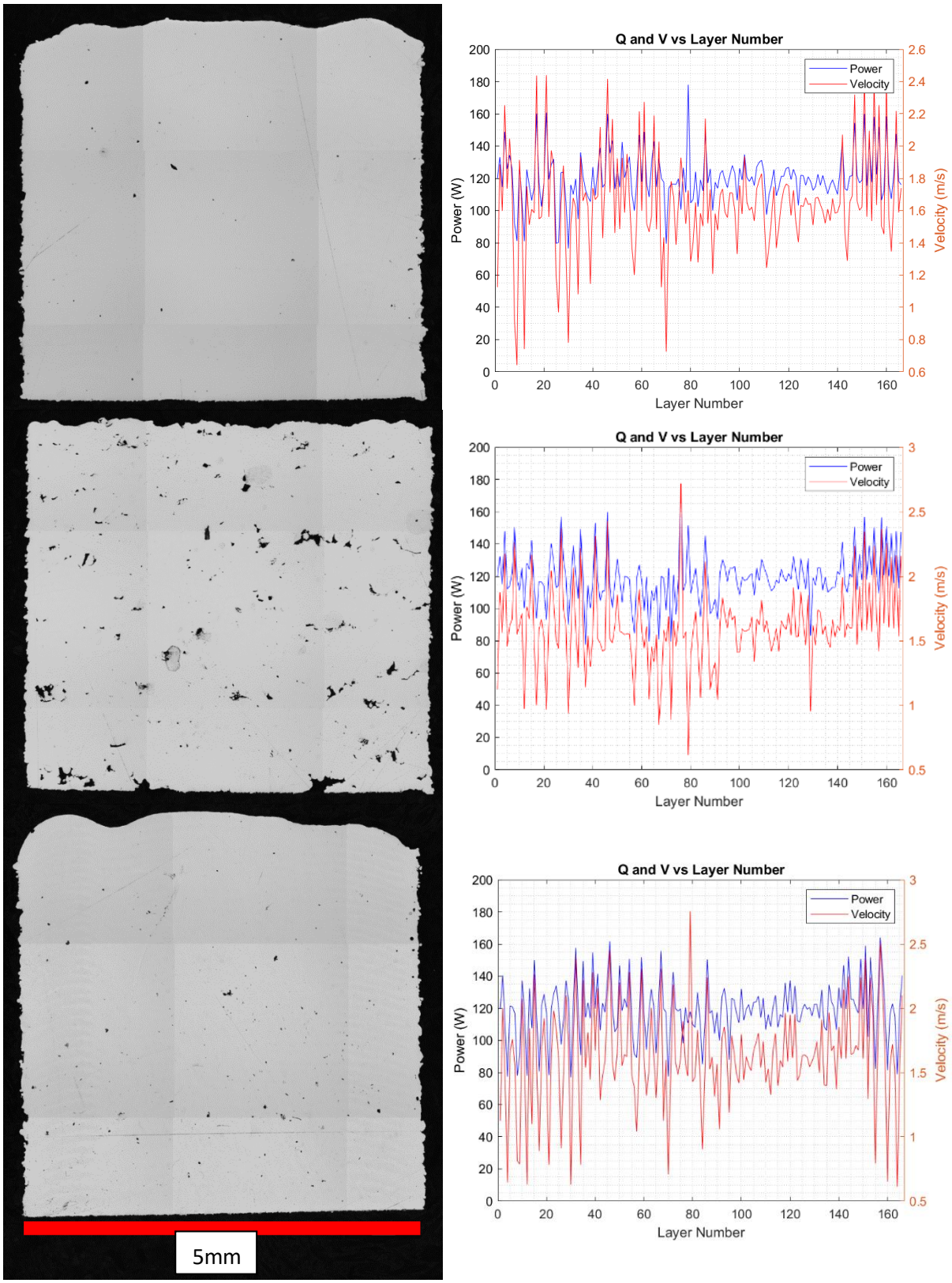

Figure 7.7: Micrographs of samples from sets 1-3 (left, top to bottom) and their corresponding temperature profiles (right, top to bottom). Scale correct for all images.

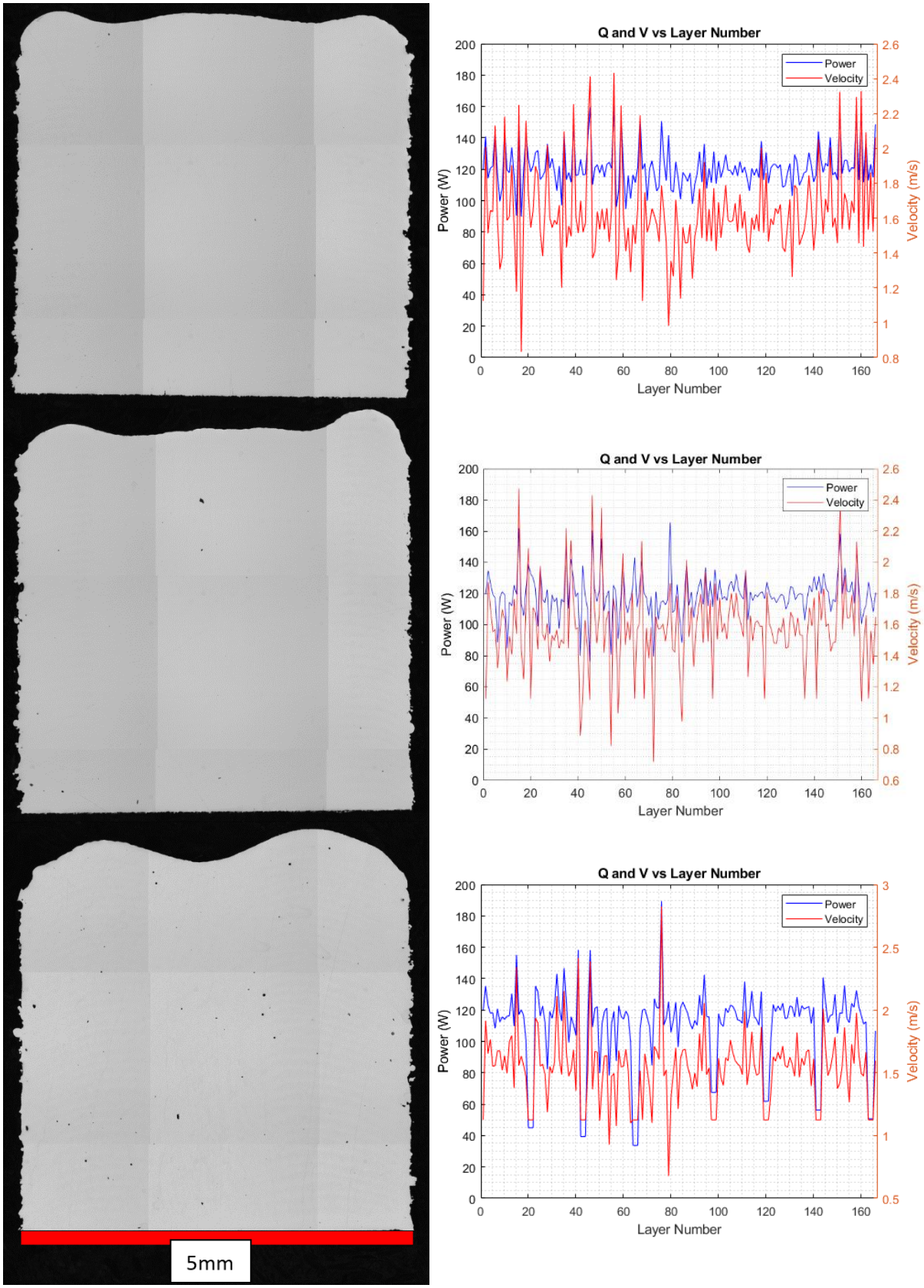

Figure 7.8: Micrographs of samples from sets 4-6 (left, top to bottom) and their corresponding temperature profiles (right, top to bottom). Scale correct for all images.

Some of the more dense samples produced using the machine learning algorithm were etched. Figure 7.9 shows the revealed microstructure of the same sample as in figure 7.5. This sample was etched alongside CM247-LC samples. This etching process took around 5 minutes longer for the IN939 to reach a satisfactory level where grains were visible. The CM247-LC took between 13 and 15 minutes to etch depending on the number of defects in the samples. Given the high quality of the samples, it is likely this has reduced the surface area for chemical attack, contributing to the alloy's longer etching time.

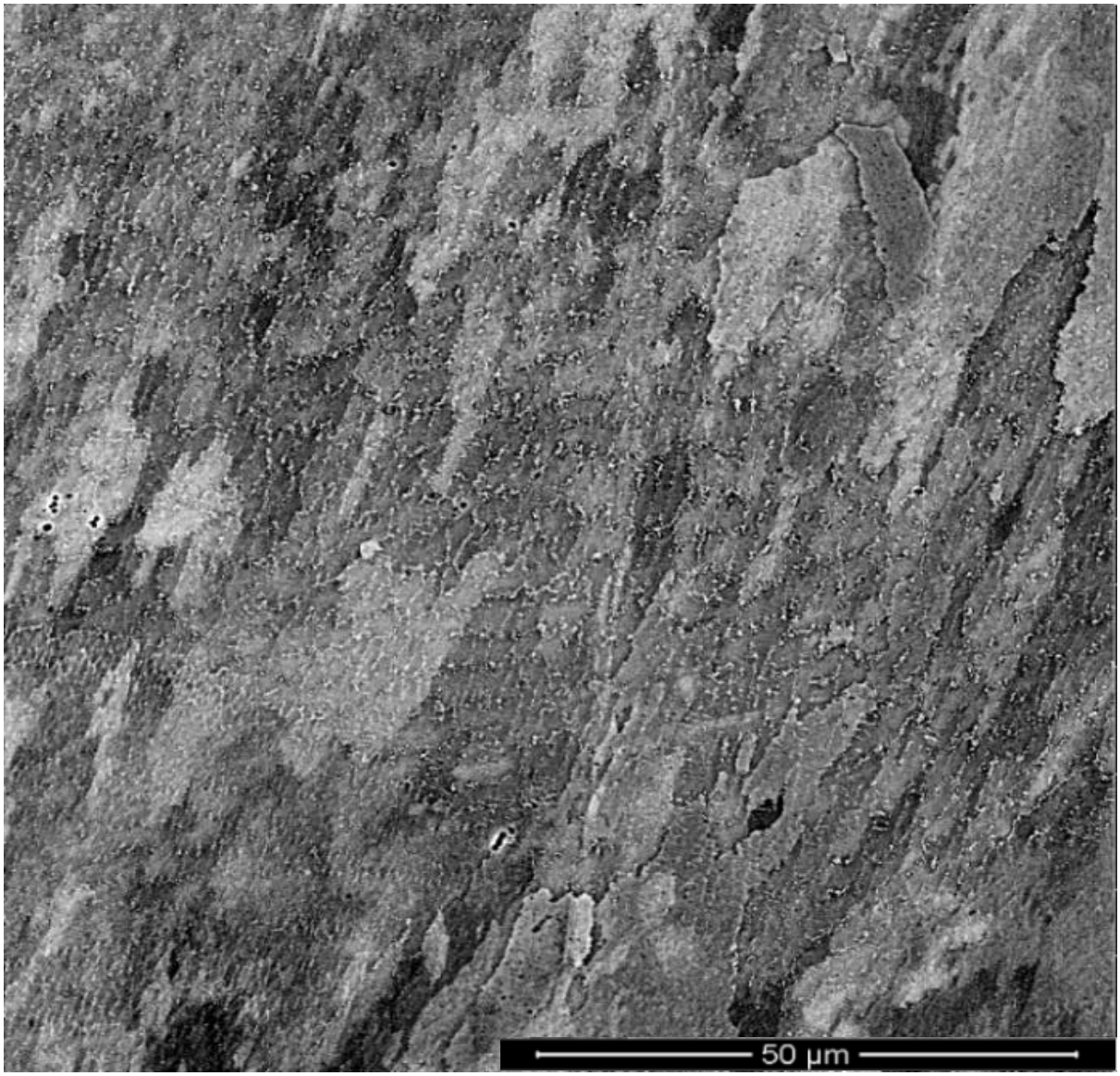

Figure 7.9: The etched microstructure of an IN939 sample produced through LPBF. This is a standard LPBF microstructure consisting of small solidification cells.

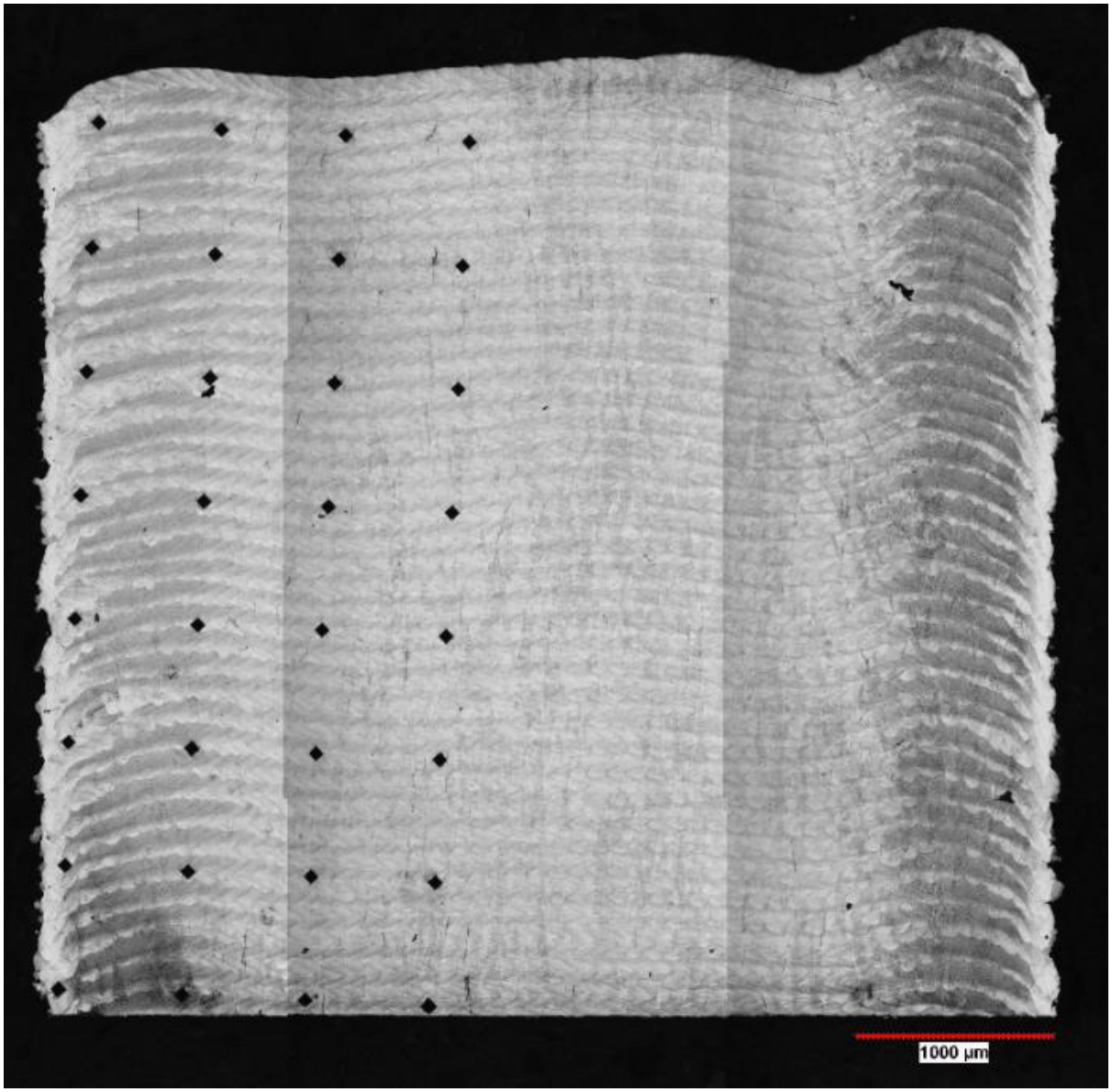

Figure 7.10: Similarly to other samples produced in this study, a more evolved microstructure is noted at the edge of the samples after etching. The black dots in the micrograph are from hardness testing indentations along the left side of the sample.

Ensuring that the automatic control process has had a tangible effect on the build is difficult with such small and non-representative components. Using density as a measure of success is one option. Another option at this geometric scale is to use hardness indentations to examine how consistently the material has been produced. To provide consistency, a similar pattern of indentations used in previous chapters (7x4, spaced by 0.625mm) was used to provide meaningful comparisons.

With the exception of one group of samples (group 2), the manufactured material was extremely consistent in terms of hardness. Sample group 2 was omitted from hardness testing due to its high level of porosity. This would have made hardness testing unreliable, as the array of points would fall on regions where no metal is present, which would artificially skew the results. Figure 7.10 shows the hardness of the remaining 15 samples produced with the ANN-assisted LPBF process.

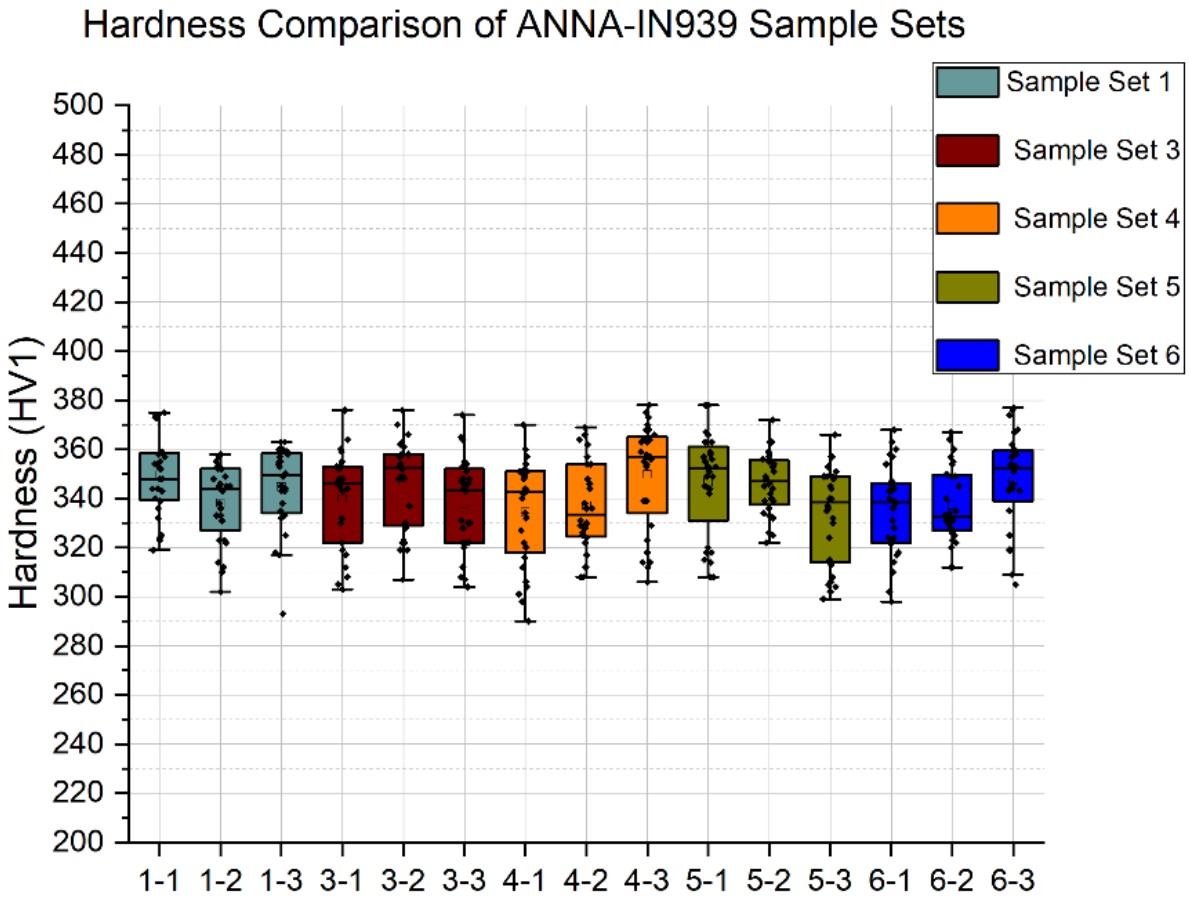

Figure 7.10: Comparison of hardness values from ANN-Assisted IN939. While there is batch-to-batch variation, the material hardness remains largely consistent.

As well as the comparison between different sets, each sample can also be displayed as a hardness map across the surface examined (figure 7.11). While the hardness is not as high as that of CM247-LC, it is likely due to the alloy's lower γ' content. As mentioned in chapter 2, many nickel superalloys (including IN939) produced by AM have a suppressed γ' phase due to the rapid solidification rates in the AM process. This phase can then be aged out through subsequent heat treatments, but this can also cause cracking in certain alloys (like CM247-LC).

As with CM247-LC, the alloy displays a tendency to lose material properties with increased proximity to its edge. However, in many of the samples produced with the machine learning algorithm, the drop-off in hardness is much more clearly defined than in samples produced with single parameter sets. The rotation strategy remained constant during all builds performed in this study, and can be ruled out as the cause.

To further characterise the impact of the machine learning algorithm on the material properties of samples, a series of tensile test coupons were planned to be performed. However, two problems arose during attempts of this procedure.

Firstly, tensile bars were attempted in the horizontal orientation. This was done to try to minimise the number of layers required for processing, as each layer slows down the machine learning algorithm due to the increased complexity of the model. With only 7 components per layer, this at first appears to be a trivial exercise for this program. With a larger area of building however, the amount of data starts to become much greater than for a series of cubes. Even after only 50 layers, the load was too great for the local computer and crashes became frequent, making use of the control algorithm impossible. The machine learning program is slightly unstable even with a small series of cubes, so the use of large parts makes the procedure extremely unreliable even with "routine" builds.

Secondly, insufficient IN939 powder was available to build tensile bars in a vertical orientation. Using a more plentiful/readily available material would present the same problem with computer crashes as mentioned previously. Whilst the computational load per layer would be less and take less time to transmit, the number of layers would make it impossible to prevent crashes. A build of around 75mm, normal for tensile coupons, would take overnight. This would make it impossible to monitor for crashes and was thus not considered for attempt.

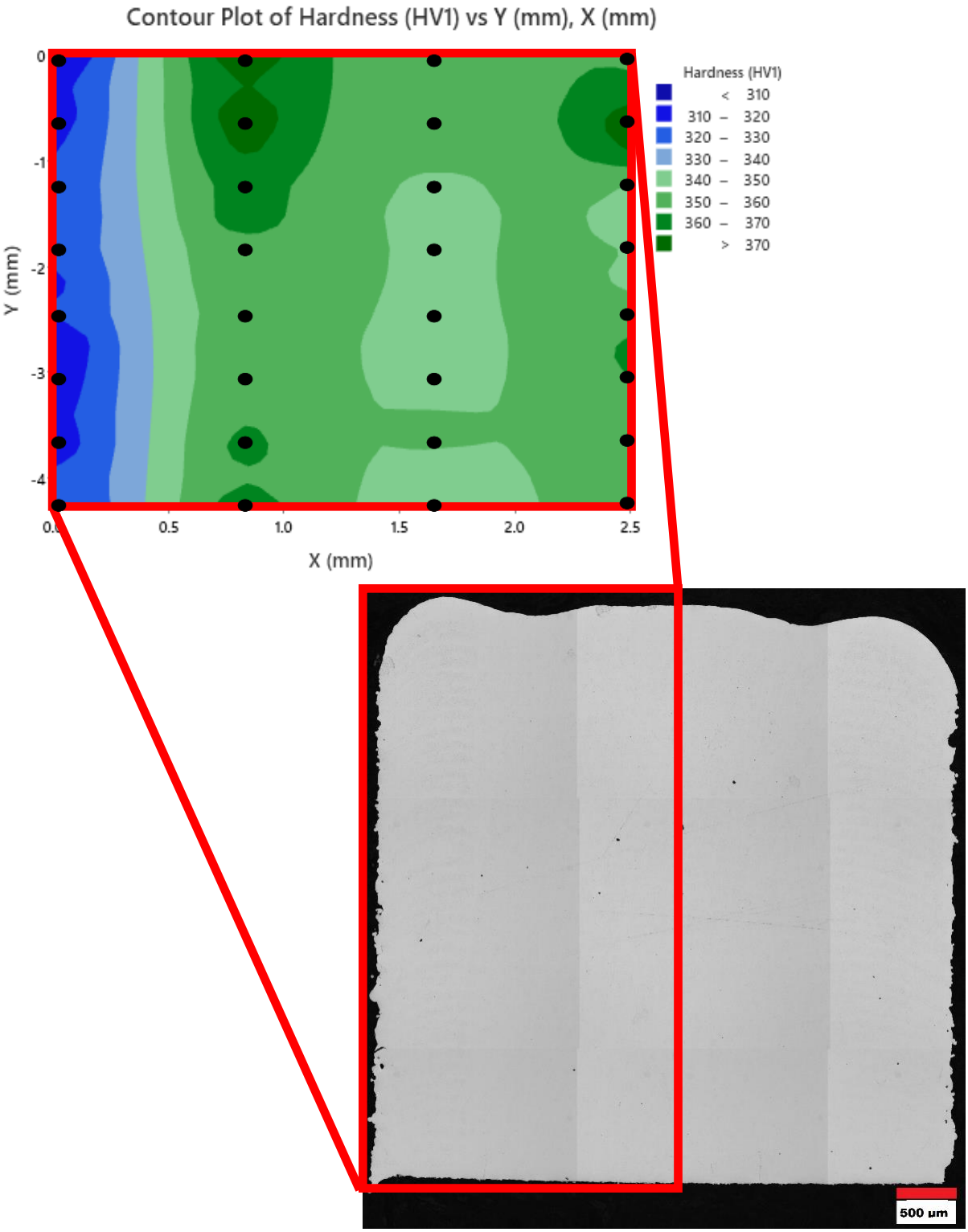

Figure 7.11: Hardness map and optical micrograph of IN939 produced using the automatic control algorithm on the Aconity Mini. The red box denotes the area tested on the sample.

7.4 Comparison to Single-Parameter Builds

In order to compare the effect of control and non-controlled builds, a traditional response-surface DOE was designed to attempt to determine a single set of parameters for manufacture of IN939. A set of 9 supported cubes of 5mm size was produced with the following parameters (table 7.2):

Table 7.2: Initial response-surface parameters used for a "standard" IN939 parameter study.

Sample Number	Power (W)	Scan Velocity (mm/s)	Hatch Spacing (µm)	Energy Density (J/mm^3)
1	100	1500	35	95.2
2	120	1500	35	114.3
3	140	1500	35	133.3
4	120	1200	35	142.9
5	120	1800	35	95.2
6	106	1288	35	117.6
7	134	1712	35	111.8
8	134	1288	35	148.6
9	106	1712	35	88.5

Once manufactured, samples were removed from the baseplate, mounted and polished to examine the quality and defect density of the material. The final sample, number 9, did not build properly and had to be cancelled shortly after the beginning of the process. Whilst the difference in energy density is relatively small, the effect on defect levels was significant. Figure 7.11 shows the response-surface diagram produced by plotting the density against the power and velocity changes. Density values for each sample were obtained using the 1340 Accupyc Pycnometer detailed in section 3.3.2.

With a parameter window determined for this initial set of samples, a second repeat of this methodology was performed. Using the parameters of the densest sample (in this case, sample number 3) as a guide, a set of new parameters were generated (table 7.3).

Again, these manufactured samples were removed from the build substrate, mounted in polyfast resin and polished to reveal the quality and defect density of the material. In this second experiment, the results are far more consistent. Most components are fully dense and little cracking or LoF is seen. Values of density were again obtained through use of the pycnometer.

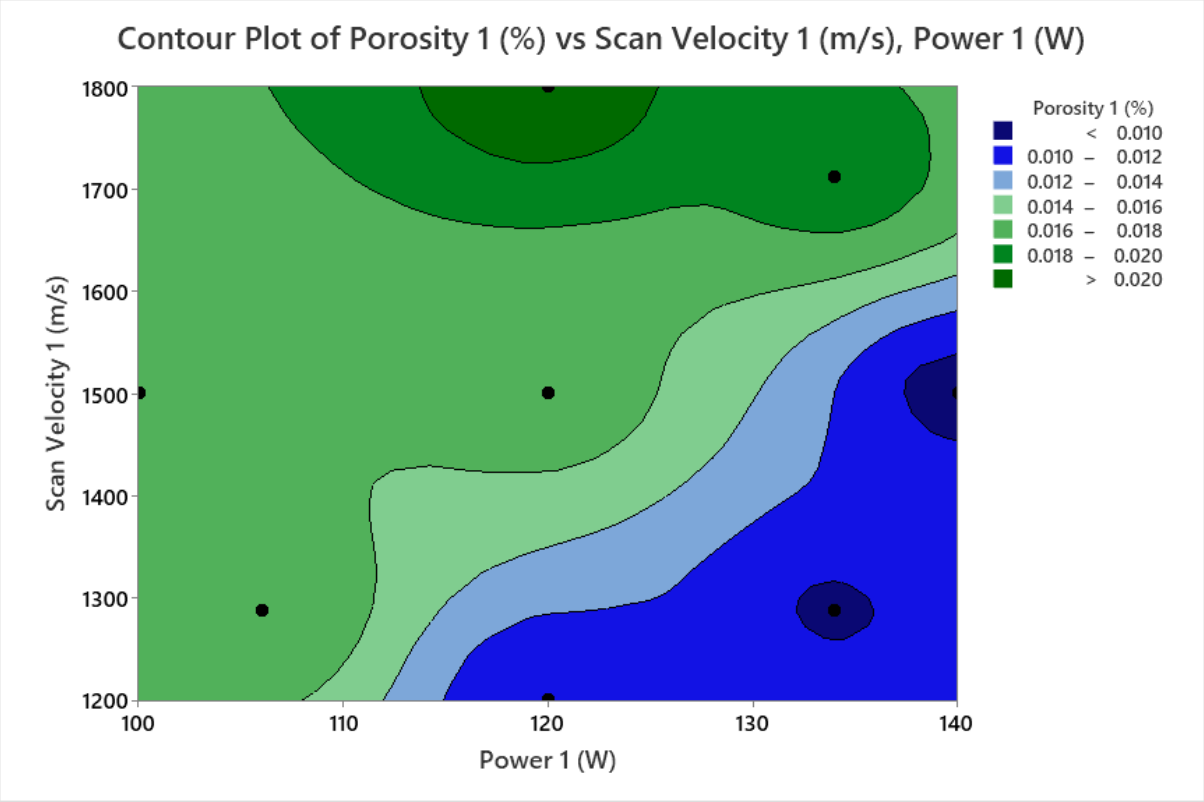

Figure 7.11: The initial iteration of a standard LPBF DOE build with 8 successful components. This graph shows the impact of laser parameters on the density of IN939 components. As can be seen by the scale, the impact is relatively small.

Table 7.3: Response-surface parameters of the second set of components manufactured with "standard" DOE methodology.

Sample Number	Power (W)	Scan Velocity (mm/s)	Hatch Spacing (µm)	Energy Density (J/mm^3)
1	126	1512	35	119.05
2	140	1300	35	153.85
3	154	1088	35	202.21
4	120	1300	35	131.87
5	154	1512	35	145.50
6	160	1300	35	175.82
7	140	1600	35	125.00
8	126	1088	35	165.44
9	140	1000	35	200.00

Final density values for all IN939 components are shown below in table 7.3. Even with two iterations of this experiment, this technique took effectively twice as long to determine a processing window than using the machine learning-assisted technique. This material only took two iterations, but more difficult-to-weld materials may take much longer to find suitable parameters for, especially if the material is extremely different to other nickel alloys.

To demonstrate further the effect of the control algorithm on the quality of the components produced, hardness mapping was utilised for both control-assisted and non-control-assisted parts. The procedure for this was identical to that described in the previous three results chapters.

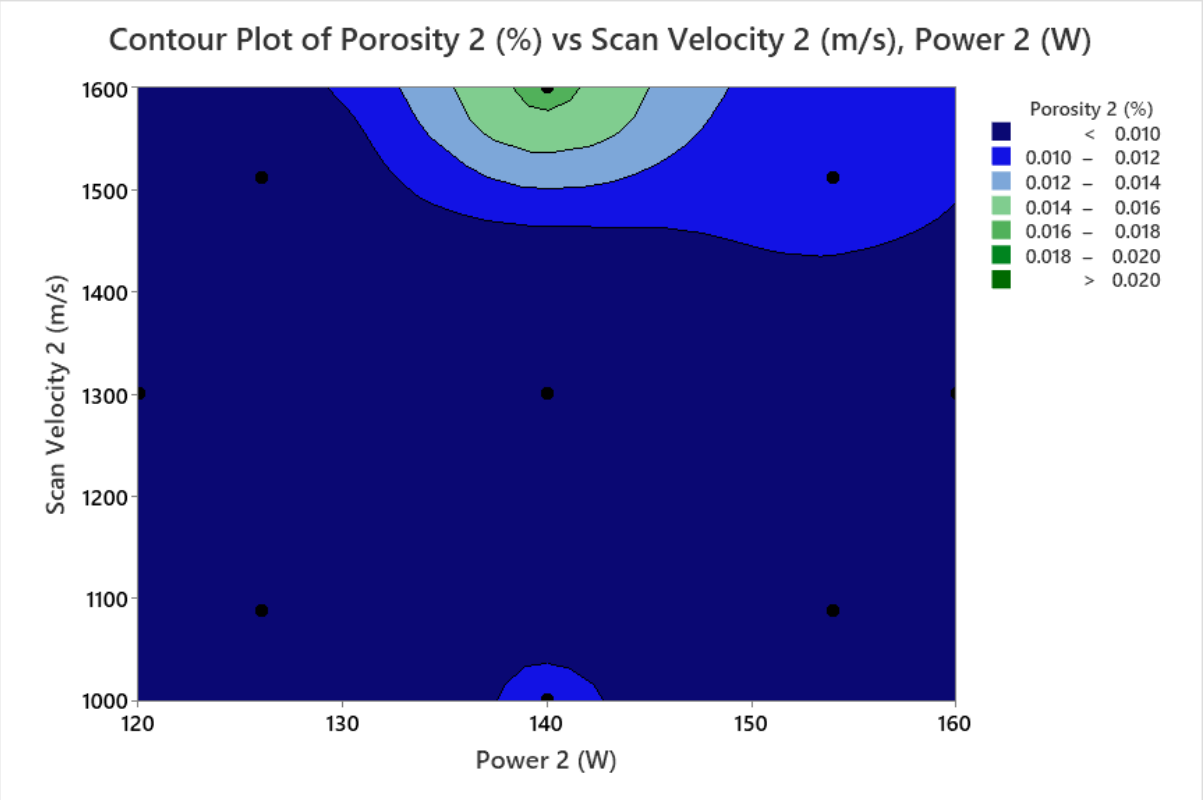

Figure 7.12: Second iteration of the IN939 DOE experiment plotted on the same hardness scale as figure 7.11 for comparison. This experiment provided a much more dense set of samples, effectively demonstrating the processing window as a "valley" through similar energy density regions.

With "ideal" parameters determined through this iterative process, these parameters were then used to produce tensile test coupons. A total of 7 coupons were built horizontally. This is the maximum that will fit in the Aconity Mini build volume. These test coupons utilised the same set of parameters that provided the most dense component – sample 6 from the second iteration. Figure 7.13 shows the results from these tensile test coupons.

A final consideration to make for the effectiveness of the automated control system is to ensure that the longer pause between layers is not the driving force for the improved material quality. Due to this long pause - often as long as a layer in itself - it is likely that the thermal profile of the build is fully dissipated, meaning that inserting an equivalent pause between layers in a single-parameter build may have the same effect on part quality.

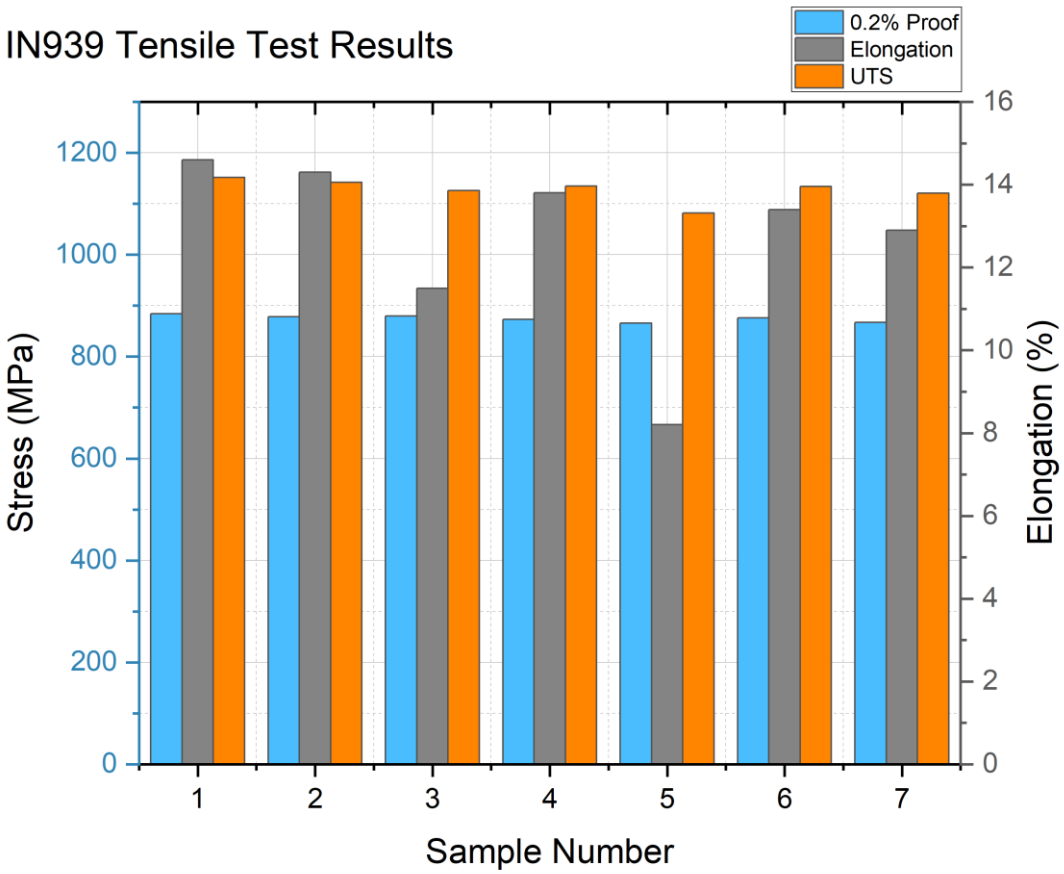

Figure 7.13: Tensile test results for as-built IN939 produced on the Aconity Mini with single-set parameters.

Examining the elongation at yield values for these tests, an average value of 132.2±4.4GPa is determined for the modulus of elasticity. Figure 7.14 shows the stress-strain curves of 5 of the 7 samples. Unfortunately, only these 5 samples were recorded by Special Testing, rather than all 7, the reason for which is unknown.

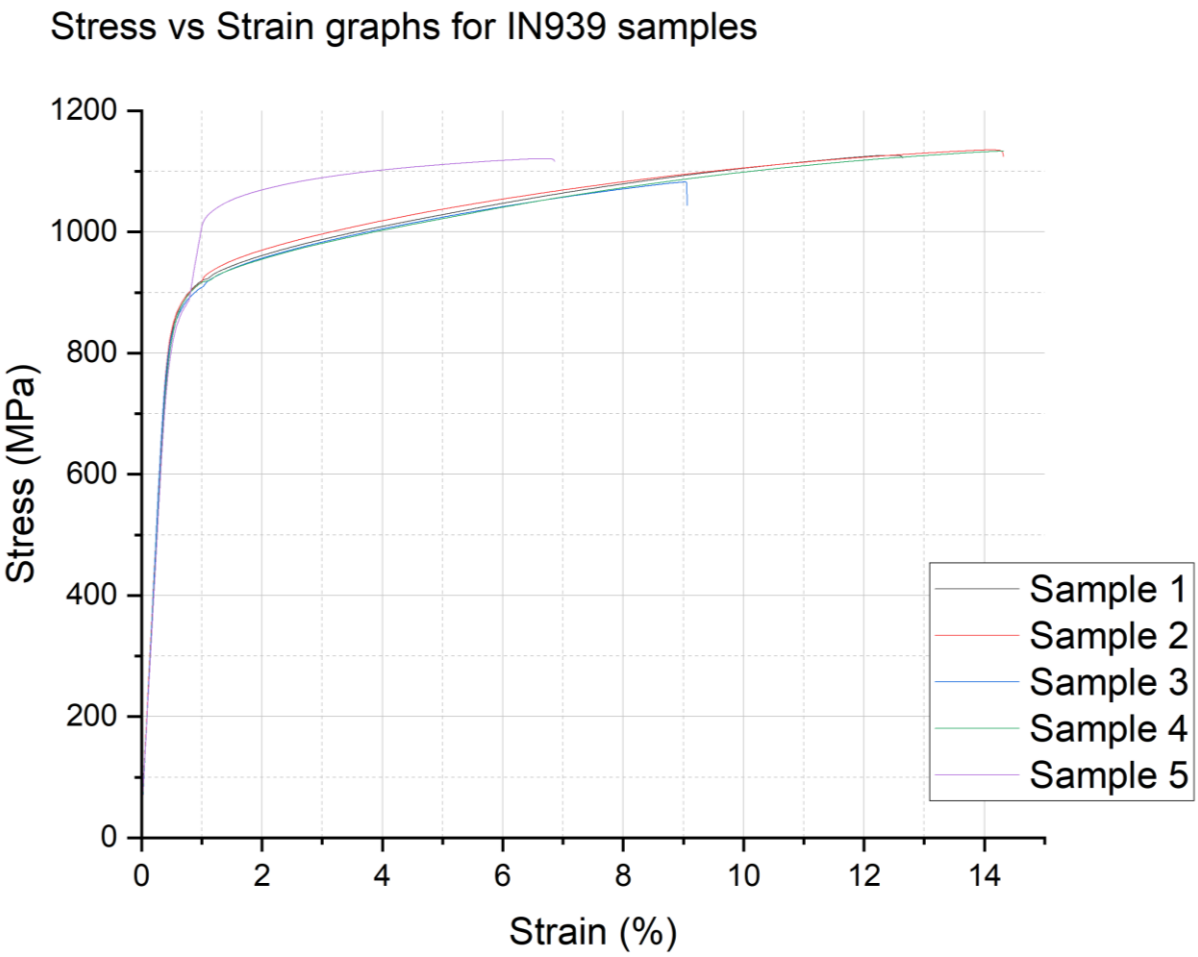

Figure 7.14: Stress-strain curves for IN939 samples produced in this study.

The IN939 tensile tests performed show similar behaviour to CM247-LC. Figure 7.15 shows the average 0.2% proof, UTS and elongation of both CM247 and IN939 test pieces that have been tested in this study.

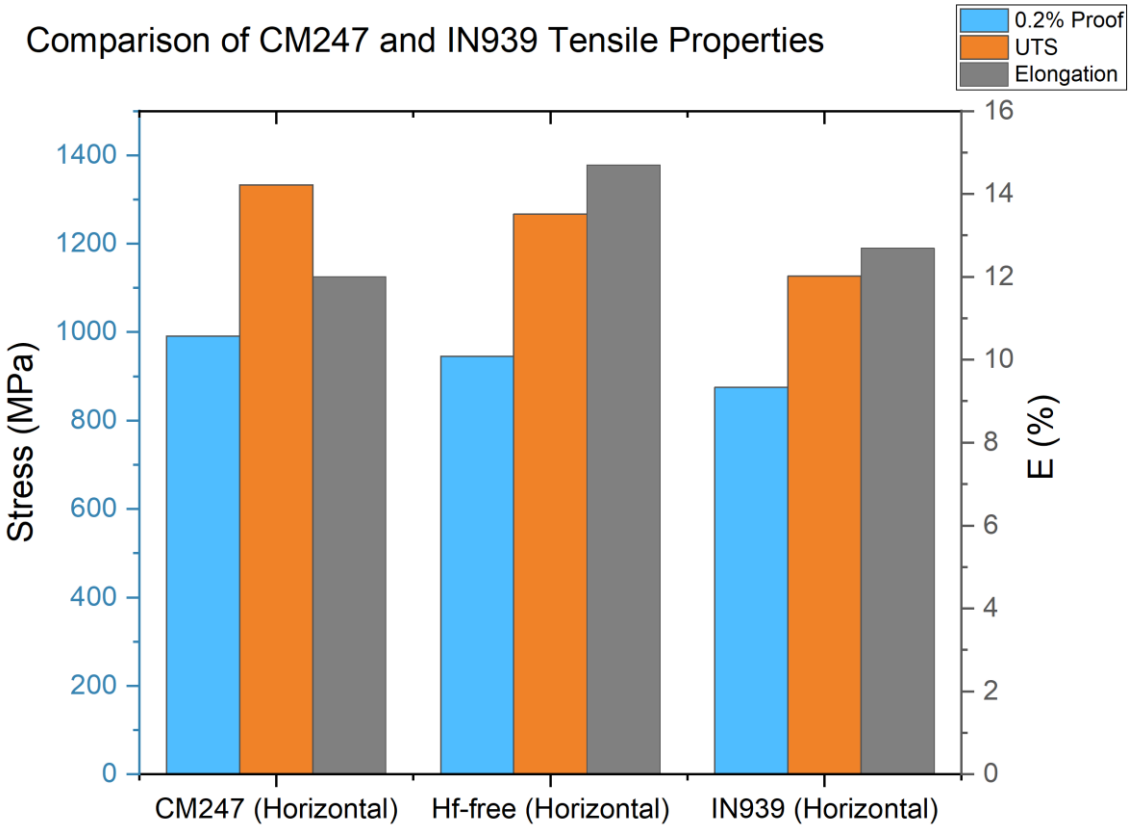

Figure 7.15: Comparisons of tensile properties of CM247 variants and IN939. Whilst its properties are not as good as CM247-LC, the alloy is much easier to process.

While this alloy does not quite possess the same outstanding strength of CM247-LC, it is still comparable to other industry-standard nickel-based superalloys of similar composition, such as IN718. Figure 7.16 shows the Scheil solidification curve for IN939. Comparing this to the Scheil curve for CM247-LC (figure 6.2), the curve for IN939 is significantly shorter in the temperature axis, from 1314°C to 1616°C, as opposed to the CM247-LC range of 1115°C to 1646°C. This is a decrease in solidification range of more than 75% between CM247-LC and IN939 – a possible explanation for the greater ease of processing experienced with this alloy.

IN939 also contains far less material that segregates into either carbide or γ' phases. Whilst this lack of segregating elements detrimentally impacts on the strength of the alloy, it does improve its weldability, making it more ideal for use in LPBF.

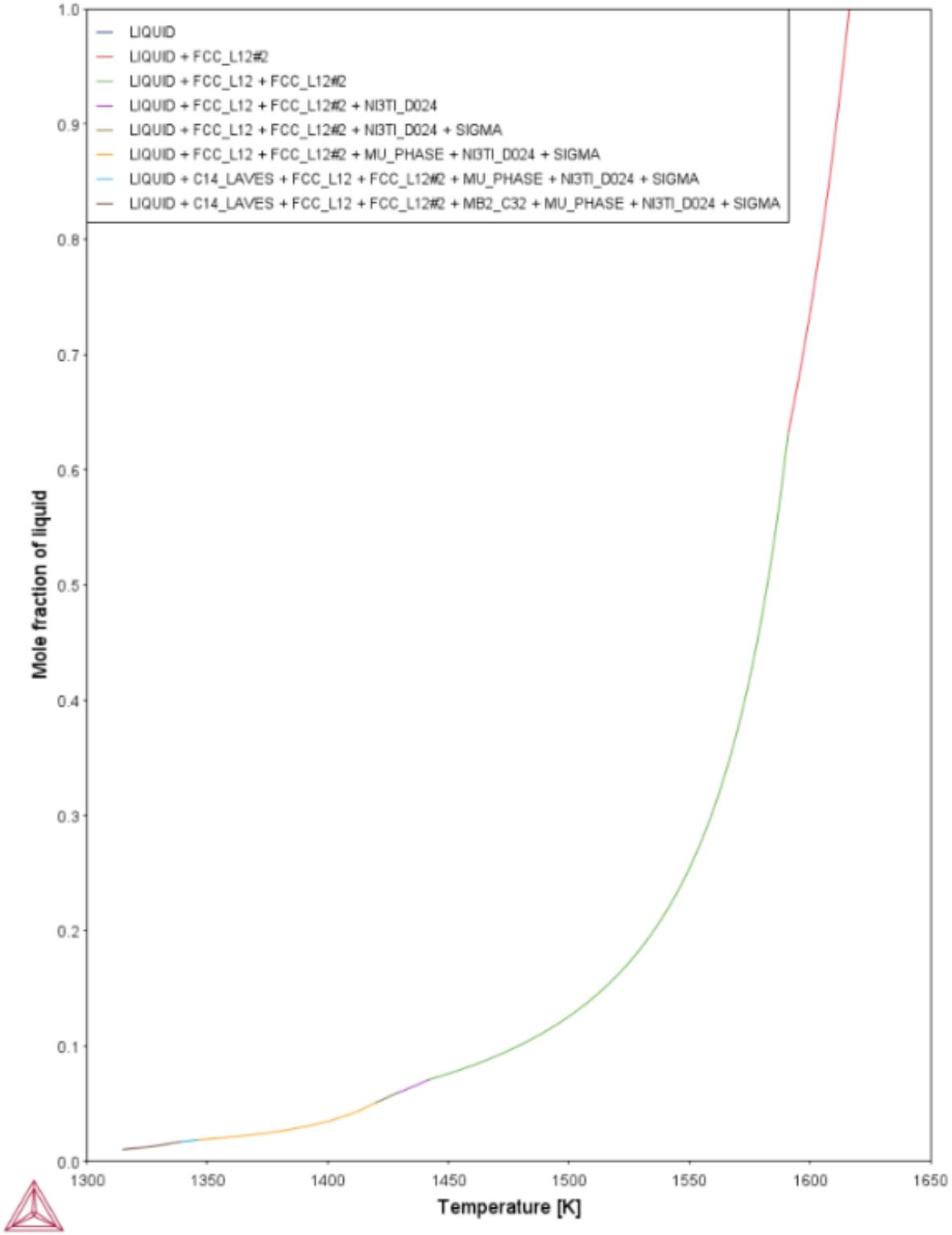

Figure 7.16: The Scheil solidification curve for IN939. This alloy has a much shorter solidification range than CM247-LC, likely contributing to its lower susceptibility to cracking.

An important consideration to include is that IN939 is designed primarily for corrosion resistance rather than extremely high strength. Given it only contains a small fraction of grain boundary strengthening alloy additions compared to CM247-LC, this slight reduction in tensile strength is not surprising. However, with heat treatment, this alloy may potentially be more impactful than CM247-LC, given its printability and lower tendency to crack.

7.5 Comparison to Literature

Given the novel nature of IN939 in LPBF, very few studies are available for comparison. One piece of work done relatively recently was by Shaikh et.al [92] which involved the use of LPBF to manufacture IN939 test pieces for heat treatment. As with many nickel superalloys produced by LPBF, the gamma-prime phase is suppressed due to the rapid solidification rates endemic to the process. While this can reduce the material properties, requiring subsequent aging treatments, it makes some extremely difficult-to-weld alloys (such as CM247-LC) printable. Shaikh et.al examined the phase composition of as-built IN939 and found almost no evidence of gamma-prime precipitation, suggesting that the alloy would demand further heat treatment to be an alloy of interest for high-temperature applications. Kanagarajah et.al [163] also studied IN939 built via LPBF, finding similar results to those produced by Shaikh, with the alloy in the as-built condition being highly ductile but not as strong as some other nickel superalloys.

Figure 7.17 shows a chart of tensile test results from the three studies. The values from Kanagarajah have been read from a figure in that paper, as no exact values are given in the text.

Given the alloy's lack of as-built γ' precipitates, it may be worth trying to process this alloy using the heated bed as a form of in-situ heat treatment/aging. If similar results to those found in chapter 5 for CM247-LC can be repeated for this alloy, it may serve as a rapid production route for components.

When the tensile properties of the alloy in the as-built condition are compared to those that have been heat treated however, it is clear that the material is not as strong without its γ' precipitates. Figure 7.18 illustrates this, comparing this study's tensile curves with those from literature. Considering the alloy's requirement for aging, any control algorithm used for the production of this alloy will need to account for either microstructural control or the use of in-situ heat treatment methods, such as those described in chapter 5 in order to evolve the microstructure of this alloy sufficiently to impart higher strength.

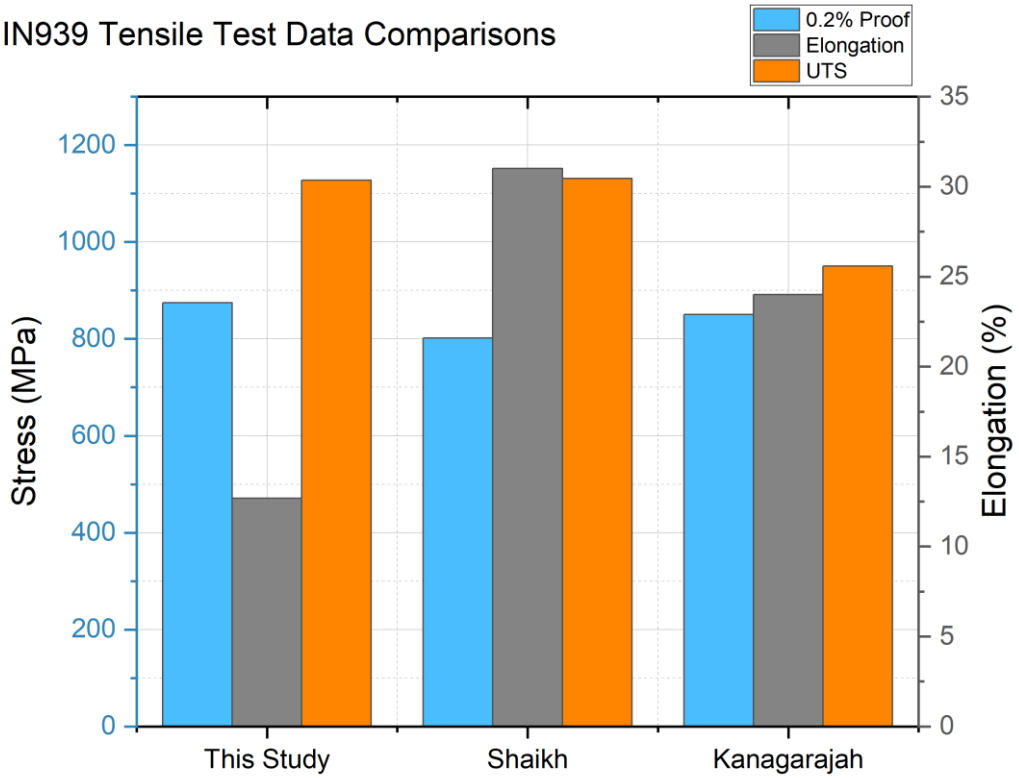

Figure 7.17: Comparison of tensile values of IN939. The samples tested in this study have produced comparable results with literature values.

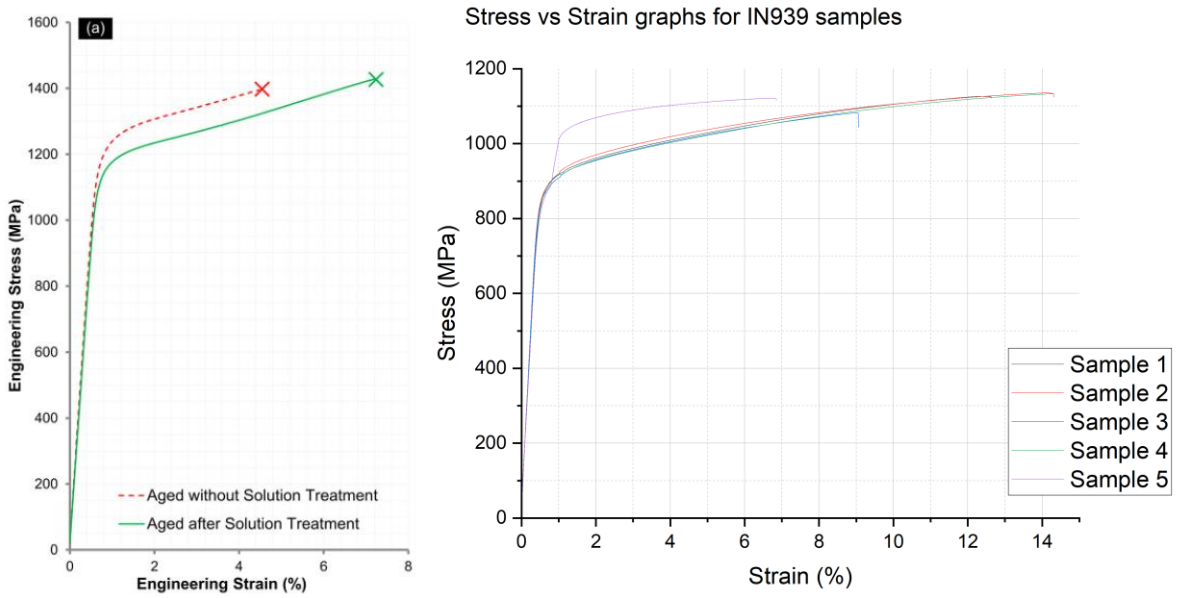

Figure 7.18: Comparison of stress-strain curves from the Shaikh paper (left) and this study (right) demonstrating the impact of aging and solutionising heat treatments on the alloy.

7.6 3D Scanning

A 3D scanner (section 3.3.6) was provided by Taraz Metrology, designed with the intention of mounting it to the top of the Aconity Mini or Lab through the window on the chamber lid. A matlab script on a connected computer (in this case, the Aconity PC) performs the calculations necessary to generate a 3D point cloud. This point cloud can then be manipulated to create a colour-contour height map of the object being scanned (figure 7.19). Automation of this process is ongoing.

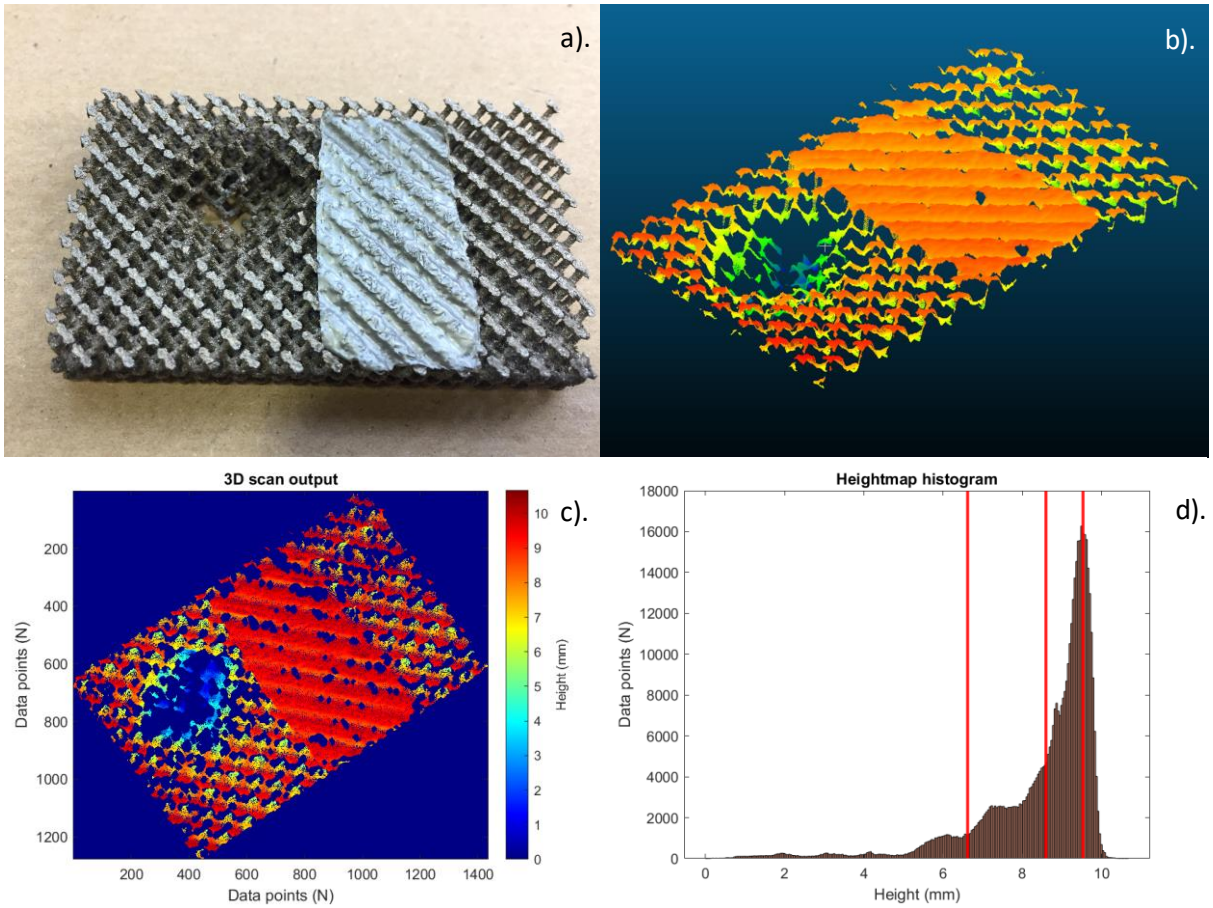

Figure 7.19: The stages of producing a 3D scan of a damaged lattice [177]*: a). The object in question, a damaged lattice with a piece of tape stuck on in order to create a clear difference between features, b).Data can be processed by CloudCompare into a useable heightmap. c). the heightmap can be exported to Matlab, where it can then be interrogated to learn more about the data displayed. d). A histogram of the height distribution of the scanned object, with D10, D50 and D90 lines.*

In addition to the automatic control aspect of this device, there is also an application for it in analysing the surface quality of manufactured components ex-situ. Completed parts can be scanned and a detailed point cloud is created. The produced point cloud can then be manipulated using a piece of open-source software known as "CloudCompare". This allows a representative height map of the top surface of the part to be exported to a program such as Matlab, where it can then be quantitatively analysed further. A distribution of heights can be created, in order to give a numerical analysis of surface roughness. This also allows for a rapid determination of which parameters can affect roughness the most, as Wire EDM is not required before this analysis can be performed.

Of particular interest are the scans taken of two different IN939 builds that were produced by machine learning. A set of square tiles of three different sizes (10, 15 and 20mm) was produced using the machine learning algorithm on the Aconity. Upon completion, it was noted that despite the build completing successfully, the top surface of each component was extremely rough.

The top surfaces of the build were imaged using the 3D scanner. The first, with a hatch spacing of 35µm, was of extremely poor quality, as seen in the image below (figure 7.20). The experiment was then repeated, but with a wider hatch spacing of 60µm, rather than 35µm. This was done in order to reduce the energy density input and reduce the swelling observed in the first instance. Again, the square tiles were imaged using the 3D scanner. To further compound the results from the 3D scanner, samples from the two builds were sectioned, polished and imaged, in order to demonstrate the effect of changing hatch spacing not only on the top surface of the part, but throughout as well.

The top surfaces of the samples were also optically imaged via the Clemex microscope. In addition to widespread cracking across melt pool tracks, the surface of the samples had undergone heavy balling (figure 7.20), a phenomenon that can occur when either too little energy is used in processing or when the melt pool is unstable. This can be catastrophic in the LPBF process [10, 11]. Data from the 3D scanner can be manipulated in CloudCompare and exported to Matlab. Once in Matlab, it is possible to create a more useful representation of the heightmap, to allow for a quantitative analysis of the surfaces imaged. The scans taken of the top surfaces of two "identical" 15mm square tiles from the IN939 builds and their corresponding data sets are shown below, along with the corresponding D10, D50 and D90 values (figure 7.21, table 7.4).

The blank squares in the heightmap images in figure 7.19 are artefacts produced during the data processing. A filter is required to make the raw signal data readable, but it is extremely sensitive and can also remove useful data, particularly on rough surfaces. Thus, the error factor

is likely to be quite high when determining the true distribution. The theoretical maximum resolution is 20µm, but this requires verification against another system (such as an alicona).

The second build was then performed with a wider hatch spacing of 60µm. The result of this change is an almost total removal of defects (figure 7.22).

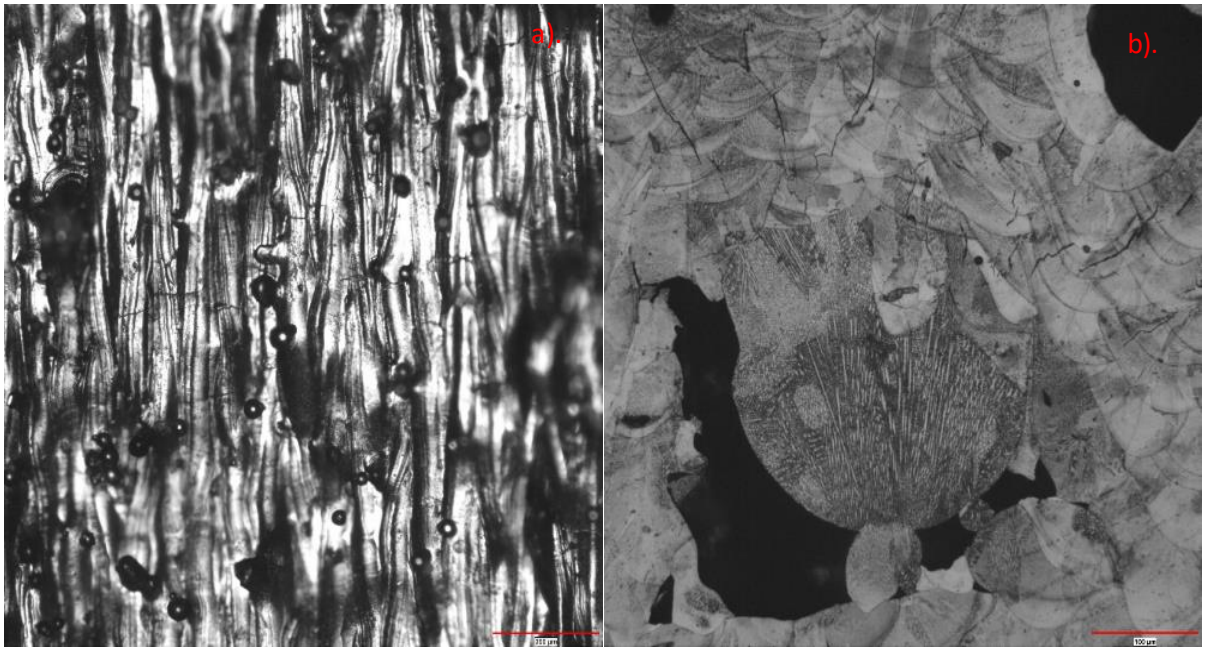

Figure 7.20: a). Optical micrograph of the first build of IN939 produced with a hatch spacing of 35µm. The material shows many poorly melted regions of material, with cracks also dispersed throughout the bulk. B). The top surface of an IN939 LPBF component with a 35µm hatch spacing (first build). The extreme surface roughness is likely caused by a form of balling, which can be seen here in the form of small bead-like structures.

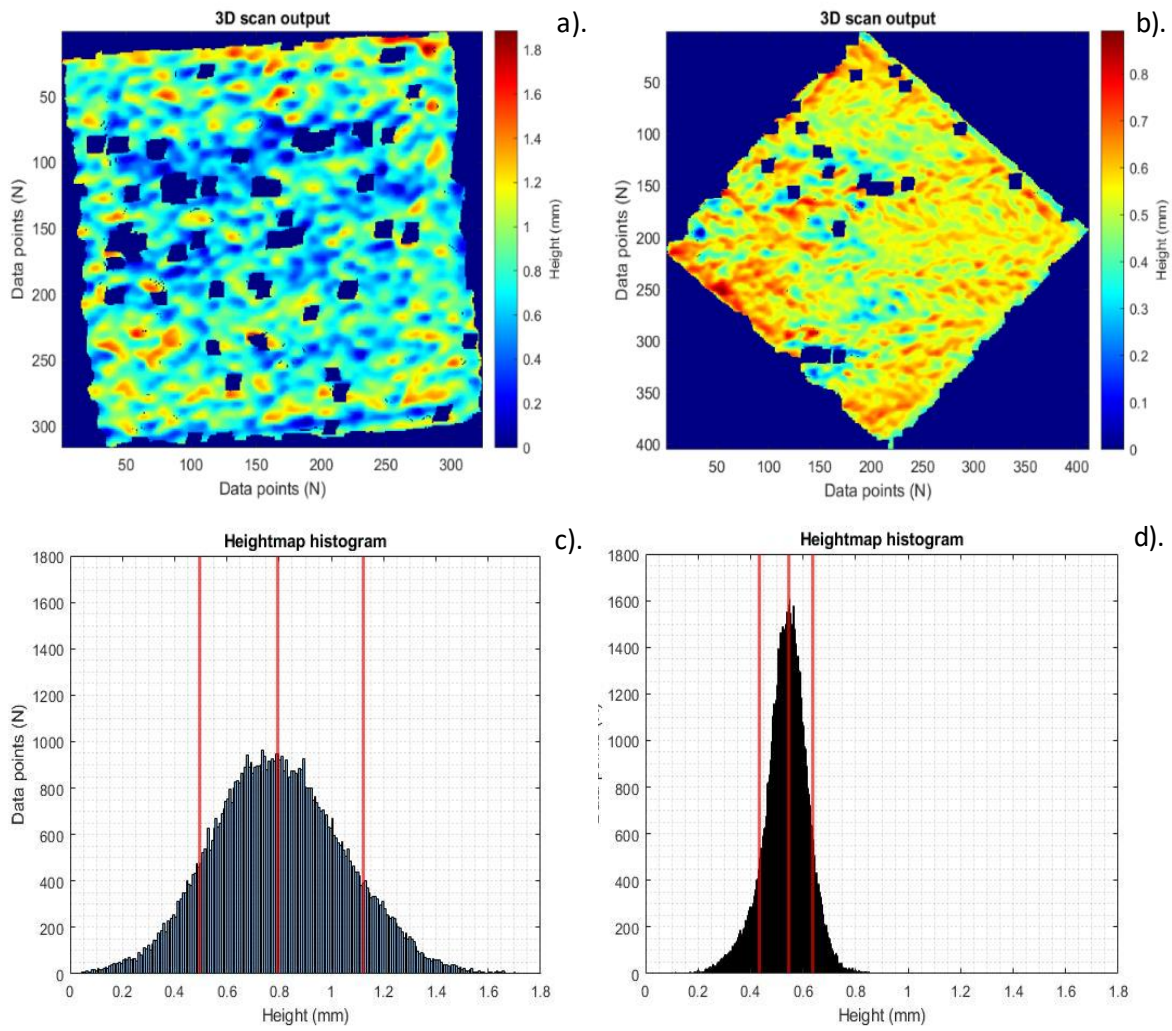

Figure 7.21: Matlab graphs representing the colour heightmaps of a). rough and b). smooth square tiles produced via LPBF. The blank squares present in the images are caused by the self-filter system in the operational script, which removes "anomalous data" from the point cloud. c). rough and d). smooth heightmaps. The red lines denote 10th, 50th and 90th percentiles.

Table 7.4: The discrete values of the percentiles shows in the case of this component, the maximum range surface roughness of IN939 is reduced by 52.7% on average, by increasing the hatch spacing from 35 to 60 microns.

Percentile	Rough (mm)	Smooth (mm)	Change (%)
D10	0.4969	0.4317	13.12
D50	0.7953	0.5452	31.45
D90	1.1236	0.6356	43.43
Max Range	1.888	0.8927	52.72

The data analysis process was then repeated for the rest of the samples produced in this fashion, giving an average reduction of 53.5% in surface roughness across all samples as a direct result of increasing hatch spacing from 35µm to 60µm. This appears at first to be a result of a reduction in balling. However, this has arisen from a reduction in energy density, which is counter to the normal cause of balling – insufficient energy to melt powder particles, resulting in surface tension instabilities. Examining the internal structure of the material shows a clear difference between samples produced from the two sets of parameters (figure 7.22).

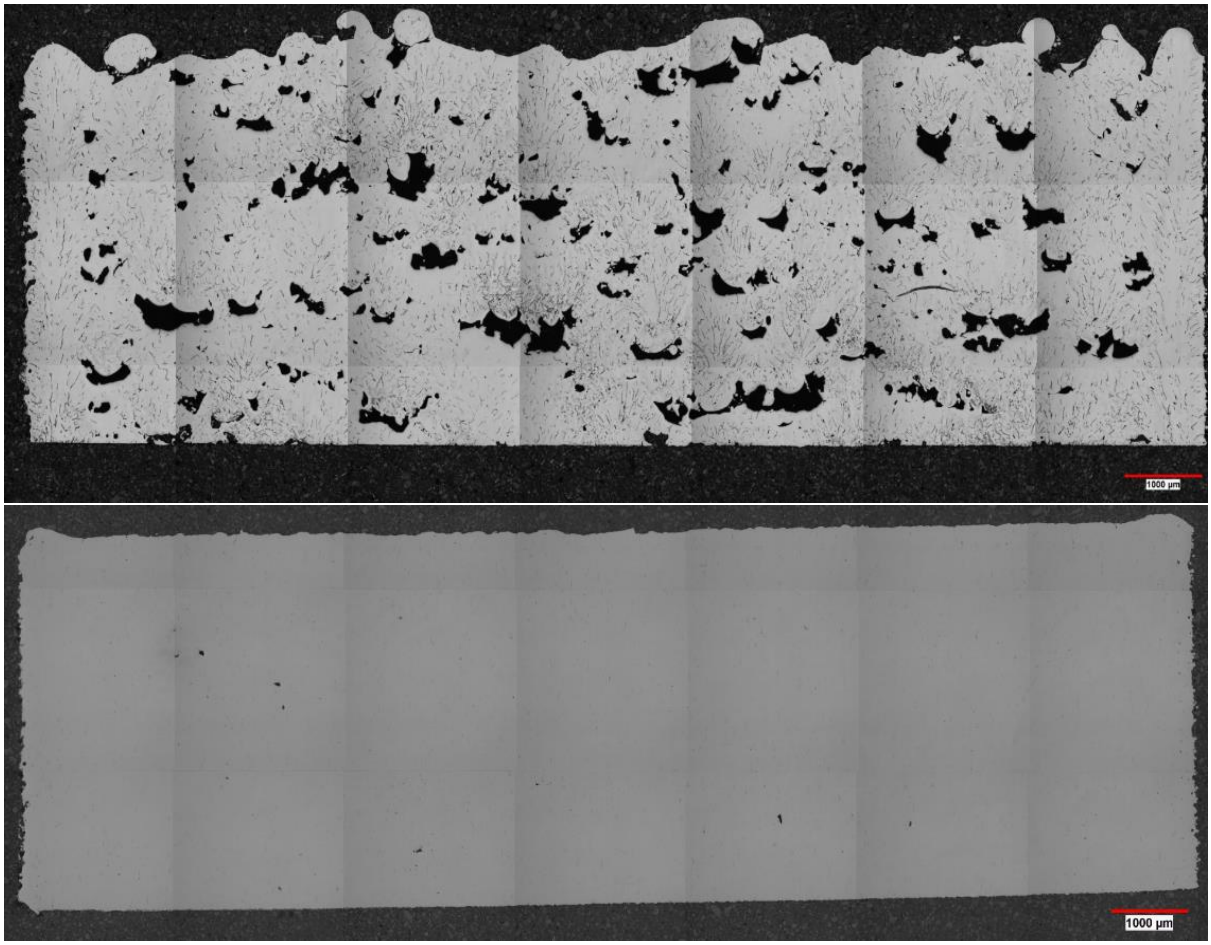

Figure 7.22: Comparison of material produced by identical parameter sets. 35µm hatch spacing (top) and 60µm hatch spacing (bottom).

The surface roughness of the component that was measured in-situ may also provide insight into the defect generation in the material. A closer optical inspection of the heavily balled samples of IN939 shows heavy levels of cracking across the melt tracks on the top surface (figure 7.23).

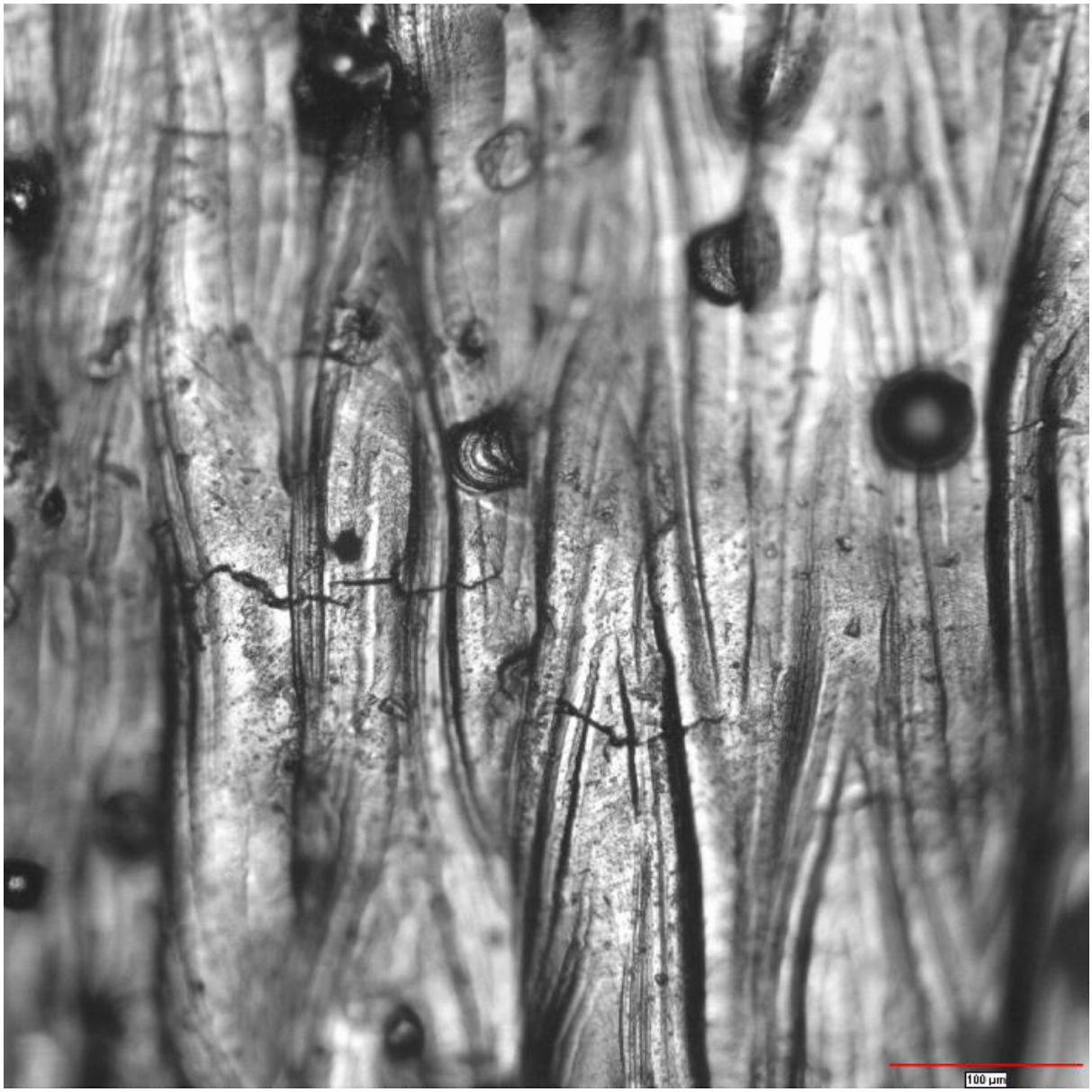

Figure 7.23: Cracking across melt pools in LPBF IN939 components produced in this study.

If a correlation can be drawn between the level of cracking in a material and its surface roughness, it may also be possible to infer the cracking behaviour of the material in-situ. What this experiment demonstrates is that it is possible to quantify surface roughness on the top surface of a component relatively quickly and that the data obtained can be utilised to inform further decisions on build or laser parameters. With this system, it may be possible to scan at a regular layer interval to determine whether a degradation in surface properties is occurring in the build for a particular component. However, in this instance there are several obstacles to progression.

The first is the application to in-situ monitoring. In order to apply this technology to the LPBF process, the device must be capable of fitting either within the chamber or must be capable of attaching to a position externally that has a clear view of the powder bed. Given that the laser travels from the top down, with a very large laser sheath over a relatively small chamber, this is not easy on either of the Aconity systems. It may be possible to incorporate this system into a larger chamber, such as that found on the BeAM DED system or even the Renishaw 250, however this is a very large amount of knowledge that would be required in too short a timescale for this project.

The second obstacle is the ability of the system to be able to adapt to instructions generated from an attached feedback system that uses data from the scanner. As shown in figure 7.22, control of the hatch spacing is a key element to producing a good quality component and must therefore be included in control systems. However, the way that Aconity toolpathing is determined (by NetFabb) does not endear it to changes. Furthermore, the Raylase scan heads on both of the Aconity systems do not permit the direct control of the laser parameters within a layer, only between layers. Because of this, true "live control" is impossible without further hardware upgrades to the laser scan heads. This may be possible to enact on the BeAM however, as shown by Freeman et.al [115], with direct control of laser power in real-time.

Finally, the data stream to go from raw point cloud to useable data is convoluted, with numerous operations between data acquisition and final output. This data processing likely is a project in and of itself, requiring much more time and concerted effort than what was possible in this project due to other areas of focus.

7.7 Summary

A closed-loop control algorithm utilising an advanced neural network has been applied to the Aconity Mini LPBF printer. This algorithm is capable of modifying the laser parameters of each part after each layer across the course of a build. Using the algorithm, a novel nickel alloy – IN939 – has been produced with an extremely high density with no prior knowledge of parameters. Density is in excess of 99% for 5 of 6 sample sets.

The ANNA-IN939 is superior to IN939 produced by single-set parameters, even when utilising a response-surface iterative approach. The best outcome of this process after two iterations was a component of 99.4% density, whereas the ANNA-IN939 components were sometimes 99.9+% dense.

This procedure demonstrates a potential future pathway for automated LPBF processing, however challenges must first be overcome in both monitoring techniques and data management for this to become a truly revolutionary tool. A vital next step for the validation of this process is to determine whether the control algorithm is actually influencing the LPBF process. Because of the time delay between layers due to the sending and receiving of data to and from the server cluster (often between 30 and 40 seconds), the thermal profile of the parts will likely have cooled significantly. To test whether this is having a greater impact, a build should be done that contains a similar delay between layers, but where the laser parameters remain constant.

3D scanning has been demonstrated to have a useful function for quantifying surface roughness, showing that an increase in hatch spacing produces a 57% reduction in the height profile of components and the removal of almost all defects for that particular parameter set. This procedure shows promise as an in-situ monitoring technique, with the possibility of integration into the Aconity systems being considered, in order to analyse the consistency of the powder bed level throughout the build. It also highlights the importance of controlling the hatch spacing during a build.

8. Conclusions and Further Work

8.1 Conclusions

This thesis began with the objective to determine methods of preventing cracking and other defects during the LPBF manufacture of CM247-LC alloy components. The following points are conclusions drawn from this study:

- Chapter 4 - Cracking and defect generation may be reduced and in some cases eliminated by determining the processing window of the alloy, as has been performed for many other alloys previously in the literature. In-situ monitoring may be used to examine how the observed temperature of the material changes between components with high and low defect densities and can help act as a method for both characterisation and prediction. Geometry plays a critical role in defect generation for builds with laser parameters that remain constant throughout the build. Ergo, parts must be built with more varied sets of parameters to compensate for this.

- Chapter 5 - Processing windows can also be controlled using ambient temperature control – in this case in the form of a heated build substrate. The microstructure of the produced CM247-LC can also be affected in this fashion to induce property changes in the material, making it harder and more consistent than without this level of control, in some cases increasing the hardness by 15% on average. This technique also reduces cracking, including that produced during hardness testing. A model utilising the ambient temperature has also been shown to predict consistent final results in terms of material hardness, with melt pool size being tied directly to properties. The value of simple sensors such as thermocouples has also been demonstrated, providing insight into how the behaviour of the material changes with different parameter sets.

- Chapter 6 - The removal of hafnium changes the cracking behaviour of the alloy significantly, particularly in regions of material where the temperature profile is different. Cracking in the edge of samples increases dramatically with the removal of hafnium, resulting in a significant property reduction. This is likely due to the removal of this grain boundary strengthening alloy causing ductility dip cracking as its main grain boundary strengthener is removed.

- Chapter 7 - IN939 has been shown to be readily printable in LPBF, with samples manufactured to a very high density and tensile strengths comparable to other nickel superalloys. In addition, an advanced neural network control model has been used to control this material's manufacture to provide consistent material production and quality. Whilst this algorithm is capable of producing material to a consistent quality, it relies on a limited prior understanding of the response of the material, requiring the correct target temperature to be provided to predict parameters with any accuracy. Hardness and tensile tests have highlighted the alloy's likely need for post-process heat treatment, in order to produce a material that is capable of withstanding the forces encountered by nickel components in aerospace applications. Using surface roughness characterisation, the impact of hatch spacing has also been demonstrated, proving that control methods will need to include control for all parameters, not just laser power and speed.

8.2 Further Work

The printability of CM247-LC through different methods of process control and alloy design has been extensively explored both in this study and others. Whilst CM247-LC has been shown to be printable in simple geometries, more complex ones still present challenges for both this and other difficult-to-weld nickel superalloys. Processing with LPBF at an elevated ambient temperature has been shown to produce high-quality material with a far higher level of hardness. This phenomenon is currently being explored and will likely require advanced microscopy techniques such as TEM to verify the root cause of the material improvement. Further study of this alloy will likely come from the use of the pre-heated substrate, though there are hardware challenges with this particular module.

The exploration of a modified CM247-LC composition is a vast region of unexplored potential. With many studies demonstrating this previously, it is likely to continue. From the perspective of this thesis, it would be a suitable continuation of this work to examine the more macroscopic properties of the modified compositions such as tensile strengths and creep and fatigue resistances. While there will likely be a drop-off in the high-temperature performance of these alloys, it may be that other alloy additions may be used to replace the lost γ' fractions from the reduction in hafnium.

The demonstration of various in-situ monitoring techniques to characterise the material being processed is likely to lead to more development in this field. In particular, the development of the high-speed thermal monitoring system for the Aconity Lab will provide greater insight into the behaviour of materials during solidification and during processing at higher ambient temperatures. The use of automatic control techniques that utilise the data produced by in-situ monitoring methods is also an ever-expanding field. This creation of control methods is likely to differ from machine to machine, particularly in industrial settings, meaning that a great deal of work will be required to determine methods of best practice for these systems. These control techniques are not limited to one family of materials, but require more understanding to become truly material-agnostic tools.

IN939 is a relatively novel alloy for LPBF and shows great potential as an alternative for highly corrosive environments. While defect-free material has been produced in this study, further characterisation of this material produced via AM methods is required for it to become an industry staple. Its performance at elevated temperatures is also poorly known, particularly for parts produced via LPBF, presenting the option for studies of in-situ heat treatment of IN939. Finally, the use of 3D scanning as a method for in-situ qualification of the powder bed and parts is likely to produce useful tools for improving build outcomes and thus warrants further investigation.

9. References

[1] A. Bandyopadhyay, K. D. Traxel, and S. Bose, "Nature-inspired materials and structures using 3D Printing," *Materials Science and Engineering R: Reports*, vol. 145, no. February, p. 100609, 2021, doi: 10.1016/j.mser.2021.100609.

[2] Y. W. Adugna, A. D. Akessa, and H. G. Lemu, "Overview study on challenges of additive manufacturing for a healthcare application," *IOP Conf Ser Mater Sci Eng*, vol. 1201, no. 1, p. 012041, 2021, doi: 10.1088/1757-899x/1201/1/012041.

[3] E. John, Y. Chen, X. Peng, L. Kong, G. Dong, and A. Remani, "Defect inspection technologies," *International Journal of Extreme Manufacturing TOPICAL*, vol. 3, pp. 1–21, 2021.

[4] A. Mostafaei *et al.*, "Defects and anomalies in powder bed fusion metal additive manufacturing," *Curr Opin Solid State Mater Sci*, vol. 26, no. 2, p. 100974, 2022, doi: 10.1016/j.cossms.2021.100974.

[5] J. T. Winowlin Jappes, A. Ajithram, M. Adamkhan, and D. Reena, "Welding on Ni based super alloys – A review," *Mater Today Proc*, vol. 60, pp. 1656–1659, 2022, doi: 10.1016/j.matpr.2021.12.208.

[6] S. Dutta, I. Kaur, and P. Singh, "Review of Film Cooling in Gas Turbines with an Emphasis on Additive Manufacturing-Based Design Evolutions," *Energies (Basel)*, vol. 15, no. 19, 2022, doi: 10.3390/en15196968.

[7] V. K. Balla, M. Das, A. Mohammad, and A. M. Al-Ahmari, "Additive Manufacturing of γ-TiAl: Processing, Microstructure, and Properties," *Adv Eng Mater*, vol. 18, no. 7, pp. 1208–1215, 2016, doi: 10.1002/adem.201500588.

[8] A. Morad and Y. Shash, "Nickel Base Superalloys Used for Aero Engine Turbine Blades," *The International Conference on Applied Mechanics and Mechanical Engineering*, vol. 16, no. 16, pp. 1–22, 2014, doi: 10.21608/amme.2014.35549.

[9] X. Wang, L. N. Carter, B. Pang, M. M. Attallah, and M. H. Loretto, "Microstructure and yield strength of SLM-fabricated CM247LC Ni-Superalloy," *Acta Mater*, vol. 128, pp. 87–95, Apr. 2017, doi: 10.1016/j.actamat.2017.02.007.

[10] J. H. Boswell, D. Clark, W. Li, and M. M. Attallah, "Cracking during thermal post-processing of laser powder bed fabricated CM247LC Ni-superalloy," *Mater Des*, vol. 174, Jul. 2019, doi: 10.1016/j.matdes.2019.107793.

[11] J. H. Boswell, D. Clark, W. Li, and M. M. Attallah, "Cracking during thermal post-processing of laser powder bed fabricated CM247LC Ni-superalloy," *Mater Des*, vol. 174, Jul. 2019, doi: 10.1016/j.matdes.2019.107793.

[12] V. D. Divya *et al.*, "Microstructure of selective laser melted CM247LC nickel-based superalloy and its evolution through heat treatment," *Mater Charact*, vol. 114, pp. 62–74, Apr. 2016, doi: 10.1016/j.matchar.2016.02.004.

[13] S. Griffiths *et al.*, "Influence of Hf on the heat treatment response of additively manufactured Ni-base superalloy CM247LC," *Mater Charact*, vol. 171, Jan. 2021, doi: 10.1016/j.matchar.2020.110815.

[14] N. Boone, C. Zhu, C. Smith, I. Todd, and J. R. Willmott, "Thermal near infrared monitoring system for electron beam melting with emissivity tracking," *Addit Manuf*, vol. 22, pp. 601–605, Aug. 2018, doi: 10.1016/j.addma.2018.06.004.

[15] K. Kempen, B. Vrancken, S. Buls, L. Thijs, J. Van Humbeeck, and J. P. Kruth, "Selective Laser Melting of Crack-Free High Density M2 High Speed Steel Parts by Baseplate Preheating," *Journal of Manufacturing Science and Engineering, Transactions of the ASME*, vol. 136, no. 6, Dec. 2014, doi: 10.1115/1.4028513.

[16] S. Griffiths *et al.*, "Combining alloy and process modification for micro-crack mitigation in an additively manufactured Ni-base superalloy," *Addit Manuf*, vol. 36, Dec. 2020, doi: 10.1016/j.addma.2020.101443.

[17] "ISO/ASTM 52900(en), Additive manufacturing — General principles — Terminology." https://www.iso.org/obp/ui/#iso:std:iso-astm:52900:dis:ed-2:v1:en (accessed Nov. 30, 2022).

[18] M. Vilanova, R. Escribano-garcía, T. Guraya, and M. S. Sebastian, "Optimizing laser powder bed fusion parameters for IN-738LC by response surface method," *Materials*, vol. 13, no. 21, pp. 1–12, Nov. 2020, doi: 10.3390/ma13214879.

[19] T. Childerhouse and M. Jackson, "Near net shape manufacture of titanium alloy components from powder and wire: A review of state-of-the-art process routes," *Metals*, vol. 9, no. 6. MDPI AG, Jun. 01, 2019. doi: 10.3390/met9060689.

[20] S. Moylan, J. Slotwinski, A. Cooke, K. Jurrens, and M. A. Donmez, "Lessons learned in establishing the NIST metal additive manufacturing laboratory," Gaithersburg, MD, Jun. 2013. doi: 10.6028/NIST.TN.1801.

[21] X. Wang, M. Jiang, Z. Zhou, J. Gou, and D. Hui, "3D printing of polymer matrix composites: A review and prospective," *Composites Part B: Engineering*, vol. 110. Elsevier Ltd, pp. 442–458, Feb. 01, 2017. doi: 10.1016/j.compositesb.2016.11.034.

[22] L. Y. Zhou, J. Fu, and Y. He, "A Review of 3D Printing Technologies for Soft Polymer Materials," *Advanced Functional Materials*, vol. 30, no. 28. Wiley-VCH Verlag, Jul. 01, 2020. doi: 10.1002/adfm.202000187.

[23] A. M. E. Arefin, N. R. Khatri, N. Kulkarni, and P. F. Egan, "Polymer 3D printing review: Materials, process, and design strategies for medical applications," *Polymers (Basel)*, vol. 13, no. 9, May 2021, doi: 10.3390/polym13091499.

[24] S. Mirzababaei and S. Pasebani, "A review on binder jet additive manufacturing of 316L stainless steel," *Journal of Manufacturing and Materials Processing*, vol. 3, no. 3. MDPI Multidisciplinary Digital Publishing Institute, Sep. 01, 2019. doi: 10.3390/jmmp3030082.

[25] M. Li, W. Du, A. Elwany, Z. Pei, and C. Ma, "Metal binder jetting additive manufacturing: A literature review," *Journal of Manufacturing Science and Engineering, Transactions of the ASME*, vol. 142, no. 9. American Society of Mechanical Engineers (ASME), Sep. 01, 2020. doi: 10.1115/1.4047430.

[26] B. S. L. Nirudhoddi, K. S. Prasad, A. Vivek, and G. S. Daehn, "High strength welds in titanium & nickel based alloys by impact welding – A practical method," *Journal of Advanced Joining Processes*, vol. 3, Jun. 2021, doi: 10.1016/j.jajp.2021.100056.

[27] M. Olabode, P. Kah, and J. Martikainen, "Aluminium alloys welding processes: Challenges, joint types and process selection," *Proceedings of the Institution of Mechanical Engineers, Part B: Journal of Engineering Manufacture*, vol. 227, no. 8. pp. 1129–1137, Aug. 2013. doi: 10.1177/0954405413484015.

[28] D. A. Levina, L. I. Chernyshev, and N. V Mikhailovskaya, "POWDER METALLURGY ABROAD CONTEMPORARY POWDER METALLURGY: ACHIEVEMENTS AND PROBLEMS," 2007.

[29] B. Zheng, Y. Lin, Y. Zhou, and E. J. Lavernia, "Gas atomization of amorphous aluminum powder: Part II. experimental investigation," *Metallurgical and Materials Transactions B: Process Metallurgy and Materials Processing Science*, vol. 40, no. 6, pp. 995–1004, Dec. 2009, doi: 10.1007/s11663-009-9277-4.

[30] J. Zegzulka, D. Gelnar, L. Jezerska, R. Prokes, and J. Rozbroj, "Characterization and flowability methods for metal powders," *Sci Rep*, vol. 10, no. 1, Dec. 2020, doi: 10.1038/s41598-020-77974-3.

[31] Q. Bao, Y. Yang, X. Wen, L. Guo, and Z. Guo, "The preparation of spherical metal powders using the high-temperature remelting spheroidization technology," *Mater Des*, vol. 199, Feb. 2021, doi: 10.1016/j.matdes.2020.109382.

[32] T. E. Shelton, G. R. Cobb, C. R. Hartsfield, B. M. Doane, C. C. Eckley, and R. A. Kemnitz, "The impact of laser control on the porosity and microstructure of selective laser melted nickel superalloy 718," *Results in Materials*, vol. 11, Sep. 2021, doi: 10.1016/j.rinma.2021.100211.

[33] Y. Cui, J. Cai, Z. Li, Z. Jiao, L. Hu, and J. Hu, "Effect of Porosity on Dynamic Response of Additive Manufacturing Ti-6Al-4V Alloys," *Micromachines (Basel)*, vol. 13, no. 3, Mar. 2022, doi: 10.3390/mi13030408.

[34] A. Y. Al-Maharma, S. P. Patil, and B. Markert, "Effects of porosity on the mechanical properties of additively manufactured components: a critical review," *Materials Research Express*, vol. 7, no. 12. IOP Publishing Ltd, Dec. 01, 2020. doi: 10.1088/2053-1591/abcc5d.

[35] G. Piscopo and L. Iuliano, "Current research and industrial application of laser powder directed energy deposition," *International Journal of Advanced Manufacturing Technology*, vol. 119, no. 11–12. Springer Science and Business Media Deutschland GmbH, pp. 6893–6917, Apr. 01, 2022. doi: 10.1007/s00170-021-08596-w.

[36] M. Liu, A. Kumar, S. Bukkapatnam, and M. Kuttolamadom, "A review of the anomalies in directed energy deposition (DED) processes & potential solutions - Part quality & defects," in *Procedia Manufacturing*, Elsevier B.V., 2021, pp. 507–518. doi: 10.1016/j.promfg.2021.06.093.

[37] C. D. Rankine, M. M. M. Madkhali, M. M. M. Madkhali, and T. J. Penfold, "A Deep Neural Network for the Rapid Prediction of X-ray Absorption Spectra," *Journal of Physical Chemistry A*, vol. 124, no. 21, pp. 4263–4270, May 2020, doi: 10.1021/acs.jpca.0c03723.

[38] R. Tamura *et al.*, "Machine learning-driven optimization in powder manufacturing of Ni-Co based superalloy," *Mater Des*, vol. 198, Jan. 2021, doi: 10.1016/j.matdes.2020.109290.

[39] G. Zenzinger, J. Bamberg, A. Ladewig, T. Hess, B. Henkel, and W. Satzger, "Process monitoring of additive manufacturing by using optical tomography," in *AIP Conference Proceedings*, American Institute of Physics Inc., 2015, pp. 164–170. doi: 10.1063/1.4914606.

[40] L. Chechik, "Process Monitoring and Control during Additive Manufacturing," 2022.

[41] M. K. Thompson and M. Mischkot, "Design of Test Parts to Characterize Micro Additive Manufacturing Processes," in *Procedia CIRP*, Elsevier, 2015, pp. 223–228. doi: 10.1016/j.procir.2015.07.065.

[42] A. S. Reddy and D. Srinivasan, "Small scale mechanical testing for additively manufactured (direct metal laser sintered) monolithic and hybrid test samples," in *Procedia Structural Integrity*, Elsevier B.V., 2019, pp. 449–466. doi: 10.1016/j.prostr.2019.05.055.

[43] R. M. Snell *et al.*, "Towards understanding and eliminating defects in additively manufactured CubeSat mirrors," SPIE-Intl Soc Optical Eng, Aug. 2022, p. 28. doi: 10.1117/12.2629935.

[44] R. Ge, G. Humbert, R. Martinez, M. M. Attallah, and A. Sciacovelli, "Additive manufacturing of a topology-optimised multi-tube energy storage device: Experimental tests and numerical analysis," *Appl Therm Eng*, vol. 180, Nov. 2020, doi: 10.1016/j.applthermaleng.2020.115878.

[45] A. Aversa *et al.*, "New aluminum alloys specifically designed for laser powder bed fusion: A review," *Materials*, vol. 12, no. 7. MDPI AG, 2019. doi: 10.3390/ma12071007.

[46] "We made L-PBF dual-metal! - Aerosint." https://aerosint.com/we-made-l-pbf-dual-metal/ (accessed Nov. 30, 2022).

[47] W. Kurz and R. Trivedi, "Rapid solidification processing and microstructure formation," 1994.

[48] L. Caprio, A. G. Demir, G. Chiari, and B. Previtali, "Defect-free laser powder bed fusion of Ti–48Al–2Cr–2Nb with a high temperature inductive preheating system," *JPhys Photonics*, vol. 2, no. 2, Feb. 2020, doi: 10.1088/2515-7647/ab7080.

[49] S. Chowdhury *et al.*, "Laser powder bed fusion: a state-of-the-art review of the technology, materials, properties & defects, and numerical modelling," *Journal of Materials Research and Technology*, vol. 20, pp. 2109–2172, 2022, doi: 10.1016/j.jmrt.2022.07.121.

[50] A. Saboori, D. Gallo, S. Biamino, P. Fino, and M. Lombardi, "An overview of additive manufacturing of titanium components by directed energy deposition: Microstructure and mechanical properties," *Applied Sciences (Switzerland)*, vol. 7, no. 9. MDPI AG, Aug. 28, 2017. doi: 10.3390/app7090883.

[51] P. R. Gradl, C. Protz, K. Zagorski, V. Doshi, and H. McCallum, "Additive manufacturing and hot-fire testing of bimetallic grcop-84 and c-18150 channel-cooled combustion chambers using powder bed fusion and inconel 625 hybrid directed energy deposition," in *AIAA Propulsion and Energy Forum and Exposition, 2019*, American Institute of Aeronautics and Astronautics Inc, AIAA, 2019. doi: 10.2514/6.2019-4390.

[52] J. Gockel, J. Beuth, and K. Taminger, "Integrated control of solidification microstructure and melt pool dimensions in electron beam wire feed additive manufacturing of ti-6al-4v," *Addit Manuf*, vol. 1, pp. 119–126, Oct. 2014, doi: 10.1016/j.addma.2014.09.004.

[53] H. K. Lee, J. Kim, C. Pyo, and J. Kim, "Evaluation of bead geometry for aluminum parts fabricated using additive manufacturing-based wire-arc welding," *Processes*, vol. 8, no. 10, pp. 1–14, Oct. 2020, doi: 10.3390/pr8101211.

[54] P. Bajaj, J. Wright, I. Todd, and E. A. Jägle, "Predictive process parameter selection for Selective Laser Melting Manufacturing: Applications to high thermal conductivity alloys," *Addit Manuf*, vol. 27, pp. 246–258, May 2019, doi: 10.1016/j.addma.2018.12.003.

[55] Y. He, M. Zhong, J. Beuth, and B. Webler, "A study of microstructure and cracking behavior of H13 tool steel produced by laser powder bed fusion using single-tracks, multi-track pads, and 3D cubes," *J Mater Process Technol*, vol. 286, Dec. 2020, doi: 10.1016/j.jmatprotec.2020.116802.

[56] Y. S. Lee *et al.*, "Asymmetric Cracking in Mar-M247 Alloy Builds During Electron Beam Powder Bed Fusion Additive Manufacturing," *Metall Mater Trans A Phys Metall Mater Sci*, vol. 49, no. 10, pp. 5065–5079, Oct. 2018, doi: 10.1007/s11661-018-4788-8.

[57] Y. Zhai, H. Galarraga, and D. A. Lados, "Microstructure, static properties, and fatigue crack growth mechanisms in Ti-6Al-4V fabricated by additive manufacturing: LENS and EBM," *Eng Fail Anal*, vol. 69, pp. 3–14, Nov. 2016, doi: 10.1016/j.engfailanal.2016.05.036.

[58] S. Yim *et al.*, "Ball-milling treatment of gas-atomized Ti–48Al–2Cr–2Nb powder and its effect on preventing smoking during electron beam powder bed fusion building process," *Addit Manuf*, vol. 51, Mar. 2022, doi: 10.1016/j.addma.2022.102634.

[59] A. Chiba, Y. Daino, K. Aoyagi, and K. Yamanaka, "Smoke suppression in electron beam melting of inconel 718 alloy powder based on insulator–metal transition of surface oxide film by mechanical stimulation," *Materials*, vol. 14, no. 16, Aug. 2021, doi: 10.3390/ma14164662.

[60] C. J. Smith *et al.*, "Dimensional accuracy of Electron Beam Melting (EBM) additive manufacture with regard to weight optimized truss structures," *J Mater Process Technol*, vol. 229, pp. 128–138, Mar. 2016, doi: 10.1016/j.jmatprotec.2015.08.028.

[61] N. S. Weston and M. Jackson, "FAST-forge of titanium alloy swarf: A solid-state closed-loop recycling approach for aerospace machining waste," *Metals (Basel)*, vol. 10, no. 2, Feb. 2020, doi: 10.3390/met10020296.

[62] G. L. Erickson, K. Harris, and R. E. Schwer, "Directionally Solidified DS CM 247 LC—Optimized Mechanical Properties Resulting From Extensive γ' Solutioning," in *Volume 4: Manufacturing Materials and Metallurgy; Ceramics; Structures and Dynamics; Controls, Diagnostics and Instrumentation; Education; Process Industries*, American Society of Mechanical Engineers, Mar. 1985. doi: 10.1115/85-GT-107.

[63] D. Ma, "Novel casting processes for single-crystal turbine blades of superalloys," *Frontiers of Mechanical Engineering*, vol. 13, no. 1, pp. 3–16, Mar. 2018, doi: 10.1007/s11465-018-0475-0.

[64] A. Sheyaa Alwan, M. Abbass, and J. M. Jalil, "Parametric Study of Metallurgical and Heat Transfer Characteristics of Manual Metal Arc Welding Process FRICTION STIR WELDING View project Effect Effect of Cerium Addition on Mechanical properties and Microstructure of Al-12%Si Alloys View project," 2009, doi: 10.13140/RG.2.1.1007.9767.

[65] M. Sheikhi, F. Malek Ghaini, and H. Assadi, "Prediction of solidification cracking in pulsed laser welding of 2024 aluminum alloy," *Acta Mater*, vol. 82, pp. 491–502, Jan. 2015, doi: 10.1016/j.actamat.2014.09.002.

[66] J. H. Boswell, D. Clark, W. Li, and M. M. Attallah, "Cracking during thermal post-processing of laser powder bed fabricated CM247LC Ni-superalloy," *Mater Des*, vol. 174, p. 107793, 2019, doi: 10.1016/j.matdes.2019.107793.

[67] C. A. Boig, "The Application of Additive Manufacturing to Nickel-base Superalloys for Turbocharger Applications," 2018.

[68] J. Song, F. Pan, B. Jiang, A. Atrens, M. X. Zhang, and Y. Lu, "A review on hot tearing of magnesium alloys," *Journal of Magnesium and Alloys*, vol. 4, no. 3, pp. 151–172, 2016, doi: 10.1016/j.jma.2016.08.003.

[69] Suyitno, W. H. Kool, and L. Katgerman, "Hot tearing criteria evaluation for direct-chill casting of an Al-4.5 pct Cu alloy," *Metall Mater Trans A Phys Metall Mater Sci*, vol. 36, no. 6, pp. 1537–1546, 2005, doi: 10.1007/s11661-005-0245-6.

[70] C. Qiu, C. Panwisawas, M. Ward, H. C. Basoalto, J. W. Brooks, and M. M. Attallah, "On the role of melt flow into the surface structure and porosity development during selective laser melting," *Acta Mater*, vol. 96, pp. 72–79, Jun. 2015, doi: 10.1016/j.actamat.2015.06.004.

[71] J. Liu and P. Wen, "Metal vaporization and its influence during laser powder bed fusion process," *Materials and Design*, vol. 215. Elsevier Ltd, Mar. 01, 2022. doi: 10.1016/j.matdes.2022.110505.

[72] I. E. Anderson, E. M. H. White, and R. Dehoff, "Feedstock powder processing research needs for additive manufacturing development," *Current Opinion in Solid State and Materials Science*, vol. 22, no. 1. Elsevier Ltd, pp. 8–15, Feb. 01, 2018. doi: 10.1016/j.cossms.2018.01.002.

[73] J. V. Gordon *et al.*, "Defect structure process maps for laser powder bed fusion additive manufacturing," *Addit Manuf*, vol. 36, Dec. 2020, doi: 10.1016/j.addma.2020.101552.

[74] T. A. Mcfalls, "The effect of hydrogen on gas porosity in Laser Powder Bed The effect of hydrogen on gas porosity in Laser Powder Bed Fusion of AlSi10Mg Fusion of AlSi10Mg," 2018. [Online]. Available: https://trace.tennessee.edu/utk_gradthes/5174

[75] M. B. Henderson, D. Arrell, R. Larsson, M. Heobel, and G. Marchant, "Nickel based superalloy welding practices for industrial gas turbine applications," *Science and Technology of Welding and Joining*, vol. 9, no. 1, pp. 13–21, 2004, doi: 10.1179/136217104225017099.

[76] C.Huang & S.Kou "Liquation Cracking in Full-Penetration Al-Cu Welds", Welding Research.

[77] M. Rappaz, J.-M. Drezet, and M. Gremaud, "A New Hot-Tearing Criterion," 1999.

[78] J. Zhang and R. F. Singer, "Hot tearing of nickel-based superalloys during directional solidification," 2002. [Online]. Available: www.actamat-journals.com

[79] "What is hot cracking (solidification cracking)? - TWI." https://www.twi-global.com/technical-knowledge/faqs/faq-what-is-hot-cracking-solidification-cracking (accessed Nov. 30, 2022).

[80] O. Adegoke, J. Andersson, H. Brodin, and R. Pederson, "Review of laser powder bed fusion of gamma-prime-strengthened nickel-based superalloys," *Metals*, vol. 10, no. 8. MDPI AG, pp. 1–26, Aug. 01, 2020. doi: 10.3390/met10080996.

[81] A. Mostafaei *et al.*, "Defects and anomalies in powder bed fusion metal additive manufacturing," *Current Opinion in Solid State and Materials Science*, vol. 26, no. 2. Elsevier Ltd, Apr. 01, 2022. doi: 10.1016/j.cossms.2021.100974.

[82] C. Bellini, F. Berto, V. Di Cocco, F. Iacoviello, L. P. Mocanu, and J. Razavi, "Additive manufacturing processes for metals and effects of defects on mechanical strength: A review," in *Procedia Structural Integrity*, Elsevier B.V., 2021, pp. 498–508. doi: 10.1016/j.prostr.2021.10.057.

[83] K. Aoyagi, H. Wang, H. Sudo, and A. Chiba, "Simple method to construct process maps for additive manufacturing using a support vector machine," *Addit Manuf*, vol. 27, pp. 353–362, May 2019, doi: 10.1016/j.addma.2019.03.013.

[84] Allied Titanium Website (accessed01/09/2023)

[85] M. Thomas, G. J. Baxter, and I. Todd, "Normalised model-based processing diagrams for additive layer manufacture of engineering alloys," *Acta Mater*, vol. 108, pp. 26–35, Apr. 2016, doi: 10.1016/j.actamat.2016.02.025.

[86] "Each Blade a Single Crystal | American Scientist." https://www.americanscientist.org/article/each-blade-a-single-crystal (accessed Nov. 30, 2022).

[87] M. K. Mani, "Development of Fe-50Co Alloy and its Composites by Spark Plasma Sintering," 2014.

[88] E. Hernández-Nava, P. Mahoney, C. J. Smith, J. Donoghue, I. Todd, and S. Tammas-Williams, "Additive manufacturing titanium components with isotropic or graded properties by hybrid electron beam melting/hot isostatic pressing powder processing," *Sci Rep*, vol. 9, no. 1, Dec. 2019, doi: 10.1038/s41598-019-40722-3.

[89] F. Freeman, "Structuring Difference The Additive Manufacture of Spatially & Functionally Differentiated Microstructures," 2018.

[90] F. S. H. B. Freeman, A. Lincoln, J. Sharp, A. Lambourne, and I. Todd, "Exploiting thermal strain to achieve an in-situ magnetically graded material," *Mater Des*, vol. 161, pp. 14–21, Jan. 2019, doi: 10.1016/j.matdes.2018.11.011.

[91] S. Tammas-Williams, P. J. Withers, I. Todd, and P. B. Prangnell, "Porosity regrowth during heat treatment of hot isostatically pressed additively manufactured titanium components," *Scr Mater*, vol. 122, pp. 72–76, Sep. 2016, doi: 10.1016/j.scriptamat.2016.05.002.

[92] A. S. Shaikh, M. Rashidi, K. Minet-Lallemand, and E. Hryha, "On as-built microstructure and necessity of solution treatment in additively manufactured Inconel 939," *Powder Metallurgy*, 2022, doi: 10.1080/00325899.2022.2041787.

[93] W. Philpott, M. A. E. Jepson, and R. C. Thomson, "COMPARISON OF THE EFFECTS OF A CONVENTIONAL HEAT TREATMENT BETWEEN CAST AND SELECTIVE LASER MELTED IN939 ALLOY."

[94] J. Belan, "GCP and TCP Phases Presented in Nickel-base Superalloys," *Mater Today Proc*, vol. 3, no. 4, pp. 936–941, 2016, doi: 10.1016/j.matpr.2016.03.024.

[95] P. Mercelis and J. P. Kruth, "Residual stresses in selective laser sintering and selective laser melting," *Rapid Prototyp J*, vol. 12, no. 5, pp. 254–265, 2006, doi: 10.1108/13552540610707013.

[96] K. Kempen, L. Thijs, B. Vrancken, S. Buls, J. Van Humbeeck, and J.-P. Kruth, "PRODUCING CRACK-FREE, HIGH DENSITY M2 HSS PARTS BY SELECTIVE LASER MELTING: PRE-HEATING THE BASEPLATE."

[97] K. A. Sofinowski, S. Raman, X. Wang, B. Gaskey, and M. Seita, "Layer-wise engineering of grain orientation (LEGO) in laser powder bed fusion of stainless steel 316L," *Addit Manuf*, vol. 38, p. 101809, 2021, doi: 10.1016/j.addma.2020.101809.

[98] F. Geiger, K. Kunze, and T. Etter, "Tailoring the texture of IN738LC processed by selective laser melting (SLM) by specific scanning strategies," *Materials Science and Engineering: A*, vol. 661, pp. 240–246, 2016, doi: 10.1016/j.msea.2016.03.036.

[99] L. N. Carter, C. Martin, P. J. Withers, and M. M. Attallah, "The influence of the laser scan strategy on grain structure and cracking behaviour in SLM powder-bed fabricated nickel superalloy," *J Alloys Compd*, vol. 615, pp. 338–347, Dec. 2014, doi: 10.1016/j.jallcom.2014.06.172.

[100] N. Kalentics *et al.*, "Healing cracks in selective laser melting by 3D laser shock peening," *Addit Manuf*, vol. 30, Dec. 2019, doi: 10.1016/j.addma.2019.100881.

[101] N. Kalentics *et al.*, "3D Laser Shock Peening – A new method for the 3D control of residual stresses in Selective Laser Melting," *Mater Des*, vol. 130, pp. 350–356, Sep. 2017, doi: 10.1016/j.matdes.2017.05.083.

[102] G. Hammersley, L. A. Hackel, and F. Harris, "Surface prestressing to improve fatigue strength of components by laser shot peening," 2000.

[103] Y. Sano *et al.*, "Retardation of crack initiation and growth in austenitic stainless steels by laser peening without protective coating," *Materials Science and Engineering A*, vol. 417, no. 1–2, pp. 334–340, Feb. 2006, doi: 10.1016/j.msea.2005.11.017.

[104] N. Kalentics, E. Boillat, P. Peyre, S. Ćirić-Kostić, N. Bogojević, and R. E. Logé, "Tailoring residual stress profile of Selective Laser Melted parts by Laser Shock Peening," *Addit Manuf*, vol. 16, pp. 90–97, Aug. 2017, doi: 10.1016/j.addma.2017.05.008.

[105] N. Kalentics *et al.*, "Healing cracks in selective laser melting by 3D laser shock peening," *Addit Manuf*, vol. 30, Dec. 2019, doi: 10.1016/j.addma.2019.100881.

[106] J. C. Ion, H. R. Shercliff, and M. F. Ashby, "DIAGRAMS FOR LASER MATERIALS PROCESSING," 1992.

[107] L. Stanger *et al.*, "Reconstruction of microscopic thermal fields from oversampled infrared images in laser-based powder bed fusion," *Sensors*, vol. 21, no. 14, Jul. 2021, doi: 10.3390/s21144859.

[108] M. Mani, B. Lane, A. Donmez, S. Feng, S. Moylan, and R. Fesperman, "Measurement Science Needs for Real-time Control of Additive Manufacturing Powder Bed Fusion Processes NISTIR

8036 Measurement Science Needs for Real-time Control of Additive Manufacturing Powder Bed Fusion Processes Mahesh Mani," *National Institute of Standards and Technology*, no. February, 2015, doi: 10.6028/NIST.IR.8036.

[109] H. K. D. H. Bhadeshia, R. C. Dimitriu, S. Forsik, J. H. Pak, and J. H. Ryu, "Performance of neural networks in materials science," *Materials Science and Technology*, vol. 25, no. 4, pp. 504–510, 2009, doi: 10.1179/174328408X311053.

[110] P. A. Hooper, "Melt pool temperature and cooling rates in laser powder bed fusion," *Addit Manuf*, vol. 22, pp. 548–559, Aug. 2018, doi: 10.1016/j.addma.2018.05.032.

[111] L. Chechik *et al.*, "Variation of texture anisotropy and hardness with build parameters and wall height in directed-energy-deposited 316L steel," *Addit Manuf*, vol. 38, Feb. 2021, doi: 10.1016/j.addma.2020.101806.

[112] A. Bellucci, M. Girolami, and D. M. Trucchi, "Thermionic and thermoelectric energy conversion," *Ultra-High Temperature Thermal Energy Storage, Transfer and Conversion*, pp. 253–284, 2021, doi: 10.1016/B978-0-12-819955-8.00010-7.

[113] J. Trapp, A. M. Rubenchik, G. Guss, and M. J. Matthews, "In situ absorptivity measurements of metallic powders during laser powder-bed fusion additive manufacturing," *Appl Mater Today*, vol. 9, pp. 341–349, Dec. 2017, doi: 10.1016/j.apmt.2017.08.006.

[114] D. Moon, S. Chung, S. Kwon, J. Seo, and J. Shin, "Comparison and utilization of point cloud generated from photogrammetry and laser scanning: 3D world model for smart heavy equipment planning," *Autom Constr*, vol. 98, pp. 322–331, Feb. 2019, doi: 10.1016/j.autcon.2018.07.020.

[115] F. Freeman, L. Chechik, B. Thomas, and I. Todd, "Calibrated closed-loop control to reduce the effect of geometry on mechanical behaviour in directed energy deposition," *J Mater Process Technol*, vol. 311, p. 117823, Jan. 2023, doi: 10.1016/j.jmatprotec.2022.117823.

[116] T. Craeghs, S. Clijsters, E. Yasa, and J.-P. Kruth, "ONLINE QUALITY CONTROL OF SELECTIVE LASER MELTING."

[117] A. Heckl, S. Neumeier, M. Göken, and R. F. Singer, "The effect of Re and Ru on γ/γ′ microstructure, γ-solid solution strengthening and creep strength in nickel-base superalloys," *Materials Science and Engineering A*, vol. 528, no. 9, pp. 3435–3444, Apr. 2011, doi: 10.1016/j.msea.2011.01.023.

[118] O. Adegoke, J. Andersson, H. Brodin, and R. Pederson, "Influence of laser powder bed fusion process parameters on voids, cracks, and microhardness of nickel-based superalloy alloy 247LC," *Materials*, vol. 13, no. 17, Sep. 2020, doi: 10.3390/MA13173770.

[119] M. M. Attallah, R. Jennings, X. Wang, and L. N. Carter, "Additive manufacturing of Ni-based superalloys: The outstanding issues," *MRS Bulletin*, vol. 41, no. 10. Materials Research Society, pp. 758–764, Oct. 01, 2016. doi: 10.1557/mrs.2016.211.

[120] V. Sankar, D. Sebastian, D. Joseph, J. Jose, A. Kurian, and B. Associateprofessor, "ScienceDirect Optimized Thermal Barrier Coating for Gas Turbine Blades," 2018. [Online]. Available: www.sciencedirect.comwww.materialstoday.com/proceedings

[121] R. A. Miller, "CURRENT STATUS OF THERMAL BARRIER COATINGS-AN OVERVIEW*," 1987.

[122] L. E. Murr, “A Metallographic Review of 3D Printing/Additive Manufacturing of Metal and Alloy Products and Components,” *Metallography, Microstructure, and Analysis*, vol. 7, no. 2. Springer New York LLC, pp. 103–132, Apr. 01, 2018. doi: 10.1007/s13632-018-0433-6.

[123] D. Cherrared, “Numerical simulation of film cooling a turbine blade through a row of holes,” *Journal of Thermal Engineering*, vol. 3, no. 2, pp. 1110–1120, Apr. 2017, doi: 10.18186/thermal.298609.

[124] “Jewel in the crown: Rolls-Royce’s single-crystal turbine blade casting foundry.” https://www.theengineer.co.uk/content/in-depth/jewel-in-the-crown-rolls-royce-s-single-crystal-turbine-blade-casting-foundry/ (accessed Nov. 30, 2022).

[125] K. Harris, G. L. Erickson, and R. E. Schwer, “MAR M 247 Derivations - CM 247 LC DS Alloy and CMSX Single Crystal Alloys: Properties and Performance.”

[126] J. Belan, “GCP and TCP Phases Presented in Nickel-base Superalloys,” in *Materials Today: Proceedings*, Elsevier Ltd, 2016, pp. 936–941. doi: 10.1016/j.matpr.2016.03.024.

[127] H. Hilal, R. Lancaster, S. Jeffs, J. Boswell, D. Stapleton, and G. Baxter, “The influence of process parameters and build orientation on the creep behaviour of a laser powder bed fused ni-based superalloy for aerospace applications,” *Materials*, vol. 12, no. 9, 2019, doi: 10.3390/ma12091390.

[128] R. I. Badiger, S. Narendranath, and M. S. Srinath, “Microstructure and mechanical properties of Inconel-625 welded joint developed through microwave hybrid heating,” *Proc Inst Mech Eng B J Eng Manuf*, vol. 232, no. 14, pp. 2462–2477, Dec. 2018, doi: 10.1177/0954405417697350.

[129] J. Zhou, Z. Chen, H. Persson, R. L. Peng, R. M’Saoubi, and D. Gustasson, “Comparative assessment of the surface integrity of AD730® and IN718 superalloys in high-speed turning with a CBN tool,” *Journal of Manufacturing and Materials Processing*, vol. 3, no. 3, Sep. 2019, doi: 10.3390/jmmp3030073.

[130] “HAYNES ® 282 ® alloy Principal Features,” 2021.

[131] S. S. Babu, “Alloy Development of Nickel-Based Superalloy Weld Filler Metals Using Computational Thermodynamics Solidification Microstructure Control in Electron Beam Additive Manufacturing View project Infrared Monitoring of the Electron Beam Melting Process View project,” 2014. [Online]. Available: https://www.researchgate.net/publication/237632049

[132] K. Bazaleeva, A. Aleksandrova, and E. Balakirev, “Structure features of the composite materials Inconel 625/TiC, produced by LMD method,” in *Journal of Physics: Conference Series*, Institute of Physics Publishing, Nov. 2018. doi: 10.1088/1742-6596/1109/1/012053.

[133] J. Sieniawski, M. Zielińska, J. Sieniawski, and B. Gajecka, “Special Issue ‘Superalloys-Currents Trends in Development of Their Microstructure and Properties’ Criterion for selection the optimal physical and chemical properties of cobalt aluminate powder used in investment casting process,” 2009, [Online]. Available: https://www.researchgate.net/publication/266592705

[134] F. Vakili-Tahami and M. R. Adibeig, “Investigating the possibility of replacing IN 738LC gas turbine blades with IN 718,” *Journal of Mechanical Science and Technology*, vol. 29, no. 10, pp. 4167–4178, Oct. 2015, doi: 10.1007/s12206-015-0911-6.

[135] V. M. Beglov, B. K. Pisarev, and G. G. Reznikova, “EFFECT OF BORON AND HAFNIUM ON THE CORROSION RESISTANCE OF HIGH-TEMPERATURE NICKEL ALLOYS,” 1992.

[136] T. Sugui, W. Minggang, L. Tang, Q. Benjiang, and X. Jun, “Influence of TCP phase and its morphology on creep properties of single crystal nickel-based superalloys,” *Materials Science and Engineering A*, vol. 527, no. 21–22, pp. 5444–5451, Aug. 2010, doi: 10.1016/j.msea.2010.05.027.

[137] F. Stein and A. Leineweber, “Laves phases: a review of their functional and structural applications and an improved fundamental understanding of stability and properties,” *Journal of Materials Science*, vol. 56, no. 9. Springer, pp. 5321–5427, Mar. 01, 2021. doi: 10.1007/s10853-020-05509-2.

[138] A. Basak and S. Das, “Microstructure of nickel-base superalloy MAR-M247 additively manufactured through scanning laser epitaxy (SLE),” *J Alloys Compd*, vol. 705, pp. 806–816, 2017, doi: 10.1016/j.jallcom.2017.02.013.

[139] M. R. Jahangiri, H. Arabi, and S. M. A. Boutorabi, “Development of wrought precipitation strengthened IN939 superalloy,” *Materials Science and Technology (United Kingdom)*, vol. 28, no. 12, pp. 1470–1478, Dec. 2012, doi: 10.1179/1743284712Y.0000000073.

[140] A. S. Shaikh, “Development of a γ’ Precipitation Hardening Ni-Base Superalloy for Additive Manufacturing,” 2018, doi: 10.13140/RG.2.2.11472.81921.

[141] J. H. Westbrook, “Segregation at grain boundaries,” *Metallurgical Reviews*, vol. 9, no. 1, pp. 415–471, 1964, doi: 10.1179/mtlr.1964.9.1.415.

[142] Y. Li, A. J. Bushby, and D. J. Dunstan, “The Hall-Petch effect as a manifestation of the general size effect,” *Proceedings of the Royal Society A: Mathematical, Physical and Engineering Sciences*, vol. 472, no. 2190, Jun. 2016, doi: 10.1098/rspa.2015.0890.

[143] “EOS NickelAlloy IN939 Material Data Sheet Metal Solutions.”

[144] B. Gleeson, N. Mu, and S. Hayashi, “Compositional factors affecting the establishment and maintenance of Al2O3 scales on Ni-Al-Pt systems,” *J Mater Sci*, vol. 44, no. 7, pp. 1704–1710, Apr. 2009, doi: 10.1007/s10853-009-3251-z.

[145] J. M. Gambogi, “ZIRCONIUM AND HAFNIUM.”

[146] A. K. Jena and M. C. Chaturvedi, “Review The role of alloying elements in the design of nickel-base superalloys,” 1984.

[147] “Nickel Based Superalloys.” https://www.phase-trans.msm.cam.ac.uk/2003/Superalloys/superalloys.html (accessed Nov. 30, 2022).

[148] R. Duan *et al.*, “In situ alloying based laser powder bed fusion processing of β Ti–Mo alloy to fabricate functionally graded composites,” *Compos B Eng*, vol. 222, no. May, 2021, doi: 10.1016/j.compositesb.2021.109059.

[149] F. Chu *et al.*, "Influence of satellite and agglomeration of powder on the processability of AlSi10Mg powder in Laser Powder Bed Fusion," *Journal of Materials Research and Technology*, vol. 11, pp. 2059–2073, Mar. 2021, doi: 10.1016/j.jmrt.2021.02.015.

[150] S. Özbilen, "Satellite formation mechanism in gas atomized powders," *Powder Metallurgy*, vol. 42, no. 1, pp. 70–78, 1999, doi: 10.1179/pom.1999.42.1.70.

[151] M. Simonelli *et al.*, "A comparison of Ti-6Al-4V in-situ alloying in Selective Laser Melting using simply-mixed and satellited powder blend feedstocks," *Mater Charact*, vol. 143, pp. 118–126, Sep. 2018, doi: 10.1016/j.matchar.2018.05.039.

[152] L. Farquhar, G. Maddison, L. Hardwick, F. Livera, I. Todd, and R. Goodall, "In-Situ Alloying of CoCrFeNiX High Entropy Alloys by Selective Laser Melting," *Metals (Basel)*, vol. 12, no. 3, Mar. 2022, doi: 10.3390/met12030456.

[153] P. Chen, X. Yao, M. M. Attallah, and M. Yan, "In-situ alloyed CoCrFeMnNi high entropy alloy: Microstructural development in laser powder bed fusion," *J Mater Sci Technol*, vol. 123, pp. 123–135, 2022, doi: 10.1016/j.jmst.2021.11.083.

[154] L. Y. Zhou, J. Fu, and Y. He, "A Review of 3D Printing Technologies for Soft Polymer Materials," *Advanced Functional Materials*, vol. 30, no. 28. Wiley-VCH Verlag, Jul. 01, 2020. doi: 10.1002/adfm.202000187.

[155] Y. Li, A. J. Bushby, and D. J. Dunstan, "The Hall-Petch effect as a manifestation of the general size effect," *Proceedings of the Royal Society A: Mathematical, Physical and Engineering Sciences*, vol. 472, no. 2190, Jun. 2016, doi: 10.1098/rspa.2015.0890.

[156] A. Gaikwad *et al.*, "Multi phenomena melt pool sensor data fusion for enhanced process monitoring of laser powder bed fusion additive manufacturing," *Mater Des*, vol. 221, Sep. 2022, doi: 10.1016/j.matdes.2022.110919.

[157] R. McCann *et al.*, "In-situ sensing, process monitoring and machine control in Laser Powder Bed Fusion: A review," *Additive Manufacturing*, vol. 45. Elsevier B.V., Sep. 01, 2021. doi: 10.1016/j.addma.2021.102058.

[158] "AconityMINI | Aconity3D." https://aconity3d.com/products/aconity-mini/ (accessed Nov. 30, 2022).

[159] "Owner's Manual."

[160] F. S. H. B. Freeman, J. Sharp, J. Xi, and I. Todd, "Influence of solidification cell structure on the martensitic transformation in additively manufactured steels," *Addit Manuf*, vol. 30, Dec. 2019, doi: 10.1016/j.addma.2019.100917.

[161] S. Banoth, C. W. Li, Y. Hiratsuka, and K. Kakehi, "The effect of recrystallization on creep properties of alloy in939 fabricated by selective laser melting process," *Metals (Basel)*, vol. 10, no. 8, pp. 1–16, Aug. 2020, doi: 10.3390/met10081016.

[162] H. Kazempour-Liasi, M. Tajally, and H. Abdollah-Pour, "Liquation cracking in the heat-affected zone of IN939 superalloy tungsten inert gas weldments," *International Journal of Minerals, Metallurgy and Materials*, vol. 27, no. 6, pp. 764–773, Jun. 2020, doi: 10.1007/s12613-019-1954-y.

[163] P. Kanagarajah, F. Brenne, T. Niendorf, and H. J. Maier, "Inconel 939 processed by selective laser melting: Effect of microstructure and temperature on the mechanical properties under static and cyclic loading," *Materials Science and Engineering A*, vol. 588, pp. 188–195, Dec. 2013, doi: 10.1016/j.msea.2013.09.025.

[164] F. Bosio *et al.*, "Production Strategy for Manufacturing Large-Scale AlSi10Mg Components by Laser Powder Bed Fusion," *Jom*, vol. 73, no. 3, pp. 770–780, 2021, doi: 10.1007/s11837-020-04523-8.

[165] "CM-247 LC « Cannon Muskegon." https://cannonmuskegon.com/cm-247-lc/ (accessed Nov. 30, 2022).

[166] L. N. Carter *et al.*, "Process optimisation of selective laser melting using energy density model for nickel based superalloys," *Materials Science and Technology (United Kingdom)*, vol. 32, no. 7, pp. 657–661, Jun. 2016, doi: 10.1179/1743284715Y.0000000108.

[167] "Mid-Size Metal 3D Printer for all kind of materials." https://www.eos.info/en/additive-manufacturing/3d-printing-metal/eos-metal-systems/eos-m-290?utm_source=google&utm_medium=cpc&utm_campaign=brand_UK&utm_content=wyn&gclid=Cj0KCQiAm5ycBhCXARIsAPldzoWT56mR4R5gE8aIz9xkJEs5ACpb4_XTqU9fj6s3mShIoID41i5LiSgaAp-nEALw_wcB (accessed Nov. 30, 2022).

[168] A. Lyle, "PhD Thesis Printability Maps for Nickel Superalloys," 2017.

[169] T. U. Tumkur *et al.*, "Nondiffractive beam shaping for enhanced optothermal control in metal additive manufacturing," *Sci Adv*, vol. 7, no. 38, pp. 1–12, 2021, doi: 10.1126/sciadv.abg9358.

[170] Y. M. Wang *et al.*, "Additively manufactured hierarchical stainless steels with high strength and ductility," *Nat Mater*, vol. 17, no. 1, pp. 63–70, Jan. 2018, doi: 10.1038/NMAT5021.

[171] Y. C. Hagedorn, J. Risse, W. Meiners, N. Pirch, K. Wissenbach, and R. Poprawe, "Processing of nickel based superalloy MAR M-247 by means of High Temperature - Selective Laser Melting (HT - SLM)," *High Value Manufacturing: Advanced Research in Virtual and Rapid Prototyping - Proceedings of the 6th International Conference on Advanced Research and Rapid Prototyping, VR@P 2013*, pp. 291–295, 2014, doi: 10.1201/B15961-54.

[172] Y. S. Lee *et al.*, "Asymmetric Cracking in Mar-M247 Alloy Builds During Electron Beam Powder Bed Fusion Additive Manufacturing," *Metall Mater Trans A Phys Metall Mater Sci*, vol. 49, no. 10, pp. 5065–5079, Oct. 2018, doi: 10.1007/s11661-018-4788-8.

[173] C. Sainte-Catherine *et al.*, "STUDY OF DYNAMIC ABSORPTIVITY AT 10.6 µm (CO2) AND 1.06 µm (Nd-YAG) WAVELENGTHS AS A FUNCTION OF TEMPERATURE," *Journal de Physique IV Proceedings*, vol. 111, no. C7, p. 1, 1991, doi: 10.1051/jp4:1991741ï.

[174] P. Pant *et al.*, "A study of the influence of novel scan strategies on residual stress and microstructure of L-shaped LPBF IN718 samples," *Mater Des*, vol. 214, Feb. 2022, doi: 10.1016/j.matdes.2022.110386.

[175] H. T. Brazing *et al.*, "Welding Research," no. February, pp. 1–8, 1971.

[176] "FURTHER INVESTIGATIONS OF DUCTILITY-DIP CRACKING IN HIGH CHROMIUM NI-BASE FILLER METALS."

[177] E. Hernández-Nava, “A study on the mechanical properties of micro-truss Ti-6Al-4V materials fabricated by Electron Beam Melting.”

Appendix A – Aconity Technical Documents

Pyrometer Specifications

KS • KG • KGA 740 - LO

KLEIBER®

High Speed
Infrared Thermometer

High speed pyrometer with fibre optics for very fast temperature measurements

- Measurement ranges from 200 . . . 3,500 °C
- Response time 6 µs
- Measuring field diameter from 0.3 mm
- Wide range of optical heads

The **KLEIBER 740 - LO** with fibre optics is a High Speed pyrometer for very fast temperature measurements.

The device is designed for applications in **research and development** areas as well as **high speed industrial applications**. It is also applicable for **material research or testing** and **temperature measurement** in **combustion engines** and **turbines**.

The device enables you to solve high speed **applications in laser areas** by using laser rejection filters. The KLEIBER 740 - LO can achieve such very fast measurements only due to its **response time of 6 µs** (t_{95}).

Also difficult applications as measurements on silicon or tungsten are possible.

Apart from the response time the KLEIBER 740 - LO excels with its variety of **fibre optic heads**. These optics offer **measuring spots from 0.3 to 11 mm** at measuring distances from 60 to 1000 mm.

The optical head and the fibre optics cable can withstand **ambient temperatures up to 260 °C** and it can be equipped with a vacuum feed through if necessary.

All connections and user controls including emissivity correction are conveniently located on the rear side of the instrument. The **emissivity** correction is adjustable between 0.1 and 1.0 (stepless). In addition to a 0 / 4 . . . 20 mA output a BNC connector for additional measurement output is positioned on the rear side.

A **LED-pilot light** is integrated as standard targeting aid. The pilot light enables quick and accurate focussing onto the measurement area.

Furthermore, wide measuring ranges has been developed to cover additional applications using this high speed pyrometer.

Applications:

- Laser applications (cutting, welding, soldering, etc.)
- Material research/-testing
- Combustion engines
- Airbag testing
- Wafer control
- Turbines
- Plasma measurements
- Explosion processes

Materials:

- Metals (also tungsten or silicon)
- Synthetic materials
- Ceramics

KLEIBER combines decades of experience with a passion for cutting-edge technology.

High Speed Pyrometer

KLEIBER 740 - LO

Device types

Device type	KS 740 - LO	KS 740 - LO	KG 740 - LO	KG 740 - LO	KGA 740 - LO
Meas. range	600 ... 1,600 °C	800 ... 2,300 °C	300 ... 1,400 °C	500 ... 2,500 °C	200 ... 1,000 °C
Spectral range	0.85 ... 1.05 µm	0.85 ... 1.05 µm	1.58 ... 1.80 µm	1.58 ... 1.80 µm	1.58 ... 2.20 µm

Device type	KGA 740 - LO	KGA 740 - LO	KGA 740 - LO	KGA 740 - LO
Meas. range	400 ... 1,300 °C	300 ... 2,300 °C	400 ... 3,000 °C	350 ... 3,500 °C
Spectral range	1.58 ... 2.20 µm	2.00 ... 2.20 µm	2.00 ... 2.20 µm	2.00 ... 2.20 µm

Other temperature ranges on request

Technical data

Measurement outlet analog	0 ... 20 mA or 4 ... 20 mA, maximum burden 500 Ω 0 ... 10 V via BNC
Accuracy	0.75 % of measured value (at 25 °C , ε = 1)
Reproducibility	< 0.3 % of measured value (at 25 °C, ε = 1)
Response time t_{95}	6 µs via voltage output 9 µs via current output
Emissivity (ε)	Adjustable from 0.1 ... 1
Aiming device	LED pilot light
Operating temperature	0 ... +40 °C pyrometer 0 ... +260 °C for optical head and fibre cable
Storage temperature	-20 ... +70 °C
Power supply	24 V DC, 0.2 A or 24 V AC, 0.2 A
Degree of protection	IP 54 according to DIN 40 050
Test base	EN 55 011 : 1998, limit class A
CE marking	According to EU regulations
Dimensions pyrometer	170 x 70 x 70 mm (LxWxH)
Weight	about 880 g

Optics

Description	Measuring distance in mm	Measuring field ⌀ in mm	Measuring range in °C	Fibre optics cable	Aperture in mm
LVO 25	80 ... 300	1.6 ... 4.3	from 200	blue	13
LVO 35	250 ... 1,000	3.5 ... 11.0	from 200	blue	21
LVA 25	110 ... 800	0.8 ... 5.0	from 200	red	13
LVO 25 S - 1	115 ... 300	0.4 ... 1.5	from 400	red	10
LVO 25 S - 2	200 ... 240	0.4 ... 1.5	from 350	red	12
LVO 25 S - 3	78	0.3	from 400	red	10
LVO 25 S - 4	60	0.5	from 200	red	11
LVO 25 S - 5	70 ... 200	1.0 ... 2.6	from 200	blue	12
LVO 25 S - 6	250 ... 500	3.5 ... 6.3	from 200	blue	16
LVO 25 S - 9	74 ... 284	0.7 ... 3.0	from 400	red	10

Fibre optics cable: Available length between 1.5 and 25 m with stainless steel housing or PTFE housing as well as vacuum lead through special fibre optics cable.

Accessories optic

Protection glass
Screw cap incl. protection glass - very fast changeable
Cooling jacket with integrated air purge
Laser rejection filter 920 ... 1100 nm
Ball and socket mounting, high grade steel
90° mirror
Air purge unit, stainless steel

Accessories pyrometer

Connecting cable, standard length 4 m (other cable length see website)
BNC-Connecting cable, standard length 4 m (other cable length see website)
Power supply in aluminum housing, 115 V AC, 24 V AC
Power supply in aluminum housing, 230 V AC, 24 V AC
Power supply KNG, 85 ... 265 V AC, 24 V DC, 600 mA
Power supply KNG-2, with 2 limit contacts, 85 ... 265 V AC, 24 V DC, 600 mA

CE
Made in Germany

KLEIBER Infrared GmbH
Am Gewände 3
D-07333 Unterwellenborn
Germany

Phone: +49 (0)3671 / 527 20 - 0
Fax: +49 (0)3671 / 527 20 - 12
E-Mail: info@kleiberinfrared.com
Internet: www.kleiberinfrared.com